UNIVERSIDADE ESTADUAL DE CAMPINAS

FACULDADE DE ENGENHARIA MECÂNICA

E INSTITUTO DE GEOCIÊNCIAS

GUSTAVO BARROSO DIAS IGNÁCIO

CRP Tomography

Tomografia CRP

CAMPINAS, SP

2021

GUSTAVO BARROSO DIAS IGNÁCIO

CRP Tomography

Tomografia CRP

Thesis presented to the School of Mechanical Engineering and Institute of Geosciences of the University of Campinas in partial fulfillment of the requirements for the degree of Doctor in Petroleum Sciences and Enginnering in the area of Reservoirsand Management.

Tese apresentada à Faculdade de Engenharia Mecânica e Instituto de Geociências da Universidade Estadual de Campinas como parte dos requisitos exigidos para a obtenção do título de Doutor em Ciências e Engenharia de Petróleo na área de Reservatórios e Gestão.

Orientador: Prof. Dr. Martin Tygel

Este exemplar corresponde à versão final da Tese defendida pelo aluno Gustavo Barroso Dias Ignácio, e orientada pela Prof. Dr. Martin Tygel.

CAMPINAS, SP

2021

Informações para Biblioteca Digital

Título em outro idioma: Tomografia CRP
Palavras-chave em inglês:
Seismic tomography
Non-linear optimization
Área de concentração: Reservatórios e Gestão
Titulação: Doutor em Ciências e Engenharia de Petróleo
Banca examinadora:
Martin Tygel [Orientador]
Armando Lopes Farias
Jorge Henrique Faccipieri Junior
Rodrigo Bloot
Tiago Antonio Alves Coimbra
Data de defesa: 26-01-2021
Programa de Pós-Graduação: Ciências e Engenharia de Petróleo

Identificação e informações acadêmicas do(a) aluno(a)
- ORCID do autor: https://orcid.org/0000-0001-9244-3607
- Currículo Lattes do autor: http://lattes.cnpq.br/9453562916732532

UNIVERSIDADE ESTADUAL DE CAMPINAS

FACULDADE DE ENGENHARIA MECÂNICA

E INSTITUTO DE GEOCIÊNCIAS

TESE DE DOUTORADO

CRP Tomography

Tomografia CRP

Autor: Gustavo Barroso Dias Ignacio

Orientador: Prof. Dr. Martin Tygel

A Banca Examinadora composta pelos membros abaixo aprovou esta Tese:

Prof. Dr. Martin Tygel
Centro de Estudos de Petróleo/UNICAMP

Dr. Armando Lopes Farias
PETROBRAS

Dr. Jorge Henrique Faccipieri Junior
Centro de Estudos de Petróleo/UNICAMP

Prof. Dr. Rodrigo Bloot
Universidade Federal da Integração Latino-Americana/Foz do Iguaçú

Dr. Tiago Antonio Alves Coimbra
Centro de Estudos de Petróleo/UNICAMP

A ata da defesa com as respectivas assinaturas dos membros encontra-se no processo de vida acadêmica do aluno.

Campinas, 26 de Janeiro de 2021

Por amor às causas perdidas

"Mapas e bússolas
Sorte e acaso
Quem sabe do que depende?
Ao sabor do acaso
Apesar dos pesares
O barco ainda flutua"

Engenheiros do Hawaii -
Mapas do Acaso

Acknowledgments

I am grateful to my parents Benícia Barroso Dias Ignácio and Lázaro Ignácio and my brother Alexandre Barroso Dias Ignácio. My supervisor Martin Tygel, all the professors, friends and staff from High-Performance Geophysics Lab. Now, let me write some words in my mother language.

Gostaria de agradecer ao meu irmão mais velho, Alexandre Barroso Dias Ignácio, minha primeira referência de inteligência e que me inspirou, pela primeira vez, a buscar, valorizar e admirar o conhecimento. Seu brilhantismo é minha fonte de inspiração intelectual desde sempre.

Gostaria de agradecer, também, aos meus pais Lázaro e Benícia, que nunca mediram esforços para me proporcionar uma educação de qualidade. Em meio a tantos problemas e obstáculos ao longo do caminho, com eles eu consegui todo apoio necessário, sempre. Obrigado por terem me ensinado a resolver meus primeiros problemas.

Ao meu orientador, Martin Tygel, que me recebeu de portas abertas em seu laboratório, mesmo não tendo, a princípio, nenhum conhecimento prévio da área de geofísica. Nossa iteração orientador/orientado me tornou, certamente, um pesquisador e pessoa melhores. Obrigado por tudo.

Agradeço ao programa de inovação tecnológica Cepid (Centro de Pesquisa, Inovação e Difusão) CCEC - Centro para Computação em Engenharia e Ciências, da Fundação de Amparo à Pesquisa do Estado de São Paulo, pelo apoio, suporte e infraestrutura à produção dessa tese. Também, agradeço à Fundação de Amparo à Pesquisa do Estado de São Paulo, processo 2016/19115-0, pelo suporte ao presente projeto de pesquisa. Finalmente, agradeço ao CCEC pela participação em eventos e ricas discussões interdisciplinares ao longo do presente projeto.

Não posso deixar de agradecer ao colega e amigo que ganhei ao longo dessa jornada, Tiago Coimbra. Obrigado por me ensinar o caminho e dar as ferramentas necessárias para iniciar minha pesquisa em Geofísica. Foi ele quem primeiro apresentou o instigante problema que veio a me guiar por todo esse período de pesquisa. Sem dúvidas, os frutos desse trabalho são consequências diretas de sua participação. Obrigado por tudo.

Não posso deixar de agradecer, também, a toda equipe, colegas e amigos do High-Performance Geophysics Lab. Nesse sentido, agradeço ao Jorge por me receber de portas abertas no laboratório. Obrigado pelos conselhos, conversas e, principalmente, por me fornecer os textos bases de tomografia e, além disso, ter fortemente me aconselhado a programar tudo do início. Agradeço também ao amigo Alexandre William Camargo, pela parceria na parte final da minha pesquisa, com o qual realizei uma dobradinha interessante entre tomografia e fwi. Obrigado Alcides, Caian, Danny, João Renato, Joe, Jonas, Nicholas, Rafael, Rodrigo Bloot, Tainá, entre outros, pela amizade, companheirismo, risadas e bons momentos proporcionados em meio a essa jornada. Agradecimentos especiais, também, ao Paulo, que literalmente me salvou de problemas computacionais, meses antes da minha defesa. Obrigado.

Quero aqui, também, dedicar agradecimentos especiais ao meu amigo Edwin Fagua. Talvez ele não saiba, mas foi fundamental para o início da minha jornada no campo de processamento sísmico. Eu o considero como meu primeiro professor, tendo ensinado, através de conversas e bate-papos na lousa ou na mesa de café, os conceitos primários de processamento sísmico.

Agradeço também à Petrobrás pelo apoio em parte do projeto, tendo me propiciado, inclusive, uma ponte entre a pesquisa puramente científica e a pesquisa com foco em aplicações reais na indústria, a partir da participação em projetos específicos.

Finalmente, gostaria de agradecer aos meus cães: Toby (o Piquira), Laro-Giro, Michael, Frederico, Tetê, Suzy, Tiara, Adriela e Luara. Muitos deles dedicaram uma vida inteira a proporcionar amor, carinho, segurança e companheirismo à minha família. Alguns, eu tenho como irmãos. Outros, como filhos. Em meio a tantas tarefas, dificuldades e cansaço, inúmeras vezes eles foram a fonte de energia e alegria necessárias para prosseguir. Obrigado a todos, do fundo do meu coração.

Resumo

As informações de subsuperfície extraídas de dados sísmicos de reflexão desempenham um papel crucial para a exploração e produção de reservatórios de petróleo e gás. Desta forma, técnicas de imageamento e inversão que fornecem essas informações estão sempre em demanda. Devido à sua importância, os modelos de velocidade têm sido os principais parâmetros para inversão sísmica. Por essa razão, o termo construção de modelos de velocidade é bastante popular em sísmica. De fato, essa terminologia é conhecida como inversões de, não apenas modelos de velocidade, mas também parâmetros gerais que descrevem os modelos geológicos de interesse. Modelos de velocidade confiáveis são essenciais para métodos de imageamento sísmico, particularmente migração. De fato, os avanços científicos e tecnológicos em migração estão diretamente relacionados com os avanços correspondentes na construção de modelos de velocidade. O foco principal dessa tese é a construção tomográfica de modelos de velocidade. Essa tese propõe um novo método de tomografia sísmica, denominado tomografia CRP. Baseado na estereotomografia, com a qual compartilha várias similaridades, a tomografia CRP tem, contudo, diferenças significantes na quantidade e natureza dos parâmetros envolvidos no processo de inversão. Ao contrário da estereotomografia, no qual os parâmetros observados são coletados/extraídos individualmente do dado de entrada, a tomografia CRP faz uso das seções CRP, extraídas e estimadas do dado de entrada. Mais especificamente, cada seção CRP consiste em pares fonte-receptor dentro dos dados de entrada para os quais os raios de reflexão primária para uma determinada interface têm o mesmo ponto de reflexão comum. Da mesma forma que na estereotomografia, alguns pontos individuais são de fato coletados na tomografia CRP. Chamados de pontos de referência CRP, esses pontos são estendidos para as correspondentes seções CRP, extraídas do dado de entrada por meio de análise de coerência performadas com tempos de trânsito paramétricos adequados. De fato, a tomografia CRP leva o nome de tais tempos de trânsito, também chamados de tempo de trânsito CRP. Essa tese mostra como a adição de mais informações relacionadas a um mesmo ponto em profundidade, previamente desconhecido, ajuda na inversão de diferentes tipos de modelos de velocidade. Todas as informações relacionadas a um mesmo ponto de reflexão comum são trabalhadas simultaneamente durante a inversão para melhor inverter a localização do respectivo ponto de modelo em profundidade. Testes numéricos que ilustram essa tese sugerem que o uso

conjunto de parâmetros provenientes de seções CRP atua como uma restrição natural incorporada ao problema tomográfico. As seções CRP permitem que mais partes do modelo de velocidade sejam analisados, uma vez que mais pares de raios são traçados e usados, trazendo mais informações internas para o problema inverso. Resultados encorajadores fornecidos por alguns testes sintéticos confirmam as boas expectativas. Dessa forma, a tomografia CRP parece ter um bom potencial para se consolidar como uma confiável técnica para construção de modelos de velocidade.

Palavras Chave: Tomografia sísmica, Otimização não-linear.

Abstract

Subsurface information extracted from seismic reflection data play a crucial role for exploration and production of oil and gas reservoirs. In this way, imaging and inversion techniques that provide such information are always in demand. Because of their importance, seismic velocities have been the main parameters for inversion. Because of that, the term velocity model building is very popular in the seismic literature. In fact, this terminology is referred to the inversion, not only of velocities, but also other model parameters that describe the geology of interest. Reliable and meaningful velocity models are essential to seismic imaging methods, most particularly migration. In fact, scientific and technological advances in migration come hand-in-hand with corresponding advances in velocity model building. The main focus of this thesis is on tomographic velocity model building. This thesis proposes a new tomography method, named CRP tomography. Based on the stereotomographic method from which it has several similarities, CRP tomography has, however, significant differences on the number and nature of the parameters involved in the inversion process. As opposed to stereotomography, for which the observed parameters are individually picked or extracted from the input data, CRP tomography makes use of parameter gathers, called CRP gathers, picked/estimated from the input data. More specifically, each CRP gather consists of source-receiver pairs within the input data for which the primary-reflection rays for a certain interface have the same (common) reflection point. In the same way as in the stereographic method, a few individual points are actually picked in CRP tomography. Referred to as reference points, these points are extended to corresponding CRP gathers extracted from the input data by means of coherence-analysis estimations performed on suitably defined parametric traveltimes. In fact, CRP tomography bears its name from such traveltimes, also referred to CRP traveltimes. This thesis shows how the addition of more information related to the same, previously unknown, point in depth, helps to constrain different kind of velocity models. All information related to each common-reflection-point are considered simultaneously to improve the localization of the particular related model common-depth-point. Practical tests that illustrates this thesis show that the use of CRP information acts as a natural constraint that is incorporated to the tomographic inverse problem. The CRP gathers allow more parts of the velocity model to be covered because more pairs of rays are traced and used bringing more internal information to the inversion

process. Encouraging results provided by quite a few synthetic-data tests confirms those good expectations. As such, CRP tomography is seen to have a good the potential of being a reliable technique for velocity model building.

Keywords: Seismic tomography, Non-linear optimization.

Contents

Chapter 1

Introduction

Subsurface information extracted from seismic reflection data play a crucial role for exploration and production of oil and gas reservoirs. In this way, imaging and inversion techniques that provide such information are always in demand. Because of their importance, seismic velocities have been main model parameters for inversion. Because of that, the term *velocity model building* (Jones, 2010) is very popular in the seismic literature. In fact, this terminology is referred to as inversions of, not only velocities, but also general parameters that describe the geological models of interest.

Reliable and meaningful velocity models are essential to seismic imaging methods such as migration (Gray et al., 2001). In fact, scientific and technological advances in migration come hand-in-hand with corresponding advances in velocity model building. The main focus of this thesis is on tomographic velocity model building. Along similar lines as the ones of the stereotomography (Billette and Lambaré, 1998; Lambaré, 2008; Billette et al., 2003; Lambaré, 2004) a new method, denoted common-reflection-point (CRP) tomography is proposed. For completeness, a brief review of full-wave-inversion (FWI), presently the most ambitious parameter-inversion approach and subject of active investigation, is provided and its relation to stereotomography emphasized. In this context, velocity models produced by proposed CRP tomography method are suggested as initial velocity models for FWI.

Following Billette and Lambaré (1998), seismic tomography methods aim to recover smooth velocity models that are able to capture the low-frequency, trend-like behavior of velocity wavefield in the subsurface region illuminated by the seismic data. Referred to as macro or background velocity models, such velocity wavefields, if accurately inverted, play an essential role in advanced imaging schemes, such as migration ad FWI. As pointed out in Billette et al. (2003), such "smooth velocity-model description that allows the use of ray-based prestack depth-imaging tools with an adaptive

model representation".

> **Tomographic velocities:** Following the literature trend, this thesis makes use of B-spline interpolation schemes to represent the smooth, macro-velocity models that are the objective of seismic tomography. As briefly reviewed in Appendix D, for a user-selected rectangular mesh that covers the depth domain of interest, the inversion aims to obtain the B-spline interpolation coefficients at all mesh points. The column vector $\mathbf{m}^{vel}$ of such coefficients is one of the key invertibles of tomography methods.

1.1   Seismic reflection tomography

Seismic tomography is a powerful tool to address velocity-model-building and imaging problems in a wide variety of situations. The word tomography derives from Ancient Greek word *tomos* ($\tau\acute{o}\mu o\varsigma$), meaning *slices*, *pieces* or *sections* and *graphō* ($\gamma\rho\acute{\alpha}\phi\omega$) meaning *to write*, *to draw* or *to describe*. In the present context, seismic tomographic methods are designed to obtain, from user-selected "pieces" (e.g., events or parameters) of the seismic data, a subsurface velocity model that "explains" those data pieces in a way that satisfies the user demands. The above, somewhat subjective assertion requires some clarification. To do that, a first observation is that the formulation of any actual tomographic problem involves the following elements: (a) a *data space*, which is a known user-selected, set of parameters picked or extracted from the input data; (b) a *model space*, which is an unknown parameter set that needs to be inverted from the data space and from which the sought-for macro-velocity model is obtained; (c) a forward-modeling engine assumed to be able to produce a synthetic version of the data space from a given trial model space and (d) a misfit function that measures the discrepancy between the synthetic and observed data sets. Based on such elements, a velocity model that "explains" the data is one that the discrepancy (misfit) between data and synthetic spaces is acceptable.

As explained in Chapter 2, the tomographic problem is solved by a least squares (LSQR) iterative approach: Starting from a user-selected initial velocity model, as well as the parameters of a user-selected set of points of the input data, updated velocity models are sequentially obtained by Gauss-Newton optimization that minimizes the residuals (misfit) between the the given observed parameters and simulated ones computed by the forward-modeling engine.

As seen from a vast literature, tomographic methods may involve, not only reflection data, as considered in this thesis (Billette and Lambaré, 1998; Duveneck and Hubral, 2002; Farra and

Madariaga, 1988; Sword Jr, 1986), but also transmission (e.g., cross-well tomography (Washbourne et al., 2002), passive seismics (Zhang et al., 2009)) and refraction (e.g., near-surface statics corrections (Chang et al., 2002; Zhu et al., 2009)) data. Moreover, tomographic approaches can be applied, not only in the unstacked time domain (Billette and Lambaré, 1998; Farra and Madariaga, 1988; Sword Jr, 1986), but also in the time- and depth-migrated domains (Kosloff et al., 1996; Stork, 1992; Dell et al., 2014). Tomographic macro-velocity models consist of either (i) a single smooth-velocity layer or (ii) a layered-cake structure of a few smooth-velocity layers bonded by piecewise-smooth key reflection interfaces. In the first case, only the velocity distribution is to be retrieved. In the second case, not only the velocities within each layer, but also the the interface positions are to be estimated. Because of their smooth character, such velocity models are amenable to the use of ray formulations (see, e.g., Cerveny, 2005; Popov, 2002) for adequate description of the seismic wave propagation involved.

In this thesis, all tomographic methods under consideration are applied to the unmigrated time domain. Moreover, ray-based solutions of the constant-density acoustic wave equation are assumed to be adequate to explain the seismic events of interest. Finally, the class of admissible velocity models is assumed to consist of smooth models of macro or background character, these being defined on a single layer in depth domain.

1.2   Classification of reflection tomography methods

Reflection tomography methods admit a simple classification in terms of their governing parameters. Such parameters are attached to user-selected (manually or automatically picked) points of interest in the seismic data. The most important parameter, being present in all methods, is reflection traveltime. Additional important parameters are slopes and curvatures, respectively first- and second-order derivatives of traveltime with respect of source and receiver locations.

(a) **Traveltime tomography:** These refer to tomographic methods for which the data space consists of reflection traveltimes and positions. Typically, those methods aim to recover the a macro-velocity model together with the position of key reflector interfaces provided by the user (Bishop et al., 1985; Sword Jr, 1986; Farra and Madariaga, 1988). A disadvantage of the traveltime tomography refers to the interpretative character of the picking process, which needs to be carried out on well identified and interpreted reflection events in the unmigrated domain. In the case low signal-to-noise ratio is low, this can be a difficult task.

(b) **Slope tomography:** These refer to methods for which the data space, in addition to traveltimes and positions, also consists of traveltime slopes, both picked from the unmigrated seismic data. For any reflection ray, the traveltime slopes (ray parameters) at the source and receiver locations provide the departure and arrival directions of that ray at the measurement surface. The theoretical and practical importance of such directional information for seismic-imaging purposes has been recognized for a long time, also with the development of acquisition technology with direction sensitivity (Rieber, 1936).

It is also important to be mentioned that the required slope picking became possible upon the introduction of the concept of locally-coherent events, each being defined by the source and receiver locations, the two-way traveltime and the slope (horizontal slowness vector components or ray parameters) at the source and receiver. As such, a locally-coherent event does not need to be associated with an interface in the model, which is now assumed to be represented by means of a smooth velocity field. Note that, for a locally-coherent event the source and receiver locations and traveltime are directly obtained from the acquisition geometry. Moreover, slopes are estimated by means of local slant stacks carried out on common-source and common-receiver gathers (Sword Jr, 1986; Sword, 1987). As pointed out in Billette and Lambaré (1998), such procedure turns out to be easier than the ones used in traveltime tomography and applied in the unstacked domain.

In the framework of this thesis, three slope-tomography methods are described. The first one, called Controlled Directional Reception (CDR) tomography (Riabinkin, 1957; Sword Jr, 1986; Sword, 1987), is briefly reviewed here for historical reasons. It pioneered the concept and use of locally-coherent events. Moreover, CDR has also introduced the use of beta splines (de Boor et al., 1978) to describe the macro-velocity model at each iteration, so that the inversion is reduced to the estimation of the spline coefficients only. This important property can be summarized as follows: The model space of CDR consists of the beta-spline coefficients from which the macro-velocity model is represented.

The CDR is the precursor of the second method, stereotomography, which is the state-of-the-art of the presently available tomographic methods. For that a dedicated exposition is provided in Chapter 3. Finally, the third method is CRP tomography, which can be considered an advanced version of setereotomography. As the main contribution of this thesis, CRP tomography has a dedicated exposition provided in Chapter 5.

(b.1) **Controlled Directional Reception (CDR) tomography:** Firstly proposed within the soviet geophysicist community (Riabinkin, 1957), the CDR method has been studied and advanced in the West (Sword Jr (1986); Sword (1987)). As it is usual in tomographic

methods, CDR method starts with the selection by the user of an initial macro-velocity model, as well as a collection of samples (source-receiver positions and traveltimes) from the input prestack data. Moreover, the source-receiver ray parameters that correspond to all those samples are assumed to be estimated by the previously-indicated procedure.

A brief description of the CDR iteration scheme is now provided. For that, it suffices to understand how, at any given iteration, the forward-modeling engine and the misfit function are formulated. From that, an application of a Gauss-Newton, least-squares (LSQR), basically reviewed in Chapter 2, is used to update that velocity model for the next iteration. Our description follows closely the CDR review in Billette and Lambaré (1998), from Figure 1.1 has been adapted. For simplicity, we consider the case of a single parameter vector of the data space. That vector can be written in terms of its components $(x_s, x_r, p_s, p_r, t_{sr})$, respectively the locations and ray parameters of the source and receiver and the two-way traveltime. Under the consideration of the current macro-velocity model, those parameters allow the construction of the source- and receiver-rays of Figure 1.1. More specifically, the source (resp. receiver) ray starts from point x_s (resp. x_r) and direction p_s (resp. p_r) and proceeds downward up to the level z, that is defined such that the sum of the one-way traveltimes along the two rays equals the given two-way traveltime t_{sr}. Note that the level z is dependent on the actual source and receiver rays. The figure also shows the horizontal separation l_{sr} between the points where the source and receiver rays hit the horizontal level z. That separation is referred to as the *crossing condition* of the source-receiver ray pair. If the velocity model is correct, the source and receiver rays finish their propagation at the same point or, in other words, the crossing condition is zero. With such understanding, for the general case of a data space with several parameter vectors, the misfit function at a given iteration is defined as the sum of the squares of the crossing conditions that of all vector parameters under consideration.

Despite the fact that CDR tomography introduced a revolutionary approach to seismic tomography, the method suffers from practical instabilities. As described in Billette and Lambaré (1998); Lambaré (2008), small errors in slope estimations, which are kept invariant during the inversion process, are bound to produce large errors in the forward-modeling step, especially for laterally varying velocity models. Nevertheless, because of its importance, improvements of CDR tomography, have been proposed (Biondi, 1992; Whiting, 1991).

As briefly described below and in more detail in Chapter 3, the most important method based on CDR is stereotomography Billette and Lambaré (1998); Billette et al. (2003); Lambaré (2004, 2008).
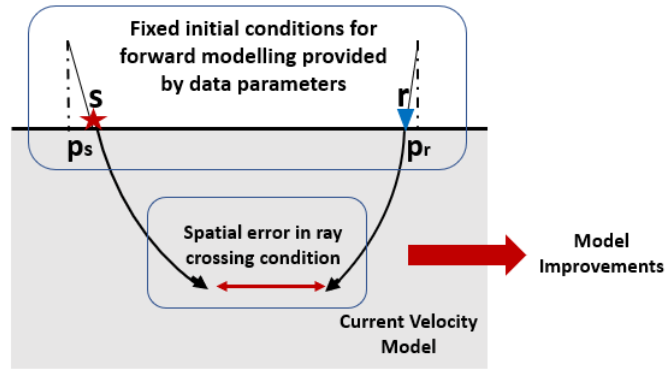
Ray crossing condition for CDR Tomography

Figure 1.1: Forward modeling engine and misfit function for CDR tomography. For a data-space vector $(x_s, x_r, p_s, p_r, t_{sr})$, and the consideration of a current velocity model, the source and receiver rays defined by locations and ray parameters (x_s, p_s) and (x_r, p_r), respectively, propagate downward until hit the horizontal line for which the sum of the one-way traveltimes of both rays equals the given two-way traveltime t_{sr}. The horizontal separation between the points where the two rays hit the level line is referred to the ray-crossing condition, The square of the ray-crossing represents the contribution of the model-space vector to the CDR misfit function.

(b.2) **Stereotomography:** Introduced in the late 1990s, stereotomography constitutes a signifi-cant advance of CDR, trying simultaneously to preserve its good features, while correcting its difficulties. A full description of stereotomography is provided in Chapter 3. As such, the focus of the present considerations lies on a more qualitative overview of the stereoto-mography method, pointing its main differences with respect to its precursor CDR.

An underlying assumption of stereotomography is that, if the velocity model is correct, then a perfect correspondence should exist between each data-space parameter vector and a depth-domain, diffraction-point, model-parameter vector in such a way that the data-space vector would be "explained". Figure 1.2 shows the depth-domain point (x, z), which is the staring point of two upgoing rays of initial direction angles θ_s and θ_r and one-way traveltimes t_s and t_r, respectively. Those rays hit, respectively, the measurement line at the points x_s and x_r with ray parameters (horizontal projection of the slowness vector) p_s and p_r. We now assume that (x_s, x_r) and (x, z) locate a source-receiver pair and a diffraction/reflection point, respectively, and also that p_s, p_r and $t_{sr} = t_s + t_r$ have been picked/extracted from the input data. Then the vector-parameter correspondence

$$\mathbf{d}^{obs} = (x_s, x_r, p_s, p_r, t_{sr}) \Longleftrightarrow \mathbf{m}^{ray} = (x, z, \theta_s, \theta_r, t_s, t_r) \tag{1.1}$$

provides the meaning that the model-vector parameter $\mathbf{m}^{ray}$ explains the data-vector pa-
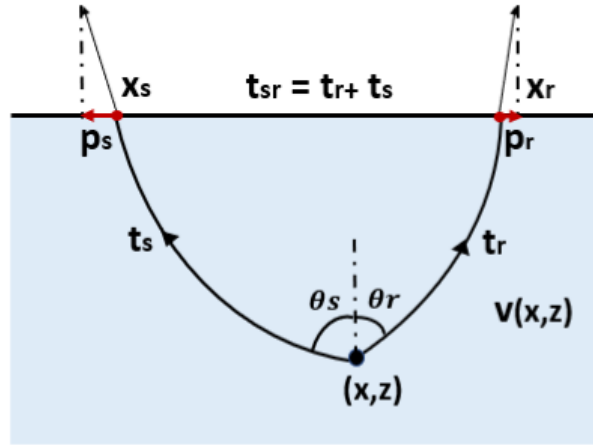
rameter $\mathbf{d}^{obs}$.

Figure 1.2: Correspondence between data and model parameters for stereotomography.

For a user-selected initial (incorrect) velocity-model parameter vector $\mathbf{m}_k^{vel}$ and a set of ray-model parameter vectors $\{\mathbf{m}_k^{ray}\}$, the corresponding set of data-vector parameters (referred to as synthetic-data parameter vectors and denoted $\{\mathbf{d}_k^{syn}\}$ or simply $\{\mathbf{d}_k\}$) that would be obtained by ray tracing applied to these initial conditions would encounter discrepancies when compared with given original observed-data parameter vectors. The task of the stereotomography method would be to iteratively update those model velocity and parameters until if successful, an acceptable solutions would be achieved.

We now comment on the key features of stereotomography that attempts to overcome the inversion difficulties of CDR. In accordance with Billette and Lambaré (1998), the main differences between CDR and stereotomography are highlighted below and further summarized in Table 1.1.

(a) The observed-data space of stereotomography and CRD consists of a user-selected set of data-parameter vectors $\{\mathbf{d}_k^{obs}\}$ picked/extracted from the input data.

(b) At each iteration, in addition to the model-velocity vector parameter $\mathbf{m}_k^{vel}$ used in CDR, stereotomography introduces a set of depth-domain ray-model parameter vectors $\{(\mathbf{m}_k^{ray})^{(n)}\}$.

(c) For each iteration, by means of a ray-based forward-model engine defined by the model-velocity parameter vector $(\mathbf{m}^{vel})^{(n)}$ and applied to the model-parameter vector set $\{\mathbf{m}_k^{(n)}\}$ simulates the data-parameter vector set $\{\mathbf{d}_k^{(n)}\}$. The stereotomographic misfit function takes into account the discrepancies (or residuals) between the simulated $\{\mathbf{d}_k^{(n)}\}$ and observed $\{\mathbf{d}_k^{obs}\}$ sets.

(d) CDR maintains fixed the data-parameter vector set $\{\mathbf{d}_k^{(n)}\} \equiv \{\mathbf{d}_k^{obs}\}$ so that its misfit functions depends on crossing conditions only. This makes CDR much more susceptible to errors in the picking/extraction data-vector input parameters.

(e) Stereotomography makes use of a relaxed (variable) data parameter-vector set $\{\mathbf{d}_k^{(n)}\}$ so that all discrepancies with respect to the observed set $\{\mathbf{d}_k^{(n)}\}$ contribute to the stereotomographic misfit function. That choice leads to significant improvement of CDR instability difficulties.

n-th iteration				
	Data space	Direction	Model space	Ray tracing
CDR	$\{\mathbf{d}_k^{obs}\}$ (fixed)	$\Longrightarrow$	$(\mathbf{m}^{vel})^{(n)}, \{l_k^{(n)}\}$ (relaxed)	Downwards
Stereo	$\{\mathbf{d}_k^{(n)}\}$ (relaxed)	$\Longleftarrow$	$(\mathbf{m}^{vel})^{(n)}, \{(\mathbf{m}_k^{ray})^{(n)}\}$ (relaxed)	Upwards

Table 1.1: **CDR:** Data-space parameter vectors $\{\mathbf{d}_k^{(n)}\} \equiv \{\mathbf{d}_k^{obs}\}$ remain fixed and equal to the picked/extracted parameters; Crossing conditions $\{l_k^{(n)}\}$ are relaxed (varies); Forward modeling engine (FME) acts from data space to model space; ray tracing is performed downwards. **Stereo:** Data-space parameter vectors $\{\mathbf{d}_k^{(n)}\}$ are relaxed (varies); Ray-model vector-parameter space $\{(\mathbf{m}_k^{ray})^{(n)}\}$ are relaxed (varies); FME acts from model space to data space; ray tracing is performed upwards. In both cases, velocity-model space coefficients $\{(\mathbf{m}^{vel})^{(n)}\}$ are relaxed (varies).

Since it was first presented, many contributions were introduced in stereotomography by further researches. With respect to picking process, further efforts were made in the sense of improve the quality and automatization of picking processes. In Lambaré et al. (2004), an automatic picking process has been proposed and tested. Moreover, the picking process can also be performed in depth-migrated domain Chauris et al. (2002); Nguyen et al. (2008) or poststack time migrated domain Lavaud et al. (2004).

Concerning the important task of assisting the stability of the inverse process, e.g., by suitable refinement of the initial macro-velocity model has been proposed in (Billette et al., 2003; Le Bégat et al., 2000).

(b.3) **Common-Reflection-Point (CRP) tomography:** Fully described in Chapter 5 and having stereotomography as its source of inspiration, CRP tomography is the main contribution of the present thesis. For the same previous reasons, the attention here is devoted to indicate and discuss the main difference between the two approaches.

The name CRP tomography stems from the fact that it relies on recent results on CRP (also referred to as offset-continuation) seismic processing and imaging, as reported in Coimbra et al. (2012, 2016b); Santos et al. (1997); Tygel et al. (1998). More specifically,

our main interest lies on the solution, described in the above literature, of the following problem (see Figure 1.3):

> Let $\mathbf{d}_0$ denote a parameter vector defined the components by source-receiver locations, slopes and two-way traveltime, all of them picked/extracted from an input data set.
>
> Assuming that $\mathbf{d}_0$ pertains to a primary-reflection event, find the corresponding *CRP gather*, namely the parameter vectors $\mathbf{d}$ that pertain to the same event and also share the same (unknown) original reflection point.

For convenience, data parameter vectors are, in the following, also called *data points*. In the framework of the above formulation, an original point $\mathbf{d}_0$, for which a corresponding CRP gather $\mathcal{G}(\mathbf{d}_0)$ is to be constructed, is called a *reference* or *central* point of the gather.
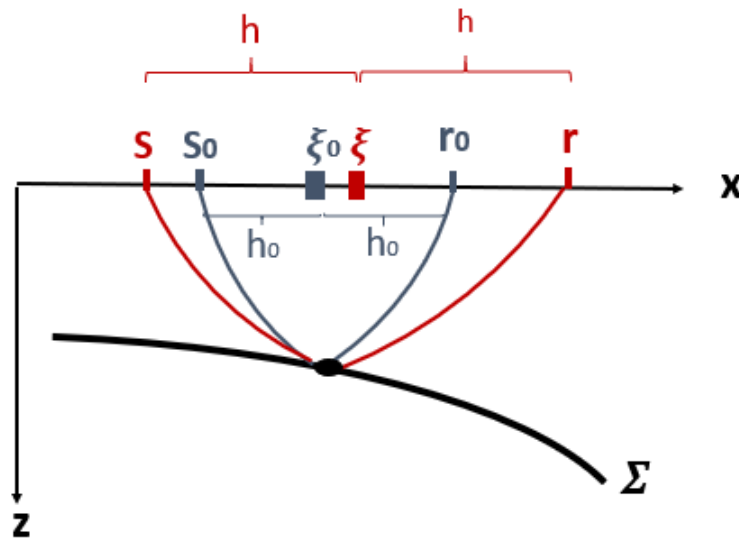
Figure 1.3: CRP primary reflections. Note the change in midpoint position for different CRP reflection rays.

Figure 1.3 shows the point $\mathbf{d} = (s, r, a_s, a_h, t)$ for which its coordinates represent the source-receiver locations and slopes, as well as two-way traveltime within the CRP gather $\mathcal{G}(\mathbf{d}_0)$ defined by the central point $\mathbf{d}_0 = (s_0, r_0, a_{s_0}, a_{h_0}, t_0)$. As described in Coimbra et al. (2016b) and briefly reviewed in Appendix F, the components of $\mathbf{d}$ satisfy multiparametric, traveltime and slope functions (see equations F.2 to F.7 in half-offset and midpoint coordinates). The parameters of those functions refer to the central point $\mathbf{d}_0$ of the gather, being estimated by coherence (semblance) analysis directly applied to the input data.

After substitution of estimated parameters, those equations estimates the points $\mathbf{d}$ within the CRP gather $\mathcal{G}(\mathbf{d}_0)$ of reference point $\mathbf{d}_0$. This estimation is valid for half-offsets that are close to the one that pertains to the central point $\mathbf{d}_0$.

As summarized in Table 1.2, the main difference between stereo and CRP tomographies is that, instead of individual, independent picked/extracted data points used in stereotomagraphy, CRP tomography uses a collection of CRP data gathers. Those gathers provide, at feasible computation costs, not only a more comprehensive coverage of the subsurface region under investigation, but also redundancy that is useful to the inversion.

	n-th iteration		
	Data space	Direction	Model space
Stereo	$\{\mathbf{d}_k^{(n)}\}$ (relaxed)	$\Longleftarrow$	$(\mathbf{m}^{vel})^{(n)}, \{(\mathbf{m}_k^{ray})^{(n)}\}$ (relaxed)
CRP	$\{\mathcal{G}(\mathbf{d}_k^{(n)})\}$ (relaxed)	$\Longleftarrow$	$(\mathbf{m}^{vel})^{(n)}, \{\mathcal{G}[(\mathbf{m}_k^{ray})^{(n)}]\}$ (relaxed)

Table 1.2: Individual data and ray-model parameter vectors $\mathbf{d}_k^{(n)}$ and $(\mathbf{m}_k^{ray})^{(n)}$ of stereotomography are replaced with CRP data and ray-model gathers $\mathcal{G}(\mathbf{d}_k^{(n)})$ and $\mathcal{G}[(\mathbf{m}_k^{ray})^{(n)}]$. Such procedure significantly increase the coverage and redundancy made available by CRP tomography. In both stereo and CRP tomography, rays are traced in upward direction. Moreover, in both cases $(\mathbf{m}^{vel})^{(n)}$ represent the velocity-model space.

Some remarks about CRP tomography picking: In this thesis, an in-depth discussion on how CRP gathers are actually extracted from the input data, is not of prime concern. In fact, active research and development on this important topic are being carried out as dedicated projects of the High-Performance Geophysics Lab. Here, a proof-of-concept framework is assumed: For illustrative synthetic-data examples for which CRP gathers are known in advance, the task is to evaluate the actual potential and benefits of CRP tomography, as compared to state-of-the-art approaches such as stereotomography.

(c) **Curvature tomography:** This terminology is attached to methods that, in addition to traveltimes, positions and traveltime slopes, also make use of curvature parameters, which are picked/extracted from the input seismic data. Main examples summarized here are Normal incidence point (NIP) wave tomography, applied to post-stack data and its analogous method, Image Incident Point (IIP) tomography, applied to time-migrated input data.

(c.1) **NIP tomography:** As described in (Duveneck and Hubral, 2002; Duveneck, 2004b), NIP tomography is conceptually aligned to the zero-offset (ZO) common reflection surface

(CRS) stacking method (see, e.g, Müller (1999), Faccipieri (2016)). As such, it is based on a second-order (hyperbolic) formulation of reflection traveltimes in the vicinity of a ZO reference or central point. Under this formulation, for a target (unknown) reflection interface, the parameters of interest of the CRS traveltime (simply called CRS parameters) are those of the primary-reflection, ZO normal ray that connects the (unknown) reflection point at the target reflector to the central point. In the present 2D situation, those parameters are the slope and wave-front curvature at the arrival point of the central (normal) at the measurement line, as well as the two-way traveltime of that ray. Besides the traveltime that is picked from the ZO (stacked) data, the slope and curvature parameters are estimated from seismic data by means of coherence analysis.

Although carried out in the ZO (stacked) domain, the inversion process of the NIP tomography is very similar to the ones previously described, for example the stereotomography method.
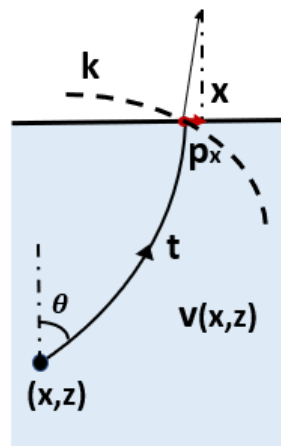
Figure 1.4: Data and model parameters for NIP tomography.

The data space consists of user-selected points picked/extracted from CRS stack panels, these being specified by positions, slopes, curvatures and two-way traveltimes. The curvature parameter (the quadratic coefficient of the CRS traveltime with respect to half-offset) is interpreted as the wave-front curvature of the so-called NIP wave (Duveneck, 2004b) that starts as a point source at the (unknown) reflection point of the central normal ray and is measured at the central point. The model space is composed by beta-spline interpolation coefficients that define the velocity model, together with a set (of the same seize as the data space) of depth-domain diffraction points. Two model parameters are attached to each diffraction point, namely its location and a direction angle. The forward-model engine for NIP tomography is kinematic and dynamic ray tracing, upon which, the lo-

cation and direction angle at a diffraction point determines, under the use of the current velocity model, the one-way upward ray to the measurement line. At the arrival point the traveltime and wave-front curvature are computed. Applied to each diffraction point an its attached ray direction, the forward-model engine produces a synthetic data space that can be compared to the given data space. An illustration of data and model parameters for NIP wave tomography is shown in Figure 1.4.

With the above ingredients, an LSQR optimization problem is formulated so that the misfit function, namely the sum of squares of the discrepancies (residuals) between point-arrival locations, slopes and curvatures of data and synthetic spaces, is minimized. As a final observation, the locally-event framework is adopted by NIP tomography. Picking locations are independent of each other and do not need to follow continuous reflection events in the seismic data. Moreover, picking is simplified by the fact that it is performed on a stacked section, with better signal-to-noise ratio. NIP tomography has also been extended to 3D media (see, e.g, Duveneck (2004a)). The easier picking process is a crucial feature for that purpose.

Remarks: The present thesis has greatly benefited from an in-depth analysis of NIP-tomography and related literature (Duveneck, 2004a,b,c; Dell et al., 2014; Dümmong et al., 2008). Valuable insights and understanding were gained from actual 2D implementations, for which the introduction of the regularization term proposed in Duveneck (2004b) played a significant role. In fact, such regularization term was the one adopted for the stereo and CRP tomographic methods, described in Chapters 3 and 5. In this connection. Pertinent results are reported or commented throughout the text, where a discussion about the use of a curvature parameter is addressed.

(c.2) **Image incidence point (IIP) tomography:** As described in Dell et al. (2014), IIP tomography has a similar approach to NIP tomography, being applied, however, in the time-migrated domain.

This represents an advantage to the picking process involved, since time-migrated data is cleaner and complications such as conflicting dips have been untangled. While NIP tomography, as applied to post-stack data, has its parameters attached to normal rays, IIP tomography, as applied to time-migrated data, has its parameters attached to image rays (see Figure 1.5). We recall that, in the same way that the point where a normal ray hits a reflector is called normal-incident point (NIP), the point where an image ray hits that reflector is referred to as the the image incident point (IIP). More information on how IIP is used on imaging problems can be found in, e.g., Tygel et al. (2012).
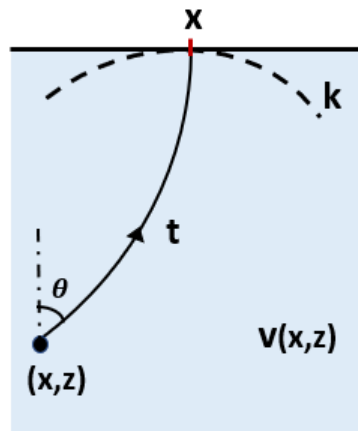
Figure 1.5: Data and model parameters for IIP tomography.

We close this section with Figure 1.6, which provides a pictorial summary of the above-surveyed tomographic methods.
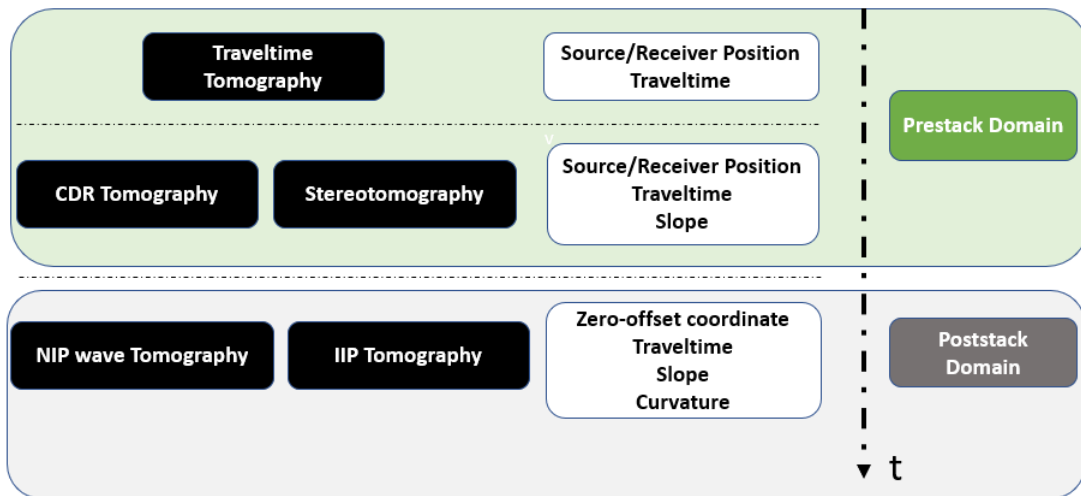
Figure 1.6: The development of seismic tomography methods has been following both the development of computer science and geophysics. The number and type of kinematic wave parameters, used by the seismic tomography methods, have been changed by the increasing computation capacity and the development of new multiparametric operators.

1.3   Numerical stability of tomographic methods

The tomographic problems addressed in this thesis fall into the category of *inverse* and *ill-posed* problems. Loosely speaking, tomographic problems are inverse problems because they aim to infer (invert) medium parameters (such as propagation velocities) from indirect measurements (such as the ones acquired by seismic surveys). At the same time, tomographic problems are ill-posed because the conditions of existence, uniqueness and stability (i.e, smooth dependence on initial conditions) are not all guaranteed to be fulfilled. As stated by Hadamard (1902) and generally accepted in Mathematics, the above conditions are required to be all satisfied for a *well-posed problem*. If at least one of them cannot be guaranteed, the problem is qualified as ill-posed or, more simply, as ill problems. Under these rather strict and idealized Hadamard's conditions, the vast majority of cases of practical interest are ill problems.

To overcome such essential difficulties, methods to tackle inverse and ill problems rely on two fundamental tools:

(i) Iterative schemes upon which the solution is searched an initial, trial-guess solution, followed by successive updates, each of them being a solution of an easier and well-posed intermediate problem.

(ii) External, user-selected regularization terms, not only to guide the inversion to a stable and meaningful solution, but also to add whatever *a prior* knowledge and information one might have on the actual problem to be solved.

Most popular iterative schemes, in particular the ones used in tomographic problems, rely on LSQR inversion schemes (Billette and Lambaré, 1998; Duveneck, 2004b; Farra and Madariaga, 1988). Such schemes make use of linear versions of the full non-linear problem, these being sequentially solved by optimization methods.

The linear sub-problems involved in the iteration process typically belong to the well-studied class of ill-conditioned matrix systems, for which the presence of even small errors in the matrix entries may lead to non-acceptable solutions. A classical and practical way to handle ill-conditioned problems is the introduction of a regularization term in the objective function to improve the stability of the inverse problem (Van Loan and Golub, 1983; Watkins, 2004). Moreover, suitable choices of numerical solvers, such as the *singular value decomposition (SVD)* (Watkins, 2004), can be of good use.

Science and art: It is to be remarked that caution must be taken with the impact and influence that a chosen regularization term might have on the inversion results. In fact, since the regularization term is not a part of the tomographic original formulation, one must calibrate the use of such external information, so that welcome features such as numerical stability and efficiency, do not compromise the search for meaningful solutions. In fact, to each regularization term, a constant factor is attached so as to control that term's influence in the inversion. The selection of a good value of that constant is, perhaps more artistic than scientific.

In this thesis, the regularization term of choice is the one that minimizes the spatial second derivatives of the velocity function. Designed to impose a smoothness condition on the velocity, this regularization term coincides with that of NIP tomography, as proposed by Duveneck (2004b). No regularization term related to *a priori* information is here considered.

We observe, in passing, that the streotomography in Billette et al. (2003) makes use of a regularization term to carry *a priori* information on model-space parameters, together with an additional term for stability purposes. That latter term is defined as centered finite-difference approximation of the 2D spatial Laplacian operator. As such it controls the smoothness level of the velocity model.

Additional strategies: Besides the introduction of regularization terms to the objective function, other strategies to the improvement of tomographic inversion are also available in the literature.

For setereotomography initialization, Billette et al. (2003) proposes constant-velocity screening procedure to optimize the localization of initial points. Also in stereotomography, Billette and Lambaré (1998), proposes a velocity-by-parts optimization scheme to assist the inversion. First, a homogeneous velocity is inverted. Secondly, a best velocity with vertical gradient is obtained. Finally, the velocity is allowed to vary in all directions. Billette et al. (2003); Le Bégat et al. (2000) propose a multi-scale optimization that increases the number of interpolation knots that are used to build the velocity model during the iterations. As the iterations proceed more details on the velocity models are considered.

Concerning NIP tomography, Duveneck (2004b) proposes a number of possibilities: (a) introduction of additional data that refer to previous knowledge of some parts of the velocity field. The new data modifies the misfit function during iterations, trying to constrain the velocity models so that the additional information is better taken tinto account; (b) introduction of an additional regularization term that forces the velocity models to locally follow *a priori* given reflector structures and (c) Consideration of spatially-varying model smoothness, namely weaker or stronger regularization in

user-selected parts of the model is allowed. Such strategy has been shown to be useful specially at the borders of the velocity field, where commonly no sufficient information is available to locally constrain the model.

CRP coverage and redundancy: In this thesis, we show that the inclusion of CRP gathers extracted from the input data provides a significant increase in coverage and redundancy to the target subsurface region of interest to the CRP tomographic purposes. As opposed to stereotomography, where the model-space diffraction points correspond to individual, isolated data-space points, the model-space points in CRP tomography are in correspondence to the data-space CRP gathers. The increased coverage and redundancy provided by data-space gathers instead of isolated points, helps, not only to better locate the model-space points, but also to better constrain the velocity model to be inverted. In fact, the additional information provided by CRP gathers is seen diminish the degree of freedom of the tomographic problem by improving its regularization.

As shown in the subsequent chapters, several tests carried out on a variety of synthetic tests confirms the good expectations of the proposed CRP tomography.

1.4   Full Waveform Inversion

Primarily aimed to tomographic methods, it may sound strange that this thesis includes a full chapter on the overall description of full waveform inversion (FWI). This can be justified, however, under the perspective that FWI can be regarded as a step forward of tomography in the solution of the seismic model inversion. As this important topic is fully addressed in Chapter 4, we content ourselves with a brief overview of the FWI approach highlighting the similarities and differences relative to its tomographic counterparts. These can be summarized as follows:

(a) **Similarities:** In the same way as tomography, FWI is a highly nonlinear, ill-posed inverse problem. Also as tomography, FWI is based on single-scattering wave propagation in combination with perturbation methods to invert medium parameters (most particularly velocities) from seismic data.

Solutions of both tomography and FWI are obtained through an iterative process that starts with a user-selected initial velocity model, that model being sequentially perturbed (updated), so as to converge to an accepted solution. Each iteration is carried out as a linearized least-squares (LSQR) approach of the residuals between observed and computed traces. The single-scattering

and perturbation-theory formulations are at the core of of the process, with the medium being considered as a set of independent diffraction points covering the medium region of interest.

(b) **Differences:** Concerning scope and purposes, tomography and FWI have significant differences. On the one hand, under the use of ray-based forward-modeling engines, tomographic methods have a "modest" design of accepting a velocity-model solution that "honors" a few kinematic data parameters (e.g., traveltimes, slopes) on a (few) collection of local-event points (of a few admissible type such as primary reflections and diffractions) picked/extracted from the input data. On the other hand, under the use of user-selected full-wave forward-model engines, FWI has the "ambitious" design of requiring that a velocity-model solution "honors" the full content of the input data, namely the variety of local events that are predicted (simulated) by the considered full-wave equation. More specifically, the FWI misfit function is based on the residuals (discrepancies) between observed and synthetic data traces, the latter given by finite-difference solutions of appropriate wave equations.

In FWI, the diffraction points are generally called pixels. Perturbations are computed for every pixel, to which a variety of local properties of the medium (e.g., acoustic/elastic, isotropic/anisotropic) parameters are attached. In this thesis, the focus is on the constant-density acoustic wave propagation, for which the scalar acoustic velocity is the single parameter attached to each pixel. Accordingly, the finite-difference solutions of that acoustic wave equation.

As compared to stereotomography, which has established itself as mainstream seismic imaging technology, FWI, albeit very attractive, has still a few challenges to overcome. In addition to mathematically more complicated than tomography, FWI has, most of the time, extreme demands on computational costs. While in stereotomography iteration updates can be carried out by efficient second-order Gauss-Newton optimization, such approach is computationally unfeasible for FWI, being replaced by notably less accurate first-order descent schemes. As a consequence, FWI is seen to have a crucial dependence on a good model-space initial guess for successful FWI inversion. As a way to mitigate such difficulties, FWI is usually applied after other methods, such as, e.g., simplified versions of full FWI (Camargo, 2019) or tomographic solutions. The use of CRP tomographic velocity as input to FWI is proposed in this thesis. Introduction of *a priori* information, such as, e.g., well-data and uncertainty estimations, can be also quite useful (Virieux et al., 2017).

1.5   Claerbout's resolution sketch

As discussed in Claerbout (1985), the interaction between seismic waves and a geological medium can be grossly divided into two main types: smooth and rough interactions. more explicitly, (a) Smooth interactions are related to the transmission regime in forward scattering. These interactions are responsible for small variations in wavefront propagation. As such, smooth interactions change wave propagation directions slightly, due to small variations of geological properties of the medium; (b) Rough interactions are related to the reflection regime in forward scattering. These interactions are responsible for significant variations in wavefront propagation. As such, rough interactions significantly changes direction of ray propagation, resulting, for example, in backward scattering.
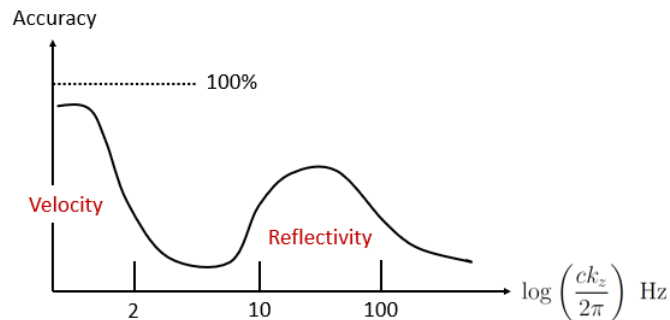

Figure 1.7: Reliability of information obtained from surface seismic measurements (reproduced from Claerbout, 1985).

Investigations of these two types of wave/medium interactions resulted in the development of corresponding two inversion techniques: (a) On the one hand, seismic tomography, based on asymptotic approximation of the wave equation, recovers the smoothly varying properties (typically velocities) of the medium in transmission regime. As such, just slow-phase variations (e.g., traveltimes), are considered. With respect to the wavenumber domain, seismic tomography is capable to recover low-wavenumber content of seismic data, generally associated with seismic-processing velocities. (b) On the other hand, migration techniques, based on Huygens principle, recover rapid variations of medium properties in the reflection regime, so that fast-phase variations are taken into account. With respect to the wavenumber domain, migration techniques are better suited to recover high-wavenumber content generally referred to as reflectivities) of seismic data.

Figure 1.7 reproduces Claerbout's resolution sketch (Claerbout, 1985, Figure 1.4-4, p. 47), which illustrates the expected resolution from those two seismic inversion methods. The Figure exhibits the capability of tomography and migration to recover specific ranges of wavenumber content

in depth direction. Seismic tomography methods are capable to recover the low wavenumber content, which is related to smooth parts of velocity model, while migration methods are capable to recover the high wavenumber content, which is related to the geological structures (interfaces) in subsurface. Clarbout's resolution sketch (Figure 1.7) shows the gap of poor wavenumber recovery in the intermediate domain. Full waveform inversion (FWI) has emerged as an alternative to remedy this situation.

1.6   Map of the thesis

As this thesis encompass different subjects, with different purposes, the present section was designed to guide the readers through the text according to their particular interest. The main contribution of this thesis for seismic tomography research is the CRP tomography method, which is first presented in chapter 5. Further chapters illustrate numerical applications of the new method and comparisons with stereotomography results are provided. Therefore, the readers familiar with seismic tomography area and interest just in the new contributions of the thesis can skip the first chapters. For the readers interested in more details about CRP tomography method, appendices C, D, E and F are dedicated to explain some important features related to CRP tomography method.

For didactic purposes, a review of the stereotomography method and FWI is provided in chapters 2, 3 and 4. The stereotomography method, chapter 3, plays an important role for this thesis, since CRP tomography is based on this traditional tomography method. On the other hand, FWI method, chapter 4, is also presented in this thesis in order to provide the reader with a broader view of the velocity model building. Although not being the central theme of this thesis, FWI is, nowadays, a remarkable important seismic method, and some similarities between seismic tomography methods and FWI are presented in chapter 2. Also, a numerical test involving both FWI and CRP tomography is illustrated in chapter 9. Appendix A illustrates an example of curvature tomography, the NIP wave tomography. Some numerical tests of this method are illustrated in appendix B. NIP wave tomography is also presented in this thesis in order to provide the reader with a broader view of different seismic tomography methods.

Following the previous explanation, this thesis is structured as follows:

Chapter 1 - Introduction

Brief comments about different seismic tomography methods. Classifications, differences and main features are provided. Natural ill-conditioning of the problem is reported. FWI is also introduced, together with its strong dependence of a good initial velocity model. CRP tomography is introduced.

Chapter 2 - Brief description of the LSQR inverse problem: The stereotomography and FWI cases

This chapter presents a general description of LSQR inverse problem, based on the stereotomography and FWI cases. Despite the different numerical methods used to solve these methods, both can be formulated as a general LSQR inverse problem.

Chapter 3 - Stereotomography

This chapter will revisit stereotomography method, presenting details about stereotomography seismic tomography inverse problem. Data, model and synthetic spaces will be presented in details, as well as regularization issues and initialization procedure. The iteration process, based on a Gauss Newton approach, will also be detailed.

Chapter 4 - Full wave form inversion

This chapter will revisit full weveform inversion method. Data, model and synthetic spaces will be presented in details, as well as regularization issues and strategies to overcome the strong dependence on good initial velocity models will be adressed. The iteration process, based on the adjoint state method, will be detailed.

Chapter 5 - CRP tomography

This chapter presents the main contribution of this thesis for seismic tomography research. It consists in the proposition of a new seismic tomography method, named CRP tomography. Based on stereotomography method, CRP tomography proposes the addition of common-reflection-point

information to improve the quality of the inversion process. A complete description of the technique will be given in this chapter.

Chapter 6 - Synthetic tests for stereotomography

Some synthetic numerical tests will validate stereotomography implementation. Then, more complex synthetic tests will be discussed and the improvement of the quality of stereotomography velocity models by providing more and better internal information, that is, more input data parameters and/or better initial velocity models, will be illustrated and discussed.

Chapter 7 - Synthetic tests for CRP tomography

In this chapter, CRP tomography implementation will be validated in a set of synthetic numerical tests, the same one proposed for stereotomography in previous chapter. Then, more complex synthetic tests and experiments will show how the addition of common-reflection-point information helps to constrain the problem, acting as a natural constraint that is incorporated to the tomographic inverse process, turning CRP tomography method more robust with respect to boundary initial conditions.

Chapter 8 - Futher numerical tests - noisy input data and interfaces

In this chapter, CRP tomography will be tested in synthetic experiments that simulate more realistic situations. Noisy input data and synthetic interfaces will be introduced in model tests. Stereotomography will also be tested in these experiments for comparison reasons.

Chapter 9 - CRP tomography velocity model as inpur for FWI - A velocity model building procedure

This chapter illustrates the velocity model building procedure proposed in this thesis, which consists in the use of CRP tomography velocity model as input for FWI application. The proposed velocity model building procedure will be validated by Marmousi model test. It will be shown how CRP tomography velocity model can overcome the strong dependence of FWI method on a good initial velocity model.

Chapter 10 - Summary and conclusions

This chapter summarizes the main contribution of this thesis. Some possible further researches will be provided.

Appendix A - NIP wave tomography

This appendix reports one example of curvature tomography, the NIP wave tomography method. A brief summary of the technique is provided. Data, model and synthetic spaces, as well as initialization procedure for NIP wave tomography, will be described.

Appendix B - Synthetic tests for NIP wave tomography

NIP wave tomography implementation will be validated in the same set of synthetic numerical tests used to validate stereotomography and CRP tomography methods. A further synthetic test will be performed and discussions about the use of curvature parameter will be addresed.

Appendix C - Ray-tracing equations for seismic tomography forward modeling engine

Before presenting the system of differential equations used to perform forward modeling engine for slope tomography methods, this appendix develop some baisc concepts of kinematic ray-tracing theory. As NIP wave tomography is addressed and reffered by this thesis, the related system of dynamic-ray tracing will also be presetend, although concepts of paraxial ray-theory will be omitted.

Appendix D - B-spline interpolation

In this appendix, B-spline basis functions will be defined and main properties of B-spline interpolation will be summarized. Also, some algorithms to compute B-spline basis functions and respective velocity model derivatives will be given.

Appendix E - Regularization matrix for CRP tomography and stereotomography

This appendix shows how to compute the regularization matrix proposed in this thesis for CRP tomography and stereotomography.

Appendix F - Equations of CRP tomography

This appendix describes and discusses the equations needed for CRP tomography validation. These equations can be used for further development of a picking strategy to build input observed-data space for CRP tomography method.

Appendix G - Example of CRP tomography implementation

This appendix provides a link to a repository with an example of CRP tomography implementation.

Chapter 2

Brief description of the LSQR inverse problem: The stereotomography and FWI cases

Seismic tomography (in particular stereotomography) and full waveform inversion (FWI) are processes designed to invert, from a given seismic data set, a set of geological/geophysical parameters that approximately models the depth region illuminated by the data. Most often, acoustic/elastic parameters, most particularly seismic velocities are the main quantities to be inverted. For that reason the terminology velocity model building for such processes is very much used in the literature (see, e.g. Jones, 2010). For the inversion processes addressed here, reflection and diffraction (mainly primary) waves are the main events of interest within a seismic data. Recorded as particle motions at the receivers, these waves typically travel large distances within rather complex geological structures. As a consequence, the detection of the data parameters of interest from the observed reflection/diffraction events, constitute a very challenging problem.

Data and model spaces: Both stereotomography and FWI formulate the inversion problem as iterative procedures. In each case, from a given data space provided, a depth-domain, unknown model space is to be inverted.

In stereotomography, the data space is made up of a collection of user-selected parameter vectors picked/extracted from the original or pre-processed seismic data. In FWI, the observed data space comprises the full original or reprocessed seismic data. In both cases, the data space remains invariant throughout the whole inversion process, acting as a reference or guide of convergence.

In stereotomography, the model space is made up of a union of two subsets; the first, referred to as velocity-model space, consists of the parameters that physically describe the depth region to be inverted. Such parameters are to be assigned to the knots of a user-selected mesh designed to provide a discretized representation of the depth model. In the present situation of constant-density acoustic propagation, that vector reduces to a (positive) scalar, namely the acoustic velocity. The second subset of the model space is referred to as the ray-model space and contains the parameter vectors that correspond, in the depth-domain, to the picked/extracted time-domain parameter vectors that comprise the data space. As explained in Chapter 3, in the present 2D situation, each parameter vector of the ray-model space has six (unknown) components, namely the two Cartesian coordinates of a depth point, two direction angles and two traveltimes.

In FWI, the ray-model space set is not present, since the data space comprises all the original data.

Forward modeling and inversion: The LSQR method assumes a forward-modeling transformation such that, for any given (trial) model space, a corresponding synthetic space is produced that represents a version of the data space. Referred to as a forward-modeling engine, that transformation in stereotomography is ray tracing. In FWI, that engine is a finite-difference solution of a wave equation. In both cases, the result of the application of the forward-modeling engine to a given model space is referred to as the synthetic data space that corresponds to that model space.

An important consequence of the forward-modeling engine is that the original (invariant) and synthetic (model-dependent) data spaces are amenable to comparison. Moreover, the ideal solution of the inversion problem would be the data space for which the discrepancies between the synthetic and original data spaces are, under some user-selected crierion, minimized.

As seen below, the discrepancy between the original and synthetic data spaces are quantified by an LSQR objective function. In this way, our inversion task can be formulated as an optimization problem, namely to find the model space that minimizes the objective function.

In this thesis, the LSQR formulation and solution of the stereotomography and FWI problems are reviewed and, along the same strategy, the new CRP tomographic problem is described and solved. In this context, the basics of LSQR inversion is provided below.
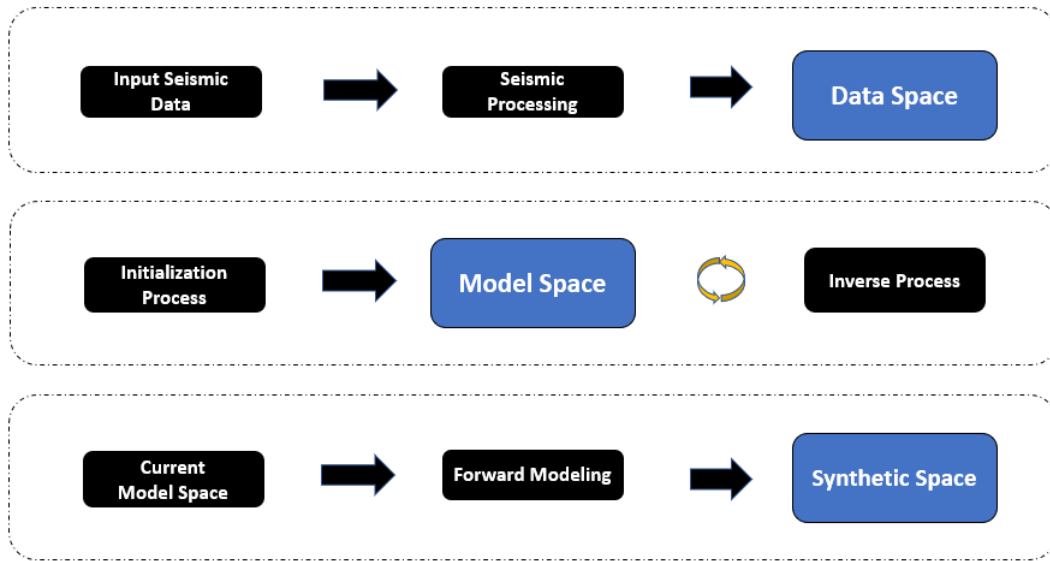
Figure 2.1: LSQR inverse problems use three main spaces (sets) during iteration process. Observed data space is one of the inputs for the methods, and their components are collected from seismic data or estimated by coherence analysis in stack panels. Model space is the set of components which inverse problem aims to invert. It is initialized by first guess or an specific initialization procedure. The initial model space is the other main input for the inversion process. During iterative process, model space is updated, based on local linearized approach to the least square misfit of data and synthetic spaces. Synthetic space is a set of components of computed quantities that simulate data components based on current model space. The computation is done by forward modeling step.

2.1   Brief description of the LSQR method

The LSQR method (see, e.g., Tarantola, 1987; Paige and Saunders, 1982) is here reviewed in the context of the stereotomography and FWI problems. As shown later, LSQR will also be our choice for describing the new CRP tomography proposed in this thesis.

Formulation: In general, the LSQR inversion method is mathematically formulated by means of the following ingredients:

(i) A given *observed-data space* $\mathbf{d}^{obs}$, which consists of an N-dimensional data-parameter (column) vector

$$\mathbf{d}^{obs} = (d_1^{obs}, ..., d_N^{obs})^T, \tag{2.1}$$

where ^{T} denotes the transpose matrix operator. For definiteness, all entries d_i^{obs} are assumed to be real. The components of the data-space parameter vector represent the results of some
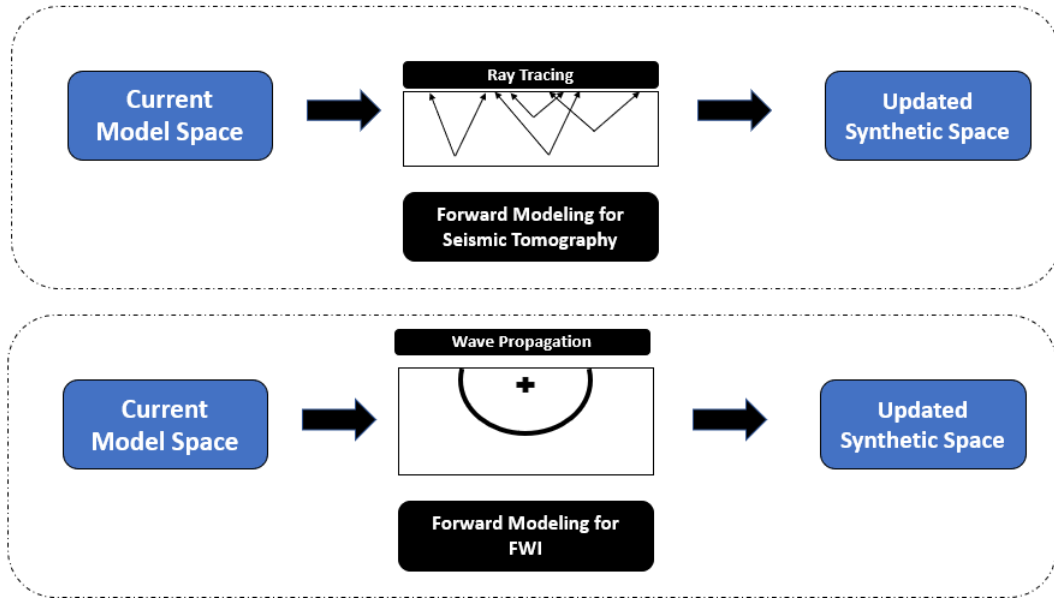
Figure 2.2: Forward modeling for LSQR inverse problems. At each iteration, synthetic space is generated by the forward modeling process, which is based on the current model space. For seismic tomography methods, forward modeling uses ray-tracing to build updated synthetic space. For FWI methods, forward modeling is performed by means of wave propagation. Both are non-linear approaches.

performed experiment. As such, $\mathbf{d}^{obs}$ remains invariant throughout the whole inversion process.

(ii) An unknown *model space* $\mathbf{m}^{mod}$ and a given *a priori model space* $\mathbf{m}^{pri}$, which consists of an M-dimensional (column) model-parameter vectors

$$\mathbf{m}^{mod} = (m_1^{mod}, ..., m_M^{mod})^T,$$

$$\mathbf{m}^{pri} = (m_1^{pri}, ..., m_M^{pri})^T,$$

(2.2)

with all components m_i^{mod} and m_i^{pri} also assumed to be real. The model space $\mathbf{m}^{mod}$ represents the (unknown) model that aims to be inverted. The *a priori* model space $\mathbf{m}^{pri}$ represents an invariant model-parameter vector that accounts for the prior information that the user might have about the $\mathbf{m}^{mod}$ model space. We finally introduce the so-called *trial* or *candidate* model spaces

$$\mathbf{m} = (m_1, ..., m_M)^T,$$

(2.3)

upon which the optimization process that leads to $\mathbf{m}^{mod}$ will be performed.

(iii) A *forward-model engine* which transforms any given model-space candidate $\mathbf{m}$ onto a corre-

sponding *synthetic data-space* candidate $\mathbf{d}^{syn}(\mathbf{m})$. In symbols,

$$\mathbf{d}^{syn}(\mathbf{m}) = [d_1^{syn}(\mathbf{m}), ..., d_N^{syn}(\mathbf{m})]^T, \tag{2.4}$$

in which $\mathbf{m} = (m_1, ..., m_M)$ is an arbitrary trial model space. We note that $\mathbf{d}^{syn}(\mathbf{m})$ represents a vector function in which the components $\mathbf{d}_i^{syn}(\mathbf{m})$ are real functions. In other words, for a given trial model space $\mathbf{m}$, the real function $d_i^{syn}(\mathbf{m})$ projects the data space $\mathbf{d}^{syn}(\mathbf{m})$ into its i-th component $d_i^{syn}(\mathbf{m})$.

The forward-modeling engine enables one to translate, at least qualitatively, a comparison between a trial model space $\mathbf{m}$ and the unknown, sought-for model space $\mathbf{m}^{mod}$, into the comparison between the corresponding synthetic and observed data spaces $\mathbf{d}_{syn}(\mathbf{m})$ and $\mathbf{d}^{obs}$. In other words, the "closer" the data spaces $\mathbf{d}^{syn}(\mathbf{m})$ and $\mathbf{d}^{obs}$ are, the closer the model spaces $\mathbf{m}$ and $\mathbf{m}^{mod}$ are expected to be.

(iv) A LSQR *misfit function*, which measures the discrepancy between (varying) synthetic and the (invariant) observed data spaces. Applied to any candidate model space $\mathbf{m}$, the misfit function is generally given in the form

$$S(\mathbf{m}) = S_0(\mathbf{m}) + S_1(\mathbf{m}) + S_2(\mathbf{m}), \tag{2.5}$$

where $S_0(\mathbf{m})$ is the non-regularized term

$$S_0(\mathbf{m}) = \frac{1}{2}\Delta\mathbf{d}^T(\mathbf{m})\mathbf{W}_D^{-1}\Delta\mathbf{d}(\mathbf{m}) \tag{2.6}$$

and $S_1(\mathbf{m})$, $S_2(\mathbf{m})$ are, respectively, the so-called Tykhonov and *a priori* model regularization terms (see Virieux et al., 2017; Tykhonov and Arsenin, 1977)

$$S_1(\mathbf{m}) = \frac{\lambda_1}{2}\mathbf{m}^T\mathbf{R}\mathbf{m},$$

$$\tag{2.7}$$

$$S_2(\mathbf{m}) = \frac{\lambda_2}{2}(\delta\mathbf{m}^{pri})^T\mathbf{W}_M^{-1}\delta\mathbf{m}^{pri}.$$

In the above equations, we have used the notations

$$\Delta\mathbf{d}(\mathbf{m}) = \mathbf{d}^{syn}(\mathbf{m}) - \mathbf{d}^{obs} \quad \text{and} \quad \delta\mathbf{m}^{pri} = \mathbf{m} - \mathbf{m}^{pri}, \tag{2.8}$$

with $\mathbf{W}_D^{-1}$ and $\mathbf{W}_M^{-1}$ are inverse diagonal matrices of dimensions $N \times N$ and $M \times M$, respectively. Also, $S_1(\mathbf{m})$ is referred to as the *Tychonov regularization term*. The $\mathbf{R}$ is an $M \times M$

matrix and λ_1 and λ_2 are scalars. All such quantities are provided by the user, being designed to make the LSQR inversion a more stable and reliable process. Better insight and clarification of all such parameters will be given below. It is to be observed that the choice of the objective function that involves a sum of squares of the discrepancies between the observed and synthetic spaces. As such, it justifies the terminology of an LSQR misfit function.

With the help of the misfit function S of equation (2.6), the sought-for model-space $\mathbf{m}^{obs}$ can be formulated as the solution of the non-linear optimization problem

> Find the model space $\mathbf{m}$ that minimizes the misfit function $S(\mathbf{m})$.

Parameters of the misfit function: A brief description and meaning of the user-selected parameters that compose the misfit function is now provided:

(a) The vector $\mathbf{m}^{pri}$, here referred to as an *a priori* model space, is composed by any previous knowledge the user may have about some local (or global) parts of the model. In situations where no previous model knowledge is available, the first scalar parameter is chosen to satisfy $\lambda_2 = 0$.

(b) $\mathbf{W}_D^{-1}$ and $\mathbf{W}_M^{-1}$ are inverses of diagonal covariance matrices which introduce previous information the user may have on the confidence or trust that can be expected from the components of the observed and *a priori* model spaces, respectively. In the case the data space is composed by elements measured by different physical dimensions (as it occurs in stereotomography), matrix $\mathbf{W}_D^{-1}$ also performs the task of bringing the numerical values of the data-space components to comparable sizes.

The larger the value of any diagonal matrix entry, the more the misfit function is constrained to allow variations on that component. Such behavior can be understood as follows: the larger the confidence that is attached to a component, the higher is the confidence of the user on that component.

From the fact that $\mathbf{W}_D^{-1}$ and $\mathbf{W}_M^{-1}$ are diagonal matrices, the corresponding covariance matrices $\mathbf{W}_D$ and $\mathbf{W}_M$ are also diagonal. Moreover, the diagonal entries of such covariance matrices are given by the variance (squared standard deviation) of the corresponding components. Actual values of such variances are provided by the user as "educated guesses" of the uncertainties (e.g., due to data quality, geological complexity) attached to those components.

The variance of a random variable is an indicator of the range that random variable oscillates around its mean. As such, the variance can be seen as an indicator of the trust one has in representing the random variable by its mean value. More specifically, a higher or smaller trust signifies a smaller or higher variance, respectively. As the inverse of a diagonal matrix is also a diagonal matrix with corresponding reciprocal elements, it turns out that higher or smaller values of such reciprocals are indicators of higher or smaller trust can be attached to the diagonal elements of the inverse matrices.

The LSQR problem described just by the misfit between synthetic and data spaces may not have enough information to constrain the model space. To handle this intrinsic ill-posedness of LSQR problem, an additional term, of global character and generally referred to as a *regularization* term, is added to the misfit function to improve numerical stability.

(c) The regularization term, taken as a quadratic operator defined by a constant operator matrix $\mathbf{R}$, acts on the entire model space and accounts for global features to be imposed to that space. The matrix $\mathbf{R}$ to be applied is selected by the user and varies from one application to another. A common practice is to consider $\mathbf{R}$ as a smoothing operator on the velocity field (see, e.g, Billette et al. (2003), Duveneck (2004c), Virieux et al. (2017)). This means that a model-space solution with smoothing properties is to be searched for.

(d) The scalar factors λ_1 and λ_2 are Tikhonov-type parameters (see, e.g., Tykhonov and Arsenin, 1977) designed to *calibrate* the influences of the *a priori* information and the model-space smoothing imposed in optimization process. In order to provide meaningful model solutions, the choice of adequate values for λ_1 and λ_2 is a fundamental and always an open issue. In fact, actual choices of scalar parameters of ill-posed problems of practical importance generally require rather significant insight and also computational testing effort. This explains why fully descriptions are rare in the literature, being hidden as proprietary issues in commercial software. In this respect, see, e.g., Pratt and Chapman (1992); Billette et al. (2003); Duveneck (2004b).

In this thesis, two examples of regularization terms are considered, one for stereotomography and another for FWI. In both cases, only the regularization term described by the matrix operator $\mathbf{R}$ is considered. In other words, in both cases we assume that $\lambda_2 = 0$.

2.2   Iteration process

As an iterative process, LSQR requires an user-selected *initial* model space $\mathbf{m}_0$, as well as an iterative scheme $\{\mathbf{m}_k\}$, $(k = 1, 2, ...)$ to progress (and hopefully converge) to the desired solution. In the present case, (see, e.g., Tarantola, 1984), given the current model space $\mathbf{m}_k$, its subsequent iteration $\mathbf{m}_{k+1}$ is given by

$$\mathbf{m}_{k+1} = \mathbf{m}_k - \alpha_k \Delta \mathbf{m}_k, \tag{2.9}$$

where α_k is a scalar that accounts for the size of the iteration step and $\Delta \mathbf{m}_k$ is the vector of model update, provided by some specific optimization scheme. The particular choice of that scheme depends on the available information, as well as computational/implementation issues.

As above indicated, both stereotomography (as well as many other seismic tomography methods) and FWI are formulated as an inverse LSQR problem. The same occurs with the new CRP tomography to be later discussed. In all cases, Newton-type iterative schemes are the ones chosen to numerically solve the optimization problem involved. In stereotomography, it is possible to a second-order, Gauss-Newton approximation of the Hessian matrix in terms of the Jacobian operator. In FWI, however, due to so-far unfeasible computational effort, first-order, local-descent optimization is chosen.

A brief review of the the LSQR iteration is provided below. For didactic reasons, the simpler case of non-reguarized misfit function, as characterized by setting the scalar parameters $\lambda_1 = \lambda_2 = 0$ in equation 2.6, is considered. The next case, in which such parameters are possibly non-vanishing, is addressed next.

It is important to observe that the inclusion of regularization terms is crucial in most realistic inverse problems, such as the ones addressed in this thesis. The reason is that those terms are necessary to avoid instabilities and guarantee that the process converges to a meaningful solution. Nevertheless, even with the knowledge that non-regularized misfit functions are rather artificial, their consideration is still justified for a clearer exposition.

Non-regularized problem: In this situation, we consider that

$$S(\mathbf{m}) = S_0(\mathbf{m}) = \frac{1}{2} \Delta \mathbf{d}^T \mathbf{W}_D^{-1} \Delta \mathbf{d}. \tag{2.10}$$

The application of standard Newton method to the non-regularized misfit function 2.10 leads

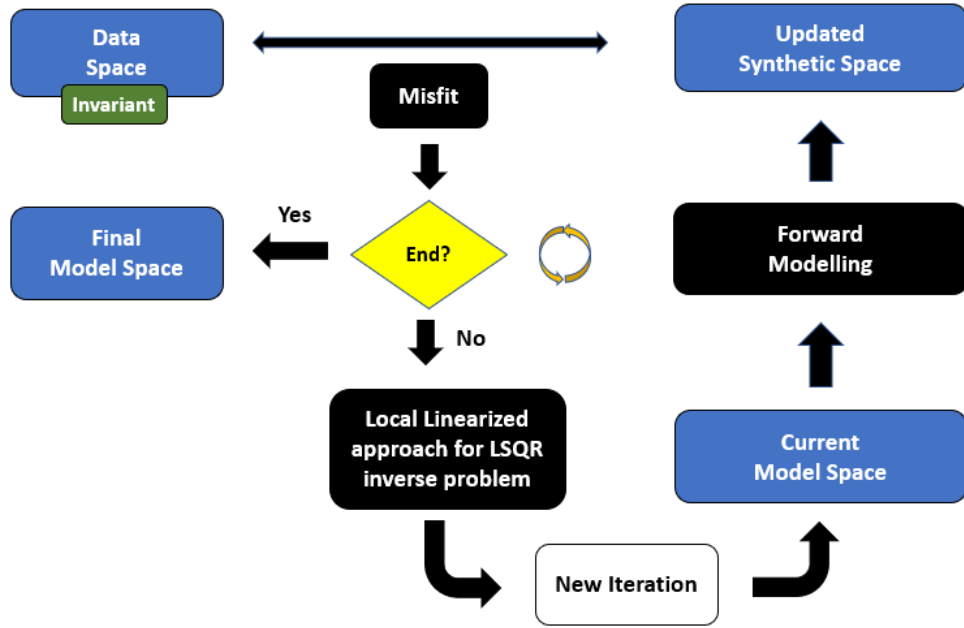Figure 2.3: Illustration of the LSQR inverse algorithm. Given a current model space, forward modeling is performed to build synthetic space. The least square misfit between data and synthetic space is computed. If the misfit follows under a previous value, a final model space is obtained. Otherwise, a local linearized approach for LSQR inverse problem is used to generate updates for model space.

to the iteration update $\Delta \mathbf{m}_k$ given by

$$\mathbf{H}_{S_0}(\mathbf{m}_k)\Delta \mathbf{m}_k = -\nabla S_0(\mathbf{m}_k), \tag{2.11}$$

in which ∇S_0 is the gradient (M-dimensional vector) and $\mathbf{H}_{S_0}$ ($M \times M$ Hessian matrix) of S, namely

$$\nabla S_0 = \left(\frac{\partial S_0}{\partial m_1}, ..., \frac{\partial S_0}{\partial m_M} \right)^T \quad \text{and} \quad \mathbf{H}_{S_0} = \left(\frac{\partial^2 S_0}{\partial m_i \partial m_j} \right)_{i,j=1}^{M}, \tag{2.12}$$

Applying the gradient to the non-regularized misfit function (2.10), leads to the gradient expression

$$\nabla S_0(\mathbf{m_k}) = \mathbf{J}(\mathbf{m_k})^T \mathbf{W}_D^{-1} \Delta \mathbf{d}(\mathbf{m_k}). \tag{2.13}$$

where $\mathbf{J}(\mathbf{m}_k)$ is the Jacobian $N \times M$ matrix operator evaluated at $\mathbf{m}_k$, namely

$$\mathbf{J}(\mathbf{m_k}) = \left. \frac{\partial \mathbf{d^{syn}}}{\partial \mathbf{m}} \right|_{\mathbf{m}=\mathbf{m}_k} = \left(\frac{\partial d_i^{syn}}{\partial m_j}(\mathbf{m}_k) \right), \quad i = 1, \ldots, N \quad \text{and} \quad j = 1, \ldots, M. \tag{2.14}$$

In the same way, the Hessian matrix $\mathbf{H}_{S_0}(\mathbf{m}_k)$ is given by

$$\mathbf{H}_{S_0}(\mathbf{m}_k) = \mathbf{J}(\mathbf{m}_k)^T \mathbf{W}_D^{-1} \mathbf{J}(\mathbf{m}_k) + \left[\frac{\partial \mathbf{J}^T}{\partial \mathbf{m}}(\mathbf{m}_k)\right] \mathbf{W}_D^{-1} \Delta \mathbf{d}(\mathbf{m}_k), \tag{2.15}$$

where

$$\left(\frac{\partial \mathbf{J}^T}{\partial \mathbf{m}}\right)_{ij} = \sum_{k=1}^{N} \left(\frac{\partial \mathbf{J}^T}{\partial m_i}\right)_{jk} \Delta \mathbf{d}_k. \tag{2.16}$$

Substitution into equation (2.11), Newton's equation can be written

$$\mathbf{H}_{S_0}(\mathbf{m}_k)\Delta \mathbf{m}_k = -\mathbf{J}(\mathbf{m_k})^T \mathbf{W}_D^{-1} \Delta \mathbf{d}(m_k). \tag{2.17}$$

with $\mathbf{H}_{S_0}$ given by equation (2.15). In principle, the solutions proposed in stereotomography and FWI derive both from the Newton equations (2.11) or (2.17). However, as the computation of the Hessian matrix $\mathbf{H}_S$ is a difficult task for realistic problems, modifications are required to yield feasible solutions. This situation is handled differently by tomography and FWI. Tomographic methods make use of a second-order numerical method in which the Gauss-Newton approximation of the Hessian matrix is employed. On the other hand, FWI makes use first-order, local descent method, which relies on gradients only.

Non-regularized Gauss-Newton (Tomography): The relevant expressions are simply obtained by replacing, typically in Newton's equations (2.17), the Hessian matrix $\mathbf{H}_S$ with by its so-called Gauss-Newton approximation (compare with equation (2.15)

$$\mathbf{H}_{S_0}(\mathbf{m_k}) \approx \mathbf{J}(\mathbf{m_k})^T \mathbf{W}_D^{-1} \mathbf{J}(\mathbf{m_k}). \tag{2.18}$$

This leads to the Gauss-Newton equation (compare with equation (2.17)),

$$\mathbf{J}(\mathbf{m_k})^T \mathbf{W}_D^{-1} \mathbf{J}(\mathbf{m_k})\Delta \mathbf{m_k} = -\mathbf{J}(\mathbf{m_k})^T \mathbf{W}_D^{-1} \Delta \mathbf{d}(\mathbf{m_k}). \tag{2.19}$$

The Jacobian matrix $\mathbf{J}(\mathbf{m}_k)$ can be efficiently computed at each iteration by applying paraxial ray theory (see, e.g., Cerveny, 2005; Popov, 2002). As a consequence, the Hessian approximation (2.18) can be readily computed, which turns Gauss-Newton optimization a very attractive procedure to estimate the model updating step $\Delta \mathbf{m}_k$.

Equation (2.19) is the Gauss-Newton equation for the original non-linear and non-regularized optimization problem. However, we can also express that equation as an LSQR solution of a simpler

matrix equation. To do that, we consider the matrix identities

$$
\begin{aligned}
\mathbf{J(m_k)}^T\mathbf{W}_D^{-1}\mathbf{J}(\mathbf{m}_k) &= [\mathbf{J(m_k)}^T\mathbf{W}_D^{-1/2}][\mathbf{W}_D^{-1/2}\mathbf{J}(\mathbf{m}_k)] \\
&= [\mathbf{W}_D^{-1/2}\mathbf{J(m_k)}]^T[\mathbf{W}_D^{-1/2}\mathbf{J}(\mathbf{m}_k)]
\end{aligned}
\tag{2.20}
$$

and

$$
\begin{aligned}
\mathbf{J(m_k)}^T\mathbf{W}_D^{-1}\Delta\mathbf{d}(\mathbf{m}_k) &= [\mathbf{J(m_k)}^T\mathbf{W}_D^{-1/2}][\mathbf{W}_D^{-1/2}\Delta\mathbf{d}(\mathbf{m}_k)] \\
&= [\mathbf{J(m_k)}\mathbf{W}_D^{-1/2}]^T[\mathbf{W}_D^{-1/2}\Delta\mathbf{d}(\mathbf{m}_k)],
\end{aligned}
\tag{2.21}
$$

which hold because $\mathbf{W}^{-1}$ (and consequently $\mathbf{W}^{-1/2}$ are positive diagonal matrices). With the help of the above identities, equation (2.19) can be written as

$$
[\mathbf{J(m_k)}\mathbf{W}_D^{-1/2}]^T[\mathbf{J(m_k)}\mathbf{W}_D^{-1/2}]\Delta\mathbf{m_k} = -[\mathbf{J(m_k)}\mathbf{W}_D^{-1/2}]^T[\mathbf{W}_D^{-1/2}\Delta\mathbf{d}(\mathbf{m_k})].
\tag{2.22}
$$

The above equation can be recognized as the so-called normal equation that relates to the LSQR solution (see, e.g, Watkins, 2004)) of the matrix equation

$$
[\mathbf{J(m_k)}\mathbf{W}_D^{-\frac{1}{2}}]\Delta\mathbf{m_k} = \mathbf{W}_D^{-\frac{1}{2}}\Delta\mathbf{d}(\mathbf{m_k}).
\tag{2.23}
$$

The computation of the updates $\mathbf{m}_k$ as a LSQR solution of equation (2.23) is justified because the Jacobian matrix $\mathbf{J}(\mathbf{m}_k)$ is an ill-conditioned matrix. In the LSQR approach, the computation of the product $\mathbf{J}^T(\mathbf{m}_k)\mathbf{W}_D^{-1}\mathbf{J}(\mathbf{m}_k)$ is avoided. Furthermore, numerical methods dedicated to solve ill-conditioned problems of the type (2.23) are available in the literature. Examples include, e.g., singular value decomposition (SVD) methods (Watkins, 2004; Van Loan and Golub, 1983) and methods based on a smart use of sparce matrices (Paige and Saunders, 1982).

Non-regularized local descents (FWI):   In a number of realistic inversion problems, even the calculation of the Jacobian operator is a difficult task. This is the case of the FWI problem. Therefore, another simplification in Newton's equation (2.11) is required in order to make estimation of model updates $\Delta\mathbf{m_k}$ a feasible process. For this purpose, the most popular, albeit rude, option, is to simply replace the Hessian $\mathbf{H}_S$ the $M \times M$ identity matrix $\mathbf{I}$. Such replacement leads to the model-update expression

$$
\Delta\mathbf{m_k} = -\alpha_k\nabla S_0(\mathbf{m}_k),
\tag{2.24}
$$

where α_k is a positive number that "calibrates" the upgrading step $\Delta \mathbf{m}_k$. Equation (2.24) characterizes the so-called local-descent method. In FWI, the gradient ∇S_0 is estimated by a continuous approach, using the adjoint state method (see, e.g, Fichtner et al. (2006)). Under such method, the estimate the gradient becomes computationally feasible, albeit the local-descent is less accurate than the Gauss-Newton method. More details about the adjoint state method will be given in Chapter 4 that treats the FWI problem.

Regularized problem: The results obtained for the previous case of non-regularized tomographic and FWI problems will now be generalized to the regularized case. Basically, this means of extending the analysis applied to the non-regularized misfit function $S(\mathbf{m})$ of equation (2.10) to its fully regularized counterpart of equations (2.5)-(2.7). As a consequence, Newton's equation for the regularized problem is given by

$$\mathbf{H}_S(\mathbf{m}_k)\Delta \mathbf{m}_k = -\nabla S(\mathbf{m}_k), \tag{2.25}$$

or from equation (2.5)

$$[\mathbf{H}_{S_0}(\mathbf{m}_k) + \mathbf{H}_{S_1}(\mathbf{m}_k)]\Delta \mathbf{m}_k = -[\nabla S_0(\mathbf{m}_k) + \nabla S_1(\mathbf{m}_k) + \nabla S_2(\mathbf{m}_k)]. \tag{2.26}$$

As can be readily seen equation (2.7), we have

$$S_1(\mathbf{m}_k) = \lambda_1 \mathbf{R}\mathbf{m}_k \quad \text{and} \quad \nabla S_2(\mathbf{m}_k) = \lambda_2 \mathbf{W}_M^{-1}(\delta\mathbf{m}^{pri})_k,$$

$$\mathbf{H}_{S_1} = \lambda_1 \mathbf{R} \quad \text{and} \quad \mathbf{H}_{S_2}(\mathbf{m}_k) = \lambda_2 \mathbf{W}_M^{-1}. \tag{2.27}$$

Collecting results, Newton's regularized solution is given by equation (2.26), together with equations (2.13), (2.15), (2.13) and (2.27). Explicitly, we have

$$[\mathbf{H}_{S_0} + \lambda_1 \mathbf{R} + \lambda_2 \mathbf{W}_M^{-1}]\Delta \mathbf{m}_k = -[\nabla S_0 + \lambda_1 \mathbf{R}\mathbf{m} + \lambda_2 \mathbf{W}_M^{-1}(\delta\mathbf{m}^{pri})_k]. \tag{2.28}$$

Regularized Gauss-Newton (Tomography): As in Newton's non-regularized solution, the corresponding solution for the regularized case is also obtained by replacing the Hessian $\mathbf{H}_{S_0}$ with its Gauss-Newton approximation (2.19). Substitution into equation (2.28 and also making use of equa-

tion (2.13). we find

$$[(\mathbf{J}(\mathbf{m}_k)^T\mathbf{W}^{-1}\mathbf{J}(\mathbf{m}_k) + \lambda_1\mathbf{R} + \lambda_2\mathbf{W}_M^{-1}]\Delta\mathbf{m}_k$$
$$= -[\mathbf{J}(\mathbf{m}_k)^T\mathbf{W}^{-1}\Delta\mathbf{d} + \lambda_1\mathbf{R}\mathbf{m} + \lambda_2\mathbf{W}_M^{-1}(\delta\mathbf{m}^{pri})_k]. \tag{2.29}$$

As previously shown in the non-regularized case, the Gauss-Newton solution (2.29) also admits a LSQR solution of simpler matrix equation.

Remind that the particular matrix $\mathbf{R}$ to be applied is an user choice. In this thesis, a matrix $\mathbf{R}$ that accounts for smoothness velocity model properties will be used for seismic tomography description. As it will be discussed in next chapter, $\mathbf{R}$ is a positive-definite matrix, namely, we have

$$\mathbf{m}^T\mathbf{R}\mathbf{m} > 0 \quad \text{for all} \quad \mathbf{m} \neq \mathbf{0}. \tag{2.30}$$

As matrix $\mathbf{R}$ is a positive-definite matrix, it admits a so-called Cholesky decomposition of the form

$$\mathbf{R} = (\mathbf{R}^{tri})^T\mathbf{R}^{tri}, \tag{2.31}$$

where $\mathbf{R}^{tri}$ and $(\mathbf{R}^{tri})^T$ are superior and inferior triangular matrices. Moreover, taking into account the identity (2.20)-(2.21), we can write the Gauss-Newton solution (2.29) in the alternative form

$$\mathbf{U}_k^T(\mathbf{U}\Delta\mathbf{m}_k) = \mathbf{U}_k^T\mathbf{V}_k \tag{2.32}$$

where

$$\mathbf{U}_k = \begin{bmatrix} \mathbf{J}(\mathbf{m}_k)\mathbf{W}_D^{-1/2} \\ \lambda_1\mathbf{R}^{tri} \\ \lambda_2\mathbf{W}_M^{-1/2} \end{bmatrix} \quad \text{and} \quad \mathbf{V}_k = - \begin{bmatrix} \mathbf{W}_D^{-1/2}\Delta\mathbf{d}(\mathbf{m}_k) \\ \lambda_1\mathbf{R}^{tri}\mathbf{m}_k \\ \lambda_2\mathbf{W}_M^{-1/2}(\delta\mathbf{m}^{pri})_k) \end{bmatrix}, \tag{2.33}$$

The above is recognized as the normal equation related to LSQR matrix equation

$$\mathbf{U}_k\Delta\mathbf{m}_k = \mathbf{V}_k. \tag{2.34}$$

Regularized local descent method (FWI):   As the model spaces for FWI and seismic tomography problems are different, another regularization matrix $\mathbf{R}$ has to be considered for FWI context. Once again, the particular matrix $\mathbf{R}$ to be applied is an user choice and varies from one application to another. In this thesis, a regularization matrix based on the referecence Virieux et al. (2017) will be considered for FWI description and more details will be given in chapter 4.

Following the discussion of the non-regularized case, the upgrade step for the local descent method for regulairized FWI is given by (compare with equation (2.24))

$$\Delta\mathbf{m_k} = -\alpha_k\nabla S(\mathbf{m}_k) = -\alpha_k[\nabla S_0(\mathbf{m}_k) + \lambda_1\mathbf{R}\mathbf{m}_k + \lambda_2\mathbf{W}_M\delta(\mathbf{m}^{pri})_k]. \tag{2.35}$$

The gradient $\nabla S_0(\mathbf{m}_k)$ is computed by the adjoint state method as earlier discussed.

Initial model space: As a last topic of this chapter, we comment on the important issue of the choice of the initial model space, for which a successful iterative procedure is achieved. The data space and the initial model space are the main inputs for LSQR seismic inverse problems. Once an initial model space is given, the subsequent models are iteratively updated using a local linearized optimization algorithm. For seismic tomography methods, the sensitivity of the initial model is not so dramatic: simple geometric rules can be applied to generate such models. For FWI, this sensitivity demand is much higher. In particular, prior information, such as well data, can be essential (Virieux et al., 2017). Another strategy consists in solving a simplified version of the FWI method is applied to produce an improved initial model [Camargo (2019)]. In this thesis, we propose to use the space model obtained from a CRP tomography the initial model for FWI. As the computational effort involved in FWI is much greater than the one required by tomography, the proposed approach is expected to improve the FWI implementation.

2.3   Summary and conclusions

The basic concepts and results of the Least Squares (LSQR) inversion have been presented in the context of their applications to stereotomography and FWI. The same formulation and methodology applies to other tomographic approaches, most particularly the new Common-Reflection-Point (CRP) tomography to be presented in Chapter 5. As seen throughout this thesis, LSQR solutions will be iteratively constructed, requiring an optimization problem to be solved in each iteration. For stereotomography and CRP tomography, the second-order, Gauss-Newton is the numerical optimization method of choice. For FWI, the first-order descent method is used. Also discussed is the important role played user-selected regularization terms to stabilize the iteration process and guide it to a meaningful solution.

It is to be noted that the update procedure for FWI employs a first-order (local descent)
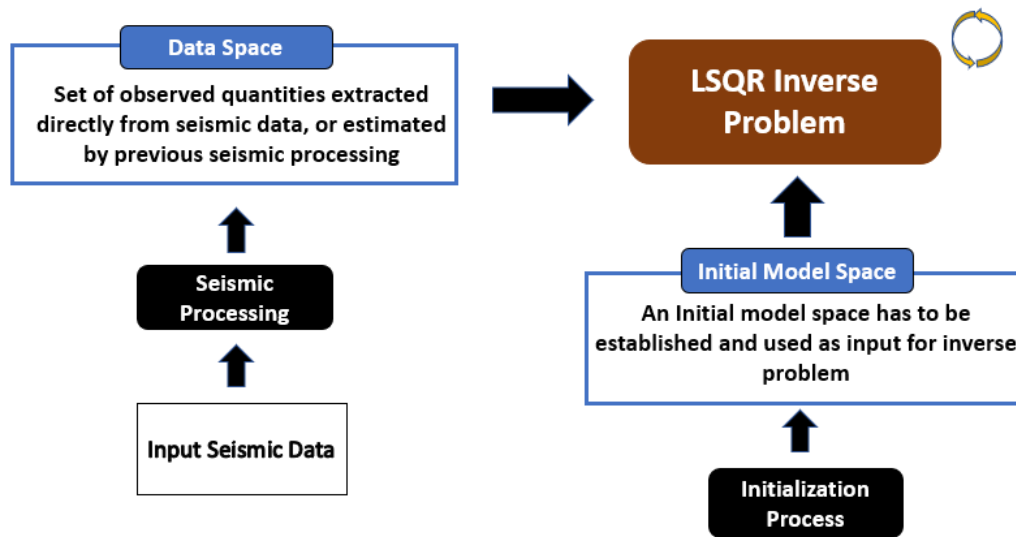
Figure 2.4: LSQR inverse problem uses two input spaces: data space and initial model space. Data space is formed by observed quantities from seismic data. The initial model can be addressed by a first guess or using some simple rules, based on previous model and/or data information. For FWI application, the initial model space is a crucial issue for a good LSQR inverse problem.

numerical method, which is less accurate that the second-order (Gauss-Newton) numerical method used in tomography. As a consequence, much higher dependency on the initial model is to be expected from FWI as compared to tomography. This justifies our proposal to have a resulting model space from a tomographic method (in this case the new CRP tomography) as an initial model for FWI.

Chapter 3

Stereotomography

Based on the general formulation of the LSQR method described in the previous chapter, the stereographic problem, originally proposed and solved in (Billette and Lambaré, 1998) is here reviewed and discussed. As such, the case of two-dimensional, isotropic acoustic media with no *a priori* model-space information is considered. As discussed in Chapter 2, the misfit function for this problem is that of equation (2.6), with the scalar parameter $\lambda_1 = 0$. The matrix parameter $\mathbf{W}_D^{-1}$ accounts for the different units (space location, slope and traveltime) of the stereotomography data spcace. Illustrative tests on implemented synthetic data are presented and discussed in Chapters 6, 7 and 8.

3.1   Observed-data and model spaces

As a first step of the description of the LSQR solution of the stereographic inverse problem, the observed-data and model spaces are now introduced.

Observed-data space: The observed-data space of stereotomgraphy, $\mathbf{d}^{obs}$, consists of N parameter vectors $\mathbf{d}_i^{obs}$ extracted from locally-coherent (primary reflection/diffraction) events of the given prestack data set. Such points are arbitrarily selected by the user by manual or automatic picking. In symbols, we can write

$$\mathbf{d}^{obs} = [\mathbf{d}_i^{obs}]_{i=1}^N = [(s, r, p_s, p_r, t_{sr})_i^T]_{i=1}^N. \qquad (3.1)$$

Omitting the subscript i, and with the help of Figure 3.1, the components refer to a primary reflection or diffraction ray that starts from a shot location s and arrives at the receiver location r at a planar horizontal seismic line, with slopes (horizontal slowness) p_s and p_r at source and receiver, respectively, and total traveltime t_{sr}. The use of information from two different directions justifies the term *stereo* of the name of the method.
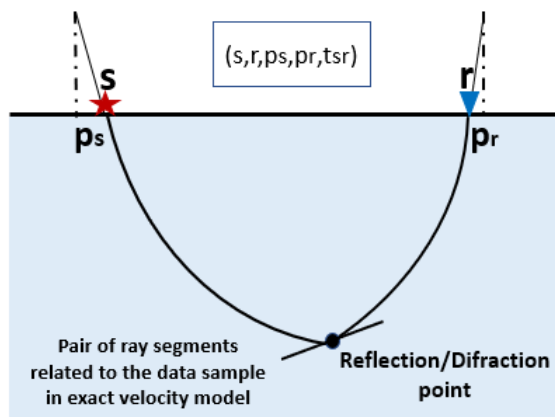

Figure 3.1: The data-parameter vector (s, r, p_s, p_r, t_{sr}) corresponds, in the exact (unknown) velocity model, to primary reflection/diffraction ray that connects the source and receiver to a primary reflection/diffraction point in depth.

It is to be noted that, while the source and receiver locations s and r, as well as the total reflection/diffraction traveltime t_{sr} are directly available from the given data set, the slope parameters p_s and p_r require some pre-processing to be extracted. Following Billette et al. (2003), the slopes p_s and p_r, can, as a possibility, be estimated by means of slant stacks of r-common-receiver and s-common-shot panels, respectively.

Model space: The M-dimensinal stereographic model space $\mathbf{m}$ is composed by the union of two model-space subsets

$$\mathbf{m} = \mathbf{m}^{vel} \cup \mathbf{m}^{ray}, \tag{3.2}$$

in which $\mathbf{m}^{vel}$ is the M_v-dimensional velocity-model space and $\mathbf{m}^{ray}$ is the N-dimensional ray-model space. It is to be noted the dimesionaly relation

$$M = M_v + 6N. \tag{3.3}$$

Velocity-model space: This is the M_v-dimensional space

$$\mathbf{m}^{vel} = [v_i]_{i=1}^{M_v} = (v_1, ..., v_{M_v})^T, \tag{3.4}$$

in which its components v_i have the task of producing a velocity function $v(x, z)$ that is needed at each iterated step. Such velocity is defined on the depth region of interest, as specified by an invariant, generally rectangular mesh provided by the user. That mesh has dimensions of M_{vx} lines and M_{vz} columns, the product of which equals the dimension M_v of $\mathbf{m}^{vel}$. As shown in Figure 3.2, the knots of that mesh are populated by the components of the $\mathbf{m}^{vel}$. More specifically, the B-spline interpolation coefficient v_{ij} at the (i, j)-knot is given by the k-th component v_k of $\mathbf{m}^{vel}$. In symbols,

$$v_{ij} \equiv v_k, \quad \text{with} \quad k = (i - 1)M_{vx} + j, \quad (i = 1, ..., M_{vx}, \quad j - 1, ...M_{vz}). \tag{3.5}$$
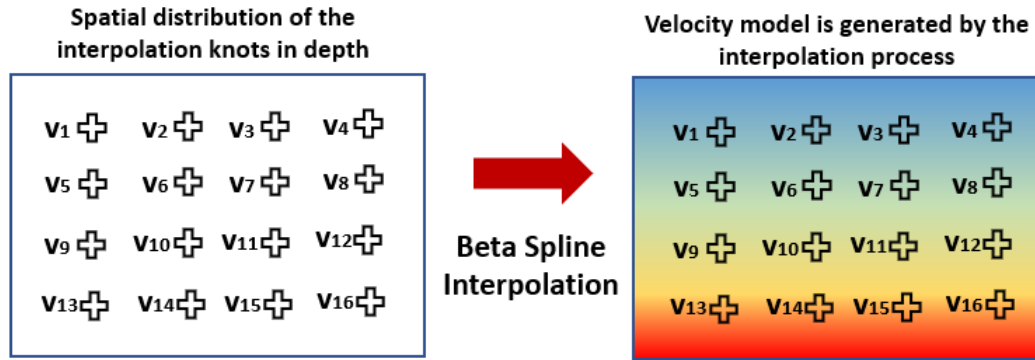

Figure 3.2: Velocity model construction: On an invariant, user-selected mesh, values of v_k are assigned and matrix entries v_{ij} which are taken as coefficients of a beta-spline representation of the velocity function. By means of iterative updates, stereotomography aims to invert those coefficients to an acceptable velocity-model solution.

With the help of the components v_{ij}, the velocity $v(x, z)$ is defined in the whole depth domain as a B-spline interpolation (de Boor et al., 1978)

$$v(x, z) = \sum_{i-1}^{M_{vx}} \sum_{j=1}^{M_{vz}} v_{ij} \beta_i(x) \beta_j(z), \tag{3.6}$$

in which $\beta_i(x)$ and $\beta_j(z)$ are one-dimensional cubic B-spines, with v_{ij} being the interpolation coefficients. A brief explanation about B-spline constructions is given in the Appendix D. For a more detailed text, the reader can refer to, e.g., de Boor et al. (1978).

Under the above considerations, it turns out that stereotomographic problem aims to invert the B-spline coefficients only, and not the entire velocity model, which is automatically given by equation (3.6). As a consequence, the procedure always produces smooth velocity models. As seen below, this is a good characteristic, as it allows the forward-modeling engine of stereotomogrphy to be based on ray-tracing algorithms. Such algorithms require continuous derivatives of the velocity function, this condition being naturally fulfilled by the beta-splice construction.

Ray-model space: That space is given by

$$\mathbf{m}^{ray} = [\mathbf{m}_i^{ray}]_{i=1}^N = [(x, z, \theta_s, \theta_r, t_s, t_r)_i]_{i=1}^N, \tag{3.7}$$

in which each six-component parameter vector $\mathbf{m}_i^{ray}$ corresponds to its counterpart five-component parameter vector $\mathbf{d}_i^{obs}$ in the observed-data space. In symbols, we have a one-to-one correspondence

$$\mathbf{m}_i^{ray} = (x, z, \theta_s, \theta_r, t_s, t_r)_i^T \iff (s, r, p_s, p_r, t_{sr})_i^T = \mathbf{d}_i^{obse} \quad (i = 1, ..., N). \tag{3.8}$$

Adopting a ray-theoretical description of the wave propagation involved and, moreover, assuming that perfect modeling conditions hold, such correspondence admits a natural interpretation.

As depicted in Figure 3.3, we assume, for simplicity, that the observed data space $\mathbf{d}^{obs}$ and, as a consequence, also the ray model space $\mathbf{m}^{ray}$, consist of single vectors. These represented by parameters (s, r, p_s, p_r, t_{sr}) and $(x, z, \theta_s, \theta_r, t_s, t_r)$, respectively. The parameters of $\mathbf{m}^{ray}$ can be seen to specify the depth point (x, z), interpreted as a diffraction point, as well as two up-going rays, both starting from that diffraction point. The first one, referred to the source ray, is defined by the angle direction θ_s with the vertical (z-axis) and traveltime t_s. The second, referred to as the receiver ray, has an analogous definition, this time for the θ_r and t_r quantities. Under the situation of perfect modeling conditions, the source and receiver rays hit the measurement seismic line, respectively at the points s, with horizontal slowness p_s, and r, with horizontal slowness p_r, respectively. Such quantities match the parameters given by the observed-data space. Moreover, in this situation, the condition $t_s + t_r = t_{sr}$, in which the traveltime parameter t_{sr} also belongs to the observed data space, is satisfied.
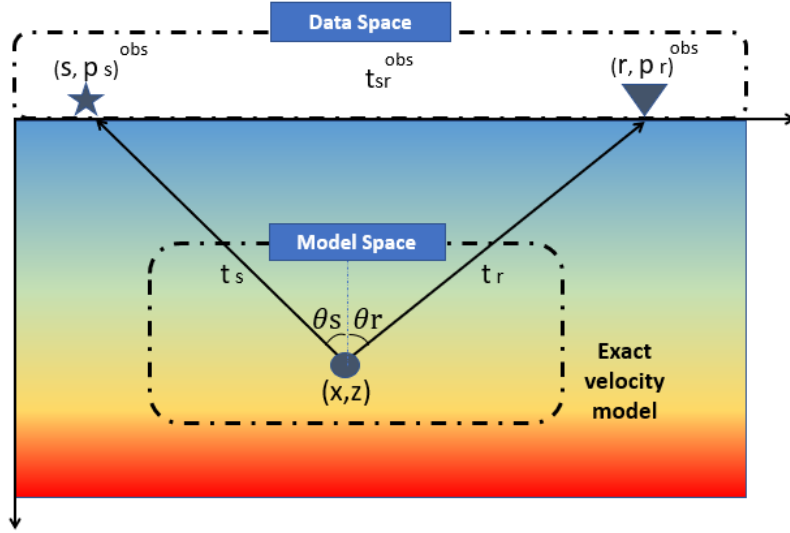
Figure 3.3: Interpretation of vector parameter $(x, z, \theta_s, \theta_r, t_s, t_r)$ of ray-model space $\mathbf{m}^{ray}$: Color map represents the beta-spline velocity function with coefficients given by velocity-model vector $\mathbf{m}^{vel}$. The parameters (x, z) locates a diffraction point (x, z), from which two up-going rays are specified by angle-direction and traveltime parameter pairs (θ_s, t_s) and (θ_r, t_r), respectively. Such rays, referred to as source and receiver rays, hit the measurement seismic line in such a way that the location and horizontal slowness pairs (s, p_s) and (r, p_r) match the parameters given by the observed data space. Finally, we also have that $t_s + t_r = t_{sr}$, namely the traveltime sum of t_s and t_r matches the observed-data traveltime parameter t_{sr}.

3.2   Forward-model engine and synthetic-data space

As previously indicated, the forward-modeling engine of stereotomography is ray tracing. Such engine results from a ray formulation of the wave equation, here considered for 2D acoustic, isotropic media. For completeness, a brief description of the basics of ray propagation as needed in this thesis is provided in Appendix C. For more details, the interested reader is referred to classical literature, e.g., Cerveny (2005) and Popov (2002).

As indicated in Chapter 2, the forward-modeling engine transforms a given model space $\mathbf{m}$ onto a corresponding synthetic data space

$$\mathbf{d}^{syn}(\mathbf{m}) = [\mathbf{d}_i^{syn}(\mathbf{m})]_{i=1}^N, \tag{3.9}$$

which has the same form as the given (invariant) observed-data space $\mathbf{d}^{obs}$.

The construction of a synthetic data space $\mathbf{d}^{syn}(\mathbf{m})$ for arbitrary model space $\mathbf{m} = \mathbf{m}^{vel} \cup \mathbf{m}^{ray}$, can be explained along the same lines previously used in the case of perfect modeling con-
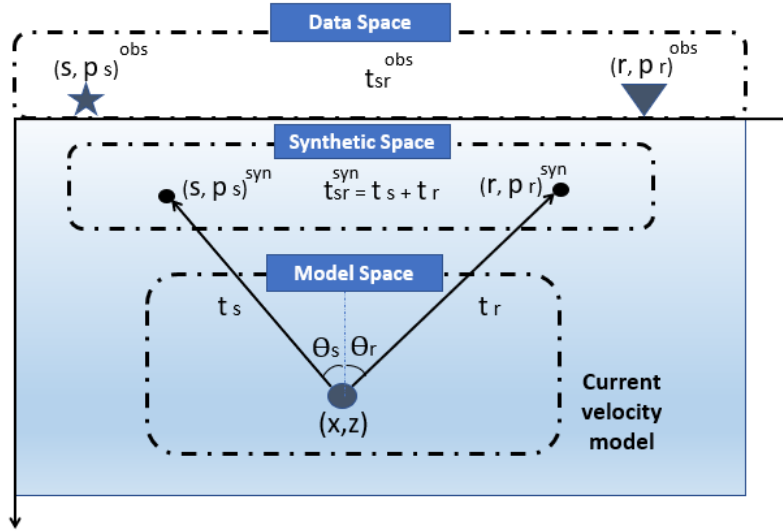
Figure 3.4: Synthetic data model $\mathbf{d}^{syn}(\mathbf{m})$ for arbitrary model space $\mathbf{m} = \mathbf{m}^{vel} \cup \mathbf{m}^{ray}$: Color map represents the beta-spline velocity function provided by $\mathbf{m}^{vel}$. Also, $(x, z, \theta_s, \theta_r, t_s, t_r)$, represents the single parameter vector of $\mathbf{m}^{ray}$. Under the same procedure of Figure 3.3, the diffraction point (x, z), as well as the up-going source and receiver rays, as defined by the parameters (θ_s, t_s) and (θ_r, t_r), respectively, are constructed. The endpoint locations and slowness vectors $[s^{syn}(\mathbf{m}), p_s^{syn}(\mathbf{m})]$ and $[r^{syn}(\mathbf{m}), p_r^{syn}(\mathbf{m})]$, as well as the traveltime $t_{sr}^{syn}(\mathbf{m}) = t_s(\mathbf{m}) + t_r(\mathbf{m})$ parameterize the synthetic data vector $\mathbf{d}^{syn}(\mathbf{m})$, Note that, in general, $\mathbf{d}^{syn}(\mathbf{m}) \neq \mathbf{d}^{obs}$.

ditions (see Figure 3.4 and related text). As before, the ray-model subset, $\mathbf{m}^{ray}$ is, for simplicity assumed to consist of a single vector. This situation is depicted in Figure 3.4, in which the color map represents the beta-spline velocity function, as determined by $\mathbf{m}^{vel}$. We now let $(x, z, \theta_s, \theta_r, t_s, t_r)$ parameterize the single vector of $\mathbf{m}^{ray}$. Then the previous procedure produces the diffraction point (x, z), as well as the up-going source and receiver rays, defined by the direction-angle and traveltime parameters (θ_s, t_s) and (θ_r, t_r), respectively (see Figure-3.3).

By means of such construction, the synthetic data vector $\mathbf{d}^{syn}(\mathbf{m})$ can be fully parameterized by the vector $(s^{syn}, r^{syn}, p_s^{syn}, p_r^{syn}, t_{sr}^{syn})$, where (s^{syn}, p_s^{syn}) and (r^{syn}, p_r^{syn}) represent the location and horizontal slowness at the endpoints of the source and receiver rays, respectively, and $t_{sr}^{sign} = t_s + t_r$. Under the use of the above computations, in the general case of a ray-model subset $\mathbf{m}^{ray}$ contains N vectors $\mathbf{m}_i^{ray}$, the corresponding synthetic data space $\mathbf{d}^{sync}(\mathbf{m})$ can be given as

$$\mathbf{d}^{syn}(\mathbf{m}) = [\mathbf{d}_i^{syn}(\mathbf{m})]_{i=1}^N = [(s, r, p_s, p_r, t_{sr})_i^{syn}]_{i=1}^N, \quad \text{with} \quad t_{sr}^{syn} = t_s + t_r, \qquad (3.10)$$

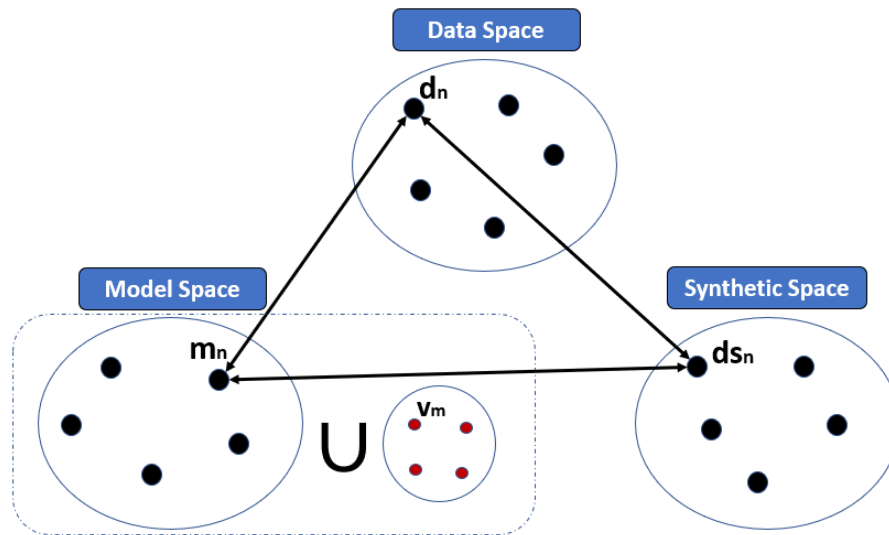Figure 3.5 provides a pictorial summary of the stereographic data, model and synthetic spaces.

Figure 3.5: Observed-data, model and synthetic-data spaces: each observed-data vector $\mathbf{d}_i^{obs}$ relates to a corresponding ray-model vector $\mathbf{m}_i^{ray}$. By means of a forward-modeling engine, trial model vectors generates a corresponding synthetic vector $\mathbf{d}_i^{syn}$. Observed- and synthetic-data vectors have the same nature and size, allowing their discrepancy by means of misfit function. The stereographic model space consists of the union of two model-space subsets. The first is the velocity-model space $\mathbf{m}^{vel}$, which is responsible for the coefficients of the beta-spline representation of the velocity function. The second is the ray-model space $\mathbf{m}^{ray}$ which consists of model-parameter vectors that correspond to the given observed-data vectors.

3.3   Misfit function and regularization

As seen below, classical least-square-root (LSQR) inversion can be applied to solve the stereography inverse problem. In agreement with the discussion provided in Chapter 2, the solution of this seismic tomographic problem is achieved by means of a Gauss-Newton iterative procedure applied to a regularized misfit function that measures, for any given trial model space $\mathbf{m}$, the discrepancy $\Delta\mathbf{d}(\mathbf{m}) = \mathbf{d}^{syn}(\mathbf{m}) - \mathbf{d}^{obs}$ between the synthetic and observed data spaces. As previously discussed in the context of the LSQR method, the introduction of regularization terms in the misfit function is of crucial importance in ill-posed inversion problems, such as tomography and FWI. A brief survey on the available regularization strategies and schemes that can be of use for a practical implementation of stereotomography is provided in (Billette et al., 2003, see references therein). Such discussion includes both strictly numerical possibilities (such as smart use of damping factors), as well as physically-oriented approaches (such as smoothing constraints on velocities).

The specific choices of the misfit and regularization functions are now introduced.

Following, e.g., Billette and Lambaré (1998); Lambaré et al. (2004), the misfit function is

assumed to be

$$S(\mathbf{m}) = \frac{1}{2}[\Delta\mathbf{d}^T(\mathbf{m})\mathbf{W}_D^{-1}\Delta\mathbf{d}(\mathbf{m}) + \lambda\mathbf{m}^{vel^T}\mathbf{R}^{(v)}\mathbf{m}^{vel}], \quad (3.11)$$

where $\mathbf{W}_D^{-1}$ is the diagonal matrix that accounts for a priori data information and brings the different data types to a comparable size.

The misfit function (3.11) follows the general description provided in Chapter 2 (see equations (2.5)-(2.7)), however with two differences. Firstly, no *a priori* model information is considered, i.e., $S_1(\mathbf{m}) = 0$. Secondly, the regularization term has the form

$$S_2(\mathbf{m}^{vel}) = \lambda(\mathbf{m}^{vel})^T\mathbf{R}^{(v)}\mathbf{m}^{vel} \quad (3.12)$$

meaning that it applies to the velocity-model space $\mathbf{m}^{vel}$ only. Matrix $\mathbf{R}^{(v)}$ is a constant, positive-definite matrix of dimension $M_v \times M_v$. Notation is also simplified by setting $\lambda_2 = \lambda$.

As seen below, it is advantageous that the regularization term $\mathbf{R}^{(v)}$, which is restricted to the velocity-model space $\mathbf{m}^{vel}$, is extended to the whole model-space $\mathbf{m} = \mathbf{m}^{ray} \cup \mathbf{m}^{vel}$. This is simply done by observing that

$$(\mathbf{m}^{vel})^T\mathbf{R}^{(v)}\mathbf{m}^{vel} = \mathbf{m}^T\mathbf{R}\mathbf{m}, \quad (3.13)$$

where the matrix $\mathbf{R} = (R_{ij})$, $(i, j = 1, ..., M)$ simply relates to its counterpart matrix $\mathbf{R}^{(v)} = [R_{ij}^{(v)}]$, $(i, j = 1, ..., M_v)$ by

$$\mathbf{R} = \begin{bmatrix} \mathbf{0}_{11} & \mathbf{0}_{12} \\ \mathbf{0}_{21} & \mathbf{R}^{(v)} \end{bmatrix}, \quad (3.14)$$

where the null submatrices $\mathbf{0}_{11}$, $\mathbf{0}_{12}$ and $\mathbf{0}_{21}$ has dimensions $6N \times 6N$, $6N \times M_v$ and $M_v \times 6N$, respectively. In other words, the matrix $\mathbf{R}$ is obtained by adding lines and columns to the matrix $\mathbf{R}^{(v)}$ matrix until a full matrix $M \times M$ is obtained. Here, the following ordering was considered for model vector $\mathbf{m}$

$$\mathbf{m} = [\mathbf{m}^{ray}, \mathbf{m}^{vel}]. \quad (3.15)$$

Substitution into equation (3.11) leads to the extended misfit function

$$S(\mathbf{m}) = \frac{1}{2}[\Delta\mathbf{d}^T(\mathbf{m})\mathbf{W}_D^{-1}\Delta\mathbf{d}(\mathbf{m}) + \lambda\mathbf{m}^T\mathbf{R}\mathbf{m}], \quad (3.16)$$

In this thesis, a single regularization function is applied to all problems under investigation. Such regularization is based on the minimization of second derivatives of the velocity model, being inspired on the one described in (see, e.g., Duveneck, 2004b) in the context of so-called Normal Incidence Point (NIP) tomography. If $v(x, z)$ is the B-splice representation that refers to a given velocity-model space $\mathbf{m}^{vel}$, the regularization function $R_v(\mathbf{m}^{vel})$ is given by

$$R_v(\mathbf{m}^{vel}) = \int_z \int_x \left(\epsilon_{xx} \left(\frac{\partial^2 v(x, z)}{\partial x^2} \right)^2 + \epsilon_{zz} \left(\frac{\partial^2 v(x, z)}{\partial z^2} \right)^2 + \epsilon_{vv} v^2(x, z) \right) dx dz, \qquad (3.17)$$

in which where ϵ_{xx}, ϵ_{zz} and ϵ_{vv} are user-selected constant positive weights. In order to keep the purpose of smoothness regularization operator, the parameters are chosen such that $\epsilon_{xx} >> \epsilon_{vv}$ and $\epsilon_{zz} >> \epsilon_{vv}$. However, to turn $R^{(v)}$ a positive definite matrix, the parameter ϵ_{vv} has to be positive (see Appendix E).

It also to be noted that a scalar factor λ is also presented in the regularization term. This factor "calibrates" the influence of the regulation term, which is external to the actual problem: If the factor λ is too large, we should expect good convergence, but poor respect to the physics of the problem. For too small value of λ, one can expect that the physics of the problem is more respected, but we may find undesired instability. In summary, the choice of λ is a mixture of science of art, in which hard testing work is required.

Following Duveneck (2004b), the matrix $\mathbf{R}^{(v)}$, which is invariant through inversion process, results from the substitution of the beta-spline representation of the velocity function $v(x, z)$ and its second derivatives into equation (3.17). The construction of regularization matrix $\mathbf{R}$ will be detailed in Appendix E.

From the above considerations, our regularized misfit function will be given by (compare with equation (3.11))

$$S(\mathbf{m}) = \frac{1}{2} [\Delta \mathbf{d}^T(\mathbf{m}) \mathbf{W}_D^{-1} \Delta \mathbf{d}(\mathbf{m}) + \lambda \mathbf{m}^T \mathbf{R} \mathbf{m}]. \qquad (3.18)$$

3.4   Iteration Process

The iteration process for stereotomography follows the formalism of Chapter 2, however under the consideration of the regularized misfit function (3.11) instead of the original one of equa-

tions (2.5)-(2.7). More explicitly, that iteration has the same form of equation (2.9), namely

$$\mathbf{m}_{k+1} = \mathbf{m}_k - \alpha_k \Delta \mathbf{m}_k, \tag{3.19}$$

in which α_k is a positive scalar that calibrates the size of the updating step. The update $\Delta \mathbf{m}_k$, however, now satisfies (compare with equation (2.29))

$$[(\mathbf{J}(\mathbf{m}_k)^T \mathbf{W}^{-1} \mathbf{J}(\mathbf{m}_k) + \lambda \mathbf{R}]\Delta \mathbf{m}_k = -[\mathbf{J}(\mathbf{m}_k)^T \mathbf{W}^{-1}\Delta \mathbf{d} + \lambda \mathbf{R}\mathbf{m}]. \tag{3.20}$$

Also to be noted is that the analysis of Chapter 2 that leads to equations (2.31)-(2.34)) fully holds. As a consequence, the update $\Delta \mathbf{m}_k$ can be alternatively obtained as the LSQR solution of the problem (compare with equation (2.34))

$$\mathbf{U}_k \Delta \mathbf{m}_k = \mathbf{V}_k. \tag{3.21}$$

with (compare with equation (2.33))

$$\mathbf{U}_k = \begin{bmatrix} \mathbf{J}(\mathbf{m}_k)\mathbf{W}_D^{-1/2} \\ \lambda \mathbf{R}^{tri} \end{bmatrix} \quad \text{and} \quad \mathbf{V}_k = - \begin{bmatrix} \mathbf{W}_D^{-1/2}\Delta \mathbf{d}(\mathbf{m}_k) \\ \lambda \mathbf{R}^{tri}\mathbf{m}_k \end{bmatrix}, \tag{3.22}$$

in which $\mathbf{R}^{tri}$ satisfies the Cholesky decomposition

$$\mathbf{R} = (\mathbf{R}^{tri})^T \mathbf{R}^{tri}, \tag{3.23}$$

where $\mathbf{R}^{tri}$ and $(\mathbf{R}^{tri})^T$ are superior and inferior triangular matrices.

Remind that the use of equation (3.21) is justified because it avoids matrix operations with ill-conditioned matrices and due to the numerical methods available in literature. In this thesis, the equation is solved by the singular value decomposition method (see, e.g, Watkins (2004), Van Loan and Golub (1983)). SVD is a standard numerical method for ill-conditioned matrix equations, and provides expression of the generalized inverse of the Jacobian matrix. Unfortunately, for even large applications, as is the case of real-sized problems, SVD has to be avoided, due to its huge computational effort. Thereby, other strategies has to be used to compute model improvement vector $\Delta \mathbf{m_k}$. The LSQR algorithm proposed in the reference Paige and Saunders (1982) can be used in those situations. It is based on conjugate gradient solution of the linear system and can appropriately explore the sparsity of the Jacobian matrix, which turns the method a standard one for real-sized seismic tomography applications.

Jacobian matrix: As introduced in Chapter 2 (see equation (2.14)), the Jacobian (or Fréchet-derivative) matrix $\mathbf{J}(\mathbf{m})$, that needs to be computed at each iteration $\mathbf{m} = \mathbf{m}_k$ of the LSQR inversion, is given by

$$\mathbf{J}(\mathbf{m}) = \frac{\partial \mathbf{d}^{syn}(\mathbf{m})}{\partial \mathbf{m}} = \left(\frac{\partial d_i^{syn}(\mathbf{m})}{\partial m_j} \right), \tag{3.24}$$

in which d_i^{syn} and m_j are, respectively, the i-th and j-th components of the synthetic-data and model spaces. The calculation of the derivatives can be obtained by the use of paraxial ray theory, the reader being referred to classical literature (see, e.g., Cerveny, 2005; Popov, 2002) for more details. More details about the Jacobian matrix for stereotomography are provided in Billette and Lambaré (1998).

As described in the previous sections, the synthetic space $\mathbf{d}^{syn} = \mathbf{d}^{syn}(\mathbf{m})$ is made up of N parameter vectors $\mathbf{d}_i^{syn} = (s, r, p_s, p_r, t_{sr})_i^{syn}$, each of them with five components. On the other hand, the model space $\mathbf{m} = \mathbf{m}^{vel} \cup \mathbf{m}^{ray}$ is composed by M_v model-velocity components, namely B-spline interpolation coefficients $(v_1, ..., v_m)$, plus N ray-model parameter vectors $\mathbf{m}_i^{\mathbf{ray}} = (x, z, \theta_s, \theta_r, t_s, t_r)$, each of them with six components. Collecting results, we have that the data spaces $\mathbf{d}^{syn}(\mathbf{m})$ and $\mathbf{m}$ spaces have $5N$ and $M_v + 6N$ components, respectively. As a consequence, the Jacobian $\mathbf{J}(\mathbf{m})$ is a generally rectangular matrix of dimension $(5N) \times (M_v + 6N)$.

From the above considerations, the stereographic Jacobian matrix $\mathbf{J} = \mathbf{J}(\mathbf{m})$ admits the following representation:

$$\mathbf{J} = \begin{bmatrix} \dfrac{\partial \mathbf{t_{sr}}^{syn}}{\partial \mathbf{x}} & \dfrac{\partial \mathbf{t_{sr}}^{syn}}{\partial \mathbf{z}} & \dfrac{\partial \mathbf{t_{sr}}^{syn}}{\partial \theta_\mathbf{s}} & \dfrac{\partial \mathbf{t_{sr}}^{syn}}{\partial \theta_\mathbf{r}} & \dfrac{\partial \mathbf{t_{sr}}^{syn}}{\partial \mathbf{t_s}} & \dfrac{\partial \mathbf{t_{sr}}^{syn}}{\partial \mathbf{t_r}} & \dfrac{\partial \mathbf{t_{sr}}^{syn}}{\partial \mathbf{v}} \\[2mm] \dfrac{\partial \mathbf{p_s}^{syn}}{\partial \mathbf{x}} & \dfrac{\partial \mathbf{p_s}^{syn}}{\partial \mathbf{z}} & \dfrac{\partial \mathbf{p_s}^{syn}}{\partial \theta_\mathbf{s}} & \dfrac{\partial \mathbf{p_s}^{syn}}{\partial \theta_\mathbf{r}} & \dfrac{\partial \mathbf{p_s}^{syn}}{\partial \mathbf{t_s}} & \dfrac{\partial \mathbf{p_s}^{syn}}{\partial \mathbf{t_r}} & \dfrac{\partial \mathbf{p_s}^{syn}}{\partial \mathbf{v}} \\[2mm] \dfrac{\partial \mathbf{p_r}^{syn}}{\partial \mathbf{x}} & \dfrac{\partial \mathbf{p_r}^{syn}}{\partial \mathbf{z}} & \dfrac{\partial \mathbf{p_r}^{syn}}{\partial \theta_\mathbf{s}} & \dfrac{\partial \mathbf{p_r}^{syn}}{\partial \theta_\mathbf{r}} & \dfrac{\partial \mathbf{p_r}^{syn}}{\partial \mathbf{t_s}} & \dfrac{\partial \mathbf{p_r}^{syn}}{\partial \mathbf{t_r}} & \dfrac{\partial \mathbf{p_r}^{syn}}{\partial \mathbf{v}} \\[2mm] \dfrac{\partial \mathbf{s}^{syn}}{\partial \mathbf{x}} & \dfrac{\partial \mathbf{s}^{syn}}{\partial \mathbf{z}} & \dfrac{\partial \mathbf{s}^{syn}}{\partial \theta_\mathbf{s}} & \dfrac{\partial \mathbf{s}^{syn}}{\partial \theta_\mathbf{r}} & \dfrac{\partial \mathbf{s}^{syn}}{\partial \mathbf{t_s}} & \dfrac{\partial \mathbf{s}^{syn}}{\partial \mathbf{t_r}} & \dfrac{\partial \mathbf{s}^{syn}}{\partial \mathbf{v}} \\[2mm] \dfrac{\partial \mathbf{r}^{syn}}{\partial \mathbf{x}} & \dfrac{\partial \mathbf{r}^{syn}}{\partial \mathbf{z}} & \dfrac{\partial \mathbf{r}^{syn}}{\partial \theta_\mathbf{s}} & \dfrac{\partial \mathbf{r}^{syn}}{\partial \theta_\mathbf{r}} & \dfrac{\partial \mathbf{r}^{syn}}{\partial \mathbf{t_s}} & \dfrac{\partial \mathbf{r}^{syn}}{\partial \mathbf{t_r}} & \dfrac{\partial \mathbf{r}^{syn}}{\partial \mathbf{v}} \end{bmatrix}. \tag{3.25}$$

In the above equation, all entries of $\mathbf{J}$, as denoted by partial derivatives, are matrices. In this way, $\mathbf{J}$ is represented as a block matrix (for more properties of block matrices, the reader can refer to Watkins (2004)).

To better understand the block matrices that compose the above Jacobian $\mathbf{J}$, we make the

following observations:

(a) The synthetic-data space $\mathbf{d}^{syn}$ contains N five-component vectors (s, r, p_s, p_r, t_{sr}). As a consequence, there are N values of each of those components in the synthetic-data space.

(b) The ray-model space $\mathbf{m}^{ray}$ contains N six-component parameter vectors $(x, z, \theta_s, \theta_r, t_s, t_r)$. As a consequence, there are also N values of each of such components in the ray-model space.

(c) The velocity-model space $\mathbf{m}^{vel}$ consists of a single parameter vector $(v_1, \ldots, v_{M_v})$ with M_v components.

As a consequence of (a) and (b), all block matrices which do not have $\partial \mathbf{v}$ (i.e., the partial derivative with respect to $\mathbf{v}$) in the denominator have dimension $N \times N$. As a consequence of (a) and (c), all block matrices that does have $\partial \mathbf{v}$ (i.e., the partial derivative with respect to $\mathbf{v}$) in the denominator have dimension $N \times M_v$. A simple inspection on the block-matrix representation of $\mathbf{J}$ shows that it consists of five lines, each of them made up of side-by-side six $N \times N$ and a last one of dimension $N \times M_v$. The Jacobian block matrix $\mathbf{J}$ has dimension $(5N) \times (6N + M_v)$ as it should.

For computational reasons, a feature of great importance is that the Jacobian $\mathbf{J}$ is sparse (i.e., many of its block-matrix entries are null matrices). One of the reasons is that, in forward modelling ray tracing is performed in an independent way. In particular, the angle direction of a ray that connects a diffraction point to a source is independent of the direction angle of the ray that connects that same point to a receiver. As a consequence, some of the partial derivatives that relate to those independent rays give rise to null matrices. More specifically, the Jacobian block matrix $\mathbf{J}$ turns out to be

$$
\mathbf{J} = \begin{bmatrix}
\dfrac{\partial \mathbf{t_{sr}}^{syn}}{\partial \mathbf{x}} & \dfrac{\partial \mathbf{t_{sr}}^{syn}}{\partial \mathbf{z}} & \dfrac{\partial \mathbf{t_{sr}}^{syn}}{\partial \theta_\mathbf{s}} & \dfrac{\partial \mathbf{t_{sr}}^{syn}}{\partial \theta_\mathbf{r}} & \dfrac{\partial \mathbf{t_{sr}}^{syn}}{\partial \mathbf{t_s}} & \dfrac{\partial \mathbf{t_{sr}}^{syn}}{\partial \mathbf{t_r}} & \dfrac{\partial \mathbf{t_{sr}}^{syn}}{\partial \mathbf{v}} \\[3ex]
\dfrac{\partial \mathbf{p_s}^{syn}}{\partial \mathbf{x}} & \dfrac{\partial \mathbf{p_s}^{syn}}{\partial \mathbf{z}} & \dfrac{\partial \mathbf{p_s}^{syn}}{\partial \theta_\mathbf{s}} & \mathbf{0} & \dfrac{\partial \mathbf{p_s}^{syn}}{\partial \mathbf{t_s}} & \mathbf{0} & \dfrac{\partial \mathbf{p_s}^{syn}}{\partial \mathbf{v}} \\[3ex]
\dfrac{\partial \mathbf{p_r}^{syn}}{\partial \mathbf{x}} & \dfrac{\partial \mathbf{p_r}^{syn}}{\partial \mathbf{z}} & \mathbf{0} & \dfrac{\partial \mathbf{p_r}^{syn}}{\partial \theta_\mathbf{r}} & \mathbf{0} & \dfrac{\partial \mathbf{p_r}^{syn}}{\partial \mathbf{t_r}} & \dfrac{\partial \mathbf{p_r}^{syn}}{\partial \mathbf{v}} \\[3ex]
\dfrac{\partial \mathbf{s}^{syn}}{\partial \mathbf{x}} & \dfrac{\partial \mathbf{s}^{syn}}{\partial \mathbf{z}} & \dfrac{\partial \mathbf{s}^{syn}}{\partial \theta_\mathbf{s}} & \mathbf{0} & \dfrac{\partial \mathbf{s}^{syn}}{\partial \mathbf{t_s}} & \mathbf{0} & \dfrac{\partial \mathbf{s}^{syn}}{\partial \mathbf{v}} \\[3ex]
\dfrac{\partial \mathbf{r}^{syn}}{\partial \mathbf{x}} & \dfrac{\partial \mathbf{r}^{syn}}{\partial \mathbf{z}} & \mathbf{0} & \dfrac{\partial \mathbf{r}^{syn}}{\partial \theta_\mathbf{r}} & \mathbf{0} & \dfrac{\partial \mathbf{r}^{syn}}{\partial \mathbf{t_r}} & \dfrac{\partial \mathbf{r}^{syn}}{\partial \mathbf{v}}
\end{bmatrix} . \tag{3.26}
$$

where $\mathbf{0}$ denotes null matrices of dimension $N \times N$.

Moreover, as the propagation of one particular ray does not depend on the propagation of any other ray during forward modelling, the derivatives of kinematic parameters between different rays are null. Hence, all block matrices which do not have $\partial \mathbf{v}$ are diagonal matrices. Thus, matrix $\mathbf{J}$ is in fact a sparse matrix and this property can be further explored. However, all block matrices which does have $\partial \mathbf{v}$ are not diagonal matrices, since all the areas of the velocity model by where the ray trajectory passes, contribute to the ray propagation.

The Jacobian matrix $\mathbf{J}$ is also referred, in seismic tomography literature, as Frechet's matrix (see, e.g, Billette and Lambaré (1998), Duveneck (2004c)). In this thesis, the name Jacobian will be used, in order to keep clear the connection of the different methods as a particular case of the generic LSQR inverse problem described at the beginning of the chapter.

For computational effort proposes, it is advantegeous to compute the Jacobian matrix $\mathbf{J}$ during the forward modelling process. Therefore, the derivatives can be computed during ray-tracing step.

3.5   Initial model space for stereotomography

As discussed in the previous sections, the here-considered stereotomography approach requires a user-selected initial model space, which is iteratively updated until an also user-selected stopping criteria is achieved. In tomographic problems, simple initial velocity models, such as homogeneous or vertically-varying linear models are popular (see, e.g., Billette and Lambaré, 1998; Duveneck, 2004b). While this is not a critical point for tomography purposes (including the proposed CRP tomography), it is seen in the next chapter that FWI has a much stronger dependence on a good initial velocity to provide meaningful solutions. In Chapter 6, illustrative synthetic-data examples show that stereotomography is able to provide satisfactory solutions for quite simple initial velocity models.

The iteration process in tomographic problems such as sterotomagraphy, requires, in addition to an initial velocity-model space, also an initial ray-model space. We recall that, at each iteration, the ray-model space consists on N parameter vectors, each of them corresponding to a counterpart parameter vector of the (invariant) observed-data space provided by the user. As explained below with the help of Figure 3.6, a top-to-bottom procedure transform each parameter vector $\mathbf{d}_i^{obs} = (s, r, p_s, p_r, t_{sr})^T$ of the observed-data space into its corresponding initial model parameter vector $\mathbf{m}_i^{ray} = (x, z, \theta_s, \theta_r, t_s, t_r)^T$. The procedure assumes that an initial velocity-model space has been already given. We now recall that the pairs (s, p_s) (resp., (r, p_r)), as given by the observed-data

vector parameter, define the ray that starts at the source position s (resp., at the receiver position r) and proceed downwards with direction provided by the horizontal slowness p_s (resp., with direction provided by the horizontal slowness p_r).

Under these considerations, both rays are traced until the same traveltime $t_{sr}/2$ with t_{sr}, as given by the observed-data vector parameter, is consumed. As shown in Figure 3.6, the endpoints of both rays have coordinates (x_s, z_s) and (x_r, z_r), respectively. Moreover, at those endpoints, the direction angles θ_s and θ_r with respect to the vertical z-axis are provided by the ray tracing.

Setting (x, z) as the midpoint between the endpoints (x_s, z_s) and (x_r, z_r) and also defining $t_s = t_r = t_{sr}/2$, all values that define the initial ray-model parameter vector $\mathbf{m}_i^{ray}$, that corresponds to the given observed-data vector parameter $\mathbf{d}_i^{obs}$, are obtained. In symbols

$$\mathbf{m}_i^{ray} = (x, z, \theta_s, \theta_r, t_s, t_r) = \left(\frac{x_s + x_r}{2}, \frac{z_s + z_r}{2}, \theta_s, \theta_r, \frac{1}{2}t_{sr}, \frac{1}{2}t_{sr} \right). \tag{3.27}$$
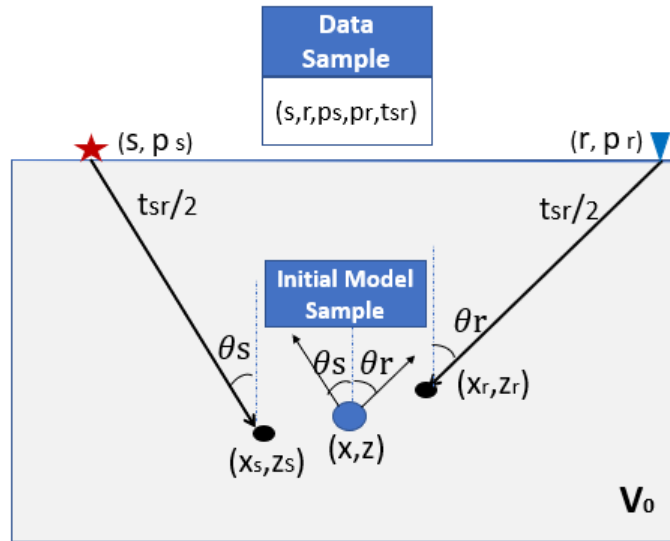
Figure 3.6: Initialization procedure for ray-model parameter vector: a velocity model, constructed by an arbitrary given initial velocity-model vector parameter is assumed. Also assumed is a data vector parameter (s, r, p_s, p_r, t_{sr}) for which the corresponding initial model vector parameter $(x, z, \theta_s, \theta_r, t_s, t_r)$ is to be constructed. Under the use of the given initial velocity model, two rays are downward propagated from source and receiver locations s and r, with directions determined by the slopes p_s and p_r, respectively. Those rays are propagated until the endpoints (x_s, z_s) and (x_r, z_r) that are attained for the traveltime $t_s = t_r = t_{sr}/2$. Setting (x, z) as the midpoint between (x_s, z_s) and (x_r, z_r) and, at those endpoints, the direction angles θ_s and θ_r with respect to the vertical z-axis provided by the ray tracing as initial model slopes and also defining $t_s = t_r = t_{sr}/2$, all values fro initial ray-model parameter vector are obtained.

Unfortunately, the initial velocity model is arbitrary. Moreover, it was used at the previous explained initialization step to compute the initial ray-model components. Despite it is not a crucial feature for seismic tomography applications, usually, the more similar is the initial velocity with the true velocity model, the better is the answer of the inversion process. However, it usually requires some previous knowledge about true velocity model. Despite the fact that the initial velocity model is an arbitrary one, strategies to invert the model by a crescent order of complexity has already been used (see, e.g, Billette et al. (2003)). By the use of this strategy, it is possible to invert first a vertical gradient model, then consider some lateral heterogeneity, etc. This could be viewed as form to provide increasingly better initial velocity models.

As a final consideration, we note that, in the same way as the choice of the regularization term, the above-described initialization of the ray-model space is an user option. The initialization procedure varies in literature from one application to another. As already explained, in most applications, simple geometric rules are applied to initialize model space. However, a previous optimization problem derived to build initial ray model space has already been applied in stereotomography applications (see, e.g, Billette et al. (2003)).

3.6   Further strategies for stereotomography

In this chapter we examined with more detail the formulation and solution of the stereographic problem. Since its introduction in Billette and Lambaré (1998), stereotomography plays an important role as a velocity-model building method from seismic-reflection data. Moreover, it is still a topic of active research devoted to overcome its various inherent challenges. These include, among others: (a) finding accurate and efficient (most particularly automatic or semi-automatic) algorithms for picking and parameter estimation of locally coherent events from prestack data; (b) extension to 3D anisotropic media; (c) incorporation of *a priori* data and model information; (d) optimal choice of initial models and (e) finding accurate, stable and computationally efficient inversion procedures. Concerning the forward-modeling engine, an upgrade from a ray-propagation to a wave-equation, is also to be envisaged.

A discussion on the ongoing advances in these topics is out of the scope of the present thesis, the interested reader being referred to specific literature (see, e.g., Billette et al., 2003; Duveneck and Hubral, 2002; Lambaré, 2008, 2004; Chalard et al., 2002; Le Bégat et al., 2000, see more references therein)

Chapter 4

Full wave form inversion

Full wave inversion (FWI) is a high-resolution seismic-parameter inversion technique based on full wave-equation propagation. As such, FWI takes into account a much wider range of seismic events, as predicted by the full wave equation, than tomographic methods that rely on much more limited, simpler events, as predicted by asymptotic, ray-propagation formulations.

As opposed to tomography methods, that rely on a (typically small) collection of picked from locally-coherent events in the input seismic data, FWI encompasses all traces of that data. Accordingly, the misfit function in FWI accounts for the residuals of all input traces with respect to their corresponding synthetic ones, generally computed by finite-differences schemes applied to suitable wave equations. As indicated in Chapter 2, the huge amount of traces encountered in realistic seismic problems, prevents to extend to FWI, the second-order (Gauss-Newton) LSQR inversion that is employed in tomography.

As a way to overcome such difficulties, implementations of FWI are based on the assumption of so-called single-scattering, perturbation-type wave-propagation modeling (Virieux and Operto, 2009; Virieux et al., 2017). According to that theory, the medium is considered as a set of diffraction points, at which weak independent interactions occur during propagation. As also outlined in Chapter 2, under such considerations, FWI is solved by an LSQR iterative inversion scheme, in which a first-order (local-descent) gradient method is employed.

In FWI literature, such diffraction points are referred to as pixels. That termilogy comes from the analogy with image processing in which a pixel represents a point of smallest resolution. In FWI, local properties, e.g., acoustic/elastic, isotropic/anisotropic parameters, are assigned to each pixel. In this case, the model space consists of multi-component parameter vectors carrying depth local information about those medium properties. Moreover, forward modeling is carried out by means of

the wave equation that is appropriate to the propagation involved. Nevertheless, the inversion process remains the same.

In this thesis, we focus on the acoustic wave propagation, so a single parameter, namely the scalar acoustic velocity is attached to each pixel. The employed (local-descent) gradient method is in agreement with the available literature (Gauthier et al., 1986; Pratt et al., 1998; Virieux and Operto, 2009).

4.1   Observed-data and model spaces

As in the previous chapter, we start with the introduction of the observed-data and model spaces that are used in FWI.

Observed-data space: In FWI, the observed-data space comprises the full original or prestack seismic data. Denoted $\mathbf{d}^{obs}$, such data consists of the amplitudes assigned at a finite (large) number of (column-vector) traces $\mathbf{d}^{obs}_{i,j}$, each of them defined by a source-receiver pair of locations $\mathbf{x}_{s_i}$, with $i = 1, ..., N_s$, and $\mathbf{x}_{r_j}$, with $j = 1, ..., N_r$, that pertains to the input acquisition geometry. We recall that 2D acquisition is considered and carried out on a horizontal seismic line. We use Cartesian coordinates $\mathbf{x} = (x, z)$ with the z-axis pointing down, to specify the subsurface region, assumed to be rectangular and denoted R. The seismic acquisition line conicedes with the x-axis, so that the coordinates of sources and receiver can be written as $\mathbf{x}_{s_i} = (s_i, 0)$ and $\mathbf{x}_{r_j} = (r_j, 0)$, respectively. In symbols, and omitting the explicit reference to the source-receiver position (s_i, r_j), the observed-data space we can be expressed as

$$\mathbf{d}^{obs} = [(d^{obs}(\mathbf{x}_{s_i}, \mathbf{x}_{r_j}, t_1), \ldots, d^{obs}(\mathbf{x}_{s_i}, \mathbf{x}_{r_j}, t_{N_t}))^T], \quad (i = 1, ...N_s, \ \ j - 1, ..., N_r). \qquad (4.1)$$

Model space: In this thesis, the model space $\mathbf{m}^{mod}$ is defined, instead of the acoustic velocities, by their squared slownesses, namely the squared reciprocals of the velocities. Those squared slownesses are assigned to all knots (pixels) of an invariant mesh that is provided by the user and covers a rectangular region R of interest. Represented as a single column vector, that mesh can be understood as a discretized representation of the medium in the region R. Physically, the knots (or pixels) are assumed as diffraction points of that medium.

In symbols, the model space $\mathbf{m}^{mod}$ can be written as an M-dimension column vector

$$\mathbf{m}^{mod} = (m_1, m_2, \ldots, m_M)^T, \tag{4.2}$$

where $m_i = 1/v_i^2$ is the squared slowness at the i-th pixel and M is the number of pixels of the velocity model.

It is important to highlight one remarkable difference between the model spaces of stereotomography and FWI. In stereotomography, the model space is the union of a velocity-model and ray-model spaces, the latter consisting of parameter vectors that are in a one-to-one correspondence to the picked/extracted parameter vectors that pertain to the observed-data space. In FWI, the observed-data space comprises the whole seismic data, so that no picking is involved and the model space simply coincides with the velocity-model space.

4.2 Forward-modeling engine and synthetic-data space

As it is usual in FWI, the forward-modeling engine is given by a finite-difference scheme applied to the wave-equation, here the acoustic wave equation. that is assumed to model the seismic propagation. The forward-modeling engine is designed to simulate, for any given velocity-model space $\mathbf{m}$, the corresponding synthetic-data space $\mathbf{d}^{syn}(\mathbf{m})$ with computed amplitudes assigned to the same sample positions as the ones that pertain to the observed-data space. More insightful, the synthetic space can be seen as a *simulated version* of the observed-data space, namely the one that would be observed if the velocity model space were represented by the model space $\mathbf{m}$. In analogy with the notation used for the observed-data space (see equation 4.1), the synthetic-space $\mathbf{d}^{syn}(\mathbf{m})$ for FWI has the form

$$\mathbf{d}^{syn}(\mathbf{m}) = [(d^{syn}(\mathbf{m}; \mathbf{x}_{s_i}, \mathbf{x}_{r_j}, t_1), \ldots, d^{syn}(\mathbf{m}; \mathbf{x}_{s_i}, \mathbf{x}_{r_j}, t_{N_t}))^T], \tag{4.3}$$

with, as before, $i = 1, \ldots N_s$, $j = 1, \ldots, N_r$ and $t = 1, \ldots, N_t$.

While assuming discrete sources and receiver pairs $(\mathbf{x}_{s_i}, \mathbf{x}_{r_j})$, for didactic and interpretation purposes, it is convenient to formulate the synthetic-data traces in continuous space-time domain $(\mathbf{x}, t)$, with points $\mathbf{x}$ in R and $0 \leq t \leq T$. Accordingly, it is assumed that the discrete model-space $\mathbf{m}$ is replaced by a real function $m = m(\mathbf{x})$, defined on R. In this situation, the notation $d^{syn}(m; \mathbf{x}_{s_i}, \mathbf{x}_{r_j}, t)$ will be used.

With the above understanding, a synthetic-data trace can be written

$$d^{syn}(m; \mathbf{x}_{s_i}, \mathbf{x}_{r_j}, t) = u_{s_i}(m; \mathbf{x}_{r_j}, t), \tag{4.4}$$

where $u_{s_i}(m, \mathbf{x}_{r_j})$ is the response of the acoustic medium observed at $\mathbf{x}_{r_j}$ due to a source point at $\mathbf{x}_{s_i}$. More generally, for any space-time observation point within $R \times [0, T]$, that amplitude satisfies the so-called *forward problem*:

Forward problem: For a given source $\mathbf{x}_{r_i}$ and any observation point $\mathbf{x}$, the wavefield $u_{s_i}(m; \mathbf{x}, t)$ satisfies the satisfies the acoustic wave equation

$$m(\mathbf{x}) \frac{\partial^2 u_{s_i}}{\partial t^2}(m; \mathbf{x}, t) - \Delta u_{s_i}(m; \mathbf{x}, t) = f_{s_i}(\mathbf{x}, t),$$

$$f_{s_i}(\mathbf{x}, t) = \delta(\mathbf{x} - \mathbf{x}_{s_i})\delta(t). \tag{4.5}$$

in which $\Delta u_{s_i}(m; \mathbf{x}, t) = (\partial^2 u_{s_i}/\partial x^2)(m; \mathbf{x}, t) + (\partial^2 U_{s_i})/(\partial z^2)(m; \mathbf{x}, t)$ is the Laplacian of $u_{s_i}(m; \mathbf{x}, t)$ and f_{s_i} represents the external point-source located at $\mathbf{x}_{si}$ and excited at time $t = 0$, namely

The wave equation (4.5) also satisfies the boundary and initial conditions

$$u_{s_i}(\mathbf{x}, t) = 0 \quad \text{and} \quad \mathbf{n} \cdot \nabla u_{s_i}(\mathbf{x}, t) = 0 \quad \text{for} \quad (\mathbf{x}, t) \in \partial R \times [0, T],$$

$$u_{s_i}(m, \mathbf{x}, 0) = \frac{\partial u_{s_i}}{\partial t}(m, \mathbf{x}, 0) = 0 \quad \text{for } \mathbf{x} \in R, \tag{4.6}$$

in which ∂R denotes the boundary of R. The boundary condition guarantees that no reflection waves from the boundary ∂R returns to the interior of R. The initial (so-called causality) conditions expresses the fact that the system is at rest before the point-source excitation at $t = 0$.

For actual implementations, the acoustic wave equation (4.5) is general computed by finite-difference methods, most popular in the literature (Holberg, 1987; Kelly et al., 1976). For more details on the necessary parameterizations, border schemes, examples of source terms and numerical tests, the reader is referred to Camargo (2019).

4.3   Misfit function and regularization

Applied to FWI, the LSQR approach the big picture presented in Chapter 2 and also in the tomographic case presented in Chapter 3. Some differences, however, that are inherently attached to FWI, require a special description. The most important one is, due to huge computaion demands, the use of first-order, local-descent optimization for the model-space update. As such, only the gradient of the misfit function is required. This is opposed to the second-order, Gauss-Newton optimization, for which the Hessian of the misfit function is required. Therefore, the main challenge of FWI is the computation of the gradient of the misfit function in an accurate and efficient way. As widely reported in the seismic literature (see, e.g., Virieux and Operto, 2009; Virieux et al., 2017; Fichtner et al., 2006; Camargo, 2019; Maharramov, 2016; Yedlin and van Vorst, 2010), that problem is solved by the so-called state-adjoint method applied to the acoustic wave equation.

In this thesis, the FWI *misfit function* $S(\mathbf{m})$, that measures the discrepancy between synthetic and observed data spaces, has the form

$$S(\mathbf{m}) = S_0(\mathbf{m}) + S_1(\mathbf{m}) = \frac{1}{2}[\Delta\mathbf{d}^T(\mathbf{m})\Delta\mathbf{d}(\mathbf{m}) + \lambda\mathbf{m}^T\mathbf{R}\mathbf{m}], \tag{4.7}$$

where $\mathbf{R}$ is a constant square matrix and

$$\Delta\mathbf{d}^T(\mathbf{m})\Delta\mathbf{d}(\mathbf{m}) = \frac{1}{2}\sum_{i=1}^{N_s}\sum_{j=1}^{N_r}\sum_{k=1}^{N_t}[u_{s_i}(\mathbf{m};\mathbf{x}_{r_j},t_k) - u^{obs}(\mathbf{x}_{s_i},\mathbf{x}_{r_j},t_k)]^2. \tag{4.8}$$

The misfit function $S(\mathbf{m})$ has the form of the general misfit function considered in Chapter 2 (see equations (2.5)-(2.7) with $\lambda_1 = \lambda$ and $\lambda_2 = 0$). The FWI misfit function of equation (4.7) also coincides with its stereographic counterpart considered in Chapter 3 (see equation (3.18)). Finally, it is to be noted that the data-covariance matrix, denoted $\mathbf{W}_D$ in the term $S_0(\mathbf{m})$, is now taken as $\mathbf{W}_D = \mathbf{I}$, where $\mathbf{I}$ is the identity matrix. The reason is that, in addition the assumption that no *a priori* data information is considered, all components of the observed-data space have the same physical (seismic-amplitude) units. As such, there are no need of a covariance matrix to be applied for unit adjustments. Observe that this was not the case in tomography, as the data-convariance $\mathbf{W}_D$ was required to bring the numerical values of the data-space components to comparable sizes. We recall that the condition $\lambda_2 = 0$ means that no *a priori* model information is considered. The case where such information is taken into account can be seen in Virieux et al. (2017).

From the previous considerations, the non-regularized term $S_0(\mathbf{m})$ will be considered in its continuous space domain, so that the model-space vector $\mathbf{m}$ is replaced by the real function $m =$

$m(\mathbf{x})$. As such, the non-regularized misfit function will be denoted $S_0(m)$, instead of $S_0(\mathbf{m})$. In this case, the synthetic and observed components which will be assumed to for continuous time $0 \leq t \leq T$ and denoted by $d^{syn}(m; \mathbf{x}_{s_i}, \mathbf{x}_{r_j}, t)$ and $d^{obs}(m; \mathbf{x}_{s_i}, \mathbf{x}_{r_j}, t)$, respectively. It is also to be noted that the regularization term of the misfit function remains discretely defined by the model-space vector $\mathbf{m}$.

In view of the above reasoning, the non-regularized misfit term $S_0(\mathbf{m})$, as well as its gradient $\nabla S_0(\mathbf{m})$, will be understood as discretized versions of corresponding continuous counterparts $S_0(m)$ and $(dS_0/dm)(m)$, for which actual expressions are to be provided. It is to mentioned that, as reported in Maharramov (2016), a discretized version of the gradient $\nabla S_0(\mathbf{m})$ can be directly obtained.

Expression of ∇S_0: As indicated above, the gradient $\nabla S_0(\mathbf{m})$ is assumed as a discretized version of the scalar derivative function $(dS_0/dm)(m)$ defined for a continuous model-space function $m = m(\mathbf{x})$ and, moreover all traces are assumed to be defined for continuous time $0 \leq t \leq T$. Inspection of equations (4.8) enables one to express $S_0(m)$

$$
\begin{aligned}
S_0(m) &= \sum_{i=1}^{N_s} \sum_{j=1}^{N_r} (S_0)_{ij}(m), \\
(S_0)_{ij}(m) &= \frac{1}{2} \int_0^T dt [u_{s_i}(m; \mathbf{x}_{r_j}, t) - u^{obs}(\mathbf{x}_{s_i}, \mathbf{x}_{r_j}, t)]^2.
\end{aligned}
\tag{4.9}
$$

Accordingly, the expression for $(dS_0/dm)(m)$ can be given by

$$
\begin{aligned}
\frac{dS_0}{dm}(m) &= \sum_{i=1}^{N_s} \sum_{j=1}^{N_r} \frac{d(S_0)_{ij}}{dm}(m), \\
\frac{d(S_0)_{ij}}{dm}(m) &= \int_0^T dt [u_{s_i}(m; \mathbf{x}_{r_j}, t) - u^{obs}(\mathbf{x}_{s_i}, \mathbf{x}_{r_j}, t)] \frac{du_{si}}{dm}(m, \mathbf{x}_{r_j}, t)].
\end{aligned}
\tag{4.10}
$$

Our task reduces, then to find an expression for $[d(S_0)_{ij}/dm](m)$. That expression is obtained by the application of the state-adjoint method. For that, the solution of the so-called adjoint problem of the original problem (4.5)-(4.6), as formulated below, is needed:

Adjoint problem: For a given source-receiver pair $(\mathbf{x}_{s_i}, \mathbf{x}_{r_j})$, the adjoint wavefield $u^{adj}_{s_i,r_j}(\mathbf{x}, t)$ satisfies the acoustic wave equation (compare with equations (4.5))

$$m(\mathbf{x})\frac{\partial^2 u^{adj}_{s_i,r_j}}{\partial t^2}(m; \mathbf{x}, t) - \Delta u^{adj}_{s_i,r_j}(m; \mathbf{x}, t) = F_{s_i,r_j}(m; \mathbf{x}, t),$$

(4.11)

$$F_{m;s_i,r_j}(m; \mathbf{x}, t) = \delta(\mathbf{x} - \mathbf{x}_{r_j})[u_{s_i}(\mathbf{x}_{r_j}, t) - d^{obs}(\mathbf{x}_{s_i}, \mathbf{x}_{r_j}, t)].$$

with boundary and initial conditions (compare with equations (4.6))

$$u^{adj}_{s_i,r_j}(\mathbf{x}, t) = 0 \quad \text{and} \quad \mathbf{n} \cdot \nabla u^{adj}_{s_i,r_j}(\mathbf{x}, t) = 0 \quad \text{for} \quad (\mathbf{x}, t) \in \partial R \times [0, T],$$
$$u^{adj}_{s_i,r_j}(m, \mathbf{x}, 0) = \frac{\partial u^{adj}_{s_i,r_j}}{\partial t}(m, \mathbf{x}, 0) = 0 \quad \text{for } \mathbf{x} \in R.$$

(4.12)

With the help of the solutions $u_{s_i}(m; \mathbf{x}, t)$ and $u^{adj}_{s_i,r_j}(m; \mathbf{x}, t)$ of the forward and adjoint problems (4.5)-(4.6) and (4.11)-(4.12), the sought-for derivative $(dS_0/dm)(m)$ can be written as (see, e.g, Camargo (2019))

$$\frac{(dS_0)_{ij}}{dm}(m) = \int_R d\mathbf{x} K_{ij}(m; \mathbf{x}, t),$$

(4.13)

where

$$K_{ij}(m; \mathbf{x}, t) = \int_0^T dt u^{adj}_{s_i,r_j}(m; \mathbf{x}, T - t)\frac{\partial^2 u_{s_i}}{\partial t^2}(m; \mathbf{x}, t).$$

(4.14)

Referred in the literature as the Fréchet derivative or sensitive kernels, the quantity $K_{ij}(m; \mathbf{x}, t)$ can be interpreted as a zero-lag correlation between the forward-propagated wavefield $u_{s_i}(m; \mathbf{x}, t)$ and a filtered (second-order derivative) backward-propagated wavefield $u^{adj}_{s_i,r_j}(m; \mathbf{x}, T - t)$. As such, it has the same structure of Claerbout's reflection condition for (Claerbout, 1971) as used in several migration schemes.

Expression of ∇S_1**:** As discussed in Chapter 2, the introduction of a regularization term in inverse problems such as tomography and FWI is essential to turn the inversion process more robust and provides consistent results. The choice of a regularization term is a particular option made by the user and varies from one application to another. In this thesis, we use the Tychonov regularization term given by (Virieux et al., 2017; Camargo, 2019)

$$S_1(\mathbf{m}) = \frac{\lambda}{2}[(\mathbf{B}_x\mathbf{m})^T(\mathbf{B}_x\mathbf{m}) + (\mathbf{B}_z\mathbf{m})^T(\mathbf{B}_z\mathbf{m})] = \frac{\lambda}{2}\mathbf{m}^T\mathbf{R}\mathbf{m},$$

(4.15)

so that

$$\mathbf{R} = \mathbf{B}_x^T \mathbf{B} + \mathbf{B}_z^T \mathbf{B}_z. \tag{4.16}$$

Here, $\mathbf{B}_x$ and $\mathbf{B}_z$ are real matrices operators that accounts for first-order spatial derivatives with respect to x and z directions, respectively.

From equation (4.15), we readily have that

$$\nabla S_1(\mathbf{m}) = \lambda \mathbf{R} \mathbf{m}. \tag{4.17}$$

For more details about Tychonov regularizion term, the intereseted reader is reffered to Virieux et al. (2017).

4.4   Iteration Process

In FWI, the second-order Gauss-Newton optimization usually employed in tomography has the serious drawback of requiring, at each iteration step, the unfeasible computation of Fréchet derivatives. In response to that, first-order, local-descent (such as conjugate-gradient) methods, albeit less accurate, offer an adequate alternative (Plessix, 2006). As based only on the gradient of the misfit function, such methods do not require Fréchet derivatives.

Local-descent methods are based on the fact that the (negative) gradient vector ∇S of the misfit function points to its maximum-descent direction. Based on this mathematical fact, the model-update iteration step is taken as

$$\mathbf{m}_{k+1} = \mathbf{m}_k + \Delta \mathbf{m}_k = \mathbf{m}_k - \alpha_k \nabla S(\mathbf{m}_k), \tag{4.18}$$

where α_k is a positive scalar parameter that controls the step size. In principle, the parameter α_k can be arbitrarily chosen by the user, some popular choices being available (Nocedal and Wright, 2006).

4.5   Initial model space for FWI

FWI has the ambitious objective of high-resolution parameter inversion in complex geological media. As such, it faces rather challenging problems, both in the adequate formulation of modeling

and inversion approaches, as well as in their accurate and efficient implementation. Present computation technology prevents the application to FWI of well-established second-order, Gauss-Newton schemes commonly used in tomographic problems. As a consequence, first-order locally descent schemes, remains, albeit less accurate, a computationally feasible alternative.

The above drawbacks impose, as crucial trade-off, the demand of an optimally chosen initial model to guarantee the convergence of FWI to a meaningful solution. As such, methodologies that help to find best-possible FWI initial-models are always in demand. As a recent example, a two-phase a scheme for initial-model construction dor 2D acoustic FWI is proposed in Camargo (2019). In the first phase, FWI is formulated as a constrained nonlinear problem by means of the augmented Lagrangian method. A first version of the initial velocity model is parametrized as a linear combination of specific basis functions, e.g., constant vertical gradient, horizontal interfaces, radial basis functions, among others. To assist the inversion process, information extracted from well-log data are, if available, applied. In second phase, the obtained first-phase, velocity-model is used as input for another, this time box-constrained, FWI problem. That problem is solved by the spectral gradient project (SPG), proposed in Birgin et al. (2000). In summary, the strategy uses a first-phase scheme to guide the initial model into a region near an attractive basin, while a second-phase scheme is applied to improve the model resolution. Different strategies, e.g., based on velocity analysis (Biondi and Almomin, 2013) and imaging techniques (Biondi and Almomin, 2013), Symes (2008)) provide additional examples.

In this thesis, as an attempt to overcome strong dependence of initial velocity model we consider the following strategy: first, a seismic tomography method is performed. Next, the output tomographic velocity model is then used as input for the FWI inversion. The less computational effort of seismic tomography, as well the more robust initial-model dependence in the tomography methods is a justification of the above strategy. As an additional bonus, seismic tomography methods are prone to recover low-frequency content of the medium, which is an important issue for FWI. The proposed two-step strategy makes use of the new CRP tomography described in the next chapter.

4.6   Summary and conclusions

In this chapter, the basics of the FWI method have been described. Although in its first stages, FWI represents a significant step forward in seismic imaging, providing additional or complementary information to migration.

An excellent review and comprehensive literature on the present achievements, as well as future goals of FWI is provided in Virieux et al. (2017). FWI is a topic of active research, with a number of hard challenges to overcome: As an iterative inverse-problem technique, FWI requires to solve, at each iteration step, a forward-modeling and optimization problems, both applied to data sets as large as the original pre-stack seismic volume. Because of the huge computational effort involved, today's applications mostly consider 2D acoustic isotropic (instead of 3D elastic anisotropic) wave equation as forward-modeling and, moreover, first-order locally descent (instead of second-order Gauss-Newton) optimization schemes. As a consequence of such limitations, meaningful FWI results much depends on an optimal choice of an initial-model. In this respect, the present thesis proposes the use of a previously-obtained tomographic velocity model as the initial model for FWI. In particular, the new CRP tomography described in the next chapter will be applied to this endeavor.

Chapter 5

CRP tomography

A new seismic tomography method will be proposed in this chapter, it is named *Common-Reflection-Point (CRP)* tomography. The new method is based on the knowledge acquired in the theoretic studies and practical implementation of stereomography (see Chapters 2 and 3), as well as other tomography methods such as the Normal-Incidence-Point (NIP) wave tomography (see Appendices A and B). In fact, most of the features of the CRP tomography can be found in the above-mentioned cases, mainly stereotomography, its main source of inspiration.

An important difference between CRP tomography and stereotomography resides on the number and nature of the points that are picked in both methods and compose the data space. Of course, such picked data points heavily impact on the corresponding points in the model space. As opposed to stereotomography, for which the data space consists of independent, picked points, the data space for CRP tomography is composed by CRP families, wich are related to the so-called CRP gathers. More specifically, each CRP gather consists of all source-receiver pairs within the input data for which the primary-reflection rays for a certain interface have the same (common) reflection point. For clarity of exposition, that point is called *CRP reference point* or *CRP central point* of the given CRP gather. For each CRP gather (a collection of parameter vectors), a CRP data family (a (big) parameter vector) is generated to composed the CRP tomography data space, where the traveltime information is taken, not individually, but simple as the sum of all reflection traveltimes that pertain to source-receiver pairs of that gather. This transformation will be further justified for computational/operational reasons.

As described in Coimbra et al. (2016a,b), CRP gathers can be extracted from the input data by means of multi-parameter coherence (semblance) analysis applied to so-called offset-continuation (also referred to as CRP traveltimes). In fact, the CRP tomography bears its name from such trav-

eltimes. Such extraction can be briefly summarized as follows. First of all, the procedure is carried out for all data samples under the assumption that each one is a candidate CRP reference point. This means that each sample is assumed to pertain to a (non-identified) primary-reflection event. For each given sample, a corresponding CRP traveltime is constructed that depends on a number of parameters to be estimated from the input data. As previously indicated, estimation of theses parameters is carried out by conventional multi-parametric coherence (semblance) analysis. The parameters allow for the localization of the CRP gather that corresponds to the candidate sample. The performed coherence analysis also provides the criteria upon which the sample candidate can actually be recognized as a CRP reference point. By means of the estimated parameters, the reflection times that correspond to the source-receiver pairs within the CRP gather can be obtained. In the process, also the slope information are estimated by a coherence approach (Coimbra et al., 2016b)). As a result of the procedure, the trace locations, two-way traveltime and slopes within a CRP gather are estimated. It is to be noted that just a single picking of a CRP reference point is necessary to obtain all the information of its corresponding CRP gather. In turns out that CRP tomography is able to enhance internal information with a minimum of pickings.

As seen below, the CRP gathers allow for a much more comprehensive and effective coverage of the depth domain under investigation. In fact, each CRP reference point incorporates to the inversion process the residuals (i.e., discrepancies between the observed and synthetic data samples) that refer to all source-receiver pairs within the CRP gather specified by that reference point. All the information collected from this CRP gather is treated simultaneously to improve the respective model parameters. This obviously enhances the quality of internal information provided to the inversion. For each CRP reference point, the corresponding CRP gather allows that more parts of the velocity model to be analyzed, when compared to other tomographic methods. Furthermore, practical tests described later indicates that the use of CRP gathers can act as a natural constraint that is incorporated to the tomographic inverse problem.

One of the possible disadvantages of the proposed CRP tomography concerns the involved computational effort. It is easy to realize that, the bigger the data-space size, the bigger is the size of the Jacobian matrix that needs to be computed. Moreover, at each iteration, from each model point in depth, more pairs of rays have to be traced to the surface. To overcome such drawbacks, some modifications of the conventional stereotomography approach has been implemented. Firstly, no traveltime parameters are used in the model space, all rays being propagated until measurement surface (seismic line) is reached. This avoids the computation of model traveltime derivatives and also decreases the number of columns in the Jacobian matrix. Secondly, following the use of CRP families, as the traveltime information is taken, not individually, but simple as the sum of all reflection traveltimes that pertain to source-receiver pairs of that gather, the size of Jacobian matrix is further

decreased, namely number of lines of the matrix is reduced. At first view, this approach does not seem to be a good choice because, in principle, less information is conveyed to the tomographic inversion process. Nevertheless, the experiments showed that good results has been achieved. Finally, he computational effort of ray propagation, together with the simultaneous computation of derivatives to compute Jacobian matrix can be minimized by the use of an efficient parallel implementation.

For comparison reasons, the regularization term in CRP tomography is the same as the one proposed for stereotomogaphy in Chapter 3. It is to be recalled that this regularization term accounts for the minimization of second derivatives of velocity model. As seen in the illustrative tests provided in next chapters, such regularization works well in constraining the iterative process to achieve an acceptable solution. Furthermore, numerical tests suggest that it will can be constrained with less dependence, of the still necessary external regularization, mainly when unfavorable boundary initial conditions are presented.

The exposition of the CRP tomography provided below follows the general lines and keeps the main characteristics as the ones found in the description of stereotomography (Chapter 3). Nevertheless, the important roles of CRP gathers and data families, which represent the heart of the new method, are very much highlighted.

5.1   Observed-data and model spaces

In this section, the observed-data and model spaces of CRP tomography are introduced. These spaces characterizes a remarkable difference between the proposed CRP tomography and stereotomography. As it will be explained, the introduction of CRP gathers turns both CRP tomography observed-data and model spaces bigger than the related stereotomography spaces. Moreover, CRP tomography observed-data and model spaces are bigger without the need of more number of pickings.

Observed data space   As a starting point, we remark that, in the same way as in stereotomography, observed-data parameter vectors of CRP tomography refer to primary-reflection events

$$\mathcal{D}^{obs}_{ref} = (s, r, p_s, p_r, t_{sr})^T_{ref}, \qquad (5.1)$$

with stereotomographic components of source-receiver locations (s, r), ray parameters (p_s, p_r) and two-way traveltime (t_{sr}) (see Figure 3.1). Therefore, each data parameter vector $\mathcal{D}^{obs}_{ref}$ refers to a

reflection or diffraction ray that starts from a shot localization s and arrives at the receiver localization r. Moreover, this ray propagation has slopes (horizontal slowness) p_s and p_r at the source and receiver, respectively. Denote t_{sr} as the traveltime of this propagation.

Subscript *ref* in Equation 5.1 denotes that these parameters are related to a CRP reference point. In CRP tomography context, each picking is related to a CRP reference point. To simplify notation, the subscript *ref* will be replaced by $f1$, where the letter f is reffered to the word *family* and the number 1 indicates that it is a reference observed-data vector parameter. In symbols, $\mathcal{D}_{ref}^{obs} = \mathcal{D}_{f1}^{obs}$. The use of the term *family* will be become clear below.

As a new important feature, Figure 5.1 shows that CRP tomography attaches, to each reference observed-data vector parameter $\mathcal{D}_{f1}^{obs}$ a corresponding CRP gather

$$\mathcal{G}(\mathcal{D}_{f1}^{obs}) = \{\mathcal{D}_{fi}^{obs}\}_{i=1}^{N_f}, \tag{5.2}$$

which is a collection N_f observed parameter vectors $\mathcal{D}_{fi}^{obs}$

$$\mathcal{D}_{fi}^{obs} = (s, r, p_s, p_r, t_{sr})_{fi}^T, \tag{5.3}$$

where each $\mathcal{D}_{fi}^{obs}$ is extracted from the input data, such that each of them pertains to the same primary-reflection event and, moreover, shares the same (common) reflection point as the original reference observed-data parameter vector $\mathcal{D}_{f1}^{obs}$. See Figure 5.1.

Note that, in fact, each CRP gather is a collection of observed-data vector parameters.

$$\mathcal{G}(\mathcal{D}_{f1}^{obs}) = \{(s, r, p_s, p_r, t_{sr})_{fi}^T\}_{i=1}^{N_f}. \tag{5.4}$$

For each CRP gather, a CRP data family is generated to composed the CRP tomography data space, where the traveltime information is taken, not individually, but simple as the sum of all reflection traveltimes that pertain to source-receiver pairs of that gather. By this transformation, each CRP gather $\mathcal{G}(\mathcal{D}_{f1}^{obs})$, that can be interpreted as a collection of vector parameters, gives rise to a respective CRP data family $\mathbf{d}_f^{obs}$, which can be interpreted as a (big) vector of observed-data parameters.

$$\mathbf{d}_f^{obs} = [t_f, (s, r, p_s, p_r)_{fi}^T]_{i=1}^{N_f}, \tag{5.5}$$

where

$$t_f = \sum_{i=1}^{N_f} (t_{sr})_{fi}. \tag{5.6}$$

The use of a single travelime parameter for each CRP family (namely the sum of all two-way traveltimes that pertain to the CRP gather) is justified by reduction of computational costs of the CRP tomographic process. Indeed, such choice reduces the size of the Jacobian matrix, as will be further discussed. As shown later, satisfactory results provided by our numerical tests show that this is a valid procedure.

The following relation reinforce the one-to-one correspondence between CRP gathers and families:

$$\mathcal{G}(\mathcal{D}_{f1}^{obs}) = \{(s, r, p_s, p_r, t_{sr})_{fi}^T\}_{i=1}^{N_f} \leftrightarrow [t_f, (s, r, p_s, p_r)_{fi}^T]_{i=1}^{N_f} = \mathbf{d}_f^{obs}. \tag{5.7}$$

Observed data space $\mathbf{d^{obs}}$ for CRP tomography is the union of CRP families $\mathbf{d}_f^{obs}$. The number of families equals the number of pickings performed in seismic data. Note that, each family is related to one specific CRP reference point. In symbols, we can write:

$$\mathbf{d^{obs}} = [\mathbf{d}_f^{obs}]_{f=1}^N \cdot, \tag{5.8}$$

Remarks: It is now instructive to make a few remarks on the above-introduced concepts:

 (i) For a CRP gather/family, the common reflection point acts like a diffraction point.

 (ii) Any source-receiver pair of a CRP gather defines the whole gather. This means that, in principle, a single picking is enough to determine the gather. The chosen point that defines the gather is called reference or central point of the CRP gather.

(iii) As a consequence of (ii), we can understand the observed-data space as defined by a collection of CRP reference points, each of them giving rise to a corresponding data family $\mathbf{d}_f^{obs}$. The CRP parameters extracted/estimated from a reference point determines the corresponding family. The details of how those parameters are extracted/estimated of such parameters and the corresponding CRP is obtained from them will be given bellow.

(iv) The number N_f of data-parameter vectors within the CRP gather is, in principle, arbitrary, being, of course, limited by the availability in the input data. However, for reasons of simplicity

of notation and without loss of generality, in this thesis, it is assumed that this number is the same for all gathers, namely $N_f = \bar{N}$ for $f = 1, \ldots, N$.

(v) As a final observation, note that, if $\bar{N} = 1$, the observed-space of CRP tomography is reduced to the observed-space of stereotomography. As will be noted until the end of this chapter, stereotomography is a particular case of CRP tomography.
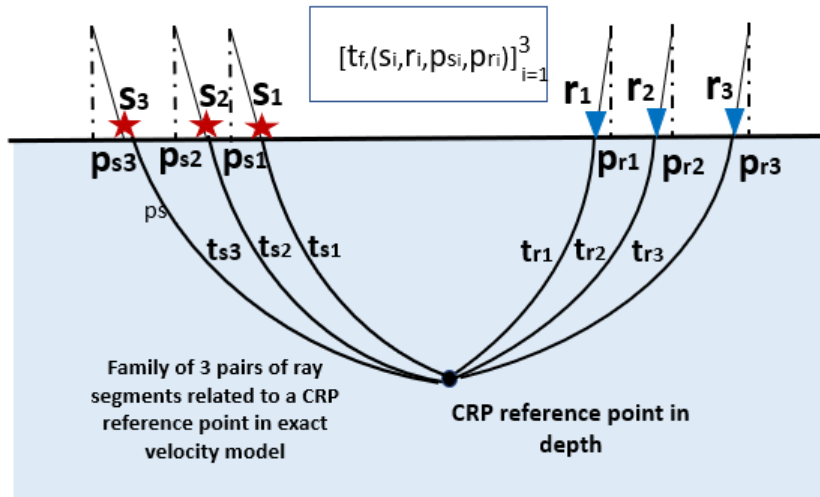
Figure 5.1: CRP family $\mathbf{d}_f^{obs}$ with three source-receiver pairs. All primary-reflection rays to a single (unknown) reflector share the same (common) reflection point. In the figure, $(s, r, p_s, p_r)_j$ represent the source-receiver location and ray parameters of the j-th ray and t_f is the sum of all two-way traveltimes $t_j = t_{s_j} + t_{r_j}$ along the three rays.

Determination of data-parameter vectors of a CRP gather: Even not being considered in this work, the problem of actual extraction of CRP gathers from the input data is of much practical relevance. As such, a few words are now devoted to this issue.

As reviewed in Appendix F, that procedure is based on recent results on offset-continuation (or CRP) seismic imaging as provided in Coimbra et al. (2016b). Of particular relevance to our purposes is the establishment of two parametric expressions. For a given CRP reference point, the first expression predicts the primary-reflections traveltimes of source-receiver pairs within a CRP gather. The second expression estimates the location of the source-receiver pairs that pertain to that CRP gather and, moreover, the ray parameters of the primary-reflection rays at those source and receiver points. In order not to disturb the present exposition, the mathematical description and discussions of all expressions relevant to CRP tomography are postponed to Appendix F.

As it is natural in the present context, the above-considered traveltime expression and corresponding parameters are called *CRP traveltime* and *CRP parameters*, respectively. The CRP parameters (two for 2D seismic data) are estimated by coherence (semblance) analysis performed on the input data in the vicinity of the CRP reference point.

In this thesis, all tests on CRP tomography were carried out on synthetic model tests, with tomographic data space being obtained under the use of dynamic ray-tracing performed on true velocity model test. Under these circumstances, no picking procedure were performed, the data space being directly given from the synthetic model.

Such rather theoretical testing choices are justified by our main objective of providing an introductory investigation and also proof-of-concept to the newly proposed CRP tomography. In this way, our main motivation is to show its potential, at least in favorable synthetic conditions. It is our hope that the here-obtained motivates its use to more realistic and practical situations.

Model Space: Following the same approach of stereotomography, CRP tomography model space **m** is the union of two model-space subsets. In symbols:

$$\mathbf{m} = \mathbf{m}^{vel} \cup \mathbf{m}^{ray}, \tag{5.9}$$

where $\mathbf{m}^{vel}$ it the velocity-model space and $\mathbf{m}^{ray}$ is the ray-model space.

Velocity-model space: The velocity-model space $\mathbf{m}^{vel}$ of CRP tomography remains the same of the one presented before for stereotomography. Therefore, $\mathbf{m}^{vel}$ is composed by M scalar components v_i, which accounts for B-spline interpolation coefficients. In symbols:

$$\mathbf{m}^{vel} = (v_1, \ldots, v_M)^T. \tag{5.10}$$

The velocity model needed at each iteration is produced on a depth region of interest, where an invariant mesh is provided by the user, with M_{vx} lines and M_{vz} columns. The product $M_{vx}M_{vz}$ equals the scalar M, which stands for the number of knots of interpolation. Each interpolation coefficient v_i is related to a particular knot of the mesh.

A B-spline interpolation scheme is applied to build, at each iteration, the current velocity model. Once the interpolation scheme of CRP tomography remains the same of stereotomographic problem, CRP tomography aims to invert the B-spline coeffcients only, and not the entire velocity model, which is automatically given by:

$$v(x, z) = \sum_{i=1}^{M_{vx}} \sum_{j=1}^{M_{vz}} v_{ij} \beta_i(x) \beta_j(z), \tag{5.11}$$

where β_i and β_j are B-spline basis functions (see Appendix D) and v_{ij} corresponds to the k-th component v_k of velocity-model space $\mathbf{m}^{vel}$ by the following rule:

$$k = (i - 1)M_{vx} + j, \quad (i = 1, \ldots, M_{vx} \quad j = 1, \ldots, M_{vz}). \tag{5.12}$$

As a consequence, the procedure always produces smooth velocity models, which allows the forward-modeling engine of CRP tomography to be based on ray-tracing algorithms. Such algorithms require continuous derivatives of the velocity function, this condition being naturally fulfilled by the beta-splice construction.

A brief explanation about B-spline constructions is given in Appendix D. For a more detailed text, the reader can refer to, e.g., de Boor et al. (1978).

Ray-model space: The ray-model space for CRP tomography is different from the one presented for stereotomography, carrying the changes made in observed-data space. Ray-model space for CRP tomography, $\mathbf{m}^{ray}$, consists of N model family vectors $\mathbf{m}_f^{ray}$, where N is the same real scalar from CRP observed-data space. In symbols:

$$\mathbf{m}^{ray} = [\mathbf{m}_f^{ray}]_{f=1}^N, \tag{5.13}$$

where each $\mathbf{m}_f^{ray}$ is given by:

$$\mathbf{m}_f^{ray} = [(x, z)_f^T, (\theta_s, \theta_r)_{fi}^T]_{i=1}^{N_f}, \tag{5.14}$$

where, for each f, N_f is the same real scalar from the related CRP data family. The Cartesian coordinates (x, z) locate a model diffraction point in depth, and, for each i, θ_s and θ_r specify two model angle directions with respect to the vertical. Moreover, given an arbitrary velocity model space $\mathbf{m}^{vel}$, each subscript i defines a pair of up-going rays that starts from a model diffraction point (x, z) in depth, each of the rays with initial slopes given by θ_s and θ_r. Therefore, each ray-model family $\mathbf{m}_f^{ray}$ defines a set of N_f pairs of model up-going rays that starts from the same model diffraction point in depth, each of these rays with a different starting angle.

Each ray-model family $\mathbf{m}_f^{ray}$ corresponds to its counterpart observed-data family $\mathbf{d}_f^{obs}$ in the

observed-data space. In symbols:

$$\mathbf{m}_f^{ray} \leftrightarrow \mathbf{d}_f^{obs}. \tag{5.15}$$

From the above relation, given a family f, there is just one data traveltime parameter t_f and one related model position in depth $(x, z)_f$. Moreover, given a specific family f, each model parameter sample $(\theta_s, \theta_r)_{fi}$ of the model family $\mathbf{m}_f^{ray}$ corresponds to its counterpart data observed parameter sample $(s, r, p_s, p_s)_{fi}$ in the respective data family $\mathbf{d}_f^{obs}$ of observed-data space. In symbols:

$$(\theta_s, \theta_r)_{fi} \leftrightarrow (s, r, p_s, p_s)_{fi}^{obs}. \tag{5.16}$$

Adopting a ray-theoretical description of the wave propagation involved and, moreover, that perfect modeling conditions hold, such correspondence admits a natural interpretation. Therefore, under the situation of perfect modeling conditions, given an arbitrary family f an also an arbitrary pair of rays of this family (each i specifies one pair of rays), the two up-going rays, starting from the cartesian coordinates $(x, z)_f$ with initial slopes given by $(\theta_s, \theta_r)_{fi}$ hit the measurement surface at the respective source and receiver points $(s, r)_{fi}$, with ray parameters $(p_s, p_r)_{fi}$. Such quantities match the respective parameters given by the observed data space. Under perfect modeling conditions, this property holds for all pairs of rays of the family and, moreover, it holds for all families. Furthermore, the sum of two-way traveltimes demanded by each pair of rays of the specific family match data total traveltime t_f. Figure 5.2 illustrates this hypothetical situation.

Note that, in contrast to stereotomography, no traveltime components are considered in CRP tomography model space. The reason is that, instead of the stereographic approach of assigning traveltime parameters for source and receiver ray tracing, in CRP tomography those rays are propagated until the seismic line is reached. To avoid numerical problems due to possible caustics and/or turning rays caused by strong-velocity variations, a threshold time is introduced to handle such situations. The no use of model traveltime parameter reduce the computational effort demanded by CRP tomography, once the Jacobian matrix is reduced, as will be further detailed.

Finally, except for the no use of model traveltime parameter, if $N_f = 1$ for $f = 1, \ldots, N$, ray-model space of CRP tomography is reduced to the ray-model space of stereotomography.
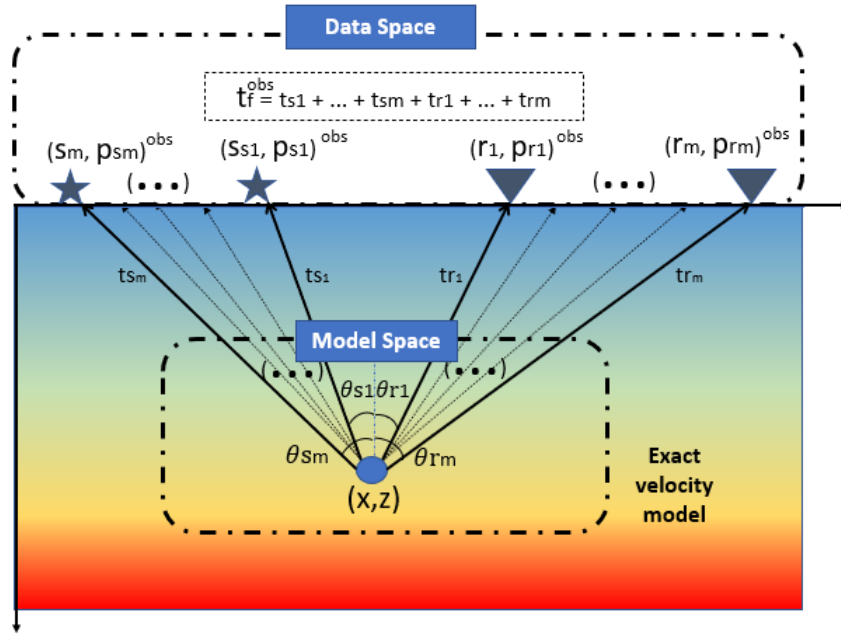
Figure 5.2: Interpretation of model family vector $\mathbf{m}_f^{ray} = [(x,z)_f^T, (\theta_s, \theta_r)_{fi}^T]_{i=1}^{N_f}$ of ray-model space. Color map represents the exact velocity model. The Cartesian parameters (x,z) locates a common diffraction model point for the family, from which a family of pairs of two up-going rays, where the i-th pair is specified by the pair of model angle directions $(\theta_s, \theta_r)_i$. Such rays hit the measurement seismic line in such way that the respective location and horizontal slowness pairs (s, p_s) and (r, p_r) match the parameters given by the observed space. Finally, the sum of two-way traveltimes demanded by each pair of ray match the data total family traveltime t_f.

5.2   Forward-model engine and synthetic data space

The forward-model engine transforms a given model space $\mathbf{m}$ onto a corresponding synthetic data space $\mathbf{d}^{syn}(\mathbf{m})$. As CRP tomography is a particular type of ray tomography, forward-model engine of CRP tomography relies on a ray formulation of wave equation. In the present thesis, the wave equation accounts for 2D constant-density acoustic wave equation.

Synthetic space $\mathbf{d}^{syn}(\mathbf{m})$ has the same form as the given and invariant observed-data space $\mathbf{d}^{obs}$, which allows comparisons between these spaces by the misfit function. Therefore, given an arbitrary current model space $\mathbf{m}$, CRP synthetic space is also composed by N synthetic family vectors $\mathbf{d}_f^{syn}(\mathbf{m})$ of (computed) kinematic parameters. In symbols:

$$\mathbf{d}^{syn}(\mathbf{m}) = [\mathbf{d}_f^{syn}(\mathbf{m})]_{f=1}^N, \tag{5.17}$$

where each $\mathbf{d}_f^{syn}(\mathbf{m})$ is given by:

$$\mathbf{d}_f^{syn}(\mathbf{m}) = [t_f^{syn}, (s, r, p_s, p_r)_{fi}^{syn}]_{i=1}^{N_f}. \tag{5.18}$$

Each synthetic family $\mathbf{d}_f^{syn}$ corresponds to its counterpart data family $\mathbf{d}_f^{obs}$ in the observed-data space. Moreover, given a family f, each synthetic parameter sample $(s, r, p_s, p_r)_{fi}^{syn}$ corresponds to its counterpart data parameter sample $(s, r, p_s, p_r)_{fi}^{obs}$ in the respective family of observed-data space. In symbols:

$$\mathbf{d}_f^{syn} \leftrightarrow \mathbf{d}_f^{obs}, \tag{5.19}$$

$$(s, r, p_s, p_r)_{fi}^{syn} \leftrightarrow (s, r, p_s, p_r)_{fi}^{obs}. \tag{5.20}$$

Remind that each data family $\mathbf{d}_f^{obs}$ its related to its counterpart model family $\mathbf{m}_f^{ray}$ in the ray-model space. Therefore, there is also a correspondence between synthetic families and model families. A pictorial description of the above correspondence is shown in Figure 5.3.

Given an arbitrary current model space $\mathbf{m}$, the construction of a synthetic data space $\mathbf{d}^{syn}$ for CRP tomography can be explained in a similar way of the construction of the analogues space of stereotomography. The changes on the explanation basically consist on the existence of families. Each ray-model family $\mathbf{m}_f^{ray}$ of current ray-model space provides, together with current velocity-model space $\mathbf{m}^{vel}$, initial conditions for kinematic ray-tracing of N_f pairs of up-going rays. These pairs of rays are propagated from the current model common-depth-point, with different starting angles given by the model slope parameters of current ray-model family. The positions that each of these pairs (each pair is denoted by the subscript i) of rays emerge at surface line, s_{fi}^{syn} for the source-ray and r_{fi}^{syn} for the receiver-ray, and the respective horizontal slowness at these positions, $(p_s)_{fi}^{syn}$ and $(p_r)_{fi}^{syn}$, respectively, are computed and compose the synthetic parameter vector $(s, r, p_s, p_r)_{fi}^{syn}$. This scheme is repeated for all pairs of rays of the family, where $i = 1, \ldots, N_f$. The synthetic total traveltime t_f^{syn} of each family is given by the sum of the two-way traveltime $t_{sr fi}^{syn}$ of each of the pairs of up-going rays of the respective family:

$$t_f^{syn} = \sum_{i=1}^{N_f} (t_{sr}^{syn})_{fi}. \tag{5.21}$$

The above procedure is repeated for all families. A illustration of the forward modeling step for CRP tomography is given in Figure 5.4.
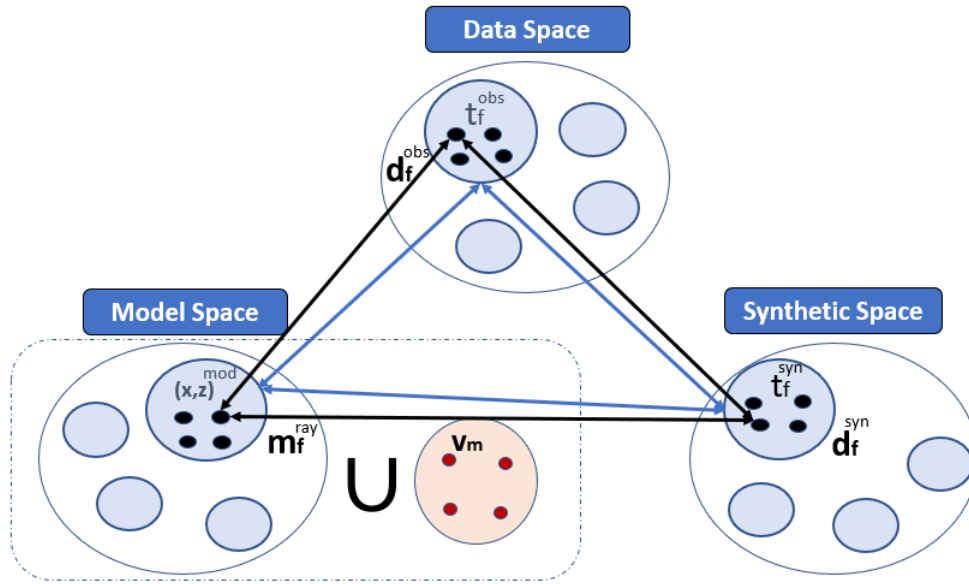
Figure 5.3: Observed-data, model and synthetic spaces. Each observed-data family vector $\mathbf{d}_f^{obs}$ relates to a corresponding ray-model family vector $\mathbf{m}_f^{ray}$. By means of forward-modeling engine, trial model vectors generates a corresponding synthetic family vector $\mathbf{d}_f^{syn}$. Family vectors are denoted by the blue sets in the figure. Moreover, each observed-data sample $\left(s^{obs}, r^{obs}, p_s^{obs}, p_r^{obs}\right)$, denoted by black dots of data space in the figure, relates to a corresponding ray-model sample (θ_s, θ_r), denoted by black dots of model space in the figure, which is also related to a corresponding synthetic-data sample $\left(s^{syn}, r^{syn}, p_s^{syn}, p_r^{syn}\right)$, denoted by black dots in synthetic space. Moreover, each observed-data family has one observed total family traveltime t_f^{obs}, while each synthetic family has one corresponding total traveltime t_f^{syn} and each ray-model family has one model depth point (x, z). Finally, CRP tomography model space consists of the union of two model-space subsets. The first is the the ray-model space $\mathbf{m}^{ray}$ and its parameter vectors were already explained. The second is the velocity-model space $\mathbf{m}^{vel}$, which is responsible for the coefficients of the B-spline representation of the velocity function. Velocity model space is denoted by the red set in the figure. The red dots denotes the interpolation coefficients.

5.3   CRP Misfit function and regularization

CRP tomography is a seismic inverse problem formulated as a non-linear LSQR optimization problem. Therefore, CRP tomography is a particular case of the general LSQR inverse problem described in chapter two. Moreover, CRP tomography makes use of a Gauss-Newton iterative procedure to solve a linearized optimization problem related to the original non-linear inverse problem at each iteration. As already mentioned, this is a classical approach to seismic tomography methods, as is the case of stereotomography and other seismic tomography methods (see, e.g, Duveneck and Hubral (2002), Iversen et al. (2012)), Sword (1987)). A regularization term is considered to improve
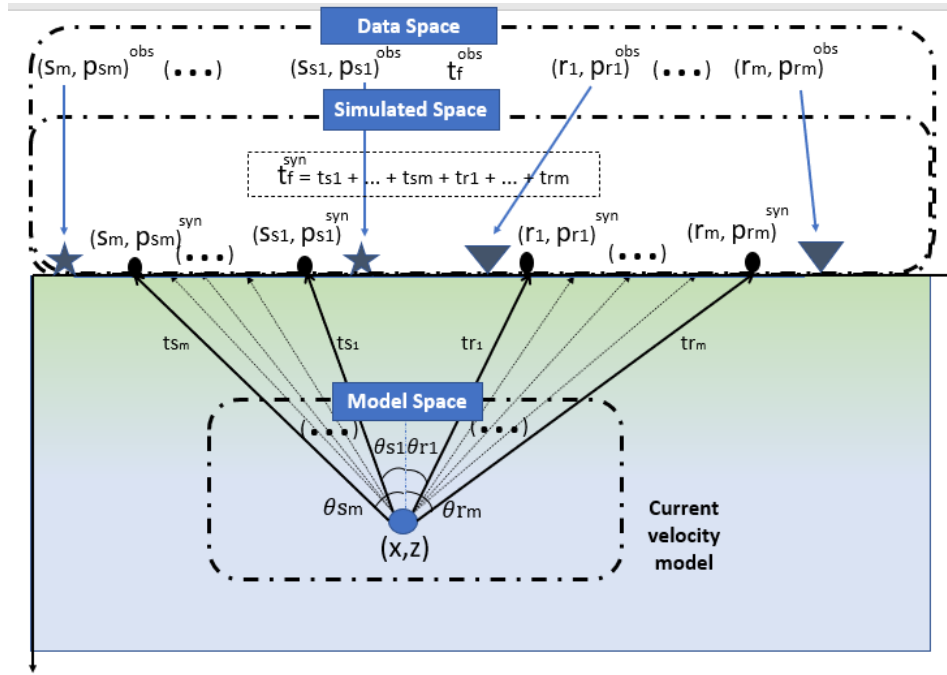
Figure 5.4: Synthetic family vector $\mathbf{d}_f^{syn}(\mathbf{m}) = [t_f^{syn}, (s, r, p_s, p_r)_{fi}^{syn}]_{i=1}^{N_f}$ for an arbitrary given model space $\mathbf{m}$. Color map represents B-spline velocity produced by velocity-model space $\mathbf{m}^{vel}$. Synthetic-data samples $[t_f, (s, r, p_s, p_r)]^{syn}$ are obtained by ray tracing applied to ray-model samples $[(x, z), (\theta_s, \theta_r)]^{ray}$. Parameters refer to rays from a same (common) reflection model point (x, z) (reflector not shown) to the seismic line. Black dots indicate the location and ray parameters, $(s, p_s)^{syn}$ and $(r, p_r)^{syn}$, of the source and receiver points where the rays hit the seismic line. The two-way traveltime t^{syn} is the sum of one one-way traveltimes t_s^{syn} and t_r^{syn} along those rays. Also shown are observed-data parameters $(s, r, p_s, p_r)^{obs}$ (blue stars and upside-down triangles). Due to incorrect model parameters, observed- and synthetic-data vector parameters do not match.

the natural instability of tomographic problem. As the same regularization term presented in stereotomography chapter will be used for CRP tomography description, most of the features related to misfit function and further iteration process of CRP tomography resembles the ones presented previously in this thesis. The great difference relies on the Jacobian matrix, which suffered some relative size reduction due to the new data, synthetic and model spaces descriptions for CRP tomography.

CRP misfit function: Given a current model space $\mathbf{m}$, CRP tomography misfit function measures the discrepancy between synthetic $\mathbf{d}^{syn}(\mathbf{m})$ and observed-data spaces $\mathbf{d}^{obs}$ by the L2 norm:

$$S(\mathbf{m}) = \frac{1}{2}[\Delta\mathbf{d}^T(\mathbf{m})\mathbf{W}_D^{-1}\Delta\mathbf{d}(\mathbf{m}) + \lambda\mathbf{m}^T\mathbf{R}\mathbf{m}], \qquad (5.22)$$

where:

$$\Delta\mathbf{d}(\mathbf{m}) = \mathbf{d}^{syn}(\mathbf{m}) - \mathbf{d}^{obs}. \tag{5.23}$$

As indicated in Chapter 2, $\mathbf{W}_d^{-1}$ is a diagonal matrix that accounts for a priori data information. However, as the misfit function of CRP tomography measures discrepancy between different types of data components, $\mathbf{W}_d^{-1}$ also brings these different types of data components to a comparable size.

The quadratic expression $\lambda\mathbf{m}^T\mathbf{R}\mathbf{m}$ denotes the regularization term applied to model space. It is the same one proposed in chapter 3 for stereotomography, inspired by the reference Duveneck (2004b). Therefore, the regularization term accounts, mainly, for the minimization of the second derivatives of the velocity model. Recalling:

$$\mathbf{m}^T\mathbf{R}\mathbf{m} = \int_z \int_x \left(\epsilon_{xx} \left(\frac{\partial^2 v(x,z)}{\partial x^2} \right)^2 + \epsilon_{zz} \left(\frac{\partial^2 v(x,z)}{\partial z^2} \right)^2 + \epsilon_{vv} v^2(x,z) \right) dx dz, \tag{5.24}$$

in which, $v(x,z)$ is the B-Spline representation of the velocity filed given by the current model space, and ϵ_{xx}, ϵ_{zz} and ϵ_{vv} are user-selected constant positive weights that calibrate the regularization term. Usually, $\epsilon_{xx} >> \epsilon_{vv}$ and $\epsilon_{zz} >> \epsilon_{vv}$.

As the same regularization approach already explained for stereotomography is used for CRP tomography, $\mathbf{R}$ is the same invariant regularization matrix proposed in chapter three and described in details in Appendix E. Finally, λ is the important scalar that calibrates the influence of the regularization term, which is external to the actual seismic tomographic problem.

It is important to highlight that the above CRP misfit function could be presented in other formats, being this format a first approach to this new tomographic problem. For instance, CRP misfit function could be formulated with a priori model information or other types of regularization terms applied to the hole current model space. Also, more than one regularization term could be considered, as it is common in other tomographic methods applications.

5.4   Iteration Process

CRP tomography is iteratively solved by a Gauss-Newton approach. Therefore, under this numerical approach, at each iteration, the method searches for approximate solutions of the original

non-linear problem. By the Gauss-Newton approach to solve the LSQR inversion problem as an iterative process, CRP tomography requires a user-selected *initial* model space $\mathbf{m}_0$, as well as an iterative scheme $\{\mathbf{m}_k\}$, $(k = 1, 2, ...)$ to progress to the desired solution. Given the current model space $\mathbf{m}_k$, its subsequent iteration $\mathbf{m}_{k+1}$ is given by:

$$\mathbf{m}_{k+1} = \mathbf{m}_k - \alpha_k \Delta \mathbf{m}_k, \tag{5.25}$$

in which α_k is a positive scalar that calibrates the size of the updating step.

The update vector $\Delta \mathbf{m}_k$, is obtained at each iteration by the Gauss-Newton solution of the optimization problem. Therefore, update vector $\Delta \mathbf{m}_k$ satisfies the following matrix equation:

$$[(\mathbf{J}(\mathbf{m}_k)^T \mathbf{W}^{-1} \mathbf{J}(\mathbf{m}_k) + \lambda \mathbf{R}] \Delta \mathbf{m}_k = -[\mathbf{J}(\mathbf{m}_k)^T \mathbf{W}^{-1} \Delta \mathbf{d} + \lambda \mathbf{R} \mathbf{m}], \tag{5.26}$$

where $\mathbf{J}$ is the CRP Jacobian matrix.

As it was explained in Chapter 2, the previous linear system can be seen as normal equations related to an associate matrix equation. Therefore, the solution of the above equation can be obtained as the least squares solution of following matrix equation:

$$\mathbf{U}_k \Delta \mathbf{m}_k = \mathbf{V}_k. \tag{5.27}$$

where matrices $\mathbf{U_k}$ and $\mathbf{V_k}$ are defined in an analogues way of the respective matrices of chapter three (see equatios 3.22), but now in CRP tomography context:

$$\mathbf{U}_k = \begin{bmatrix} \mathbf{J}(\mathbf{m}_k) \mathbf{W}_D^{-1/2} \\ \lambda \mathbf{R}^{tri} \end{bmatrix} \quad \text{and} \quad \mathbf{V}_k = - \begin{bmatrix} \mathbf{W}_D^{-1/2} \Delta \mathbf{d}(\mathbf{m}_k) \\ \mathbf{R}^{tri} \mathbf{m}_k \end{bmatrix}, \tag{5.28}$$

in which $\mathbf{R}^{tri}$ satisfies the Cholesky decomposition

$$\mathbf{R} = (\mathbf{R}^{tri})^T \mathbf{R}^{tri}, \tag{5.29}$$

where $\mathbf{R}^{tri}$ and $(\mathbf{R}^{tri})^T$ are superior and inferior triangular matrices.

In practice, the system of equations (5.26) is not solved, and the model improvement vector $\Delta \mathbf{m_k}$ is given by the least squares solution of the associated matrix equation (5.27). The reasons for the previous approach rely both on the ill-conditioning of the problem and on the sparsity of the CRP Jacobian matrix. Moreover, once CRP tomography usually demands a more number of rays to be traced at each iteration, which is a direct result of the use of CRP gathers/families, in CRP tomogra-

phy applications, Jacobian matrix can become huge. Therefore, the inverse of such matrix has to be numerically avoided. Also, numerical calculations of $\mathbf{J(m_k)^T W^{-1} J(m_k)}$ and $\mathbf{J(m_k)^T W^{-1} \Delta d}$ can result in numerical inaccuracies. Thereby, numerical methods as SVD (singular value decomposition) (see, e.g, Watkins (2004)) can be used to directly solve matrix Equation (5.27), and return $\mathbf{\Delta m_k}$ as the least square solution of this matrix equation. SVD is a standard numerical method for ill-conditioned matrix equations, and provides expression of the generalized inverse of the Jacobian matrix. Unfortunatly, for even large applications, as is the case of real-sized problems, SVD has to be avoided, due to the demanded computational effort of the method. Thereby, other strategies has to be used to derive the model improvement vector $\mathbf{\Delta m_k}$. The LSQR algorithm proposed by Paige and Saunders (1982) could be used in those situations. It is based on conjugate gradient solution of the linear system and can appropriately explore the sparsity of the Jacobian matrix, which can turn the method a standard one for real-sized seismic CRP tomography applications. In this thesis, SVD method was applied to all numerical tests to derive Gauss-Newton solutions for CRP tomography at each iteration.

In the next section, an analysis of the Jacobian matrix of CRP tomography is provided. Moreover, the proposed modifications to reduce its size will be detailed.

5.5   CRP Jacobian matrix

One of the possible disadvantages of the proposed CRP tomography is the need of more computational effort in comparison with other standard tomography methods, as is the case of stereotomography. The computational effort is a direct result of the greater number of rays to be traced at each iteration of forward modeling step. However, the computational effort of ray-tracing step is a problem that can be easily solved nowadays by the use of an efficient parallel implementation, as the ray propagation of one specific ray is independent of any other ray during forward modeling step. However, the more is the number of rays used during inverse problem, the bigger is the resulting Jacobian matrix of the method. As a consequence, the linear system to be solved at each iteration of the inverse process makes use of a considerably bigger Jacobian matrix. Moreover, the numerical solution of the ill-conditioned linear system can not be amenable to efficient parallel implementation. To partially handle these problems, some modifications in traditional stereotomography approach were implemented to CRP tomography in order to decrease the size of Jacobian. The modifications are described bellow:

- No traveltimes are considered in model space. At each iteration, all rays are upwards propagated until the surface (horizontal seismic line) is reached. This avoids the computation of traveltime

derivatives with respect to model parameters, so that the number of columns of Jacobian matrix decreases. Possible problems of locally strong velocity variations, such as caustic regions or turning rays that do not reach the surface, are controlled by imposing threshold traveltime limits for allowed ray propagation.

- Individual two-way traveltimes of all primary-reflection rays that pertain to a same CRP data gather (i.e., related to a same reference point) will be replaced by their total sum in related data family vector. As such, further reductions on the Jacobian-madrix sises are achieved. This time, the number of lines of the matrix is reduced.

At first glimpse, that latter choice, seems counter intuitive, since it conveys less information to the inversion process. As shown later, all our illustrative experiments seemed not to be affected. Moreover, the choice of total two-way traveltime as the single traveltime parameter of the CRP data gather can be seen as a reduction of the degree of freedom of the unstable inverse problem, which could help the constrain of the model. The CRP Jacobian matrix will be described bellow taking these modifications.

Description of CRP Jacobian as a block matrix: As described in the previous sections, synthetic space for CRP tomography $\mathbf{d}^{syn} = \mathbf{d}^{syn}(\mathbf{m})$ is made up of N families, each of them composed by N_f parameter vectors $(s, r, p_s, p_r)_{fi}$, and a total traveltime t_f for each family. On the other hand, the model space $\mathbf{m} = \mathbf{m}^{vel} \cup \mathbf{m}^{ray}$ is composed by M model-velocity components, namely B-spline interpolation coefficients $(v_1, ..., v_m)$, and N ray-model families, each of them composed by N_f model parameter vectors $(\theta_s, \theta_r)_{fi}$ and a model depth position of the family $(x, z)_f$. Therefore, we have that the synthetic space $\mathbf{d}^{syn}$, model space $\mathbf{m}$ and Jacobian matrix $\mathbf{J}$ have the following dimensions:

- Dimension of CRP synthetic space: $\sum_{f=1}^{N}(4N_f + 1)$,

- Dimension of CRP model space: $M + \sum_{f=1}^{N}(2N_f + 2)$.

- Dimension of CRP Jacobian matrix: $[\sum_{f=1}^{N}(4N_f + 1)] \times [M + \sum_{f=1}^{N}(2N_f + 2)]$.

From the above considerations, the CRP tomography Jacobian matrix $\mathbf{J} = \mathbf{J}(\mathbf{m})$ admits the

following representation:

$$
\mathbf{J} = \begin{bmatrix}
\dfrac{\partial \mathbf{t}^{syn}}{\partial \mathbf{x}} & \dfrac{\partial \mathbf{t}^{syn}}{\partial \mathbf{z}} & \dfrac{\partial \mathbf{t}^{syn}}{\partial \theta_{\mathbf{s}}} & \dfrac{\partial \mathbf{t}^{syn}}{\partial \theta_{\mathbf{r}}} & \dfrac{\partial \mathbf{t}^{syn}}{\partial \mathbf{v}} \\[3mm]
\dfrac{\partial \mathbf{p_s}^{syn}}{\partial \mathbf{x}} & \dfrac{\partial \mathbf{p_s}^{syn}}{\partial \mathbf{z}} & \dfrac{\partial \mathbf{p_s}^{syn}}{\partial \theta_{\mathbf{s}}} & \dfrac{\partial \mathbf{p_s}^{syn}}{\partial \theta_{\mathbf{r}}} & \dfrac{\partial \mathbf{p_s}^{syn}}{\partial \mathbf{v}} \\[3mm]
\dfrac{\partial \mathbf{p_r}^{syn}}{\partial \mathbf{x}} & \dfrac{\partial \mathbf{p_r}^{syn}}{\partial \mathbf{z}} & \dfrac{\partial \mathbf{p_r}^{syn}}{\partial \theta_{\mathbf{s}}} & \dfrac{\partial \mathbf{p_r}^{syn}}{\partial \theta_{\mathbf{r}}} & \dfrac{\partial \mathbf{p_r}^{syn}}{\partial \mathbf{v}} \\[3mm]
\dfrac{\partial \mathbf{s}^{syn}}{\partial \mathbf{x}} & \dfrac{\partial \mathbf{s}^{syn}}{\partial \mathbf{z}} & \dfrac{\partial \mathbf{s}^{syn}}{\partial \theta_{\mathbf{s}}} & \dfrac{\partial \mathbf{s}^{syn}}{\partial \theta_{\mathbf{r}}} & \dfrac{\partial \mathbf{s}^{syn}}{\partial \mathbf{v}} \\[3mm]
\dfrac{\partial \mathbf{r}^{syn}}{\partial \mathbf{x}} & \dfrac{\partial \mathbf{r}^{syn}}{\partial \mathbf{z}} & \dfrac{\partial \mathbf{r}^{syn}}{\partial \theta_{\mathbf{s}}} & \dfrac{\partial \mathbf{r}^{syn}}{\partial \theta_{\mathbf{r}}} & \dfrac{\partial \mathbf{r}^{syn}}{\partial \mathbf{v}}
\end{bmatrix}. \qquad (5.30)
$$

In the above equation, all entries of $\mathbf{J}$, as denoted by partial derivatives, are matrices. In this way, $\mathbf{J}$ is represented as a block matrix. More details about each block matrix will be given bellow.

For computational reasons, a feature of great importance is that the CRP Jacobian $\mathbf{J}$ is sparse (i.e., many of its block-matrix entries are null matrices). One of the reasons is that forward modeling ray tracing is performed in an independent way. In particular, the angle direction of a ray that connects a diffraction point to a source is independent of the direction angle of the ray that connects that same point to a receiver. As a consequence, some of the partial derivatives that relate to those independent rays give rise to null matrices. More specifically, the CRP Jacobian block matrix $\mathbf{J}$ turns out to be:

$$
\mathbf{J} = \begin{bmatrix}
\dfrac{\partial \mathbf{t}^{syn}}{\partial \mathbf{x}} & \dfrac{\partial \mathbf{t}^{syn}}{\partial \mathbf{z}} & \dfrac{\partial \mathbf{t}^{syn}}{\partial \theta_{\mathbf{s}}} & \dfrac{\partial \mathbf{t}^{syn}}{\partial \theta_{\mathbf{r}}} & \dfrac{\partial \mathbf{t}^{syn}}{\partial \mathbf{v}} \\[3mm]
\dfrac{\partial \mathbf{p_s}^{syn}}{\partial \mathbf{x}} & \dfrac{\partial \mathbf{p_s}^{syn}}{\partial \mathbf{z}} & \dfrac{\partial \mathbf{p_s}^{syn}}{\partial \theta_{\mathbf{s}}} & \mathbf{0} & \dfrac{\partial \mathbf{p_s}^{syn}}{\partial \mathbf{v}} \\[3mm]
\dfrac{\partial \mathbf{p_r}^{syn}}{\partial \mathbf{x}} & \dfrac{\partial \mathbf{p_r}^{syn}}{\partial \mathbf{z}} & \mathbf{0} & \dfrac{\partial \mathbf{p_r}^{syn}}{\partial \theta_{\mathbf{r}}} & \dfrac{\partial \mathbf{p_r}^{syn}}{\partial \mathbf{v}} \\[3mm]
\dfrac{\partial \mathbf{s}^{syn}}{\partial \mathbf{x}} & \dfrac{\partial \mathbf{s}^{syn}}{\partial \mathbf{z}} & \dfrac{\partial \mathbf{s}^{syn}}{\partial \theta_{\mathbf{s}}} & \mathbf{0} & \dfrac{\partial \mathbf{s}^{syn}}{\partial \mathbf{v}} \\[3mm]
\dfrac{\partial \mathbf{r}^{syn}}{\partial \mathbf{x}} & \dfrac{\partial \mathbf{r}^{syn}}{\partial \mathbf{z}} & \mathbf{0} & \dfrac{\partial \mathbf{r}^{syn}}{\partial \theta_{\mathbf{r}}} & \dfrac{\partial \mathbf{r}^{syn}}{\partial \mathbf{v}}
\end{bmatrix}. \qquad (5.31)
$$

To better understand the block matrices the following observations can be made:

(a) Synthetic-data space $\mathbf{d}^{syn}$ contains $\sum_{f=1}^{N} N_f$ four-component vectors $(s, r, p_s, p_r)^{syn}$. As a consequence, there are $\sum_{f=1}^{N} N_f$ values of each of those components in synthetic-data space.

(b) Synthetic-data space $\mathbf{d}^{syn}$ contains N traveltime parameters t^{syn}.

(c) Ray-model space $\mathbf{m}^{ray}$ contains $\sum_{f=1}^{N} N_f$ two-component parameter vectors (θ_s, θ_r). As a consequence, there are $\sum_{f=1}^{N} N_f$ values of each of such components in ray-model space.

(d) Ray-model space $\mathbf{m}^{ray}$ contains N two-component parameter vectors of the type (x, z). As a consequence, there are N values of each of such components in ray-model space.

(e) Velocity-model space $\mathbf{m}^{vel}$ consists of a single parameter vector $(v_1, \ldots, v_M)$ with M components.

Therefore, by the above observations, the matrices denoted by $\dfrac{\partial \mathbf{p_s}^{syn}}{\partial \theta_{\mathbf{s}}}, \dfrac{\partial \mathbf{p_r}^{syn}}{\partial \theta_{\mathbf{r}}}, \dfrac{\partial \mathbf{s}^{syn}}{\partial \theta_{\mathbf{s}}}, \dfrac{\partial \mathbf{r}^{syn}}{\partial \theta_{\mathbf{r}}}$ and $\mathbf{0}$, are matrices of dimension $(\sum_{f=1}^{N} N_f) \times (\sum_{f=1}^{N} N_f)$. In the particular case where N_f is equal for all families, that is, $N_f = \bar{N}$ for $f = 1, \ldots, N$, then the size of these matrices become $N\bar{N} \times N\bar{N}$. On the other hand, following the above observations, the matrices denoted by $\dfrac{\partial \mathbf{p_s}^{syn}}{\partial \mathbf{x}}, \dfrac{\partial \mathbf{p_s}^{syn}}{\partial \mathbf{z}}, \dfrac{\partial \mathbf{p_r}^{syn}}{\partial \mathbf{x}}$, $\dfrac{\partial \mathbf{p_r}^{syn}}{\partial \mathbf{z}}, \dfrac{\partial \mathbf{s}^{syn}}{\partial \mathbf{x}}, \dfrac{\partial \mathbf{s}^{syn}}{\partial \mathbf{x}}, \dfrac{\partial \mathbf{r}^{\mathbf{syn}}}{\partial \mathbf{x}}$ and $\dfrac{\partial \mathbf{r}^{syn}}{\partial \mathbf{z}}$, are matrices of dimension $(\sum_{f=1}^{n} N_f) \times N$. In the previous mentioned particular case, the size of these matrices are $N\bar{N} \times N$. However, due to the use of the family total two-way traveltime, the matrices denoted by $\dfrac{\partial \mathbf{t}^{syn}}{\partial \mathbf{x}}$ and $\dfrac{\partial \mathbf{t}^{syn}}{\partial \mathbf{z}}$ are matrices of dimension $N \times N$, while the matrices denoted by $\dfrac{\partial \mathbf{t}^{syn}}{\partial \theta_{\mathbf{s}}}$ and $\dfrac{\partial \mathbf{t}^{syn}}{\partial \theta_{\mathbf{r}}}$, are matrices of dimension $N \times (\sum_{f=1}^{N} N_f)$ where, again, in the particular case, the size of these matrices become $N \times N\bar{N}$. The matrix denoted by $\dfrac{\partial \mathbf{t}^{syn}}{\partial \mathbf{v}}$ has dimension $N \times M$. Finally, all other block matrices that does have $\partial \mathbf{v}$ in the denominator (i.e., the partial derivative with respect to $\mathbf{v}$) have dimension $\sum_{f=1}^{N} N_f \times M$, and $N\bar{N} \times M$ in the particular case. Therefore, the Jacobian block matrix $\mathbf{J}$ has dimension $[\sum_{f=1}^{N}(4N_f + 1)] \times [M + \sum_{f=1}^{N}(2N_f + 2)]$ as it should. In the special case where $N_f = \bar{N}$ for $f = 1, \ldots, N$, the CRP Jacobian matrix $\mathbf{J}$ has dimension $[N(4\bar{N} + 1)] \times [M + N(2\bar{N} + 2)]$.

Comparisons between Jacobian matrix of CRP tomography and stereotomography: Note the importance of the proposed modifications in the reduction of the size of CRP Jacobian matrix in comparison with the traditional approach of stereotomography. If all two-way traveltimes of each source receiver pair would be taken into account, that is, instead of of being a union of family vectors, data space would be composed by the union of CRP gathers, then the dimension of CRP synthetic space would be $\sum_{f=1}^{N} 5N_f$, while if traveltimes would be kept in model space description, as it is done in stereotomography, then the dimension of CRP model space would be $M + \sum_{f=1}^{N}(4N_f + 2)$. Compare with the dimensions previously given. As a consequence, CRP Jacobian matrix would be of

dimension $[\sum_{f=1}^{N} 5N_f] \times [M + \sum_{f=1}^{N}(4N_f + 2)]$. Therefore, this modifications reduced the dimension of Jacobian matrix by $(\sum_{f=1}^{N}(N_f - 1))$ lines and $(\sum_{f=1}^{N} 2N_f)$ columns.

It is important to highlight that the use of CRP gathers/families, at the core of CRP tomography method, also helps the decrease of the size of Jacobian matrix. To illustrate this benefit, consider the following hypothetical situation where the same elements of CRP data space would be collected and used for stereotomography method, which does not consider the concepts and use of CRP gathers/families. Therefore, any data sample $(s, r, p_s, p_r, t_{sr})_i$ would be related to one specific model depth-point-position $(x, z)_i$. Thus, the model space in this situation would be composed by $2\sum_{f=1}^{N} N_f$ coordinates of model depth positions. The introduction of CRP gathers/families turned possible the reduction of this amount to just $2N$ components. This approach reduced, once again, the number of lines in CRP tomography Jacobian matrix. This time, a reduction of $2\sum_{f=1}^{N}(N_f - 1)$ lines was possible. Also, the use of a total family traveltime was just possible because of the use of CRP families.

Finally, to finish the comparison, consider the following hypothetical situation: if an observed-data space is given and composed by pre-stack two-way traveltimes, and pairs of positions and slopes collected in input seismic data by some arbitrary technique, where common-reflection-point information is also available, one could be choose between the stereotomography and CRP tomography to invert the related model. To turn the comparison easier, consider that N_f, the number of kinematic samples of each (possible) family, is the same for all families, that is $N_f = \bar{N}$ for $f = 1, \ldots, N$. Consider that N of these families were given. In stereotomography, the common-reflection-point information is ignored, and at each iteration, a linear system would have do be solved taking into account a Jacobian matrix of dimension $[5N\bar{N}] \times [M + 6N\bar{N}]$, as discussed in chapter 3. On the other hand, if CRP tomography is chosen, the Jacobian matrix is reduced to dimension $[N(4\bar{N}+1)] \times [M + N(2\bar{N}+2)]$, which stands for a considerable smaller matrix. Moreover, it is done providing more and better internal information to the tomographic problem.

The good results and further increase of the stability provided by this approach for CRP tomographic inverse problem will be illustrated in next chapters, where also a comparison with stereotomography results will be provided.

Computational aspects: At each CRP tomography iteration, Jacobian matrix **J** is computed element by element by a discrete approach. Hence, paraxial ray theory is applied and computed, during forward-modeling step, to provide first order estimations of ray paths perturbations with respect to initial conditions. Ray paths account for synthetic space, while initial conditions are given by the elements of model space. Therefore, paraxial ray theory provides a way to compute the demanded first

order partial derivatives of the elements of the synthetic space by the elements of the current model space, which stands for the elements of Jacobian matrix. The calculation of the demanded derivatives by the use of paraxial ray theory can be adressed in classical literature (see, e.g, Cerveny (2005), Popov (2002)). As the derivatives are computed iteratively by each ray path, which is independent of any other ray path, the derivatives used to build each element of the Jacobian matrix for CRP tomography is computed by the same expressions used to build Jacobian matrix for stereotomography or any other ray slope tomography method.

Good sparsity features of Jacobian matrix J comes because of the independence of different ray propagations. Thus, as the propagation of a particular ray does not depends of the propagation of any other ray during forward modeling step, the derivatives of kinematic parameters between different rays are null. Also, the derivatives with respect to velocity coefficients are different of zero just at coefficients related to regions of the velocity model by where the ray trajectory passes. Therefore, all submatrices of the block matrix J presents strong sparsity properties. Moreover, all block matrices which do not have $\partial\mathbf{v}$ or $\partial\mathbf{t}^{syn}$ are diagonal matrices. Thus, matrix J is a sparse matrix and this property can be further explored by an appropriate numerical algorithm.

In all numerical experiments of this thesis, $N_f = \bar{N}$ was set for all families, where $\bar{N}$ varies between performed experiments. However, this was made in order to turn the implementation and further analysis easier. Despite the fact that this first implementation of CRP tomography consider this special case, there is no theoretical problem in set different values of N_f for each family.

5.6   Aspects of stability, regularization and initial model dependence

All tomographic methods developed so far has one unwanted feature: they are all ill-posed optimization problems. In other words, seismic tomography methods may not have a solution or, if it has, it might not be unique. The linear system performed by each iteration, as a result of the linearization of the non-linear optmization problem (see, e.g, Billette and Lambaré (1998), Duveneck (2004b), Farra and Madariaga (1988)), belongs to the class of ill-condicioned linear systems (see, e.g,Van Loan and Golub (1983)). Ill-condicioned linear systems results in poor quality of the provided answer in the presence of errors at the matrix, even when the errors are small (see, e.g, Watkins (2004)). A classical and practical way to handle this problem is the introduction of a regularization term in the objective function to improve the stability of the inverse problem, as it was proposed

so far for the seismic inverse problems in this thesis. Also, a suitible choise of algorithm, as singular value decomposition (see, e.g, Watkins (2004)), also known as *SVD*, or other related method (see, e.g, Paige and Saunders (1982)), is needed to solve the ill-condicioned linear system. As the regularization term is not a part of the tomographic original formulation, it adds external information to the inverse problem. While it brings more stability, the solution passes to be guided by external features.

CRP tomography method was derived based on previous implementation and further numerical tests of two other seismic tomography methods: stereotomography and NIP wave tomography. Stereotomography was explained in chapter three, while NIP wave tomography is presented in Appendix A. Both of the methods, as is the case of all other tomography methods, are strongly dependent of external regularization to constrain the model. In other words, no enough internal information is available to recover true model space. The tests that will illustrate next chapter will show how stereotomography improves the ability to constrain different kinds of velocity models by the addition and improvement of the quality of internal information. There, the internal information is represented by the increase of observed-data space, provided as input to the inversion process, and better initial velocity models. This approach turned stereotomography less dependent of the particular choice of initial regularization parameter. Therefore, is like some part of the necessary regularization was provided by more internal information. This strategy prevents the expensive search of an optimum regularization parameter. Furthermore, it is never known if just by changing the level of external regularization, it is possible to really constrain the model. However, the numerical tests of next chapters use observed-data spaces generated direct by dynamic-ray tracing. Therefore, it was an easy task to generate more quantity of input data information, since no picking process was necessary. Picking processes is an expensive and hard task, mainly when a lower signal-to-noisy data is treated. On the other hand, when just synthetic models are handled, as it will be the case of next chapters, it is also an easy task the improvement of the quality of initial velocity models. When the velocity model is not previously known, this can become a difficult task.

CRP tomography goes one step further in the difficult task of treat the natural instability of seismic tomography problem. Although it is still a unstable problem that needs an external regularization to provide reasonable solutions to inverse problem, numerical tests that will illustrated next chapters suggest that CRP tomography can enhance the regularization and stability of the inverse problem by providing more and better internal information. This is done by considering the important extra feature, so far not used in tomographic approaches, the use of a common-reflection-point information. Consequently, at each iteration, CRP tomography uses the information provided by many different pairs of rays, not only one, starting from the same model-depth-position. All the related information generated by this set of pairs of rays is compared to the related observed quantities. This family of data information is treated simultaneously to improve model space. Also, note that, by

the use of a family of ray pairs propagated to the surface from each common model depth point, it is possible to evaluate the model by many different directions. It obviously enhances the quality of internal information provided to inverse process. Moreover, from each of model depth position, more parts of the velocity model can be analysed, when compared to other tomographic methods. It will be shown, by means of numerical tests in next chapters, how these features can decrease the necessity of providing a big data input observed data space or better initial velocity models. Moreover, at least in some synthetic tests performed, CRP tomography could become less sensitive to variations in the scalar parameter λ that regulates the level of external regularization, which can suggest that part of the necessary regularization came from the use of more internal information, the common-reflection-point information.

The above properties will be illustrated in next chapters by means of comparisons between the results provided by different seismic tomography methods on synthetic numerical tests.

5.7 Further strategies for CRP tomography

Strategies to assist the inverse process: As it is done in some others tomographic methods, more then one regularization could be applied to proposed CRP tomography in order to improve even more the stability features and help to constrain different kind of models. Therefore, all different types of regularizations that have already been applied for NIP wave tomography, stereotomography and other seismic tomography methods, could be adapted CRP tomography. Thus, regularizations related to previous knowledge about some parts of velocity model or even interface structures, which is suggested for NIP wave tomography in Duveneck (2004b), or numerical regularization applied to all components of model space, which is suggested for stereotomography in Billette and Lambaré (1998), could be applied at the new method. Also, the different kind of strategies to assist the inversion model as multiscale optimization or initial localization and slopes optimization (see, e.g, Billette et al. (2003)), could be used. As it will be shown in next chapters, CRP tomography provided reasonable results during the task of invert different kind of synthetic velocity models just by the presence of one regularization term. However, in further researches, where more complex models can be proposed, these strategies can be incorporated for CRP tomography.

Decrease of the regularization parameter: An heuristic algorithm can be used in order to decrease the value of the regularization weight parameter λ during the inverse process. Decrease the weight

regularization parameter λ along the iterations can lead to improved solution stability and can accelerate the convergence of the inversion method (see, e.g, Nemeth et al. (1997), Williamson (1990)). At tomographic context, it can works as a search of long-wavelength features at the early iterations, while more details are pursue at the last iterations. This decrease can be performed by uncounted different ways. In this thesis, a simple heuristic will be used to execute this task. The proposed heuristic is given by:

$$\lambda_{k+1} = \sqrt{\frac{S(\mathbf{m_k})}{S(\mathbf{m_{k-1}})}}\lambda_k, \quad \text{for} \quad k > 1, \tag{5.32}$$

where $S(\mathbf{m_k})$ is the value of objective function, equation (5.22), at k-th iteration.

The heuristic will be applied to all numerical tests of this thesis. This also include the tests with other seismic tomography methods, as stereotomography and NIP wave tomography methods.

Note that, by the previous heuristic, the regularization parameter is not invariant over the inverse process. However, it still has to be initialized and the hard task of choose a good initial regularization parameters still is a remarkable problem for tomographic proposes.

5.8 Initial model space for CRP tomography

Following the same characteristics of other seismic tomography methods, an initial velocity model is not a remarkable critical point for CRP tomography. In fact, illustrative synthetic-data examples in next chapters will show that CRP tomography could provide satisfactory solutions for quite simple, usually homogeneous ones, initial velocity models. However, given an arbitrary initial (simple) velocity model, CRP tomography requires, in addition to an initial velocity-model space, also an initial ray-model space $\mathbf{m}^{ray}$. A rule to initialize CRP ray model space $\mathbf{m}^{ray}$ will be given in this section.

A simple geometric procedure was derived to set initial values for the components of ray model space $\mathbf{m}^{ray}$ for CRP tomography. It can be seen as a generalization of the initialization step, also proposed in this thesis, for stereotomography.

Firstly, recall that, at each iteration, the ray-model space consists on N families of model parameters, each of them corresponding to a counterpart family of data parameters of the (invariant) observed-data space provided by the user. Each of the N families in model space is composed by N_f model parameter vectors of the type $(\theta_s, \theta_r)_{fi}$, with $i = 1, \ldots, N_f$, plus a common-model-depth

position $(x,z)_f$. These quantities have to be initialized. The counterpart family in observed-data space is composed by N_f parameter vectors of the type $(s,r,p_s,p_r)_{fi}$, plus a total family traveltime t_f. Assume that an initial velocity-model space $\mathbf{m}^{vel}$ has been given. With the help of Figure 5.5, a top-to-bottom procedure transform each observed-data parameter vector $(s,r,p_s,p_r)_{fi}$, together with the related total traveltime t_f, from the observed-data space, into its corresponding initial model parameter vector $(\theta_s,\theta_r)_{fi}$ together with the related common-model-depth position $(x,z)_f$. For now on, the procedure is very similar to the one proposed in chapter 3 for stereotomography.

Recall that the pairs $(s,p_s)_{fi}$ (resp., $(r,p_r)_{fi}$), as given by the observed-data vector parameter, define the ray that starts at the source position $(s)_{fi}$ (resp., at the receiver position $(r)_{fi}$) and proceed downwards with direction provided by the horizontal slowness $(p_s)_{fi}$ (resp., with direction provided by the horizontal slowness $(p_r)_{fi}$). Under these considerations, both rays are traced until the same traveltime $t_f/(2N_f)$ is consumed. As shown in Figure 5.5, the endpoints of both rays have coordinates $((x_s)_i,(z_s)_i)$ and $((x_r)_i,(z_r)_i)$, respectively. Moreover, at those endpoints, the direction angles $(\theta_s)_i$ and $(\theta_r)_i$ with respect to the vertical z-axis are provided by ray tracing. Set (x_i,z_i) as the midpoint between the endpoints $((x_s)_i,(z_s)_i)$ and $((x_r)_i,(z_r)_i)$. Repeat the following procedure for each sample of the family.

From the above procedure, N_f direction angles $(\theta_s)_i$ and $(\theta_r)_i$ are obtained, as well as N_f depth positions (x_i,z_i). Setting (x,z) as the midpoint of all depth positions (x_i,z_i), all values that define the initial ray-model parameters for the family are obtained. In symbols:

$$\mathbf{m}_f^{ray} = \left((x,z)_f, [(\theta_s,\theta_r)_{fi}]_{i=1}^{N_f}\right) = \left(\frac{\sum_{i=1}^{N_f}(x_s+x_r)_i}{2N_f}, \frac{\sum_{i=1}^{N_f}(z_s+z_r)_i}{2N_f}, [(\theta_s,\theta_r)_i]_{i=1}^{N_f}\right). \quad (5.33)$$

The above procedure is repeated for every family, which completes the ray-model space initialization step.

It is important to highlight that an arbitrary initial velocity model space was used at the previous explained initialization step to compute the initial ray-model components. Despite it is not a crucial feature for seismic tomography applications, usually, the more similar is the initial velocity with the true velocity model, the better is the answer of the inversion process. However, it usually requires some previous knowledge about true velocity model.

Despite the fact that the initial velocity model is an arbitrary one, strategies to invert the model by a crescent order of complexity, which was metioned in chapter three for stereotomography, could also be applied for CRP tomography applications, although it was not considered in this thesis.
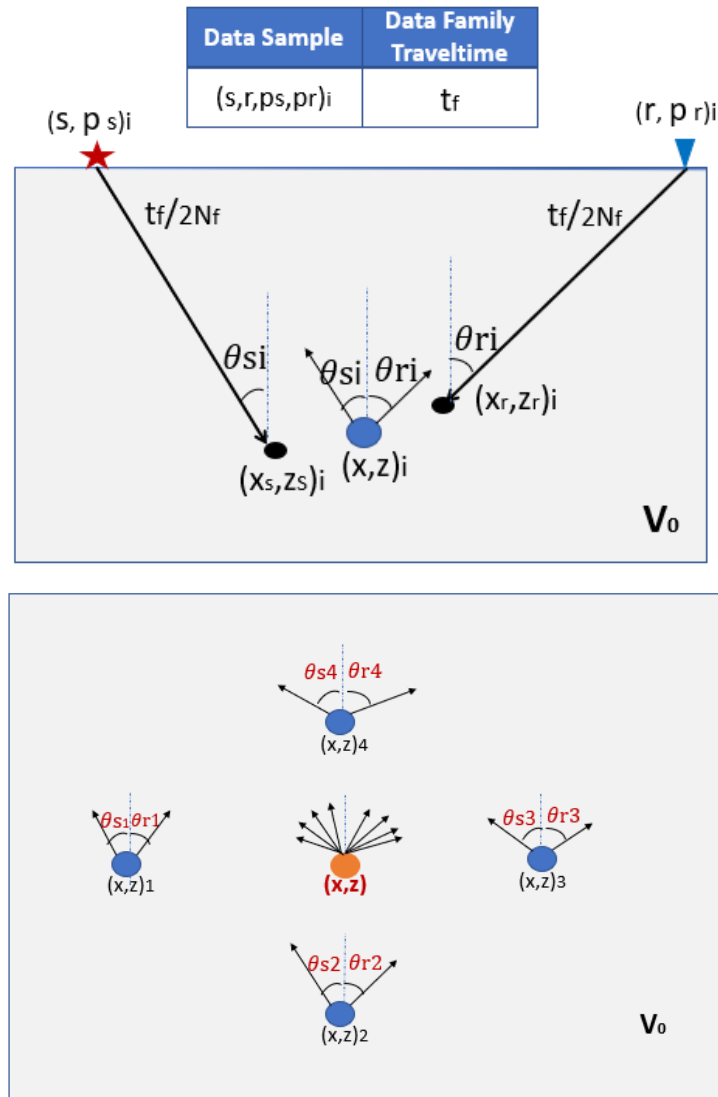
Figure 5.5: Initialization procedure for ray-model parameter vector. A initial velocity model, constructed by an arbitrary given initial velocity-model vector parameter is assumed. Also assumed is a observed vector parameter of $\mathbf{d}_f^{obs}$, composed by a total family traveltime t_f and N_f samples of $(s_i, r_i, p_{si}, p_{ri})$ data parameters $(i = 1, \ldots, N_f)$, for which the corresponding initial ray-model vector paramter $\mathbf{m}_f^{ray}$, composed by a model depth position (x, z) and N_f samples of $(\theta_{si}, \theta_{ri})$ model parameters, is to be constructed. Under the use of the given initial velocity model, each of the N_f data samples defines two rays that are downward propagated from respective source and receiver locations s_i and r_i (top image), with directions determined by the slopes p_{si} and p_{ri} respectively. Those rays are propagated until the endpoints (x_{si}, z_{si}) and (x_{ri}, z_{ri}) that are attained for the traveltimes $t_s = t_r = t_f/(2N_f)$. Take (x_i, z_i) as the midpoint between (x_{si}, z_{si}) and (x_{ri}, z_{ri}). Setting (x, z) as the midpoint between all (x_i, z_i) (bottom image, where an arbitrary $N_f = 4$ was assumed for illustration purposes), all values that define the initial ray-model parameter $\mathbf{m}_f^{ray}$ are obtained.

In this sense, one could firstly invert a vertical gradient model, then consider some lateral heterogeneity, etc. This could be viewed as form to provide increasingly better initial velocity models.

Furthermore, the same optimization problems, executed before stereotomography applications in some references (see, e.g, Billette et al. (2003)), derived to find same kind of optimum set of initial model depth positions and slopes, could be adapted for CRP tomography method. However, as it represents a great help in the difficult task of constrain more complex models, it will be not applied in this thesis. As has been repeatedly mentioned during this text, one of the objectives of the thesis is to analyse the ability of the different seismic tomography methods to constrain proposed synthetic models. The use of these kind of strategies, or other types of extra regularization, would turn this analysis unfair.

5.9   A Pseudocode for CRP Tomography

During the development of this phd thesis, CRP tomography was fully implemented. All features of the inversion method were derived from actual implementations. That included all schemes employed for ray tracing, B-spline interpolations, mathematical methods to solve ill-conditioned linear systems, initialization procedure and regularization. None previous software was used. The same was done to other seismic tomography methods, as stereotomography and NIP wave tomography. Building all those schemes from scratch was of paramount importance to fully understand the relevant aspects of the tomographic inverse process, as well as to spot possible points where advances could be made.

The implementation of CRP tomography method (as well as the other seismic tomography methods implemented) followed what were exposed until now and can be summarized by the following pseudocode, organized by steps.

1. Observed-data space is constructed by means of a picking procedure in seismic data. The use of a CRP stacking procedure was suggested in this thesis to build the desired observed space. For synthetic numerical problems, observed-data space can be computed by means of direct ray tracing on true velocity model.

2. Initial parameters of the inversion process are set: number and positions of interpolation velocity knots, values for initial regularization parameters terms, data covariance matrix W_d^{-1}, etc.

3. Ray-model space is initialized by the proposed initialization procedure. An initial velocity model is arbitrarily chosen by setting values to the interpolation coefficients.

4. Forward modeling step, which stands for ray-tracing system, is performed to compute the components of simulated space. The boundary initial conditions are given by current model space.

5. In order to reduce computational effort, first order partial derivatives of components of synthetic space with respect to the components of current model space are numerically computed during dynamic-ray tracing. Jacobian matrix is constructed.

6. The regularized matrix equation (5.27) is solved in order to compute improvements for the model data space. An appropriate numerical method is applied. In this thesis, SVD method was used.

7. A vector of model update is generated by step 6. An arbitrary scalar path (usually 1 at first try) is chosen and multiplied to the vector of model update to generate a candidate for new model space. If under the use of the candidate for new model space the misfit function is decreased, then the iteration is finished. Model space is updated and the candidate for new model space becomes current model space. Regularization weight parameter is decreased by the proposed heuristic and the algorithm returns to step 4.

8. If under the use of the candidate for new model space the misfit function is not decreased, reduced scalar paths for model update are tested and further evaluations are done until the misfit function is decreased. If if happens, the iteration is finished, model space is updated, regularization weight parameter is decreased and the algorithm returns to step 4.

9. If no decreases could be detected during all of the reduced scalar path performed for model update in previous item, the algorithm is stopped.

The algorithm can also be stopped if a maximum number of iterations is reached or if the objective function falls bellow an specific inferior limit value.

Chapter 6

Synthetic tests for stereotomography

6.1 Validation Tests

Stereotomography method was fully implemented during phd period. All features of the inversion method were derived from actual implementations. In order to validate the implementation, some validation tests were performed. The following tests will be shown next. All the validation tests use observed-data space composed by kinematic parameters calculated direct by dynamic-ray tracing on proposed velocity model tests. Thus, despite of numerical errors and theory approximations, data set is composed by perfect accurate components. All simulations apply just one regularization term, the miminization of second derivatives of velocity model explained in this thesis (see Chapter 3 and Appendix E). The same initial tests were used to validate NIP wave tomography implementation. The results obtained by NIP wave tomography are illustrated in Appendix B. Some comparisons between the results obtained by both methods will be addressed in this chapter. In next chapter, this same set of validation tests will be used to validate CRP tomography implementation.

The chosen tests encompass a variety of different kind of continuous velocity variations. All of them were built analytically by means of simple math expressions. In all validation tests, a squared grid of 2km×2km was considered. Velocity models were constructed by B-spline interpolation, with knots uniformly distributed through the model. The knots were spaced by a constant distance of 0.4km, both in vertical and horizontal directions.

Validation tests are composed by the following velocity models. They will be illustrated in next figures, together with stereotomography provided results.

1. Model with trigonometric variation in vertical direction.

2. Model with linear variation in vertical direction.

3. Model with quadratic variation in vertical direction.

4. Model with linear variation in horizontal direction.

5. Model with linear variation in horizontal direction and quadratic variation in vertical direction.

For validation testes, input spaces and initial parameters were set as follows:

Input observed-data space: To generate observed-data space, 49 depth positions were uniformly distributed through model tests (data depth positions will be illustrated in next figures). These positions are displayed in next figures. They play the role of the localizations of primary reflection or diffraction events for these synthetic experiment. From these positions, two rays were propagated to surface direction, with initial double aperture, with respect to vertical direction, of $30°$. In surface line, the kinematic parameters of emergence positions, slopes and traveltime were computed, providing the 49 samples that compose the observed-data space. This, the components of observed-data space was computed directly by ray-tracing performed at the true velocity model. Therefore, despite numerical errors and theoretical approximations, observed-data space is composed by perfect accurate data components.

The uniform distribution of data positions in depth guarantees that all regions of the velocity model are covered by information in observed-data space. This procedure will be repeated along all synthetic tests of this chapter. In next chapters, this configuration will be dropped.

Note that 49 is not an elevate number of data positions in respect with the size of the velocity model and the amount often used in synthetic validation tests to construct data-observed space. Since observed-data space is computed directly by dynamic-ray tracing, more rays could be easily taken into account, which would result in a bigger observed-data space. The objective is to test the performance of the methods under a not elevate number of input data information, which turns comparisons easier between the different seismic tomography methods.

Initial model space: Initial velocity model space for all validations tests were set as a homogeneous initial velocity of 1km/s, except for fourth validation test (model with linear variation in horizontal direction), where a homogeneous initial velocity of 1.5km/s was applied. Initial velocity model resembles true velocity model just at surface. Interpolation velocity knots were uniformly distributed

through the model, with vertical and horizontal spacing of 0.4km. Ray-model space was initialized with the proposed initialization procedure for stereotomography described previously in this thesis (see Chapter 3). The initialization procedure returned, based on the 49 observed-data samples, the 49 initial ray-model samples, each of them composed by one depth model position, two model slopes and two model traveltimes. Each model sample is related to the respective sample of observed-data space. Initial model depth positions for each validation test will be illustrated by following figures.

Initial regularization weight parameter: In terms of initial parametrization, only the initial weight parameter for regularization term varies through the tests. This was necessary due the different types of velocity variations. For those where the velocity varies in a non-linear way, a smaller parameter was used. Some previous search was made in order to find reasonable initial values for initial regularization weight parameter. The parameter decreases thought iterations by the previously proposed heuristic (see Chapter 5).

Data a-priori matrix: Following Billette and Lambaré (1998), the precision of slopes, traveltime and shot/receiver positions was set as $2.10^{-5}s/m^{-1}$, 0.004s and 1m, respectively. These values are used to construct the diagonal a-priori data-covariance matrix $\mathbf{W}$. These values were kept the same for all over the stereotomography synthetic tests of this thesis. Therefore, these values will be omitted in other synthetic tests descriptions.

Stereotomography validation test results: The small number of data components, plus a initial velocity that does not resemble true velocity models, challenges the method in constrain the model tests. Figures 6.1, 6.2, 6.3, 6.4, 6.5, 6.6, 6.7, 6.8, 6.9 and 6.10 illustrate the results provided by stereotomography method on validation tests. Firstly, the results obtained by stereotomography on validation tests are noted satisfactory, which contributes to validate stereotomography implementation. Secondly, the results provided by stereotomography in validation tests are slightly better than those obtained by NIP wave tomography (see Appendix B). For almost all tests performed, relative difference between inverted velocity model (final velocity model) and true velocity model falls under 1%. The figures that illustrate slices of velocity models present almost perfect inverted slices. Also, when compared with NIP wave tomography results, note the better results obtained by stereotomography when laterally heterogeneous velocity models are presented. Therefore, stereotomography seems to be a more promising technique to handle this type of heterogeneity.
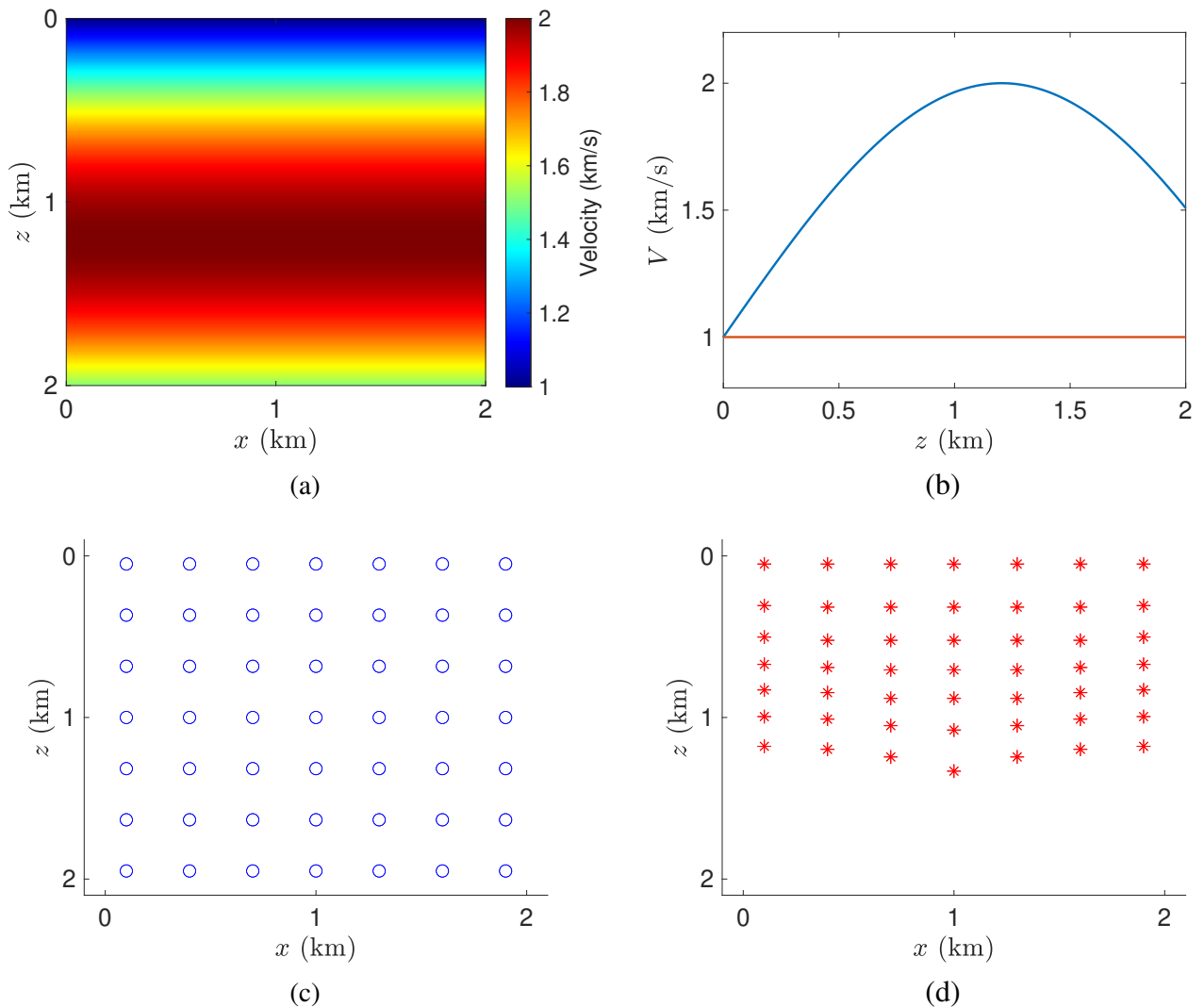
Figure 6.1: First validation test: model with trigonometric variation in vertical direction. (a) True velocity model for first validation test. (b) Vertical slices of initial (red) and true (blue) velocity models. Slices were taken at the middle of the models. (c) Data positions. Observed-data space is composed by kinematic parameters computed by a series of dynamic-ray tracing starting at these positions. (d) Initial positions of ray-model space returned by initialization process. Note that initial positions are concentrated at the upper part of model, because initial velocity model is slower than true velocity model.
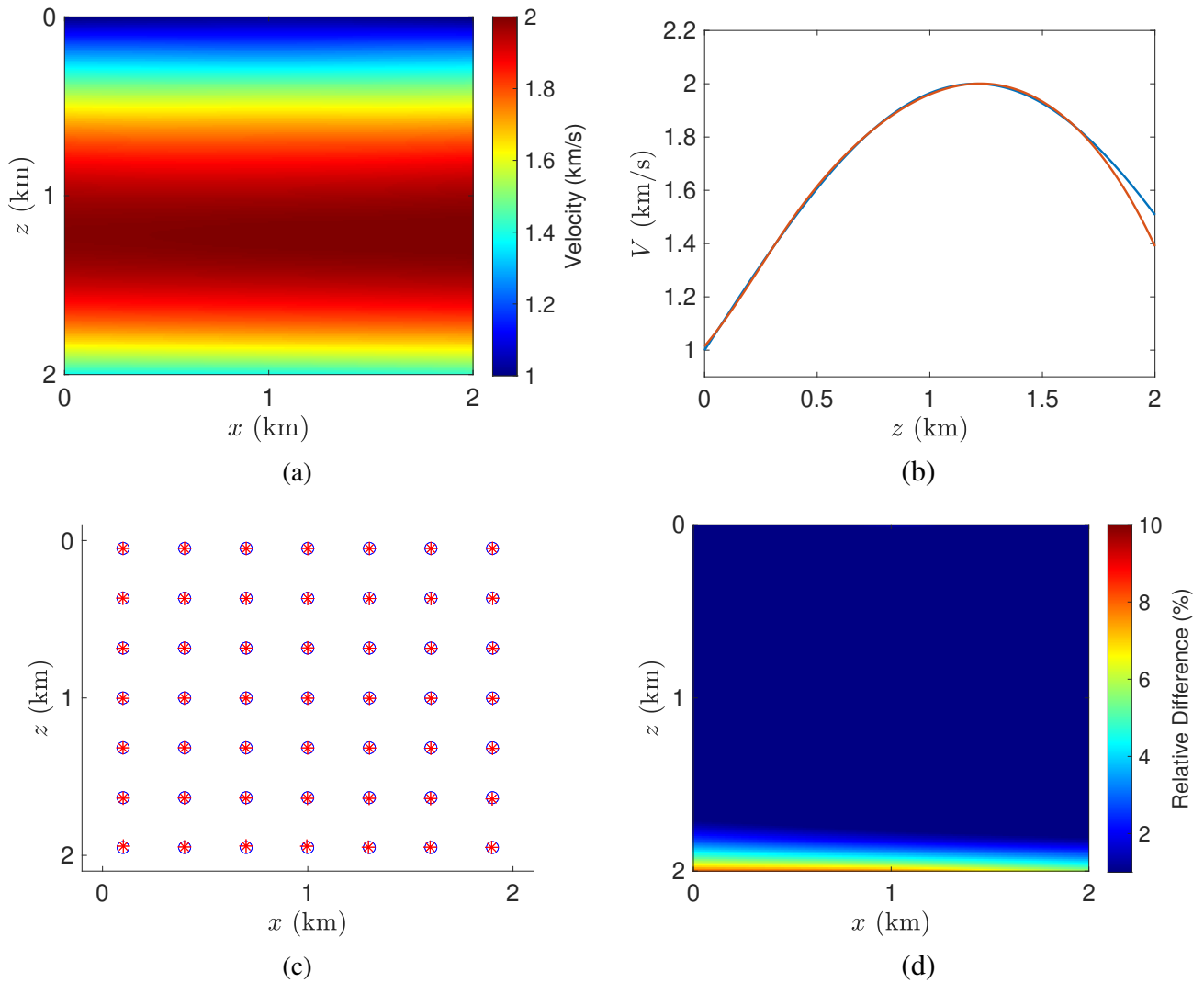
Figure 6.2: Stereotomography final result for first validation test. (a) Inverted velocity model. (b) Vertical slices of inverted (red) and true (blues) velocity models. Slices were taken at the middle of the models. (c) Inverted model (red) positions and true data (blue) positions. (d) Percentage difference between inverted and true velocity models.
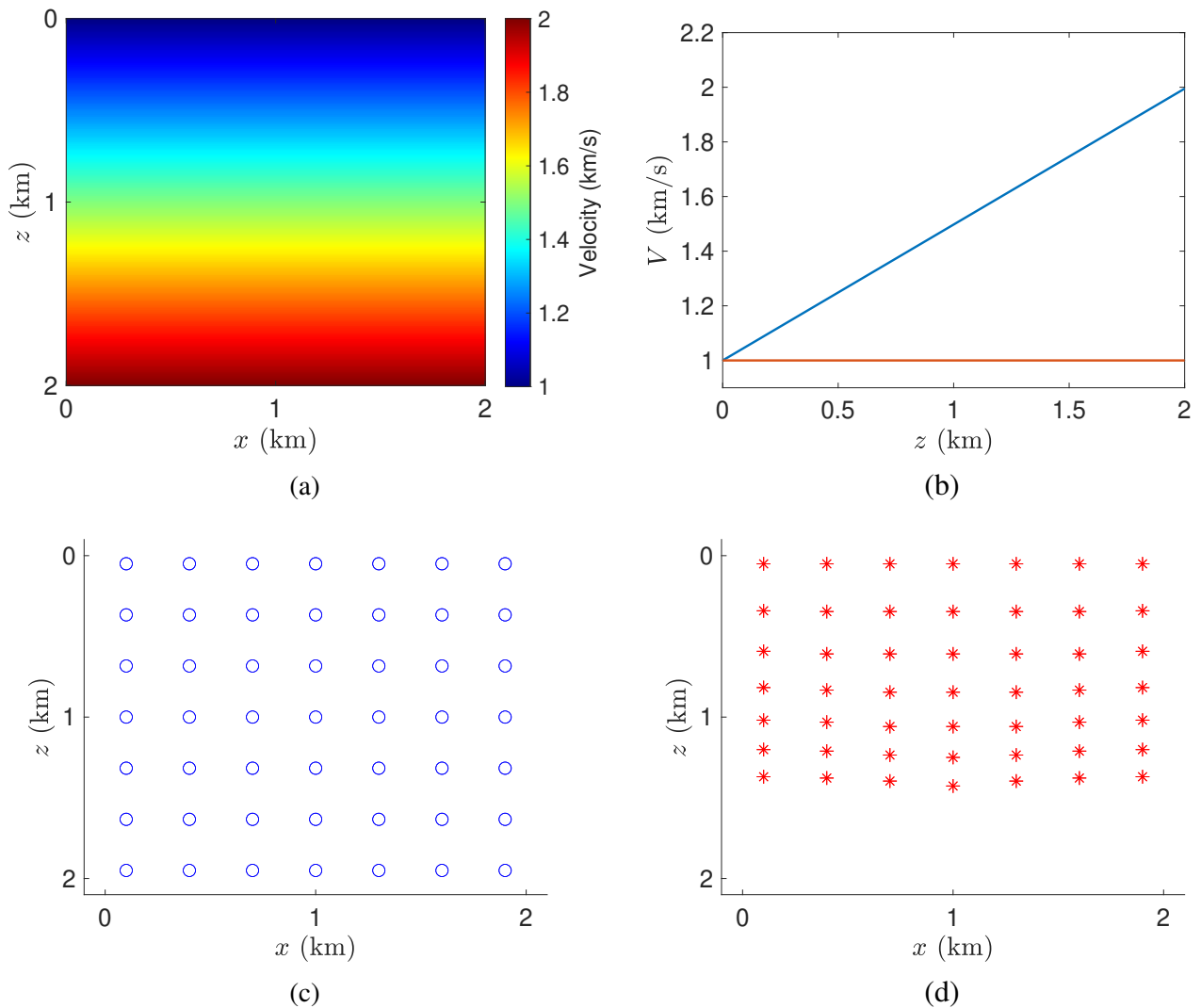
Figure 6.3: Second validation test: model with linear variation in vertical direction. (a) True velocity model test. (b) Vertical slices of initial (red) and true (blue) velocity models. Vertical slices were taken at the middle of the models. (c) Data positions. Observed-data space is composed by kinematic parameters computed by a series of dynamic-ray tracing starting at these positions. (d) Initial positions of ray-model space returned by initialization process. Initial positions are concentrated at the upper part of model, because initial velocity model is slower than true velocity model.
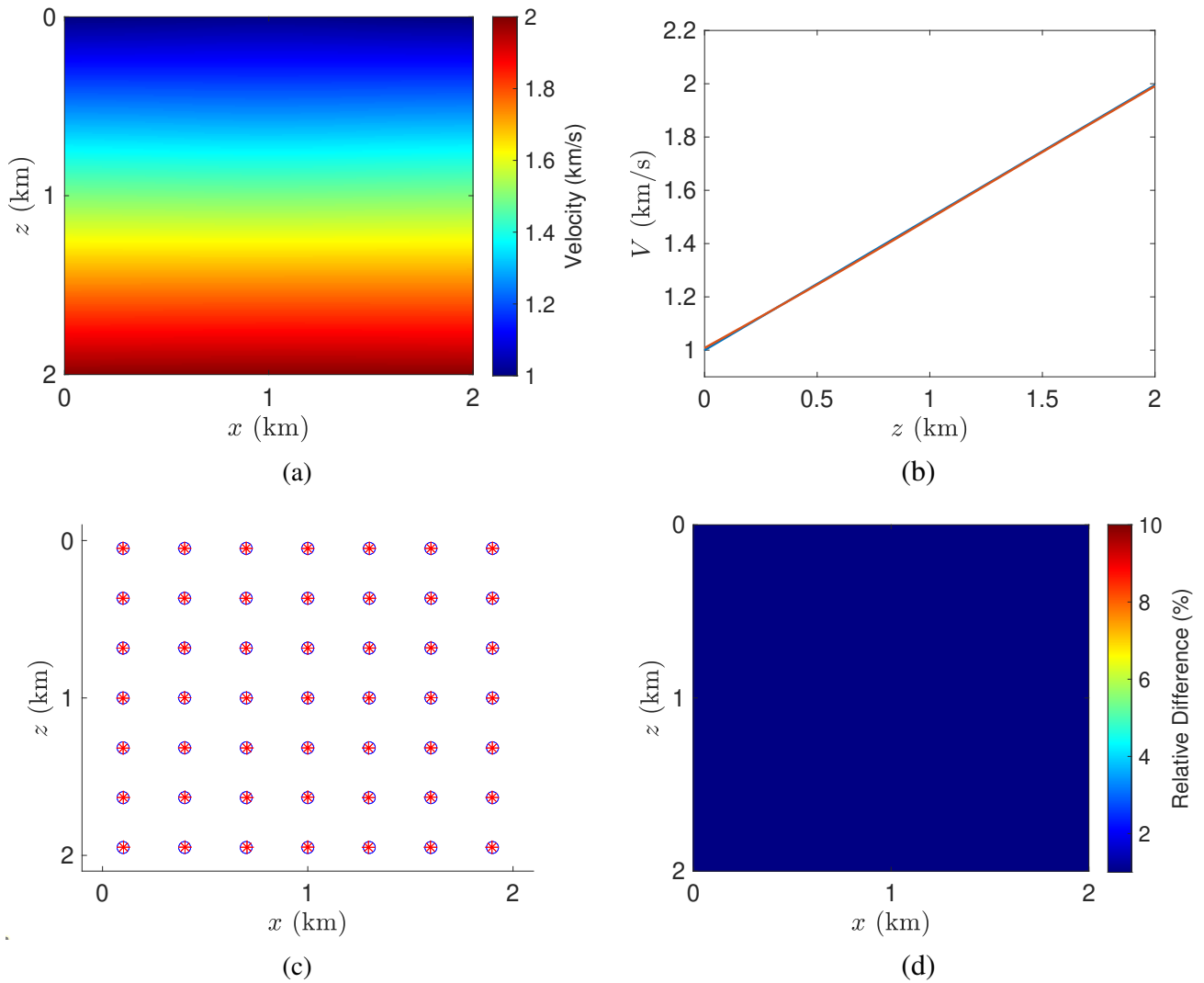
Figure 6.4: Second validation test: model with linear variation in vertical direction. (a) Inverted velocity model. (b) Vertical slices of inverted (red) and true (blue) velocity models. Vertical slices were taken at the middle of the models. (c) Final model (red) positions and true (blue) data positions. (d) Percentage difference between inverted and true velocity models.
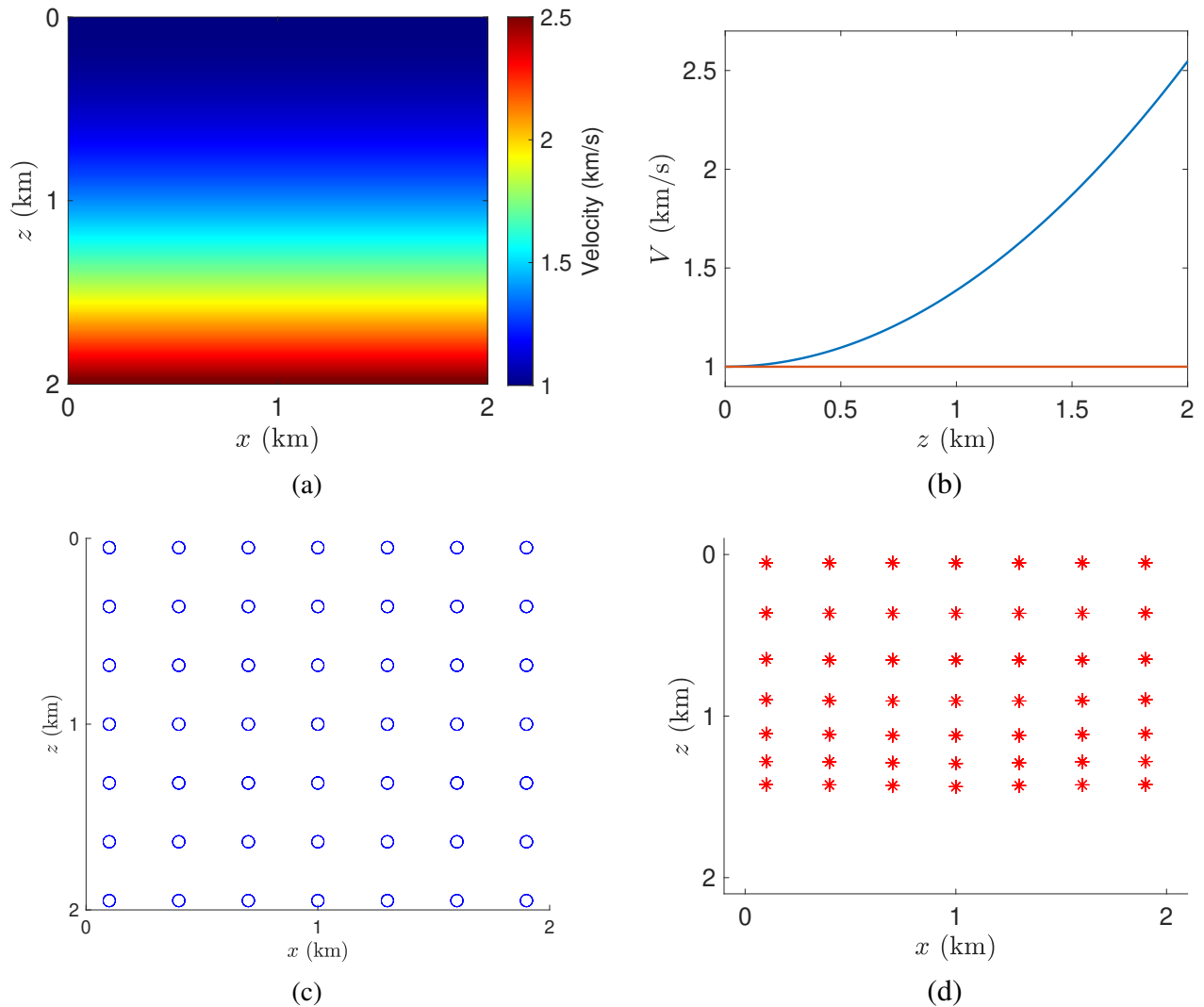
Figure 6.5: Third validation test: model with quadratic variation in vertical direction. (a) True velocity model test. (b) Vertical slices of initial (red) and true (blue) velocity models. Vertical slices were taken at the middle of the models. (c) Data positions. Observed-data space is composed by kinematic parameters computed by a series of dynamic-ray tracing starting at these positions. (d) Initial positions of ray-model space returned by initialization process.
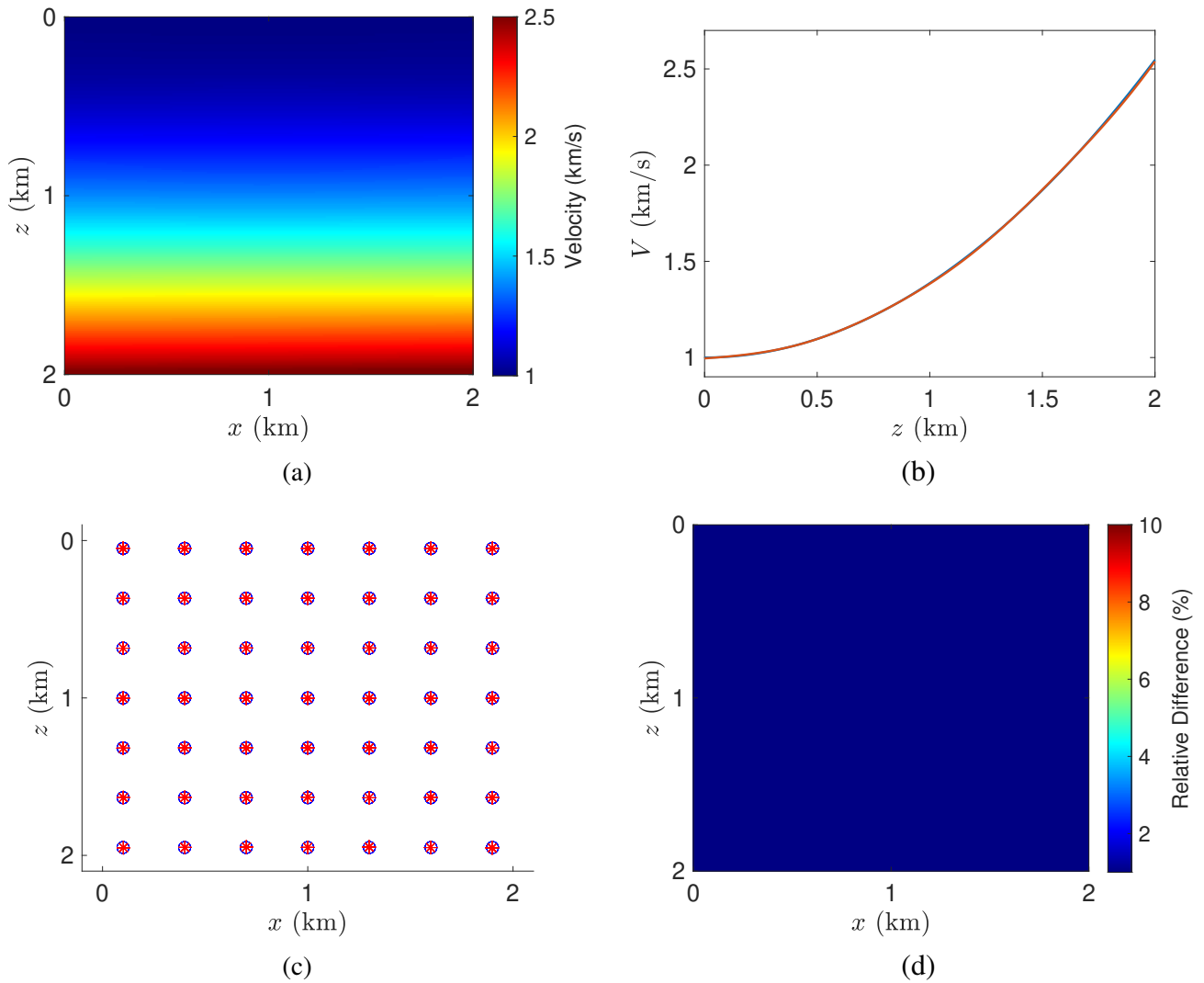
Figure 6.6: Third validation test: model with quadratic variation in vertical direction. (a) Inverted velocity model. (b) Vertical slices of inverted (red) and true (blue) velocity models. Vertical slices were taken at the middle of the models. (c) Final model (red) positions and true (blue) data positions. (d) Percentage difference between inverted and true velocity models.

(a)

(b)

(c)

(d)
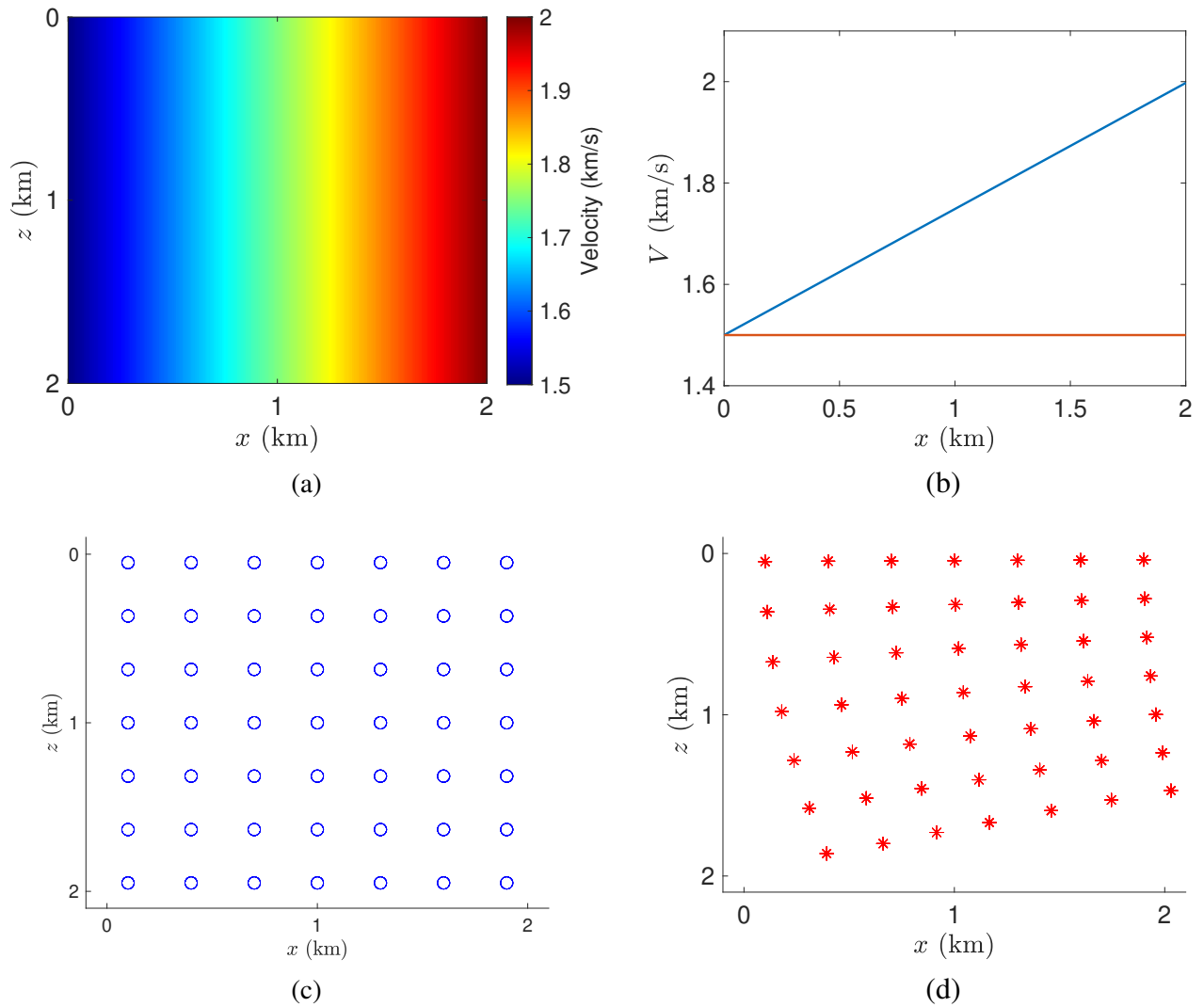
Figure 6.7: Fourth validation test: model with linear variation in horizontal direction. (a) True velocity model test. (b) Hotizontal slices of initial (red) and true (blue) velocity models. Slices were taken at the middle o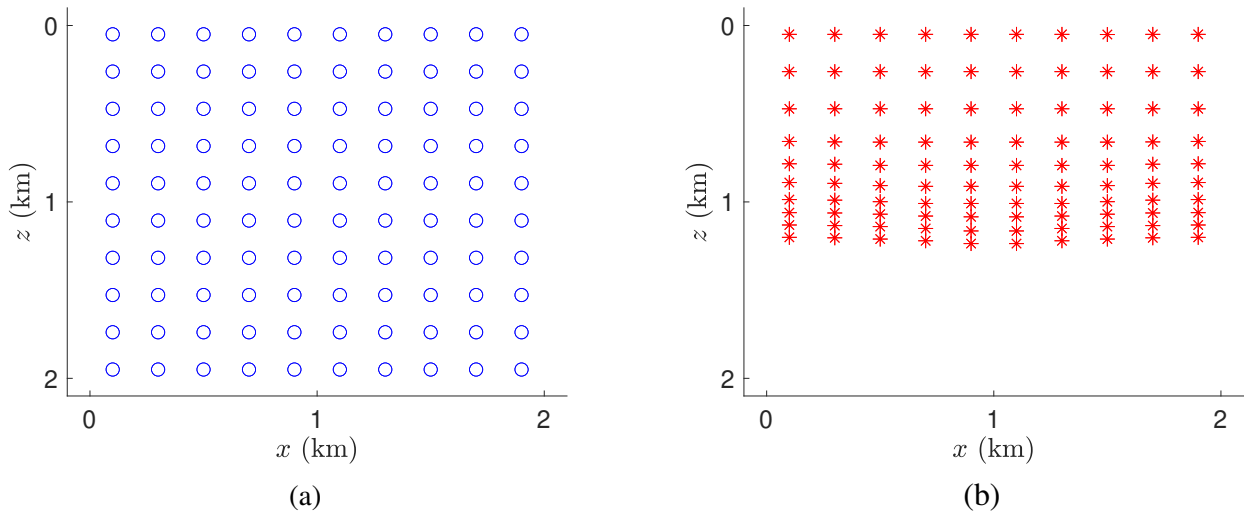f the models. (c) Data positions. Observed-data space is composed by kinematic parameters computed by a series of dynamic-ray tracing starting at these positions. (d) Initial positions of ray-model space returned by initialization process.
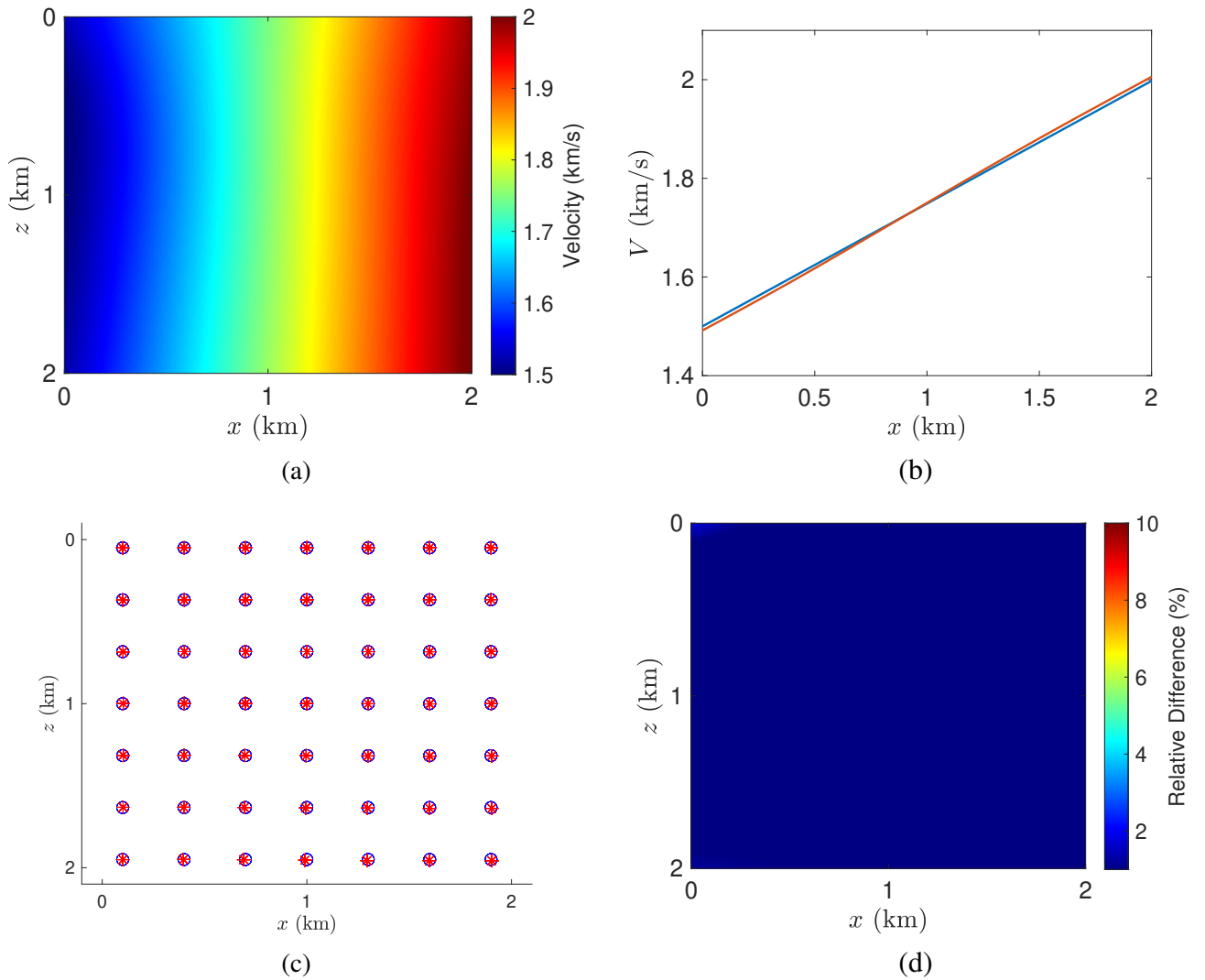
Figure 6.8: Fourth validation test: model with linear variation in horizontal direction. (a) Inverted velocity model. (b) Horizontal slices of inverted (red) and true (blue) velocity models. Slices were taken at the middle of the models. (c) Final model (red) positions and true (blue) data positions. (d) Percentage difference between inverted and true velocity models.
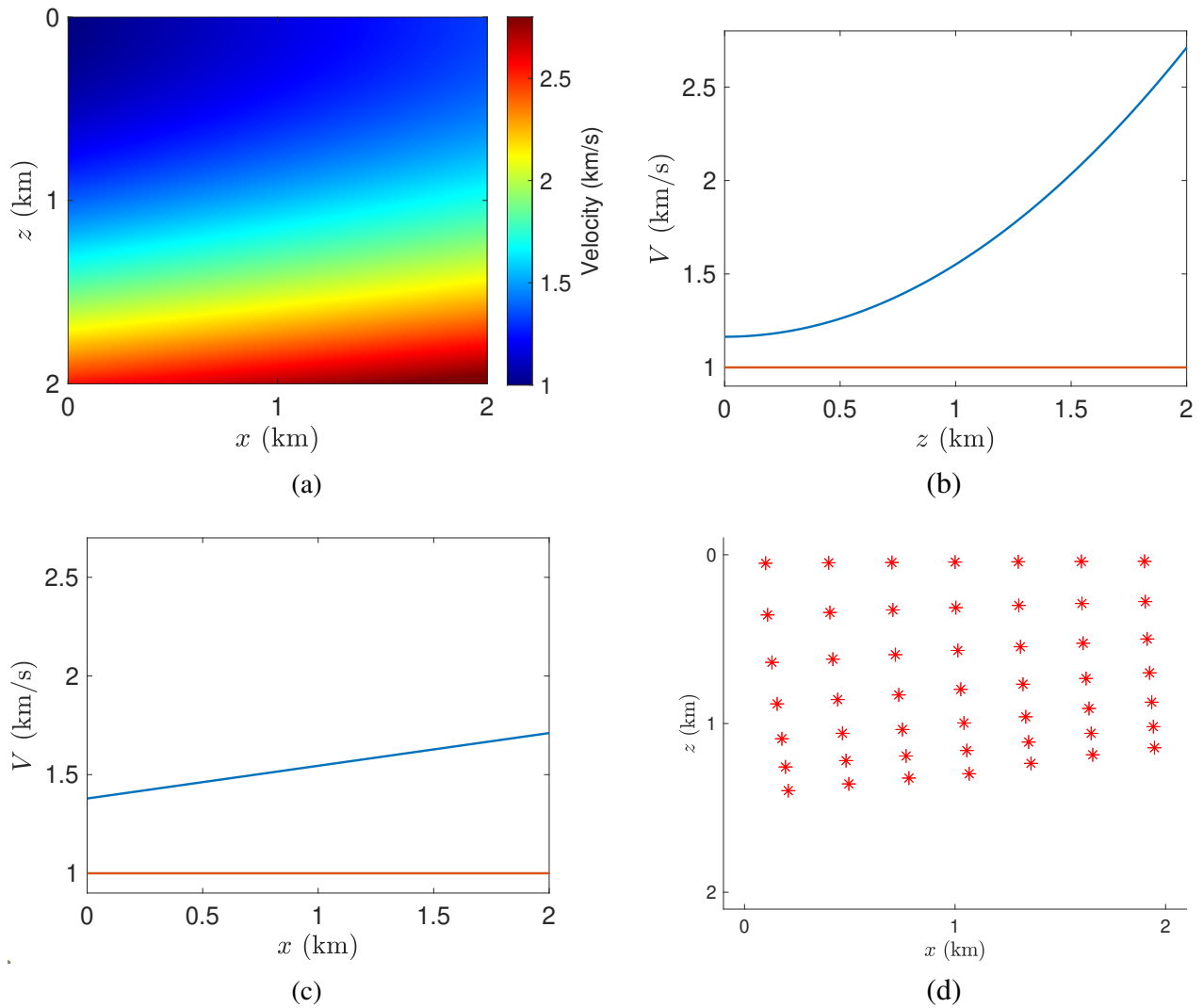
Figure 6.9: Fifth validation test: model with linear variation in horizontal direction and quadritic variation in vertical direction. Data positions are the same from previous validation tests. (a) True velocity model test. (b) Vertical slices of initial (red) and true (blue) velocity models. Slices were taken at the middle of the models. (c) Hotizontal slices of initial (red) and true (blue) velocity models. Slices were taken at the middle of the models. (d) Initial positions returned by initialization process.

(a)

(b)

(c)

(d)
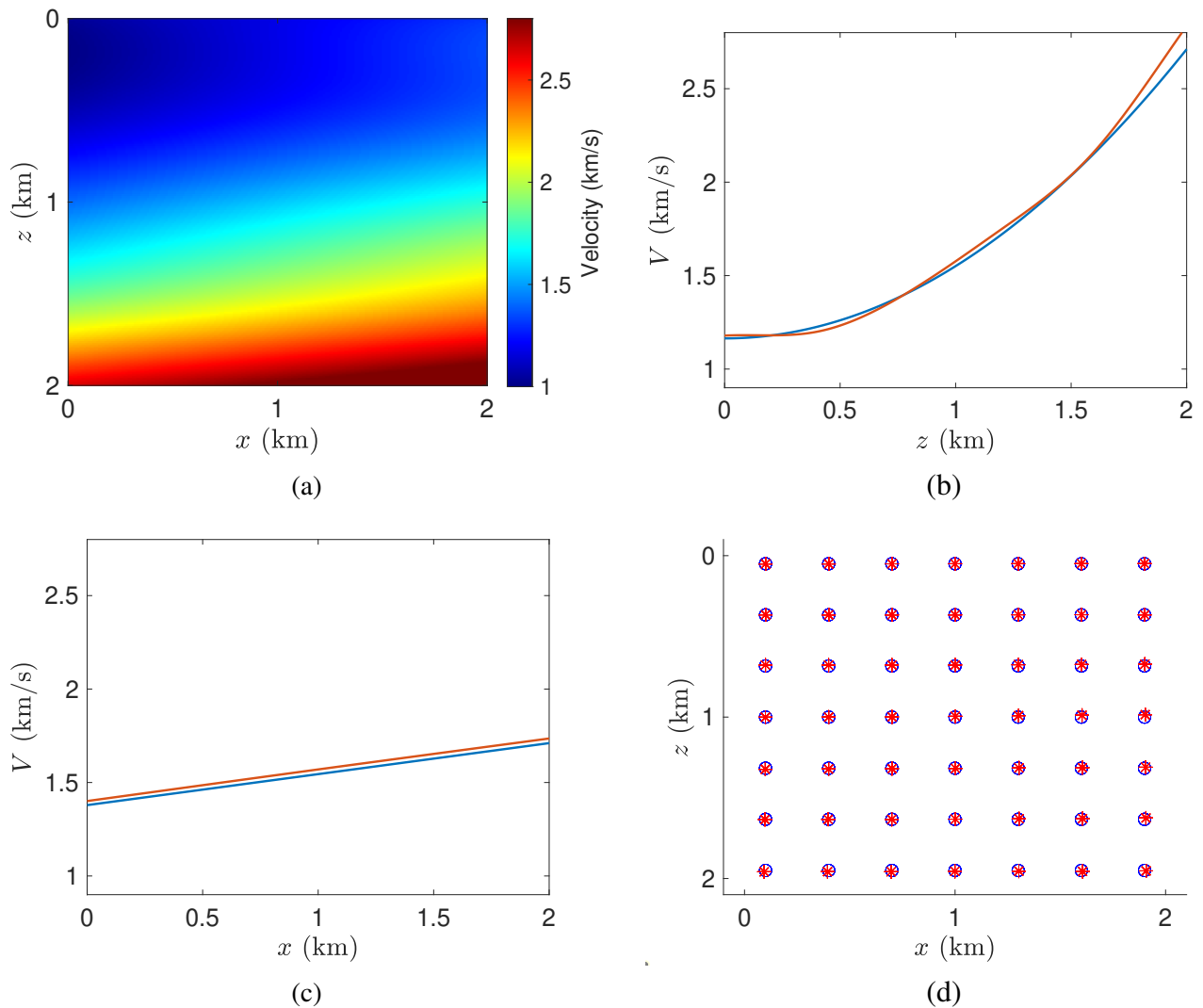
Figure 6.10: Fifth validation test: model with linear variation in horizontal direction and quadritic variation in vertical direction. Data positions are the same from previous validation tests. (a) Inverted velocity model. (b) Vertical slices of inverted (red) and true (blue) velocity models. Slices were taken at the middle of the models. (c) Horizontal slices of inverted (red) and true (blue) velocity models. Slices were taken at the middle of the models. (d) Final model (red) positions and true (blue) data positions.

6.2   The Three-layer Test

This section is dedicated to test the performance of stereotomography method to invert a three-layer model. In crescent order of depth, the layers present homogeneous velocity of 1km/s, 2km/s and 3km/s, respectively. Because rays will be traced through the model to generate observed-data space, smoothness properties are required. Thus, it is, in fact, a three-layer model without discontinuity at interfaces. Figure 6.11 illustrates the proposed model. The velocity model was constructed by means of B-spline interpolation, in a grid of dimension 2km×2km. Interpolation knots were uniformly distributed with vertical and horizontal spacing of 0.2km. B-spline functions of third order were applied, which assures the derivatives demanded both by dynamic-ray tracing, as well as computations of the derivatives for Jacobian matrix.

$$\text{(a)} \hspace{6cm} \text{(b)}$$
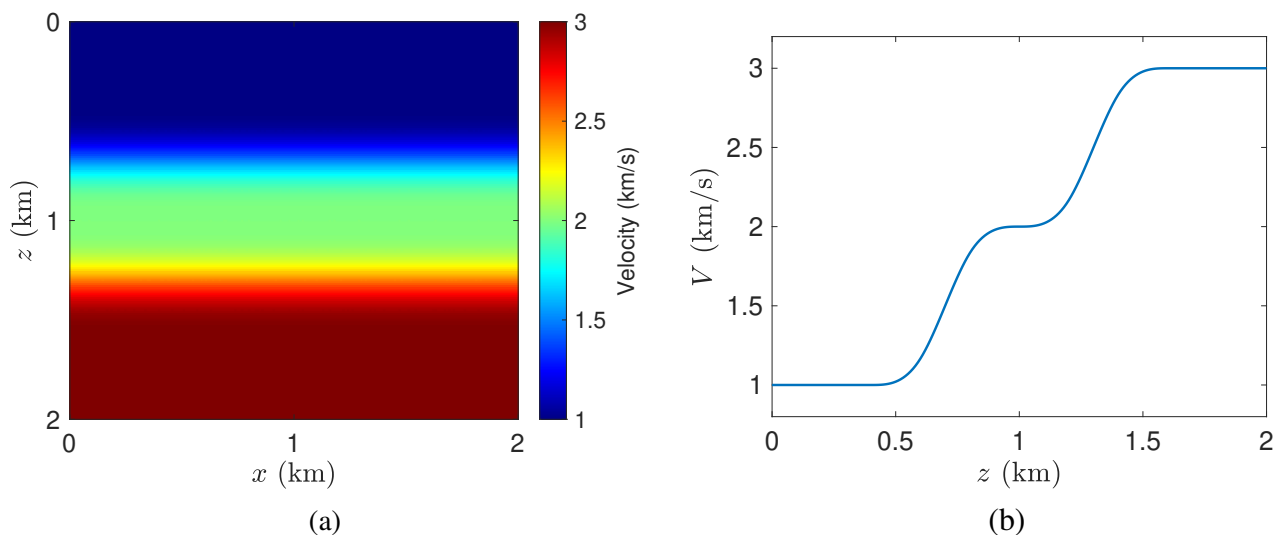
Figure 6.11: (a) Three-layer velocity model. (b) Vertical slice of the velocity model. The slice was taken at the middle of the model. Note that the second layer is smaller than the others.

Despite the fact of the model consists just by three layers, it is not a trivial test. Some reasons reinforce this point of view. Firstly, there are two abrupt variations of velocity in a small grid. Even after the smoothness of these velocity variations due to B-spline interpolation proporties, these abrupt velocity variations are an extra challenge to the inversion process. Moreover, the velocity model varies through 1km/s to 3km/s in less then 2km at vertical direction. However, the biggest challenge is that the second layer is considerably small. The test is designed to find out if stereotomography will be able to detect this small layer or not. In Appendix B, NIP wave tomography was tested by this same three-layer test, with similar boundary and initial conditions. There, NIP wave tomography failed to

precisely detect the presence of this small layer. The interest reader can consult the Appendix B for more details about the results obtained by NIP wave tomography on this test.

However, this velocity model offers another problem: since it presents strong oscillations at vertical direction, in this particular case, the regularization term plays against the inversion problem, once it guides inverse process to smoothness solutions. Thus, a small value of regularization parameter λ will be applied and the method will have the task to constrain the model in the presence of small values of the necessary regularization.

The proposed three-layer smooth velocity model was illustrated in Figure 6.11, where also a vertical slice of the velocity model was exhibited. The vertical slice illustrates the abrupt variation of the velocity model in the small grid. Note that the second layer is smaller than the others.

For stereotomography three-layer test, input data, model spaces and initial parameters were set as follows:

Input observed-data space: To generate observed-data space, 100 positions in depth were uniformly displayed thought the model (see Figure 6.12). These positions play the role of the localizations of primary reflection/diffraction events for this synthetic experiment. From these positions, two rays were propagated to surface line with initial double aperture, whith respect to horizontal direction, of $30°$. In surface line, the kinematic parameters of emergence positions, slopes and traveltime were computed, providing 100 samples that compose the observed-data space. Computed directly by ray-tracing performed at the three-layer velocity model test, despite numerical errors and theoretical approximations, observed-data space is composed, therefore, by perfect accurate data components. The uniform distribution guarantees, once again, that all regions of the velocity model are covered by informations in observed-data space. In order to compare with NIP wave tomography result, the data positions are the same of first test performed for NIP wave tomography (see Appendix B).

Initial model space: Initial velocity model is a homogeneous velocity model of 1km/s, which equals the velocity of first layer. Through inverse process iterations, velocity models are build under the same number and position of knots used to build the three-layer velocity model test. Therefore, with respect to interpolation limitations, three-layer model test can be reconstructed thought inverse process. Ray-model space was initialized with the proposed initialization procedure for stereotomography in this thesis (see Chapter 3). Therefore, the initialization procedure returned 100 initial ray-model samples, each of them composed by one depth-model position, two mode slopes and two model traveltimes. Each model sample is related to the respective sample of observed-data space. Initial model depth positions returned by initialization step under the initial homogeneous velocity

model of 1km/s are illustrated in Figure 6.12.

(a)

(b)

Figure 6.12: Three-layer test. (a) Data positions. Observed-data space is composed by kinematic parameters computed by a series of dynamic-ray tracing starting at these positions. (b) Initial model positions returned by initialization procedure, under the initial constant velocity model of 1km/s.

Initial regularization weight parameter: A previous search was made in order to find a good initial value for regularization parameter. Due to the observations made at the presentation of this test, a small initial regularization parameter value had to be set in order to handle with the trade-off between smoothness, which is a feature searched by the regularization term, and invert the abrupt velocity oscillations of true velocity model. For this test, λ was set in order to, at first iteration, the relation between the regularization term with respect to the objective function would be 4.10^{-6}. Moreover, $\epsilon_{zz} = 10^{-3}$, $\epsilon_{xx} = 1$ and $\epsilon_{vv} = 10^{-4}$ were set to calibrate the regularization term.

Figure 6.13 illustrates the final model proposed by stereotomography. It is easy to note that the inverted model of stereotomography is superior of the one proposed by NIP wave tomography in Appendix B. Velocity oscillations are not presented inside layers, the second layer was detected and velocity was reasonably inverted. Just at regions very close to bottom area, where almost no information is available, the stereotomography inverted velocity model deviates from true velocity model. Therefore, except at regions near the bottom area, the relative difference between true and inverted velocity model fall under 2%. Model depth positions were also well repositioned, which reinforces the good quality of the inverted model. Other challenge presented by this test, to set a good trade-off between regularization and provide a velocity model near the true velocity model, was overcomed by stereotomography. Differently of curvature tomography methods, stereotomography

is not too dependent of a strong smoothness of velocity model in order to compute curvatures and, moreover, Jacobian components related to this kinematic parameter. Therefore, small regularization parameter could be set, without decreasing the quality of final model solution. In Appendix B, an even greater number of input observed-data information (a bigger data space) was given to NIP wave tomography. Even though, the result presented by stereotomography is still better.
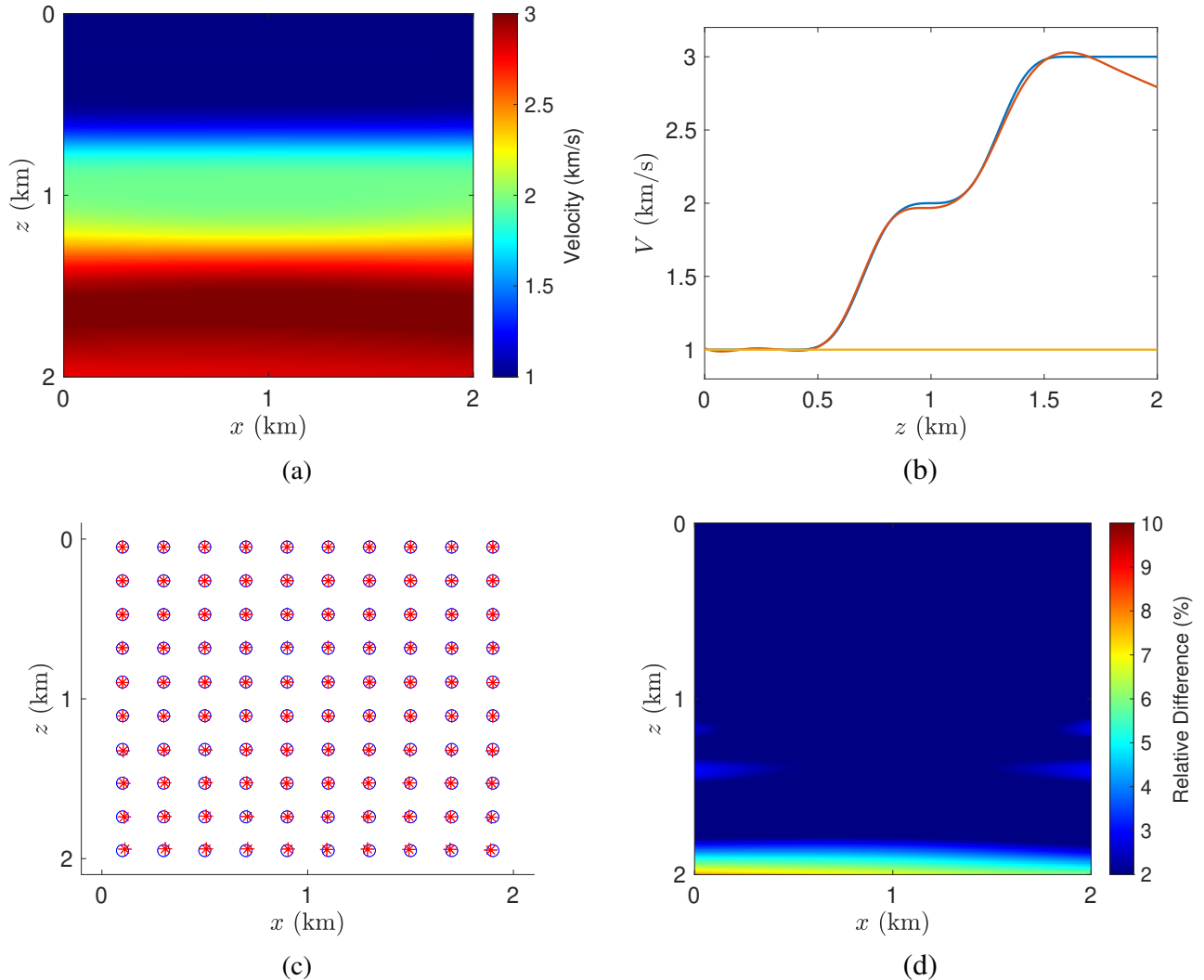
Figure 6.13: Three-Layer Test. (a) Stereotomography inverted velocity model. (b) Vertical slices of inverted (red), true (blue) and initial (yellow) velocity models. Slices were taken at the middle of the models. (c) Inverted model positions (red) and true data positions (blue). (d) Percentage difference between inverted and true velocity models.

Despite the fact that the provided stereotomography solution was good, it is important to highlight that it still presents a strong dependence on the right choice for initial regularization parameter λ. To almost fit true velocity model, a small initial parameter λ was set. However, if the parameter

choice would be even smaller, the inverted model proposed by stereotomography would lose the good features previously presented, and became more meaningless. On the other hand, higher values for regularization parameter turn the model too smooth, which it is not a characteristic of true velocity model. Figure 6.14 illustrates these situations, and reinforce the strong dependence of good solutions by a good initial choice for regularization parameter.

(a)   (b)
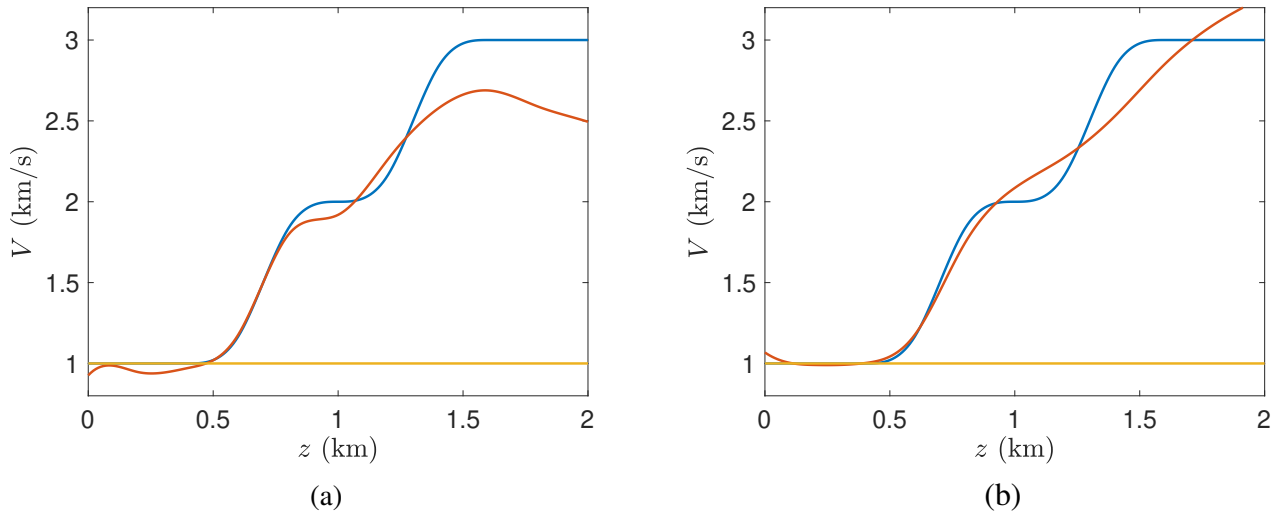
Figure 6.14: Three-Layer Test. (a) Vertical slices of stereotomography inverted (red), true (blue) and initial (yellow) velocity models under a smaller initial regularization parameter. Note the presence of oscillations in first layer region. (b) Vertical slices of stereotomography inverted (red), true (blue) and initial (yellow) velocity models under a stronger regularization. Note that the inverted velocity model doesn't recognize the presence of second layer.

In order to keep the investigation about the ability of stereotomography to invert the proposed three-layer model, one more difficult will be proposed: a reduced number of observed-data components will be given as input to inverse process. Therefore, in this new test, observed data space will be generated by just 49 positions in depth (see Figure 6.15). Other features of the test will be kept the same. From each of the 49 data positions, two rays are propagated to surface with initial double aperture, with respect to vertical direction, of $30°$. In surface line, demanded kinematic parameters are computed, providing 49 data samples that compose observed-data space. Initial velocity model is the same of previous test, as well as other features as initial regularization parameter.

Although slightly worse, the result remains considerably good, as it is shown by Figure 6.17. This is a great achievement for stereotomography. By this result, the method showed its ability to constrain the model by an even smaller number of input data information. However, if just 36 samples of data information are provided (once again, generated by 36 uniformly distributed positions in depth, Figure 6.16, from where a pair of rays are traced to compute the kinematic parameters at
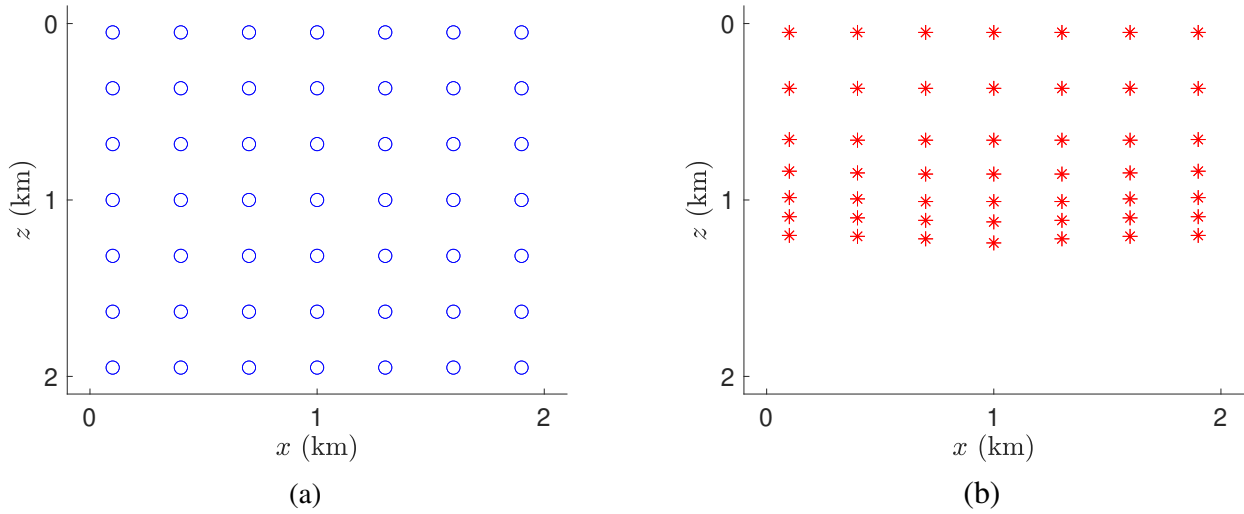
Figure 6.15: Three-Layer Test with 49 data samples. (a) Data depth positions. (b) Initial model depth positions.
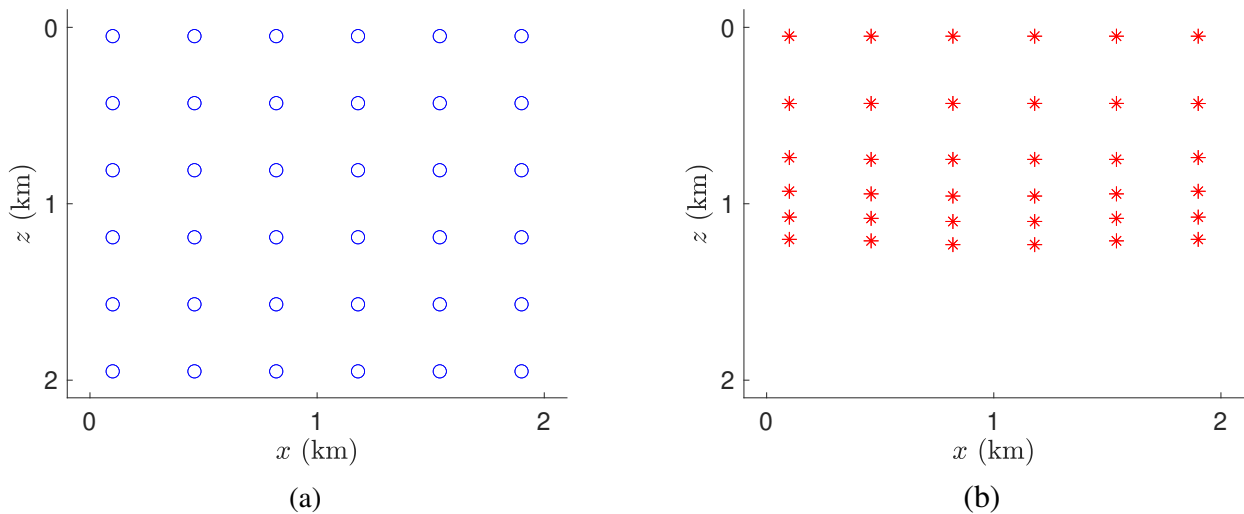
Figure 6.16: Three-Layer Test with 36 data samples. (a) Data depth positions. (b) Initial model depth positions.
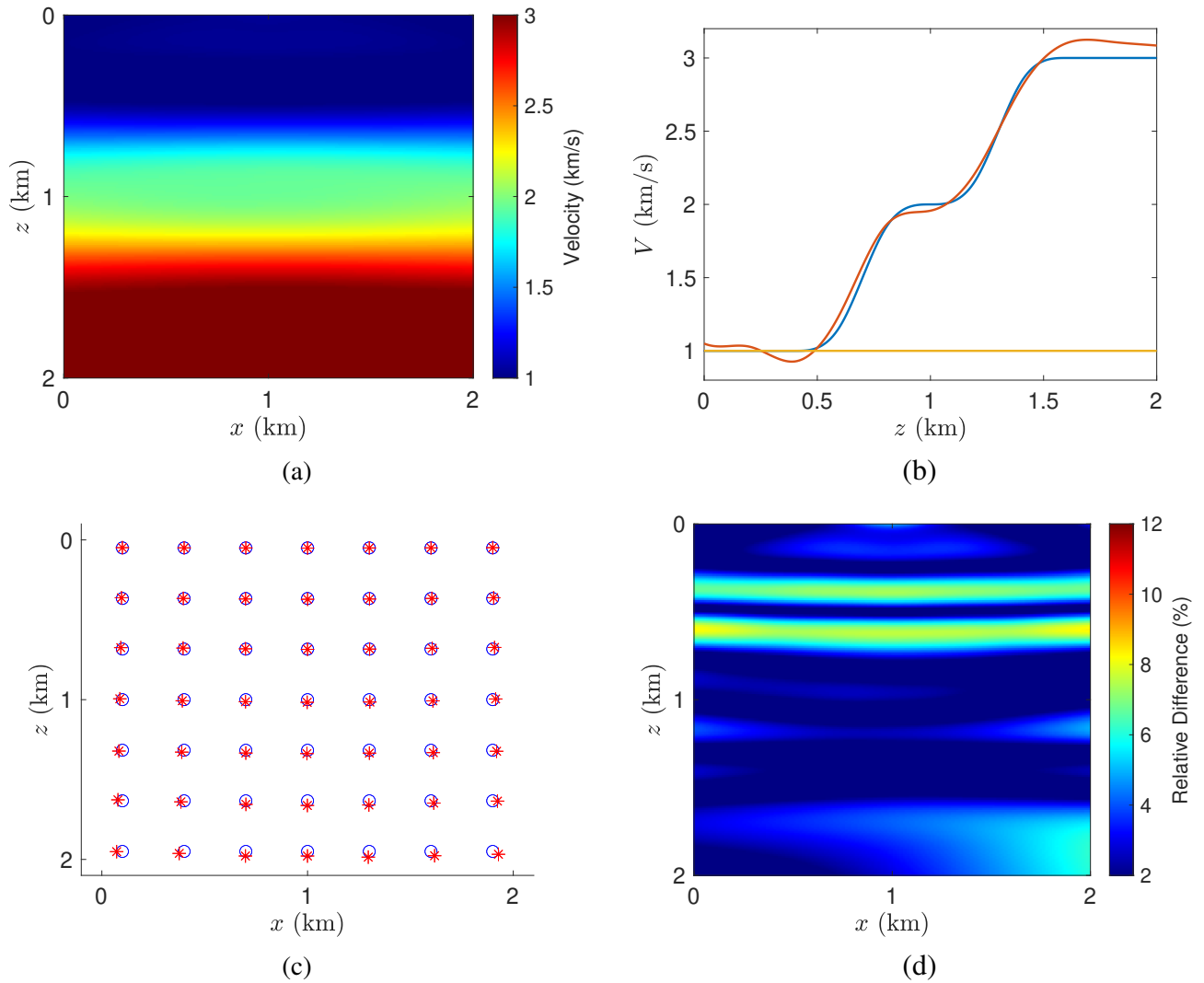
Figure 6.17: Three-Layer Test with 49 data samples. (a) Stereotomography inverted velocity model. (b) Vertical slices of inverted (red) and true (blue) velocity models. Slices were taken at the middle of the models. (c) Final model depth positions (red) and true data depth positions (blue). (d) Percentage difference between inverted and true velocity models.

surface line), the velocity model couldn't be reasonably inverted. The method does not identify the presence of the second layer. This time, no enough information is available to constrain the model. Once again, initial velocity model was kept the same, as well as initial regularization parameters. Figure (6.18) illustrates this limit case, where the small number of input data information does not allow a good performance of stereotomography in inverting the proposed model test. However, note that, even in this situation, model depth positions were reasonably inverted.
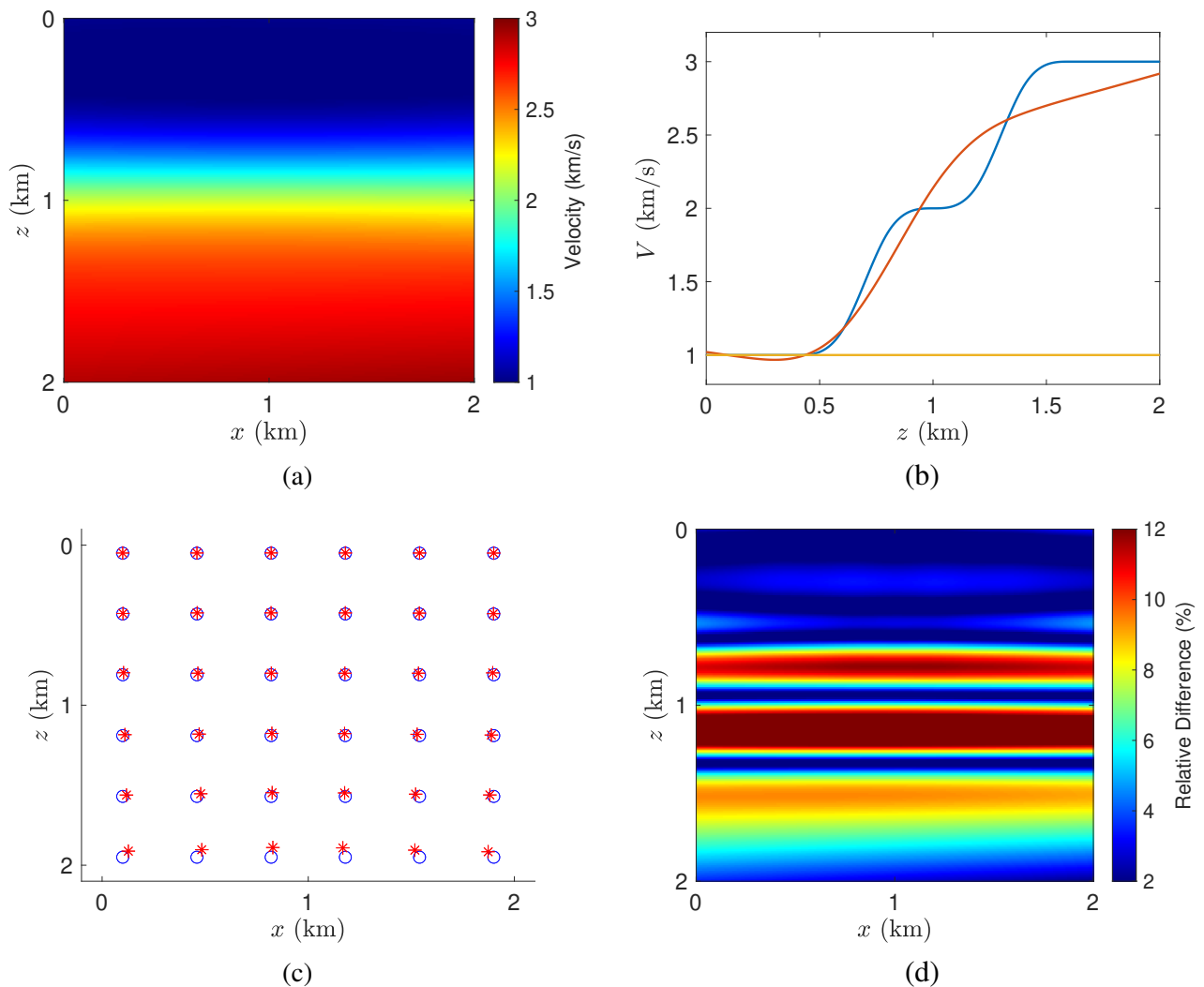
Figure 6.18: Three-layer test with 36 data samples. (a) Stereotomography nverted velocity model. (b) Vertical slices of inverted (red) and true (blue) velocity models. Slices were taken at the middle of the models. (c) Inverted model depth positions (red) and true data depth positions (blue). (d) Percentage difference between inverted and true velocity models.

6.3 Laterally Heterogeneous Model Test

In this section, stereotomography method will be tested on a synthetic laterally heterogeneous model. In fact, the method has already been tested in laterally heterogeneous models during validation tests. However, the model that will be used in this section presents a kind of higher level of heterogeneity, both in vertical and horizontal directions. It is described in a grid of $3\text{km} \times 4\text{km}$, which is a bigger grid than the ones used in previous tests.

The main objective of this section is to analyse how stereotomography method can constrain a more complex velocity model by improving the quality and quantity of both input-data information and initial velocity model, which represent internal information for tomography problem. Thus, differently of what has been made in previous sections, the focus won't be at the level of regularization.

The proposed laterally heterogeneous model is illustrated in Figure 6.19. Velocity model presents high levels of heterogeneity in both directions. Note the presence of a region of higher velocity at the bottom of the model. Models that presents this type of characteristics are famous to be difficult to be inverted by tomography methods (see, e.g, Billette and Lambaré (1998), Neckludov et al. (2006)).
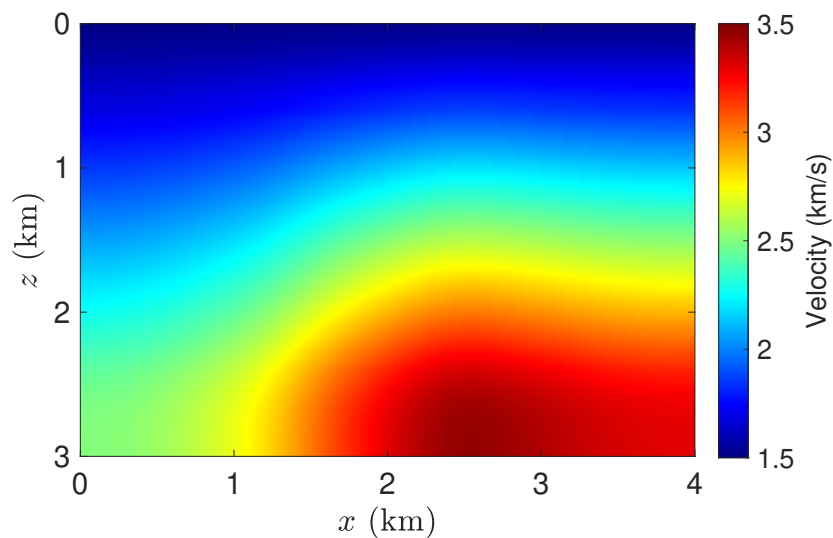
Figure 6.19: Laterally heterogeneous model test. Velocity model presents heterogeneity in both directions. Note the presence of a region of high velocity at the bottom of the model.

To build the proposed velocity model test, B-spline interpolation was applied. To this issue, interpolation knots were spaced with an horizontal distance of 0.4km and a vertical distance of 0.3km through the grid. Therefore, the model illustrated in Figure 6.19 presents the necessary smoothness

to perform ray-tracing. Also, with respect to interpolation issues, the model test can be perfectly recovered, since the same number of interpolation knots, positioned at the same places, will be used by the inverse process to construct stereotomography velocity models. A homogeneous initial velocity model, Figure 6.20, will be used used in a first test.
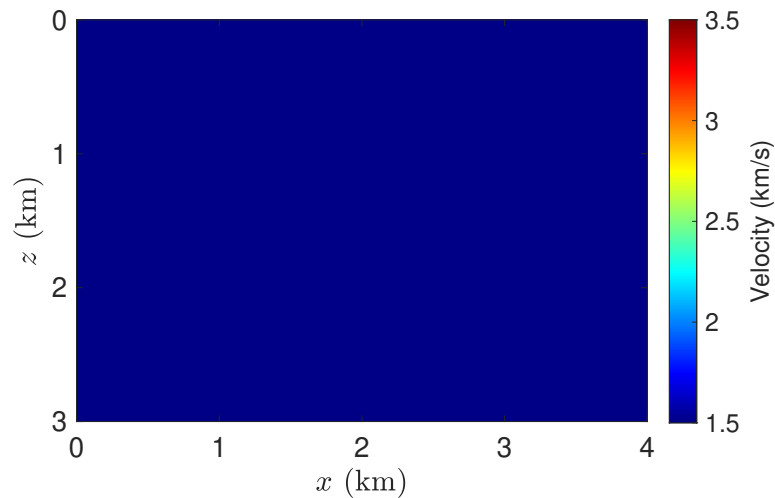
Figure 6.20: Initial homogeneous velocity model used for stereotomography first try on lateral heteregenous test.

For this test, input data and model spaces and initial parameters were set as follows:

Input observed-data space: To generate observed-data space, 121 positions in depth were displayed thought the model (see Figure 6.21). These positions play the role of the hypothetical localizations of primary reflection/diffraction events for this synthetic experiment. From these positions, two rays were propagated to surface line, with initial double aperture, with respect to vertical direction, of $30°$. In surface line, kinematic parameters of emergence positions, slopes and traveltime were computed, providing 121 data samples that compose the observed-data space. Despite numerical errors and theorical approximations, observed-data space is composed by perfect accurate data.

Initial model space: At first try, initial velocity model is a homogeneous velocity model of 1.5km/s. The initial velocity model is illustrated by Figure 6.20. Through stereotomography inverse process, velocity models are constructed under the same number and positions of knots used to build the true velocity model test. Ray-model space was initialized with the proposed initialization procedure for stereotomography in this thesis (see Chapter 3), which returned 121 ray-model samples, each of them composed by one depth-model position, two model slopes and two model traveltimes. Each model

sample is related to the respective sample of observed-data space. Figure 6.21 exhibits initial model positions returned by the initialization step under the initial homogeneous velocity model of 1.5km/s.

(a)   (b)
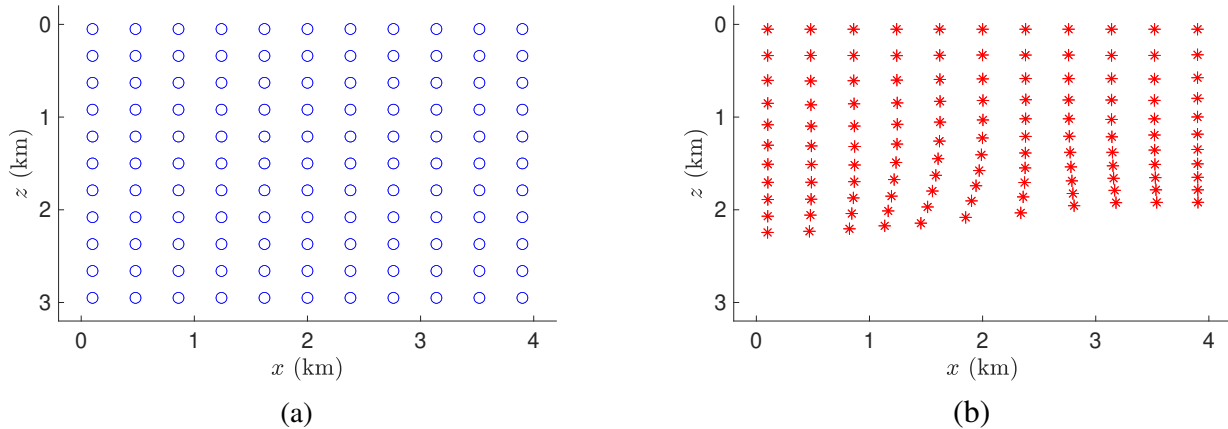
Figure 6.21: Laterally heterogeneous model test. (a) Data depth positions used to generate observed-data space components by means of ray-tracing. (b) Initial model positions returned by initialization step under the initial homogeneous velocity model of 1.5km/s.

The solution proposed by stereotomography will be presented by subsequent attempts. Each subsequent attempt (try) will be performed considering improvements in initial velocity model or increasing the size of input observed-data space. The objective is to show how the quality of stereotomography final velocity model can be increased by providing better and more initial/input information.

First try - Discussion about initial regularization parameter and two initial tests: By the use of the parametrization and initial boundary conditions mentioned before, two model solutions proposed by stereotomography are exhibited in Figure 6.22. Obviously, none of the proposed final velocity models resemble the true velocity model. The top figure represents stereotomography inverted velocity model obtained under an initial weight regularization parameter λ set in order to put the relation between regularization term, with respect to original stereotomography objective function, to a value of 10^{-2} at the first iteration. The middle figure represents the inverted velocity model obtained under an initial weight regularization parameter λ set in order to put the relation between regularization term, with respect to original stereotomography objective function, to a value of 10^{-4} at the first iteration. Note the effect of the regularization parameter on the main aspects of the velocity model. The more regularized one presents almost a linear vertical variation, since the minimization of second derivatives does not allow higher velocity variations. The less regularized one is not constrained neither by the information provided from observed-data space, nor by the regularization term.
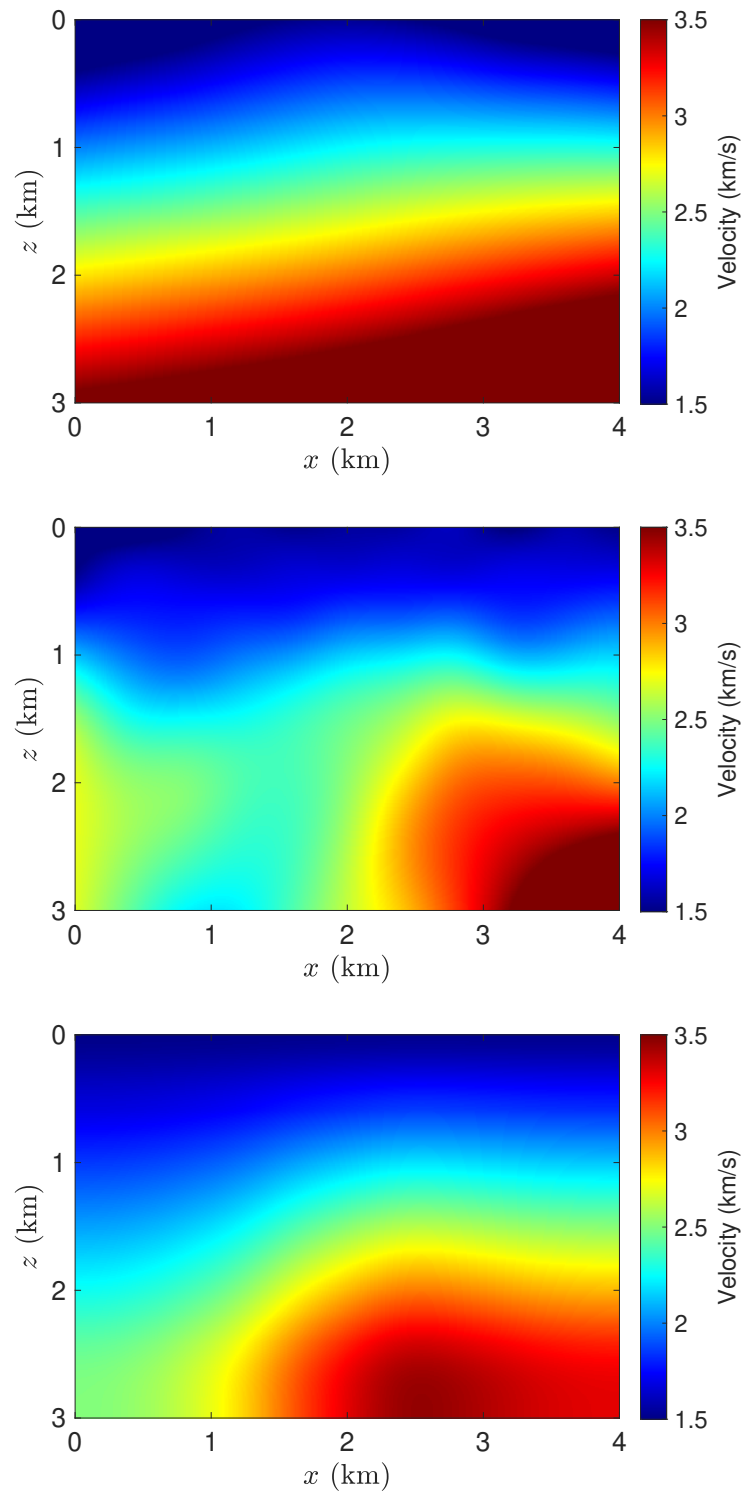
Figure 6.22: Laterally heterogeneous model test - First try. Top: Stereotomography inverted velocity model with higher level of initial regularization. Middle: Stereotomography inverted velocity model with lower level of initial regularization. Bottom: laterally heterogeneous model test.

So far, what has been done in all previous tests to derive a reasonable final velocity model solution is to find some kind of an optimum value for initial regularization parameter λ that helps to constrain the model. Besides the fact that it is an expensive task, since a lot of tomographic inverse process have to be performed, it is a way to constrain the model by means of external information. In this section, it will be analysed how the proposed model test can be constrained by providing more and better internal information, keeping the level of initial regularization invariant. The more and better internal information account for improving both the quality of initial velocity model and the amount of input data components given to the inverse process. The case of the less regularized velocity model of Figure 6.22 (middle figure) will be adopted. So far, it is only a meaningless velocity model. Keeping the initial level of regularization constant, it will be shown how improvements of the quality of the inverted velocity model is possible by means of better internal information.

Second try: The second try consists in chaging initial velocity model. The initial regularization level applied is the same one used in less regularized case in first try (see Figure 6.22). Previously, the initial velocity model used in first try was a homogeneous velocity model of 1.5km/s. This velocity does not resembles at all the true velocity model. Therefore, a better initial velocity model will be provided now to stereotomography second try. This new initial velocity model consists in a velocity model described by a linear variation in vertical direction. It starts from 1.5km/s at surface line and linearly increases until 2.5km/s at the bottom line. The new initial velocity model, as well as the new initial model depth positions returned by initialization step, are illustrated in Figure 6.23. Note how the initial model positions are better localized because of the use of a better initial velocity model.

(a)   (b)
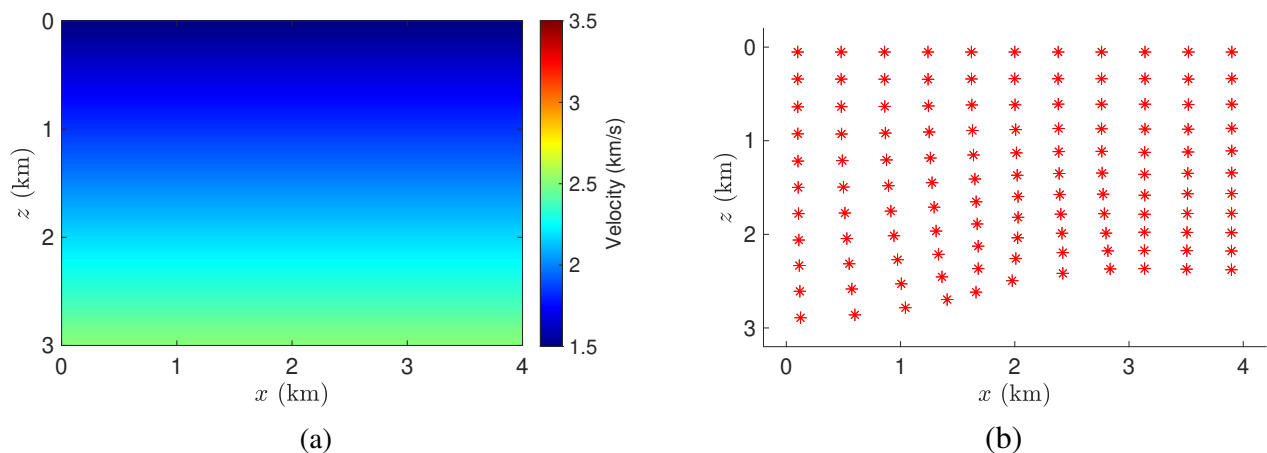
Figure 6.23: Laterally Heterogeneous Model - Second Try. (a) New initial velocity model described by a constant vertical variation in vertical direction. (b) Initial positions provided by initialization step under the use of new initial velocity model.

With the introduction of a better initial velocity model, stereotomography method returned the final velocity model illustrated in Figure 6.24. True laterally heterogeneous velocity model test was displayed again to turn comparisons easier. The quality improvement when compared to previous solution presented in first try is notable. Outside the bottom area, most of the relative errors fall under 2%. Also, until 2km in depth, all inverted model positions (Figure 6.25) are quite correct. Only at most deepest areas, errors are evident. It is an expected feature, due to the less number of information available in this area.

It is remarkable how the solution has changed, from a meaningless velocity model, to a reasonably good one, just by the introduction of a better velocity model. However, more can be done in order to improve the quality of stereotomography result if more input-data information is provided. This will be done in the following third try.

Third try: The third try consists in increasing the number of input-data information provided to the inverse process. In other words, a bigger data space will be provided. In first and second try, 121 data samples were provided as input for inverse process. However, this number can be considered small, due to the complexity and size of the true model test. In third try, 256 data samples will be provided. Once again, they are generated by ray-propagation of rays starting at 256 data depth positions, with initial double aperture, with respect to vertical direction, of $30°$. The new data positions, as well as new initial model positions, are illustrated in Figure 6.26. Due to the correspondence between observed data samples and model data samples, initial model positions almost cover all areas of velocity model. This is an important feature for tomographic inversion aspects. The same initial velocity model of second try was be used (Figure 6.23).

Stereotomography final velocity model for third try is illustrated in Figure 6.27. The inverted velocity model was noted improved by the use of a bigger input-data space. Now, just two regions at the bottom area presents relative errors bigger than 2%. Between these two regions, one of them is situated in the border of bottom area, where practically no input data information is available. The other region is the high velocity area, which is a classical problem to tomographic inverse problems, mainly when it is localized near the bottom of the model. Except by these two regions, almost all contour velocity lines are similar between true and inverted velocity models. Furthermore, inverted final model depth positions (Figure 6.28) are quite good.

The present laterally heterogeneous model test showed how it is possible to significantly increase the quality of stereotomography inverted model by providing more and better input information and initial conditions to the problem. The initial level for regularization term was kept initially constant for all of the tries performed. With this strategy, it was possible to improve the proposed
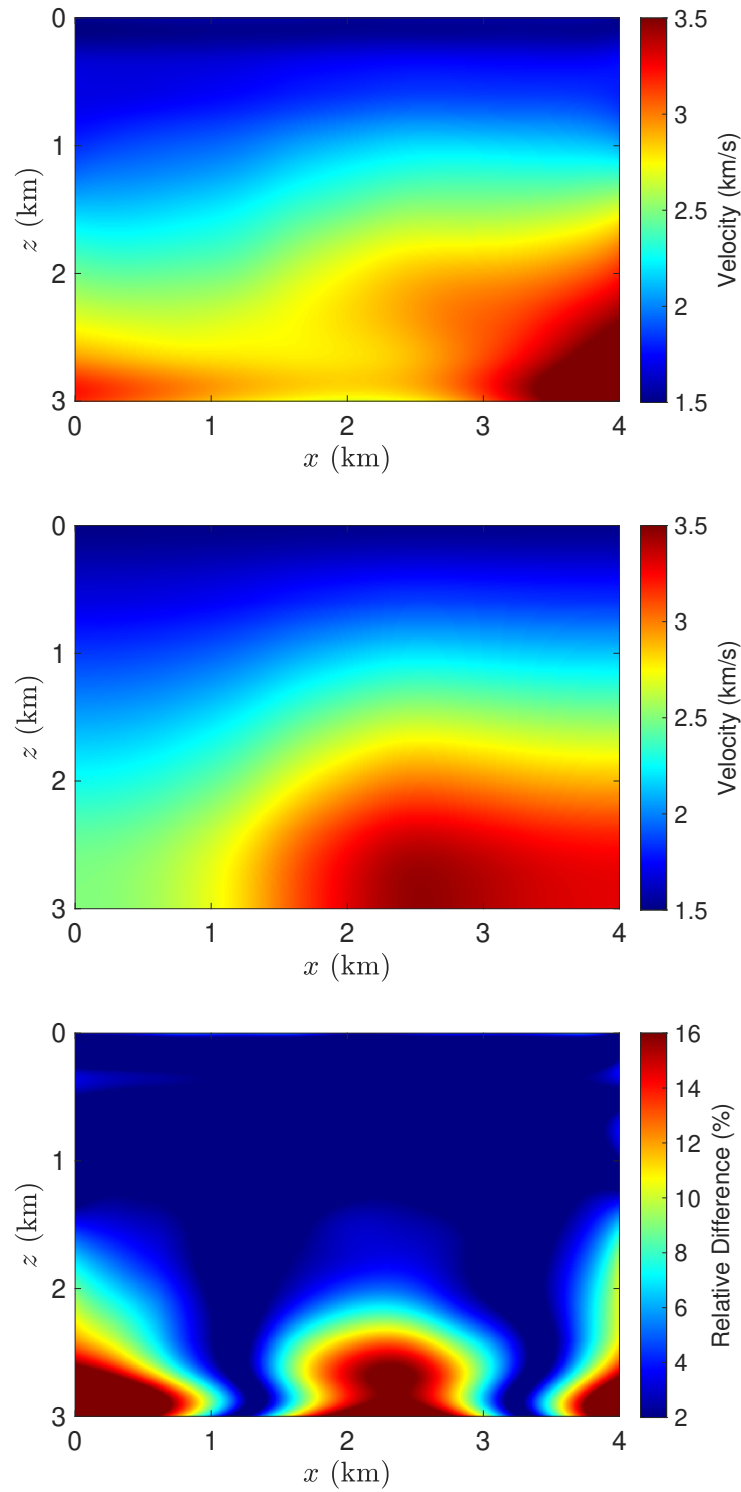
Figure 6.24: Laterally heterogeneous model test - Second try. Top: Inverted velocity model. Middle: True velocity model test. Bottom: Percentage difference between inverted and true velocity models.
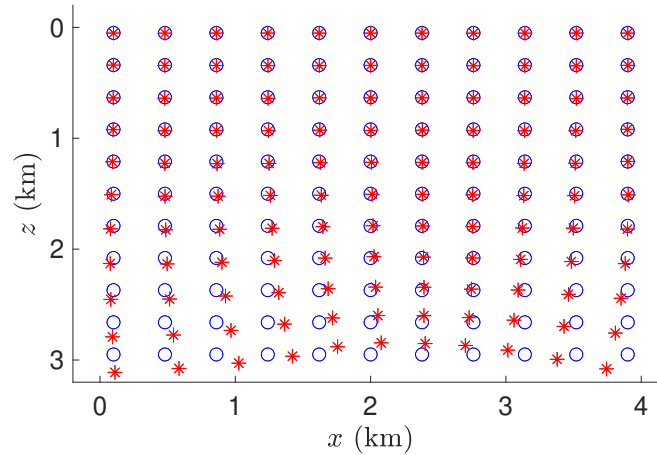
Figure 6.25: Laterally heterogeneous model test - Second try. Inverted model positions (red) and true data positions (blue).
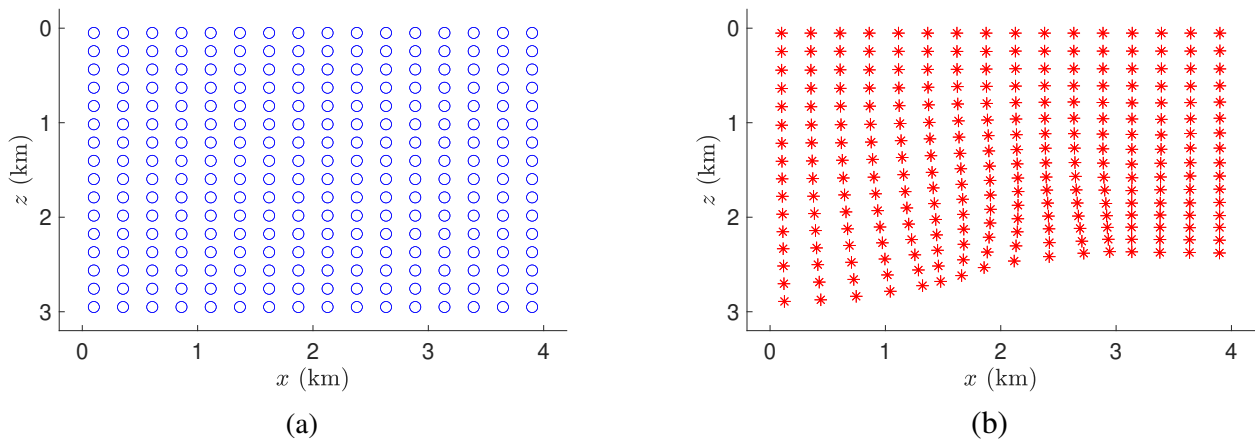
Figure 6.26: Laterally Heterogeneous Model - Third Try. (a) Data positions. (b) Initial positions provided by initialization step under the use of initial velocity model of second try (Figure 6.23). Initial model depth positions cover almost all areas of the velocity model.
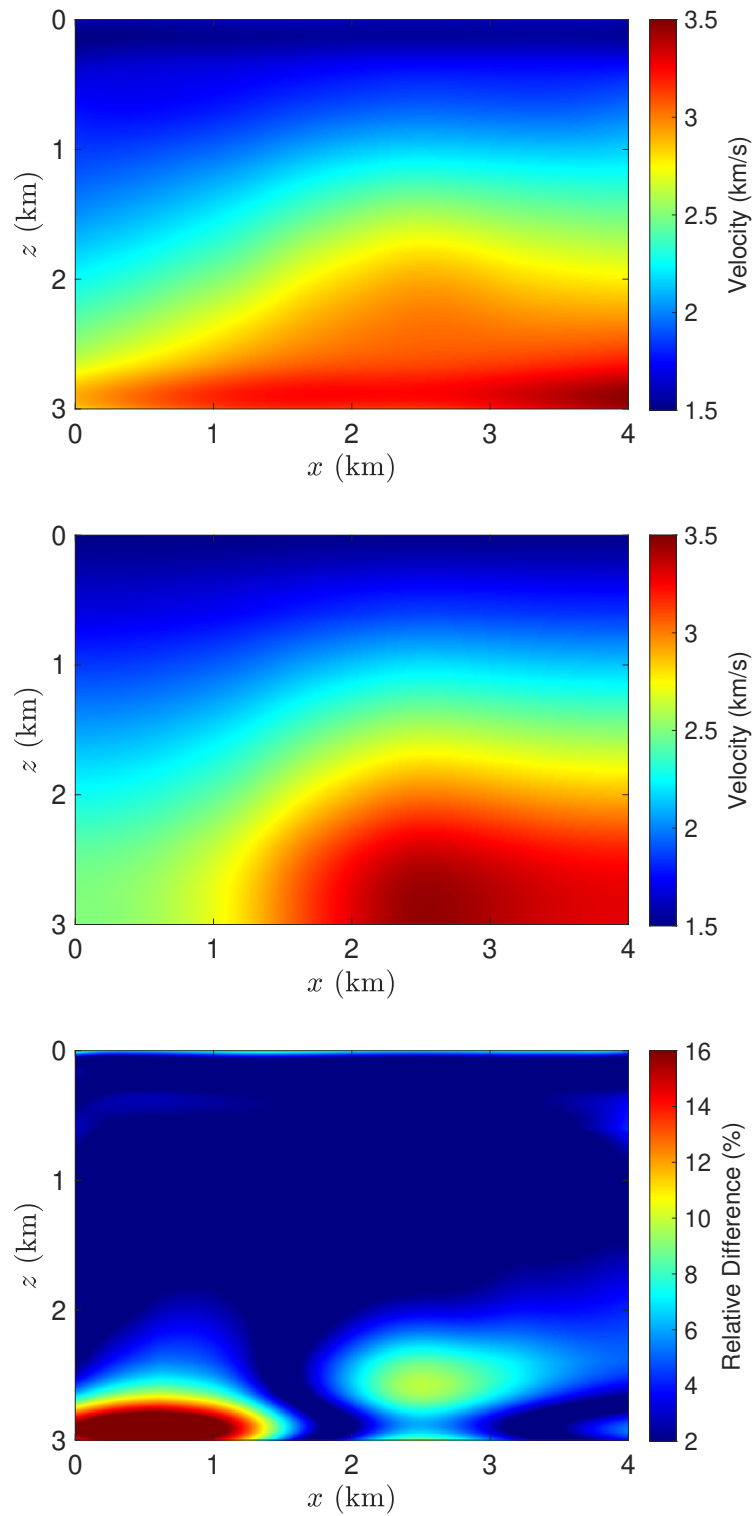
Figure 6.27: Laterally heterogeneous model test - Third try. Top: Inverted velocity model. Middle: True velocity model test. Bottom: Percentage difference between inverted and true velocity models.
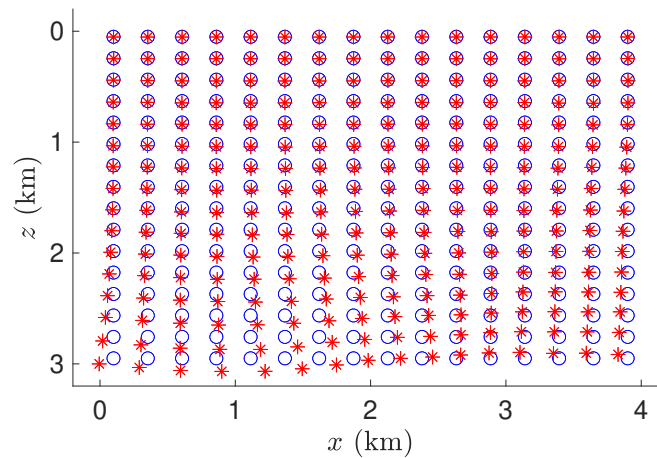
Figure 6.28: Laterally heterogeneous model test - Third try. Inverted model positions (red) and true data positions (blue).

stereotomography inverted velocity model, from a meaningless velocity model (first try), to a very good proposed solution (third try). It is possible to say that providing more number of input data samples and also a better initial velocity model, worked as a internal regularization to the problem, in the sense that it brought stability to the inverse process. The first initial inverted model, which was meaningless, resulting of an unstable inverse process, could be transformed into a very good model solution. In this case, more internal information were provided, which turned the task of constrain the model easier. Similar strategy will be applied in next section. However, it will be done in a more famous synthetic data set.

6.4   Soft Marmousi Test

The 2D Marmousi model have been widely used to test different velocity model building techniques. The difficulties arise from a high complex model structure. For seismic tomography methods of this thesis and ray propagation purposes, Marmousi model is an intractable model. In this section, the approach used in Billette et al. (2003) will be followed, and a smooth version of the original Marmousi model will be considered. The smooth version of Marmousi model, namely soft Marmousi, is illustrated in Figure 6.29. As it was done in previous section, stereotomography method will be applied in subsequent tries, always improving some aspect related to quantity or quality of initial data and or initial model information given to stereotomography inverse problem. Once again, it will be clear how these features may be used to constrain the proposed model.
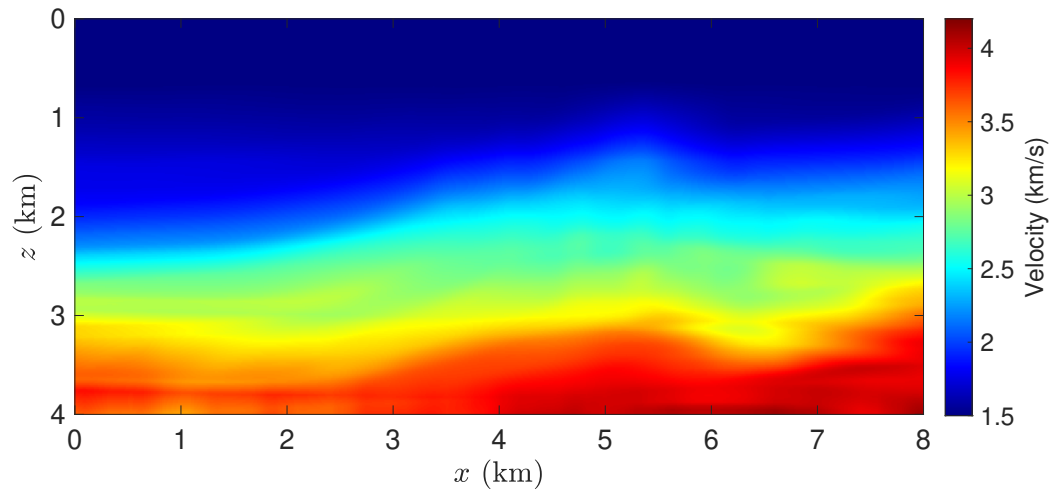
Figure 6.29: Soft Marmousi model.

For the first try, input data and model spaces and initial parameters were set as follows:

Input observed-data space: To generate observed-data space, at first try, 208 data depth positions were displayed through soft Marmousi model (see Figure 6.31). From each of these positions, a pair of rays were traced to surface line, with initial double aperture, with respect to vertical direction, of 40°. kinematic parameters of position, traveltime and slopes were computed at surface line. Therefore, 208 data samples were provided to observed-data space. Despite the fact that they were generated directly by ray-tracing, which results in perfect accurate data information, it can be consider a small number of input data. For comparisons, in Billette et al. (2003), more then three thousands data samples were applied. However, there, these samples were picked and estimated in slant stack panels.

Initial model space: Differently of what was done in last section, at first try, no homogeneous initial velocity model will be provided, in order to avoid the illustration of a first non-regularized try, where commonly meaningless velocity model is generated by tomographic inverse process. At first try, an initial velocity model described by a linear velocity variation in vertical direction will be used. Initial velocity model is illustrated by Figure 6.30. It starts from 1.5km/s at surface line and grows until the value of 3km/s at bottom line. Through iterations, velocity models will be constructed by B-spline interpolation with knots distributed with vertical spacement of 0.4km and horizontal spacement of 0.5km. Differently of last tests, true velocity model, the soft Marmousi model, was not constructed by means of B-spline interpolation. It was generated by a smoothing average operator applied to original Marmousi model (see Chapter 9 for more details). Therefore, it is not previously known if B-spline interpolation is capable to perfectly construct soft Marmousi velocity model. Thus,
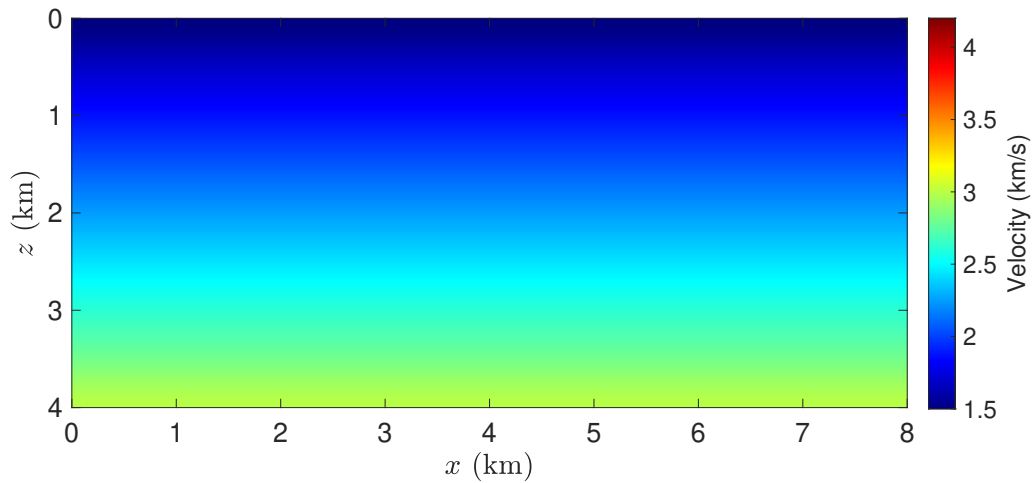
Figure 6.30: Soft Marmousi test - First try. Initial velocity model.

another difficult is presented to stereotomography inverse process. Initial ray-model components were generated by the initialization procedure proposed in this thesis in chapter 3, returning 208 initial ray-model samples, each of them composed by one initial model depth position, two model slopes and two model traveltimes. Initial model-depth positions provided by initialization step under the use of the proposed initial velocity model are illustrated in Figure 6.31.

Initial regularization weight parameter: For this test, λ was set in order to, at first iteration, the relation between the regularization term with respect to the objective function would be 5.10^{-5}. Moreover, $\epsilon_{zz} = 10^{-2}$, $\epsilon_{xx} = 1$ and $\epsilon_{vv} = 10^{-4}$ were set to calibrate regularization term. This values will be the same for all the tries performed for stereotomography soft Marmousi test.

First try results: The results obtained by first try are illustrated in Figure 6.32. As it can be noted, it is not a bad result at all. Even considering the small number of input data provided to first try, the shallower half of the model, except for some details, already exhibits the main characteristics of the true model, the soft Marmousi. The deeper half of the model demands some adjusts to reasonably describe the true velocity model. Final model depth positions are illustrated in Figure 6.33.

Second try: The second try consists in improving the number of data samples provided to the method. Now, 357 data positions are displayed through the model, from where a pair of rays will be traced from each of these points to surface line. At surface line, the kinematic parameters of positions, slopes and traveltime are computed, providing 357 data samples. Note, again, that this number of samples is still a considerable small number of input data, since it is still approximately 10% of the
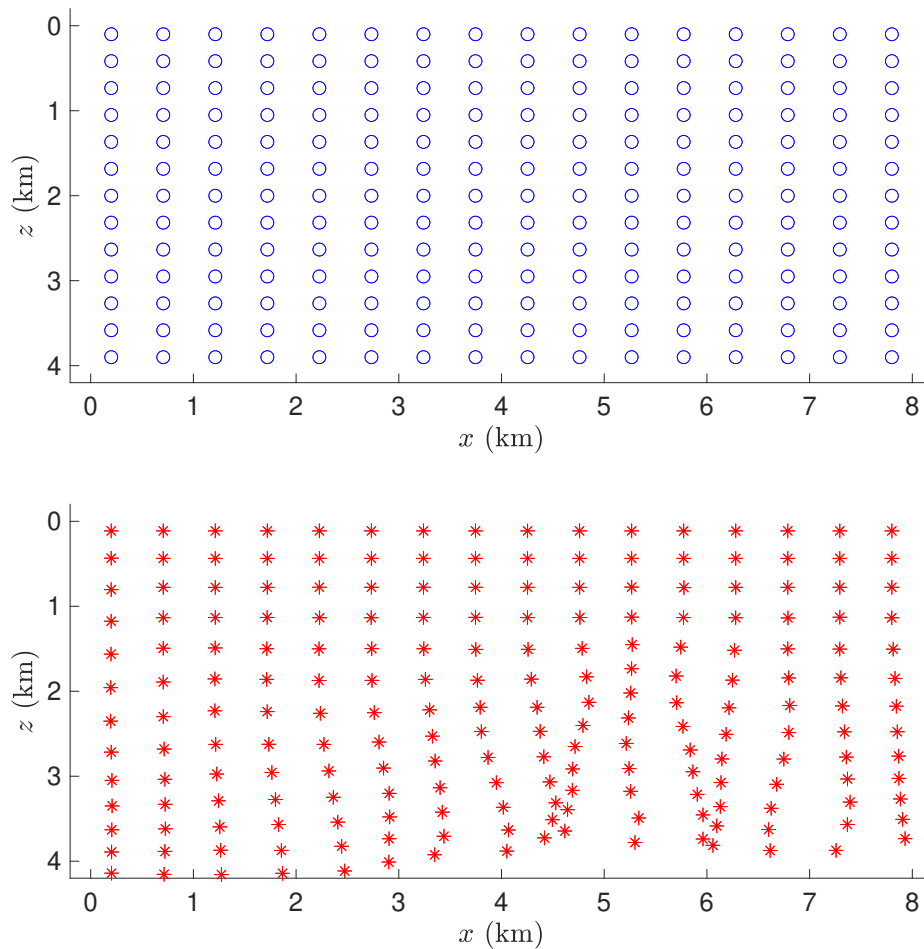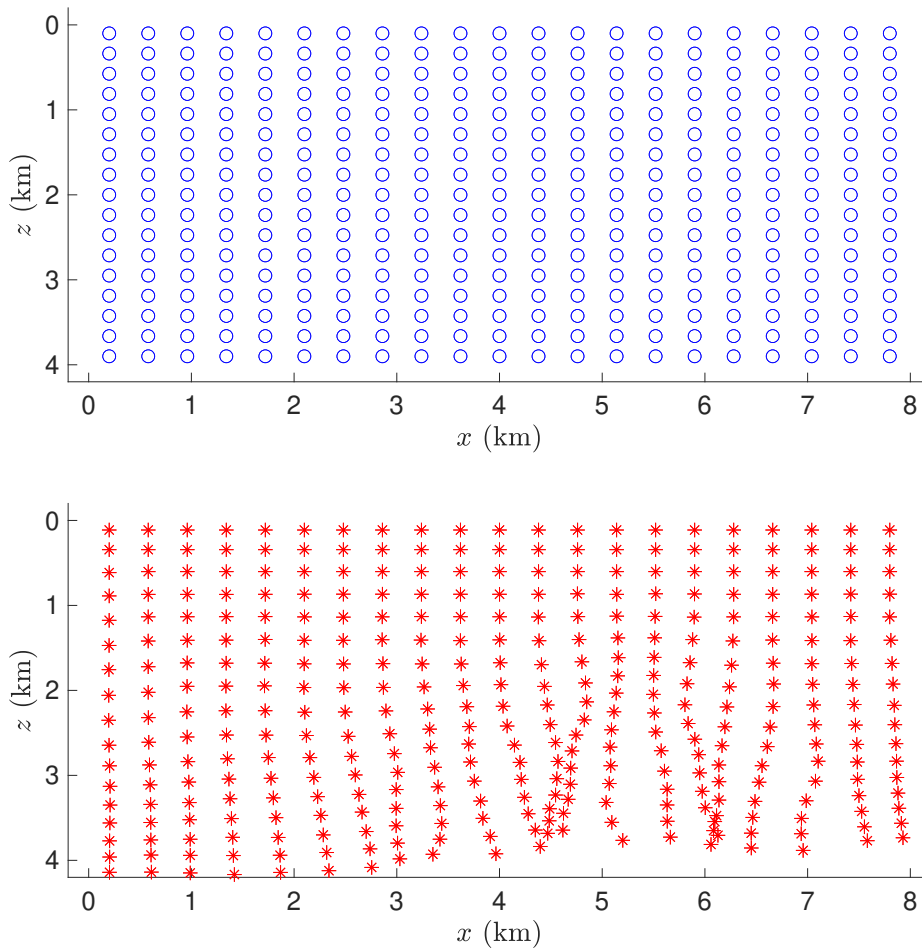
Figure 6.31: Soft Marmousi test - First try. Top: Data positions. Bottom: Initial model positions returned by initialization step under initial velocity model of Figure 6.30.

amount applied in Billette et al. (2003). Other aspects of first try are kept the same. The distribution of new data positions, and consequent new initial model positions, are illustrated in Figure 6.34.

Second try results: The results obtained by second try are exhibited in Figure 6.35. The improvements on the quality of stereotomography final model are easily noted. Providing more input data to the inverse problem turned possible a better resolution of the deeper half of the model. Note how most of the model depth positions were correctly inverted (Figure 6.36). Once again, it could be showed how providing more and better input information acts as a kind of internal regularization, assisting the inverse problem to constrain the model. The second try already exhibits an inverted model of good quality. For comparisons, it recovered more details of true velocity model then those reported in Billette et al. (2003), even with the considerably smaller number of data provided. However, here the
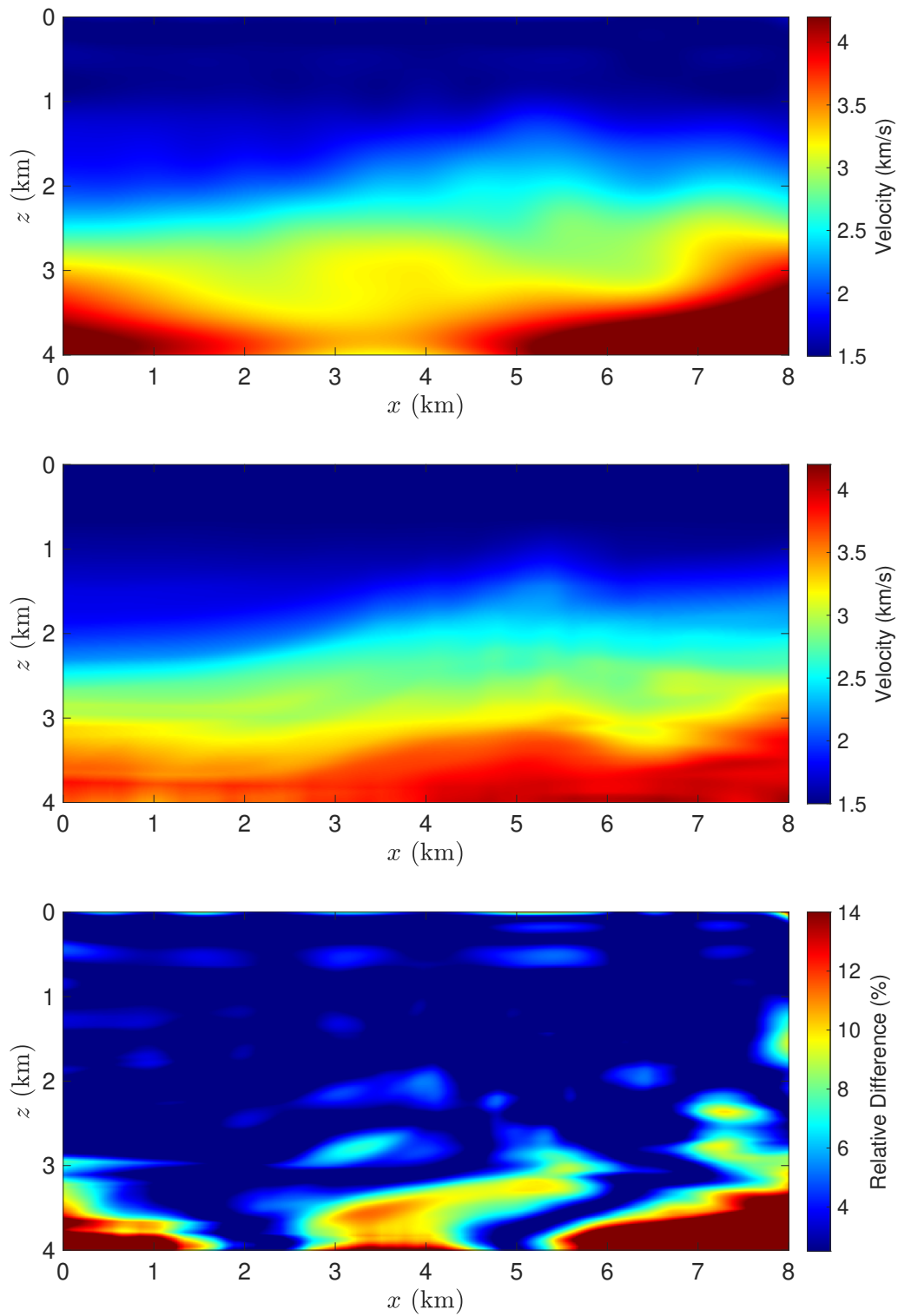
Figure 6.32: Soft Marmousi test - First try. Top: Inverted velocity model. Middle: True velocity model test - Soft Marmousi. Bottom: Percentage difference between inverted and true velocity models.
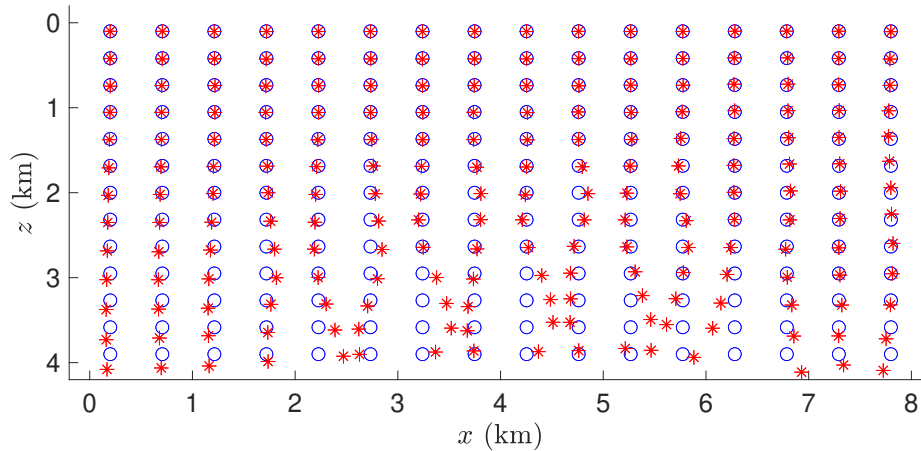
Figure 6.33: Soft Marmousi test - First try. Inverted model positions (red) and true data positions (blue).

input data was perfectly accurate and related to depth positions (primary reflection/diffraction events) almost uniformly distribution through the model, which helps, a lot, the inverse process. To recover more details of the model, the present result of second try could be used, for instance, as an input for full waveform inversion method. This strategy will be done in chapter 9, but CRP tomography velocity model will be provided as input for FWI.

The last result could be continuously slightly improved with the introduction of more data points or even better velocity initial models. However, the objective of this section has already been showed. Other strategy to provide even better velocity models is the search of the optimum value of initial regularization parameter, keeping constant the other features of inverse problem. Therefore, it is probable that, keeping the same features applied to performed tests, a better solution could be found by searching an optimum value of initial regularization parameter. Remind that, as the all tomographic methods are naturally unstable, this parameter plays a fundamental role in the inverse process. However, the process of searching an optimum value to initial regularization parameter is another optimization problem, which is not the focus of this thesis. Furthermore, the search of a good initial value for initial regularization parameter is too expensive, since it could accounts for many tomographic inverse process. Thus, this thesis focus in another strategy to assit the constrain of the models by providing a kind of "internal" regularization to tomographic inverse process. This could be done, as has been showed, by improving both quality and quantity of initial information given to the inverse process. In next chapter, a new slope tomographic method will be proposed, which enhance the regularization of the problem by using more and better internal information, the common-reflection-point information.

Figure 6.34: Soft Marmousi Test - Second Try. Top: Data positions. Bottom: Initial model positions returned by initialization step under the use the same initial velocity model of first try (Figure 6.30).
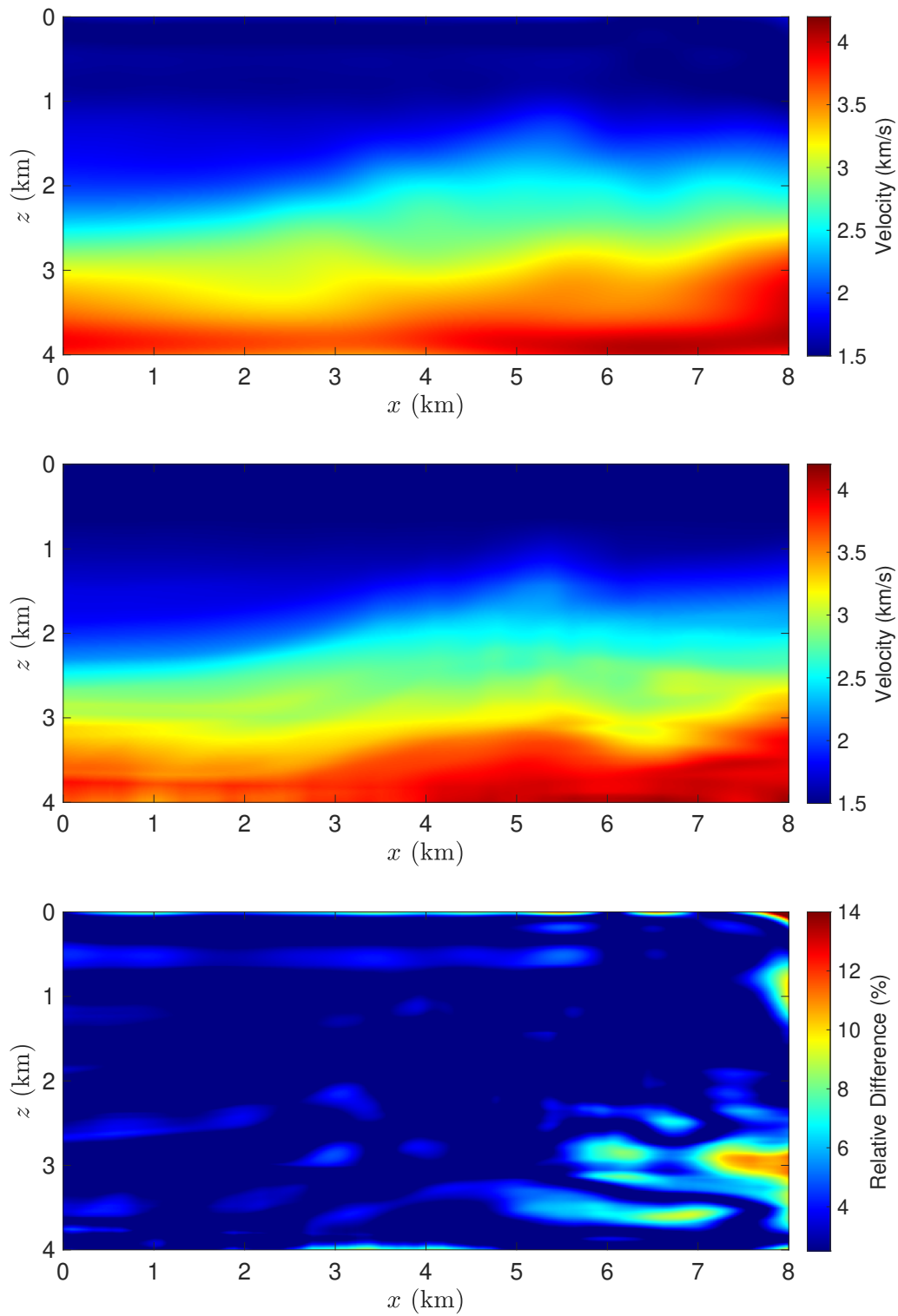
Figure 6.35: Soft Marmousi test - Second try. Top: Inverted velocity model. Middle: True velocity model test - Soft Marmousi. Bottom: Percentage difference between inverted and true velocity models.
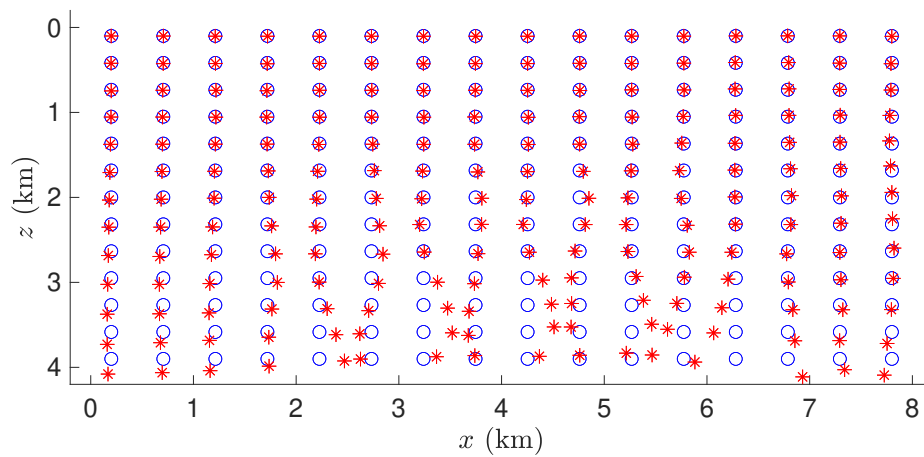
Figure 6.36: Soft Marmousi test - Second try. Inverted model positions (red) and true data positions (blue).

Chapter 7

Synthetic tests for CRP tomography

7.1   Validation Tests

CRP tomography, the main contribution of this thesis for seismic tomography research, was fully implemented during phd period. All features of the inversion method were derived from actual implementations. That included all schemes employed for ray tracing, B-spline interpolations, mathematical methods to solve ill-conditioned linear systems, initialization procedure and regularization. In order to test CRP tomography implementation, the method was tested by the same set of validation tests used to validate stereotomography and NIP wave tomography implementations. As CRP tomography is a brand new method, these tests works, also, as a first validation set of tests for the technique. In order to be a promising method, it has, at least, to solve the simple problems already solved by other standard methods.

Being the same tests applied to validate previous implementations, the following velocity model tests will be used to validate CRP tomography:

1. Model with trigonometric variation in vertical direction.

2. Model with linear variation in vertical direction.

3. Model with quadratic variation in vertical direction.

4. Model with linear variation in horizontal direction.

5. Model with linear variation in horizontal direction and quadratic variation in vertical direction.

In order to be fair and compare results provided by all tomographic methods, the same parametrization used in previous chapter for stereotomography validation tests will be kept. Therefore, for CRP tomography validation tests, input data and model spaces and initial parameters were set as follows:

Input observed-data space: To generate data space, 49 positions (common-depth points) were uniformly distributed in depth through the model. These positions are exactly the same used for stereotomography validation tests. These positions play the role of hypothetical localization of primary reflection or diffraction events for these synthetic experiments. Therefore, for comparison reasons, these tests simulate the results that would be obtained by both tomography methods under the same number of pickings. From theses positions, five pairs of rays were propagated to surface directions, with double aperture, with respect to vertical direction, varying from $10°$ to $40°$. In further tests, more pairs of rays will be propagated from each data common-depth-point. In surface line, the kinematic parameters of emergence positions, slopes and traveltimes were computed. All traveltimes computed by rays starting from the same common-depth-position were summed. Therefore, data space is composed by 49 families (gathers), each of them with one data total traveltime and five samples composed by two data positions and two data slopes parameters. As the components of data space were computed directly by ray-tracing performed at the true velocity model test, despite numerical errors and theoretical approximations, observed-data space is composed by perfect accurate data components. Moreover, the uniform distribution of positions in depth guarantees that all regions of the velocity model are covered by informations in observed-data space.

Initial model space: All initial velocity model spaces for validation tests were set as a homogeneous velocity model of 1km/s. The exception is, once again, the initial velocity model of fourth validation test, where an initial homogeneous velocity model of 1.5km/s was considered. The B-spline interpolation knots were uniformly distributed through the model, with vertical and horizontal spacing of 0.4km. Its is exactly the same parametrization applied to build the true velocity model tests. Ray-model space was initialized with the proposed initialization procedure for CRP tomography (see Chapter 5). Therefore, the initialization procedure returned 49 samples of model families, each of them composed by an initial model position in depth and five pairs of initial model slopes.

Initial regularization weight parameter: The initial regularization weight parameter varies through the tests. This was necessary due the different types of velocity variations. For those where the velocity varies in a non-linear way, a smaller parameter was used. Again, some previous search was made in order to find reasonable initial values for initial regularization parameter. The parameter decreases

through iterations by the previously proposed heuristic in chapter 5. The same heuristic was applied to stereotomography tests.

Data a-priori matrix: For CRP tomography validation tests, a similar data a-priori matrix $\mathbf{W}$ described for stereotomography validation test was applied. Therefore, both tests were performed considering the same values of precisions for the different types of data kinematic parameters of CRP tomography. The interest reader can go back to chapter 6 for more details about these chosen values. As these values will be kept the same for all over the tests performed in this thesis, discussions about data-a-priori matrix will be omitted.

CRP tomography validation tests: The results obtained by CRP tomography are illustrated by Figures 7.1, 7.2, 7.3, 7.4, 7.5, 7.6, 7.7, 7.8, 7.9 and 7.10. The results exhibited are quite good. In fact, at almost all tests, the relative errors fall under 1%. Also, the vertical and horizontal slices of the CRP tomography inverted model almost fitted true velocity model tests. In the most challenger validation test, the one with quadratic variation in vertical direction and linear variation in horizontal direction, the final model provided by CRP tomography is slightly better then the one obtained by stereotomography. It is important to remind that initial velocity models used in all tests were simple constant velocity models. Also, just a few data common-depth-points, with just 5 pairs of rays related to each point, were used to generate input observed-data space. Results could be even better if at least one of these conditions was improved.

By the results exhibited, the implementation of CRP tomography method was approved by proposed validation tests. In next sections, other synthetic tests that have already been presented in this thesis will be proposed for new CRP tomography method.
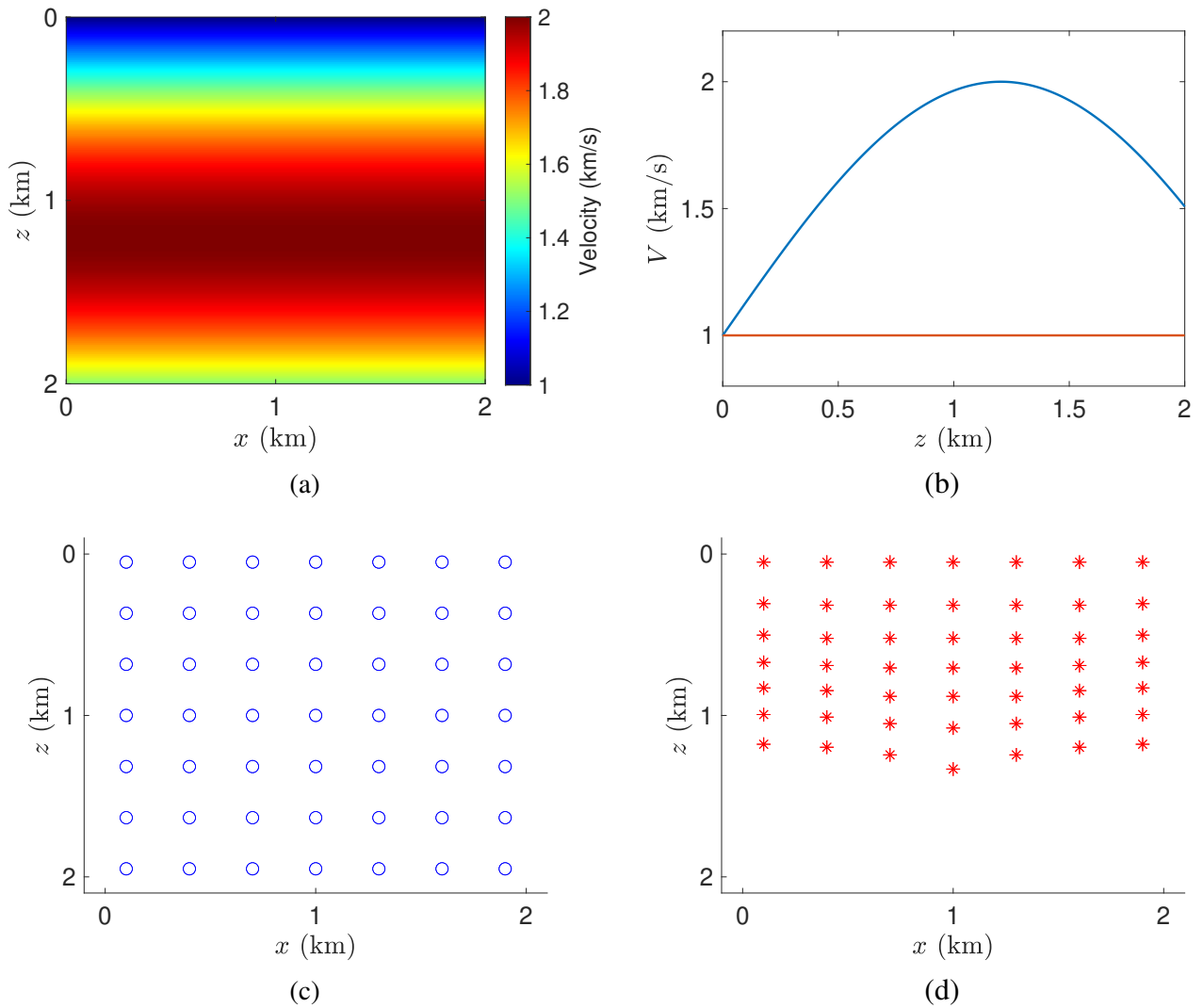
Figure 7.1: First validation test: model with trigonometric variation in vertical direction. (a) True velocity model for first validation test. (b) Vertical slices of initial (red) and true (blue) velocity models. Slices were taken at the middle of the models. (c) Data positions. Observed-data space is composed by kinematic parameters computed by a series of dynamic-ray tracing starting at these positions. (d) Initial model positions of ray-model space returned by initialization process.
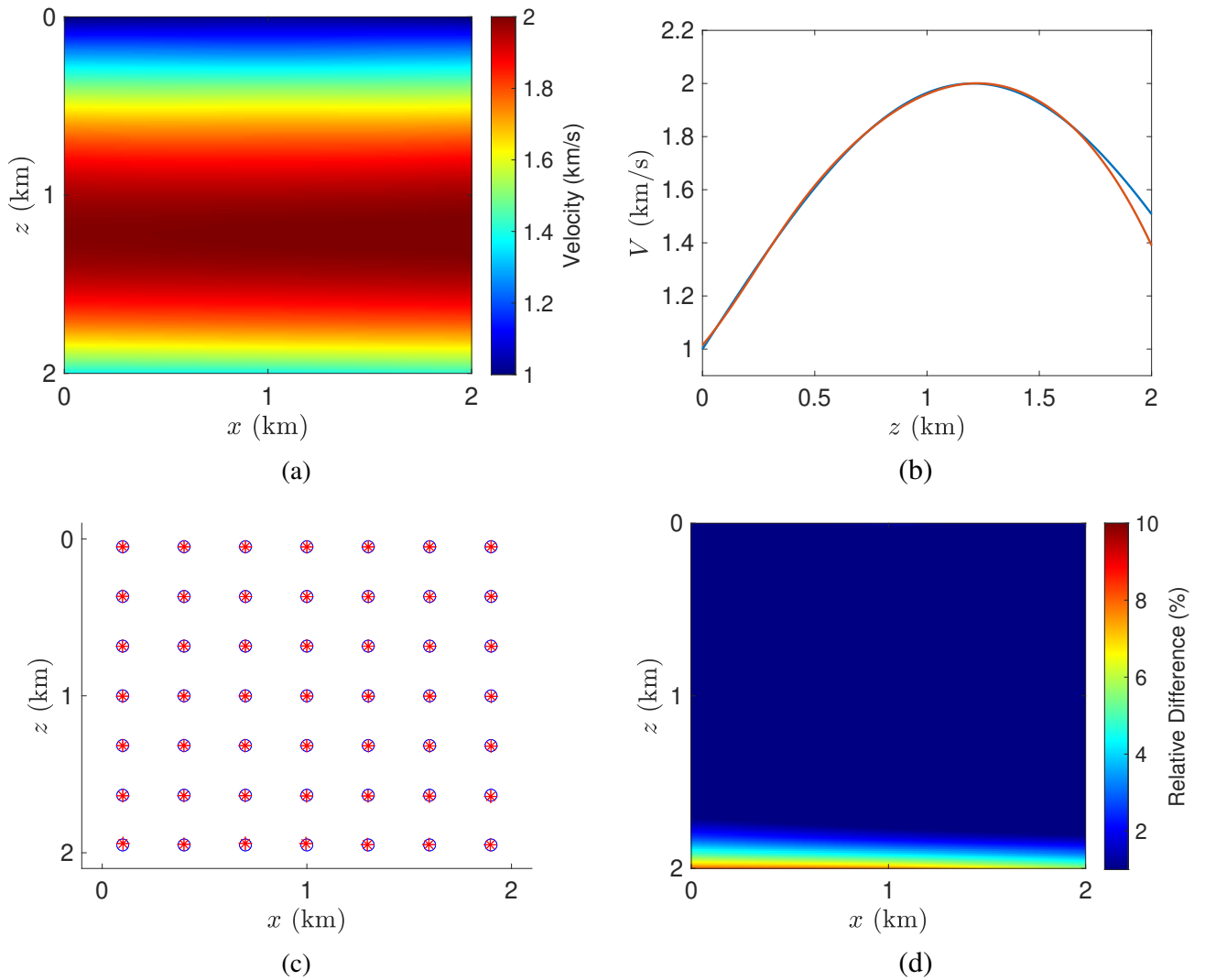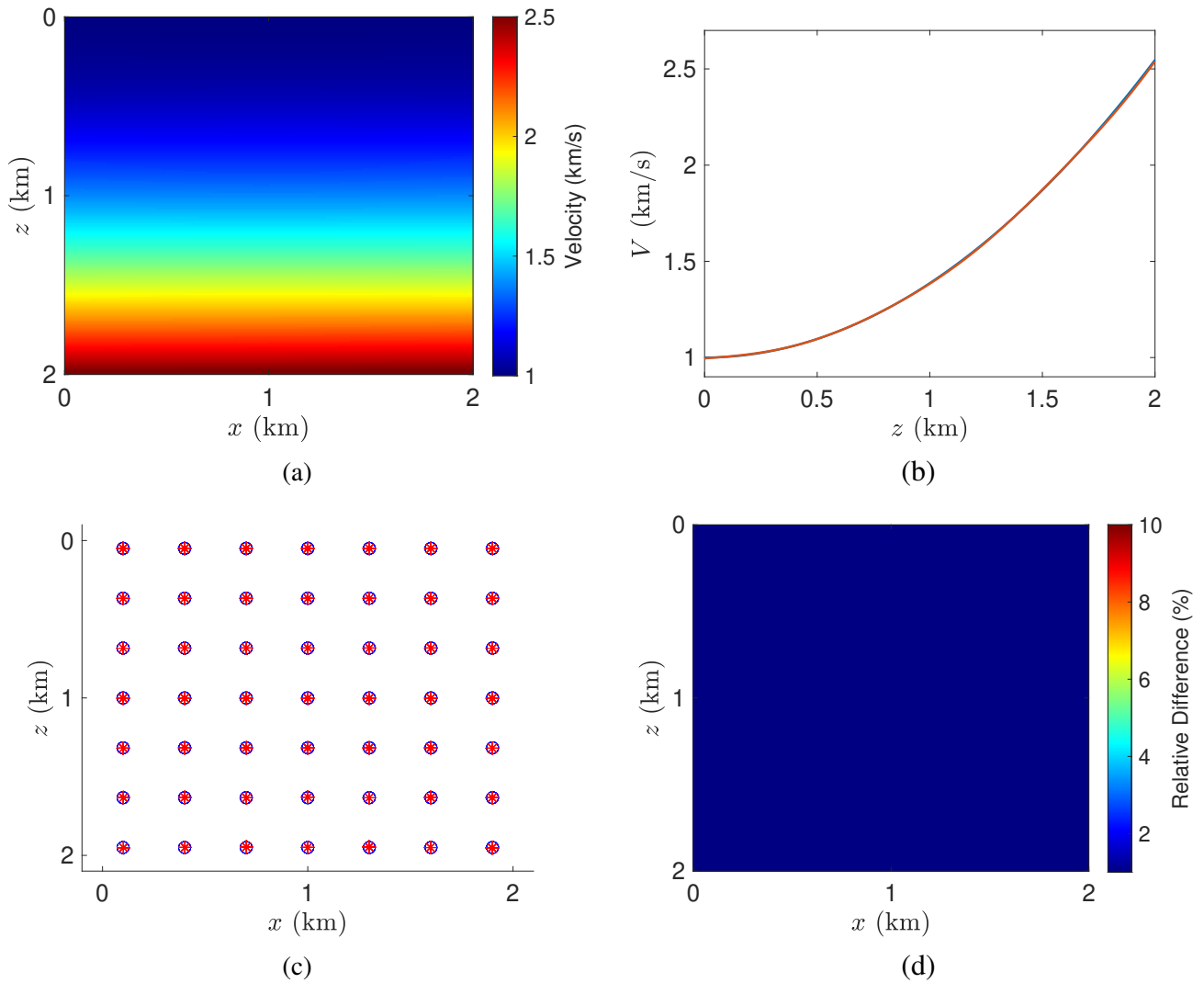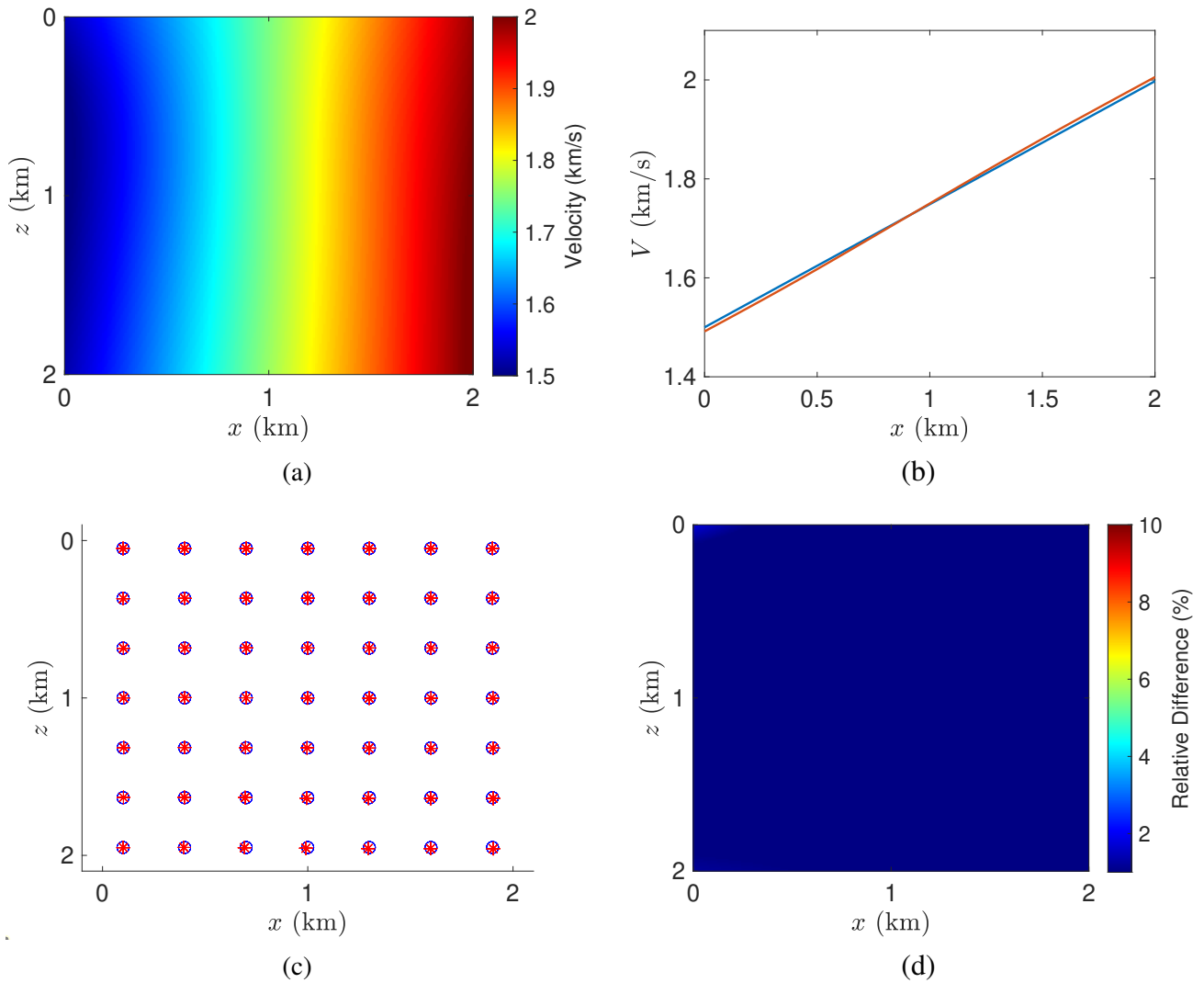
Figure 7.2: CRP tomography final result for first validation test. (a) Inverted velocity model. (b) Vertical slices of inverted (red) and true (blues) velocity models. Slices were taken at the middle of the models. (c) Inverted model (red) positions and true data (blue) positions. (d) Percentage difference between inverted and true velocity models.
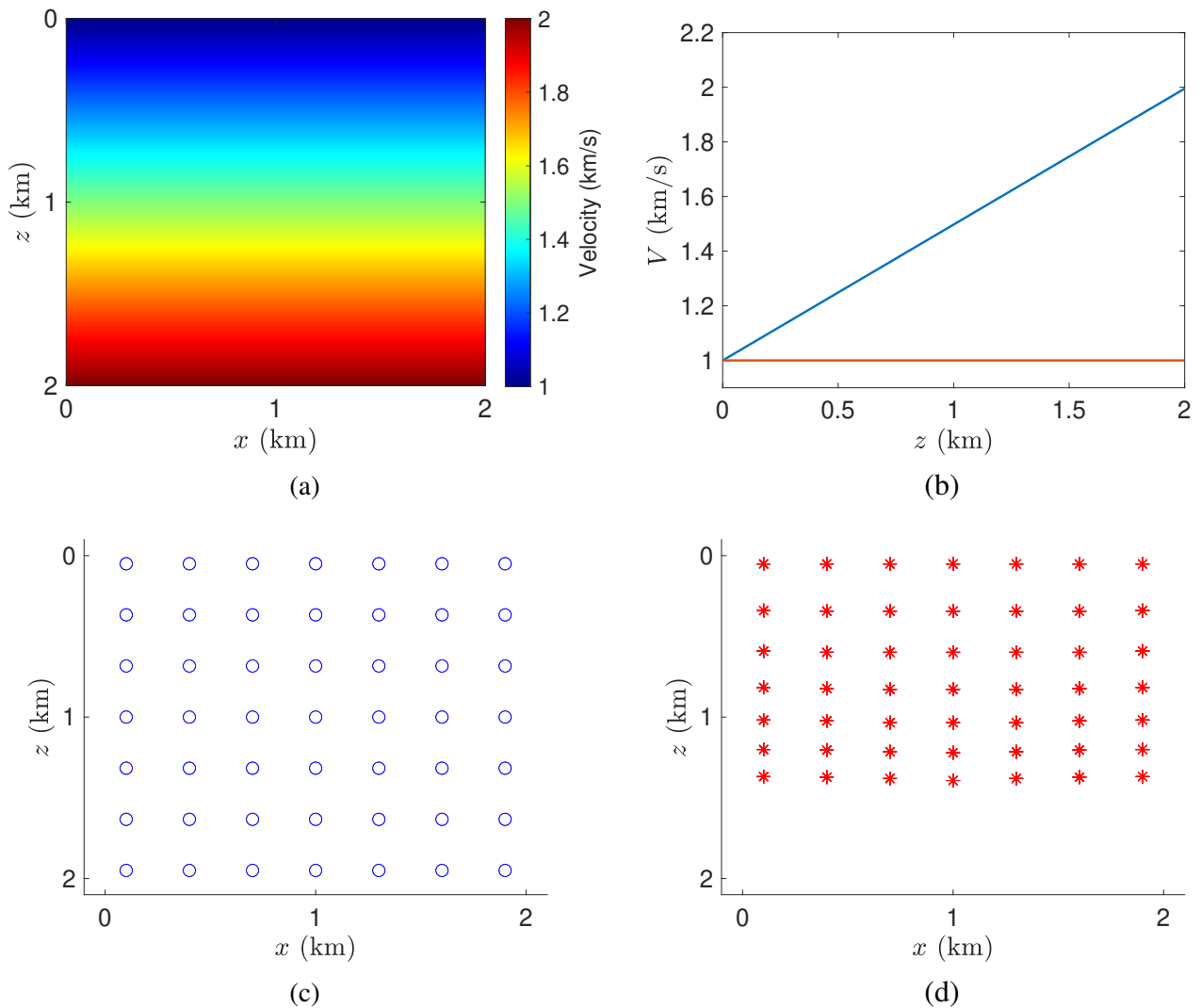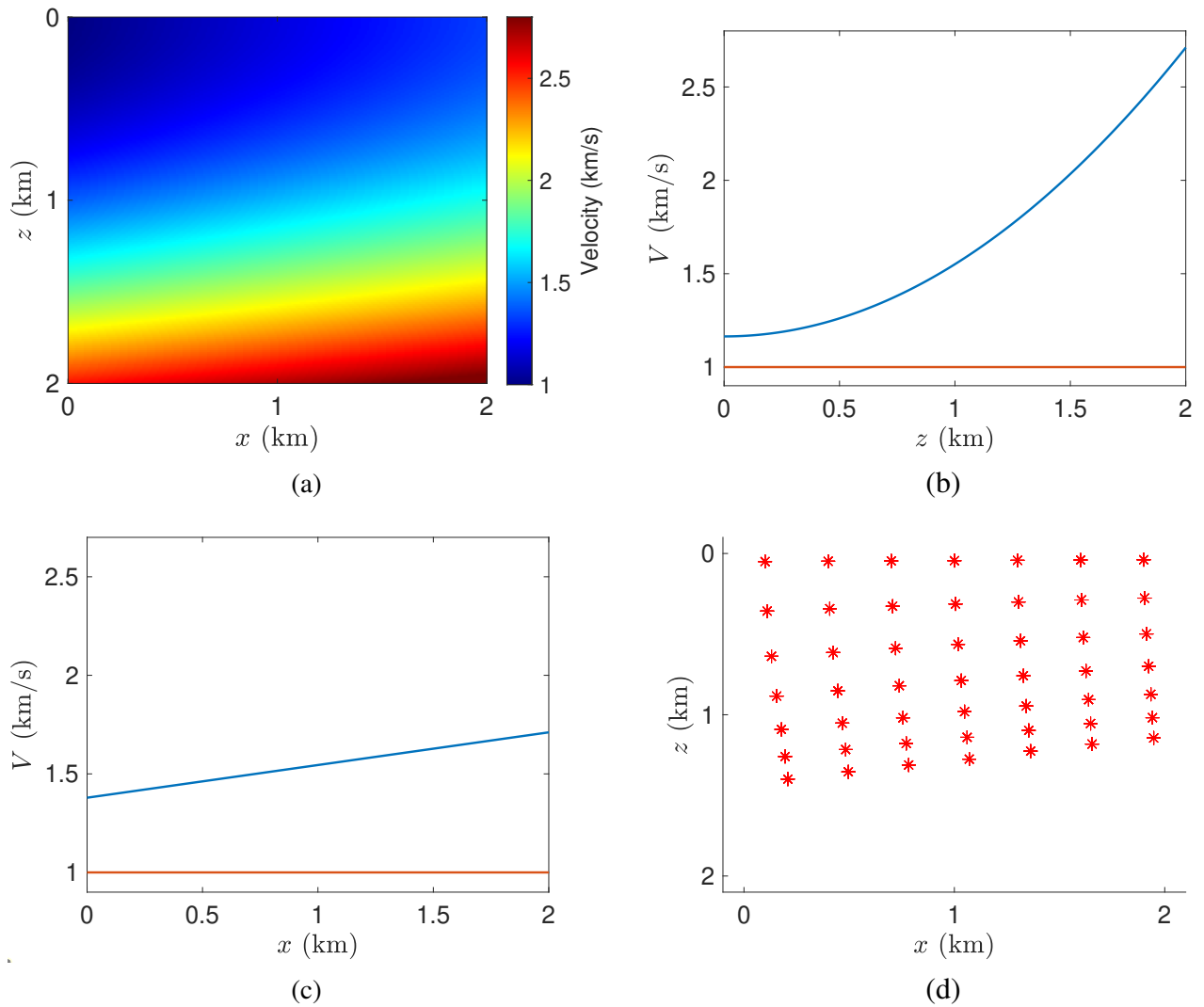
Figure 7.3: Second validation test: model with linear variation in vertical direction. (a) True velocity model test. (b) Vertical slices of initial (red) and true (blue) velocity models. Vertical slices were taken at the middle of the models. (c) Data positions. Observed-data space is composed by kinematic parameters computed by a series of dynamic-ray tracing starting at these positions. (d) Initial positions of ray-model space returned by initialization process. Initial positions are concentrated at the upper part of model, because initial velocity model is slower than true velocity model.
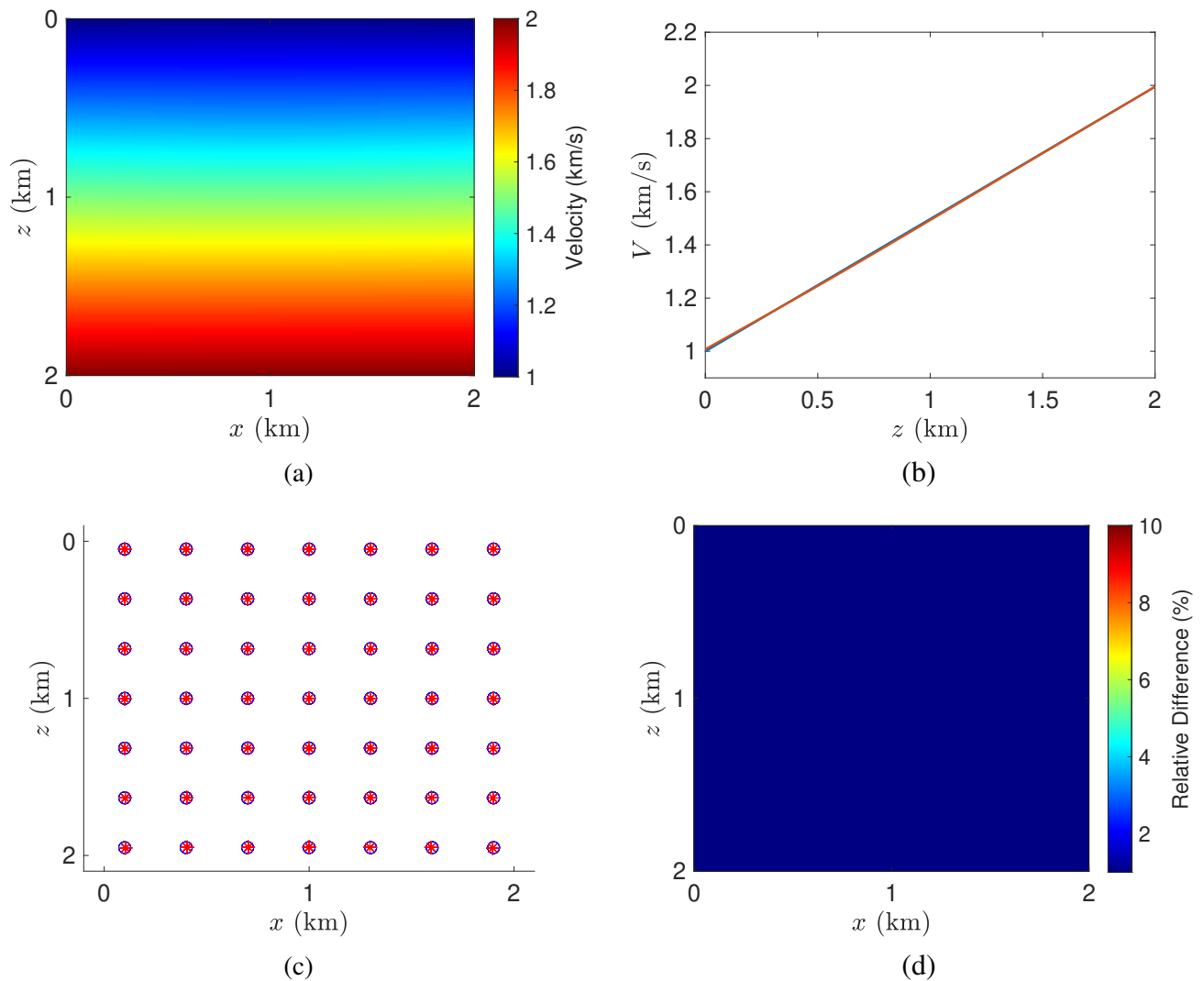
Figure 7.4: CRP tomography results for second validation test. (a) Inverted velocity model. (b) Vertical slices of inverted (red) and true (blue) velocity models. Vertical slices were taken at the middle of the models. (c) Final model (red) positions and true (blue) data positions. (d) Percentage difference between inverted and true velocity models.
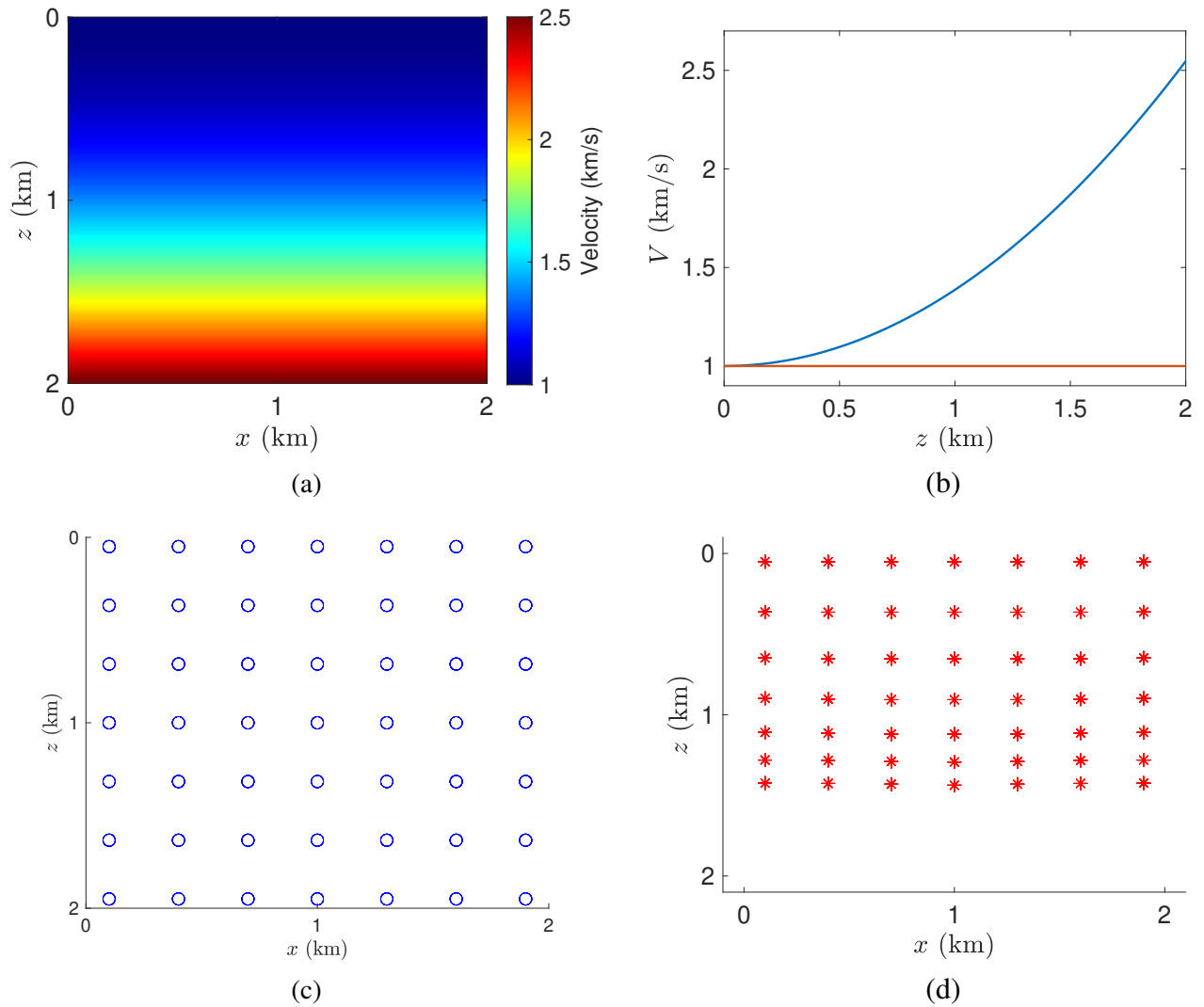
Figure 7.5: Third validation test: model with quadratic variation in vertical direction. (a) True velocity model test. (b) Vertical slices of initial (red) and true (blue) velocity models. Vertical slices were taken at the middle of the models. (c) Data positions. Observed-data space is composed by kinematic parameters computed by a series of dynamic-ray tracing starting at these positions. (d) Initial positions of ray-model space returned by initialization process.

Figure 7.6: CRP tomography final result for third validation test. (a) Inverted velocity model. (b) Vertical slices of inverted (red) and true (blue) velocity models. Vertical slices were taken at the middle of the models. (c) Final model (red) positions and true (blue) data positions. (d) Percentage difference between inverted and true velocity models.
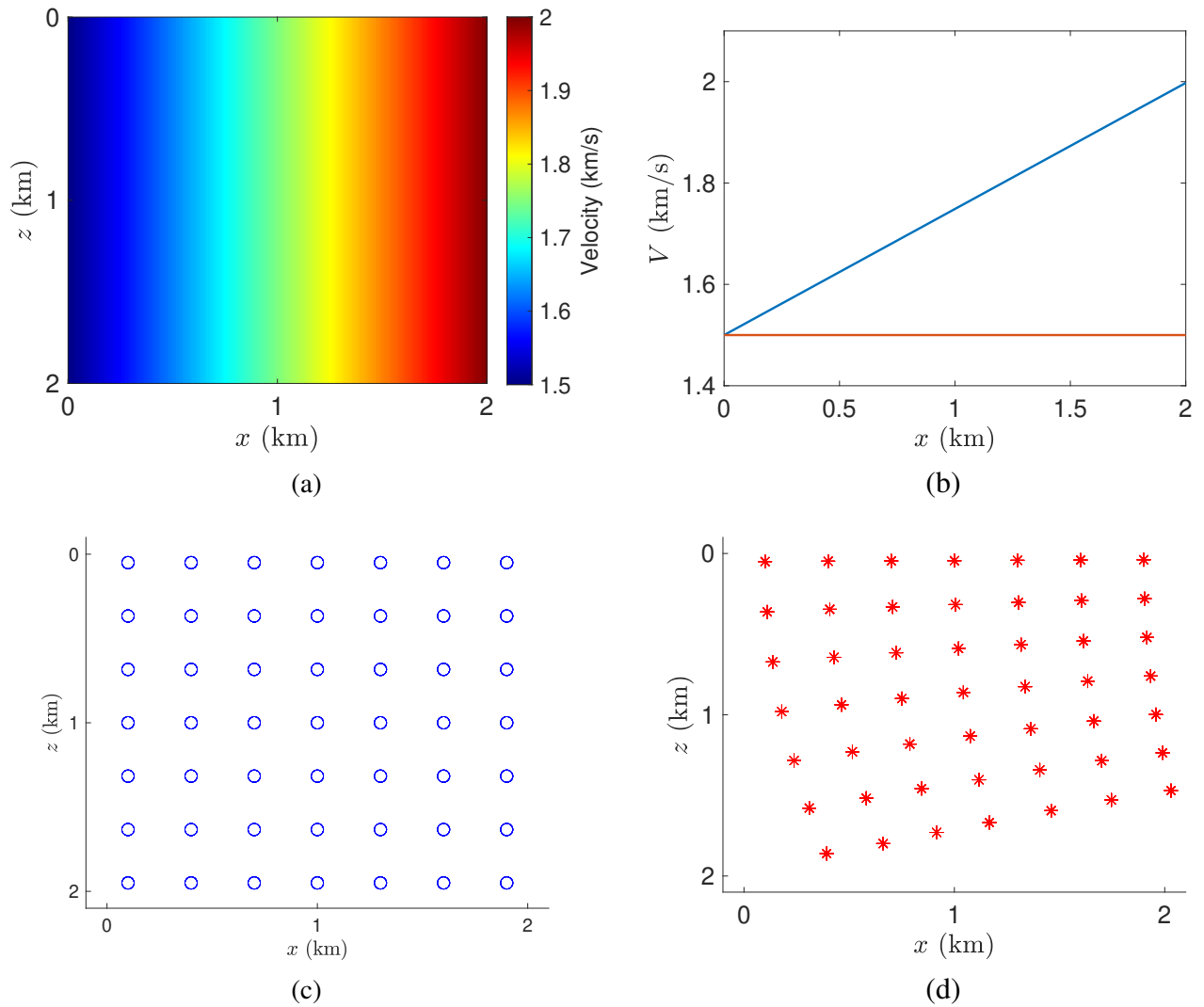
Figure 7.7: Fourth validation test: model with linear variation in horizontal direction. (a) True velocity model test. (b) Hotizontal slices of initial (red) and true (blue) velocity models. Slices were taken at the middle of the models. (c) Data positions. Observed-data space is composed by kinematic parameters computed by a series of dynamic-ray tracing starting at these positions. (d) Initial positions of ray-model space returned by initialization process.

Figure 7.8: CRP tomography final result for fourth validation test. (a) Inverted velocity model. (b) Horizontal slices of inverted (red) and true (blue) velocity models. Slices were taken at the middle of the models. (c) Final model (red) positions and true (blue) data positions. (d) Percentage difference between inverted and true velocity models.

Figure 7.9: Fifth validation test: model with linear variation in horizontal direction and quadritic variation in vertical direction. Data positions are the same from previous validation tests. (a) True velocity model test. (b) Vertical slices of initial (red) and true (blue) velocity models. Slices were taken at the middle of the models. (c) Hotizontal slices of initial (red) and true (blue) velocity models. Slices were taken at the middle of the models. (d) Initial positions returned by initialization process.
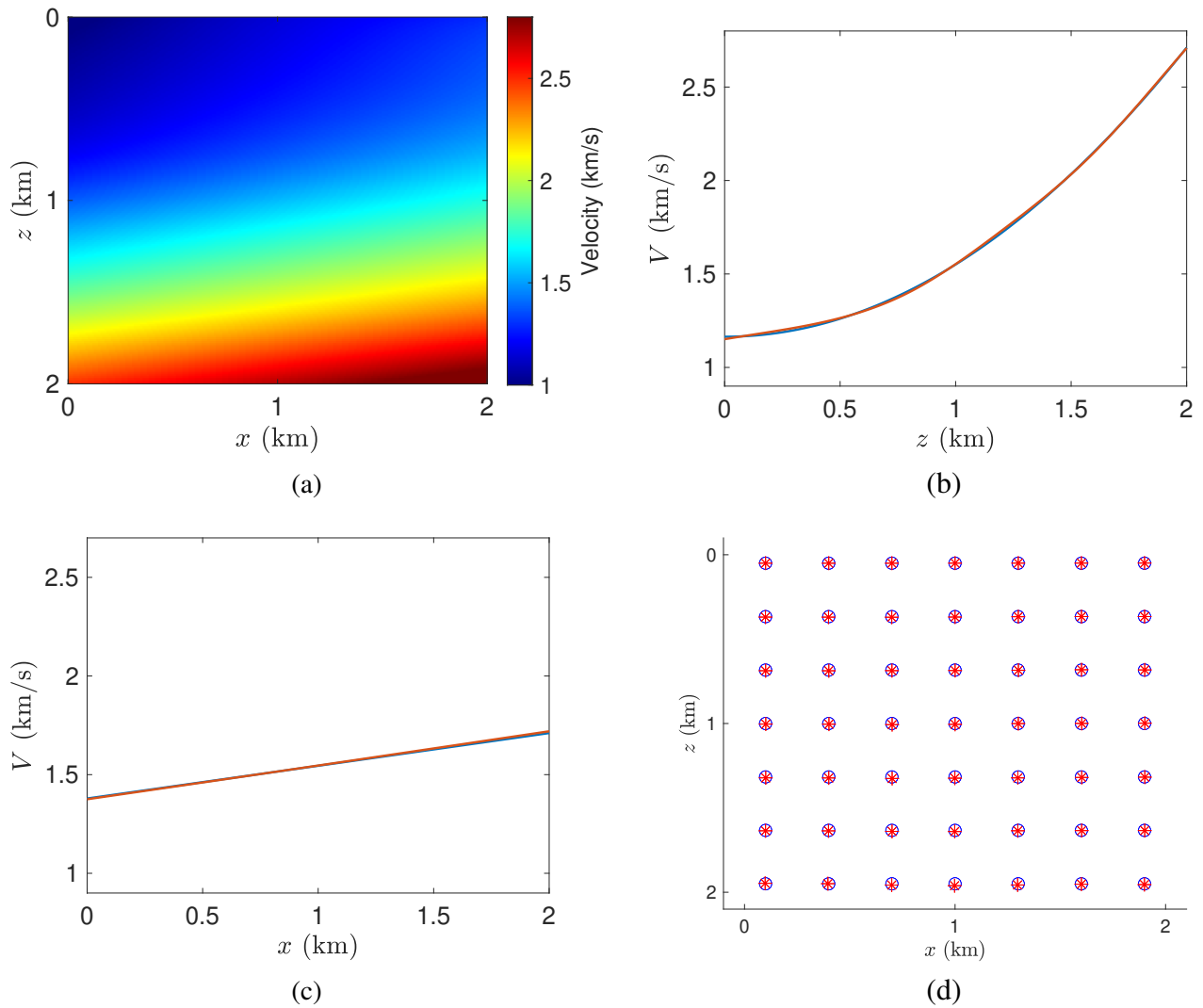
Figure 7.10: CRP tomography final result for fifth validation test. Data positions are the same from previous validation tests. (a) Inverted velocity model. (b) Vertical slices of inverted (red) and true (blue) velocity models. Slices were taken at the middle of the models. (c) Horizontal slices of inverted (red) and true (blue) velocity models. Slices were taken at the middle of the models. (d) Final model (red) positions and true (blue) data positions.

7.2   Laterally Heterogeneous Model Test

Laterally heterogeneous model test has already been proposed in this thesis in last chapter, where stereotomography method was applied. The proposed laterally heterogeneous velocity model is presented again in Figure 7.11. Note, again, that velocity model presents high levels of heterogeneity in both directions. Also, the model presents a region of higher velocity at the bottom of the model, which represents a traditional challenge for tomographic models.
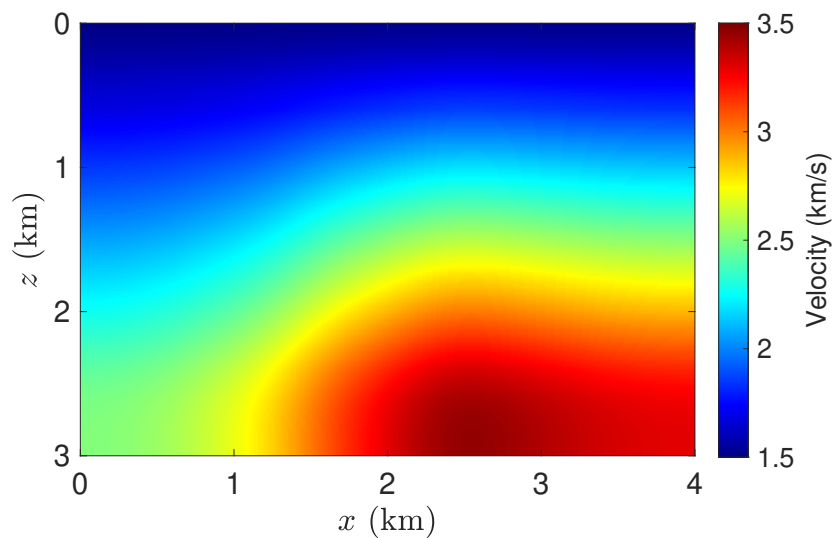
Figure 7.11: Laterally heterogeneous model test. Velocity model presents heterogeneity in both directions. Note the presence of a region of high velocity at the bottom of the model.

In last chapter, in order to show how it is possible to constrain the model by improving quality and quantity of internal information, different tries of stereotomography inversions were done. In first stereotomography try, input observed-data space was generated by 121 data positions distributed through true velocity model test. From these positions, rays were traced to surface line in order to compute the data samples of kinematic parameters. An initial homogeneous velocity model was used. The result provided by stereotomography in this first try was meaningless and couldn't be considered reasonable at all. Then, in a second try, a better initial velocity model was proposed. The new initial velocity model was described by a vertical linear gradient, which represented an improvement of the quality of initial boundary conditions. After this modification, the quality of stereotomography inverted velocity model was improved, in comparison with the previous one, and recovered many features of true velocity model test. However, the deepest half of the model sill presented considerable errors. So, in a third try, the number of data positions used to generate observed-data space was improved. Therefore, 256 data samples were provided to inverse process, more than the double of the

amount used for first and second tries. The inverted velocity model generated by stereotomography at this third try was remarkably good. Almost all errors were concentrated in regions near bottom line. Furthermore, almost all relative errors were below 2%. The exception, again, was due to the deepest part of the model. The reader can go back to Chapter 6 for more details about stereotomography test on this model.

The same laterally heterogeneous model test will be proposed again, in this chapter, to test CRP tomography method. Since comparisons will be done, the same parametrization will be used. However, differently of what was done for stereotomography, where three inversions were performed (three tries) in order to reach a satisfactory inverted model, just one try of CRP tomography will be presented. It will be done because CRP tomography was capable to provide a reasonable final velocity model using the same parametrization and conditions used at very first try of stereotomography. There, with 121 data positions and an initial homogeneous velocity model, stereotomography returned a final velocity model that did not resemble at all the true velocity model test. Following, it will be shown that these conditions were sufficient to CRP tomography method to constrain the proposed laterally heterogeneous model.

For CRP tomography test, input data and model spaces and initial parameters were set as follows:

Input observed-data space: To generate observed-data space, 121 positions (common-depth points) were distributed in depth through the model test (see Figure 7.13). These positions are exactly the same ones used for stereotomography test at first try. Therefore, for comparison reasons, this experiment simulate the results that would be obtained by both tomography methods under the same number of pickings. From theses positions, eight pairs of rays were propagated to surface directions, with initial double aperture, with respect to vertical direction, varying from $8°$ to $40°$. In surface line, the kinematic parameters of emergence positions, slopes and traveltimes were computed. All traveltimes computed by rays starting from the same common-depth-position were summed. Therefore, data space is composed by 121 families, each of them with one data total traveltime and eight samples composed by two data emergence positions and two data slope parameters.

Initial model space: A homogeneous velocity model of 1.5km/s was used as initial velocity model, exactly the same one used before for stereotomography first try. The B-spline interpolation knots were distributed through the model with vertical spacing of 0.3km and horizontal spacing of 0.4km. Its is exactly the same parametrization applied to build the true velocity model for the test. Therefore, in respect with B-spline interpolation issues, the model test can be perfectly recovered. Ray-model space

was initialized with the proposed CRP tomography initialization procedure proposed (see Chapter 5). Therefore, the initialization procedure returned 121 model families, each of them composed by one initial model position in depth and eight pairs of initial model slopes. Initial model depth positions returned by CRP tomography initialization procedure, under initial homogeneous velocity model of Figure 7.12, are displayed in Figure 7.13.
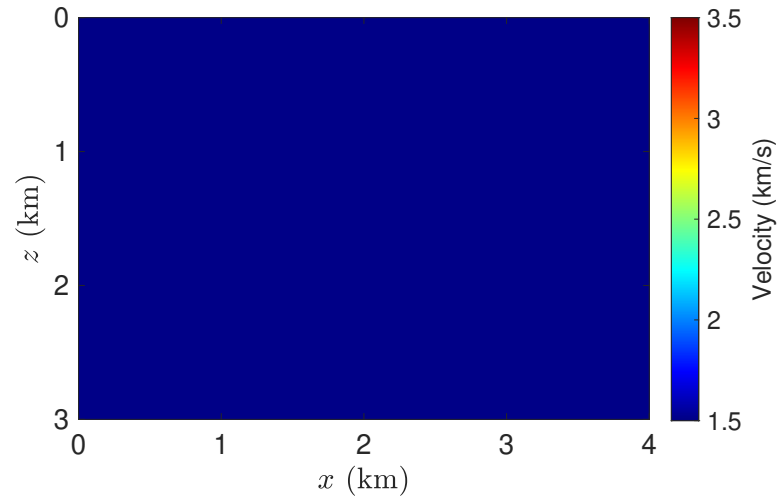

Figure 7.12: Initial homogeneous velocity model for CRP tomography laterally heterogeneous test.

(a)

(b)
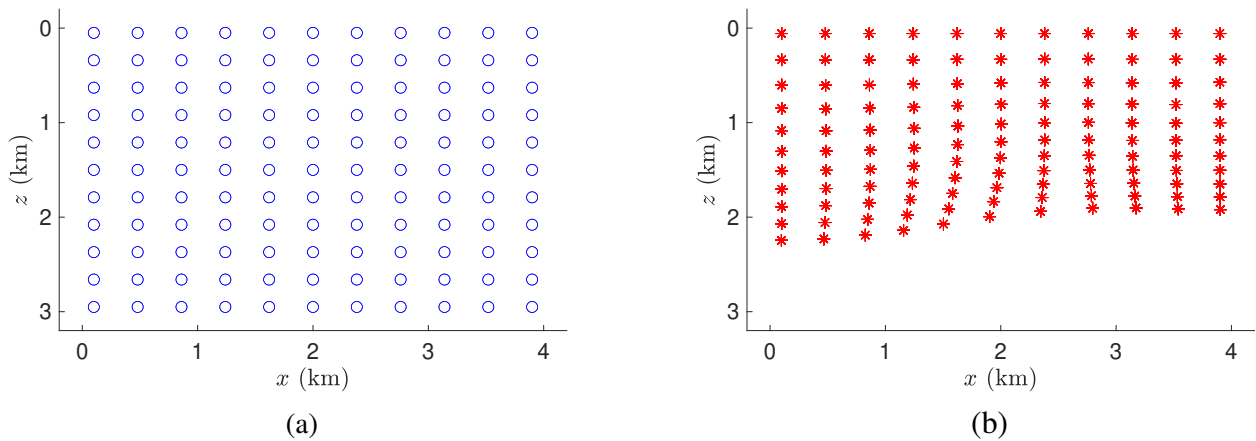
Figure 7.13: Laterally heterogeneous model test. (a) Data depth positions used to generate observed-data space components by means of ray-tracing. (b) Initial model positions returned by initialization step under the initial homogeneous velocity model of 1.5km/s.

Initial regularization weight parameter: The same level of initial regularization used for stereotomography test will be used for CRP tomography test. Therefore, initial regularization parameter λ was

set in order to put the relation between regularization term, with respect to CRP tomography objective function, to a value of 10^{-4} at the first iteration.

CRP tomography results: The results obtained by CRP tomography method, under the previous boundary and initial conditions, are illustrated in Figure 7.14. The CRP tomography inverted velocity model is very similar to the true laterally heterogeneous velocity model test. Differences occur just in regions very near the bottom area. Until 2.5km in depth, relative errors fall under 2%. Note how the velocity contour lines are similar between inverted and true velocity models. Even at the regions near the bottom line of the model, presented errors are smaller than those presented by third try of stereotomography, where more data samples (more "pickings") and a better initial velocity model were applied. Also, as illustrated by Figure 7.15, model depth positions were correctly inverted, except by errors, again, at the deepest positions.

It is remarkable how CRP tomography method returned a quite good final velocity model under the same conditions where stereotomography provided a final velocity model with no similarities at all with true velocity model test. At least in the present context of the proposed synthetic test, CRP tomography seems to be less dependent of the particular choice of initial velocity model and to number of data positions (which corresponds to pickings for synthetic tests).

It is important to highlight that the result presented by stereotomography in last chapter could be slightly improved if an optimum value of initial regularization parameter was searched and further applied. By this same strategy, the resulted presented by CRP tomography method could also be improved. However, the search of an optimum value to initial regularization parameter is not an objective of this thesis. It is still an open area of research. Here, the focus is on the ability of tomography methods in constrain different velocity models without the use of excellent initial conditions or regularization terms. More specifically, the ability of the different tomographic methods in return reasonable final velocity models, without a strong dependence of the specific choice of initial velocity, initial value for regularization parameter and, also, the number of data samples provided as input.

One possible argument that could be used, in order to justify the better solution provided by CRP tomography when compared to stereotomography solution, is that CRP tomography method makes use of more number of rays during tomographic inverse process. In fact, as eight data samples of pairs of positions and slopes were considered for each common-depth-point, sixteen rays were traced from each of model positions at each iteration. On the other hand, in stereotomography, just two rays were traced from each model depth position. Therefore, even after the introduction of more data positions in third try of laterally heterogeneous test for stereotomography, more rays were used
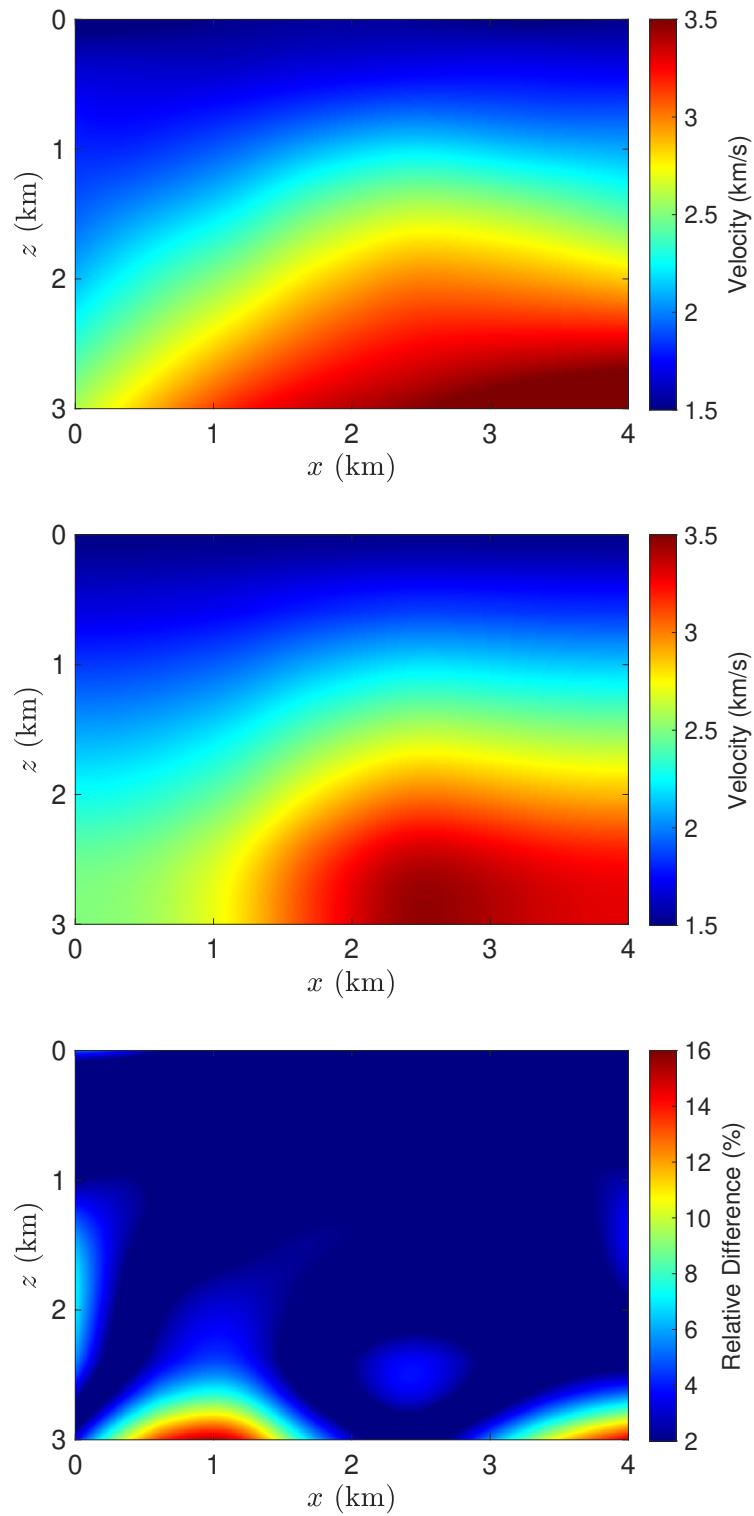
Figure 7.14: Laterally heterogeneous model test - CRP tomography final result. Top: Inverted velocity model. Middle: True velocity model test. Bottom: Percentage difference between inverted and true velocity models.
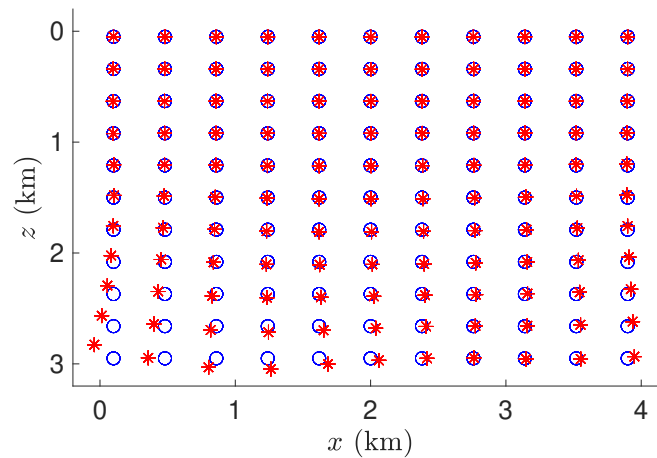
Figure 7.15: Laterally heterogeneous model test - CRP tomography. Inverted model positions (red) and true data positions (blue).

by CRP tomography method at each iteration of inverse process. Thus, more internal information was available in order to constrain the model. This is a true fact. However, there is a more important feature than the number of rays used at each iteration: the common-reflection-point information. The next experiment will show that common-reflection-point information plays a fundamental role in the ability of constrain the model, mainly when adverse conditions are provided.

7.3   The Three-point Test

The test to be performed in this section is very simple. True velocity model is the same velocity model used in the second validation test, which is illustrated, once again, in Figure 7.16. Thus, a velocity with linear variation in vertical direction. The velocity starts with 1km/s at surface line and grows until 2km/s at bottom line. The grid has dimension 2km×2km. To generate the model, knots were uniformly distributed with constant spacing of 0.4km in both directions. As it was done during validation tests, a initial velocity model of 1km/s will be used. However, a great difference appears with respect to the number and localization of data positions: just three data positions will be used to generate kinematic parameters for input observed-data space. This is the analogues, for synthetic tests, of just three pickings performed to build observed-data space. Furthermore, the three positions in depth will be located near the bottom area of the model, at 1.8km in vertical direction. The use of just three data positions justifies the name of the present test. In Figure 7.16, these data positions are displayed.
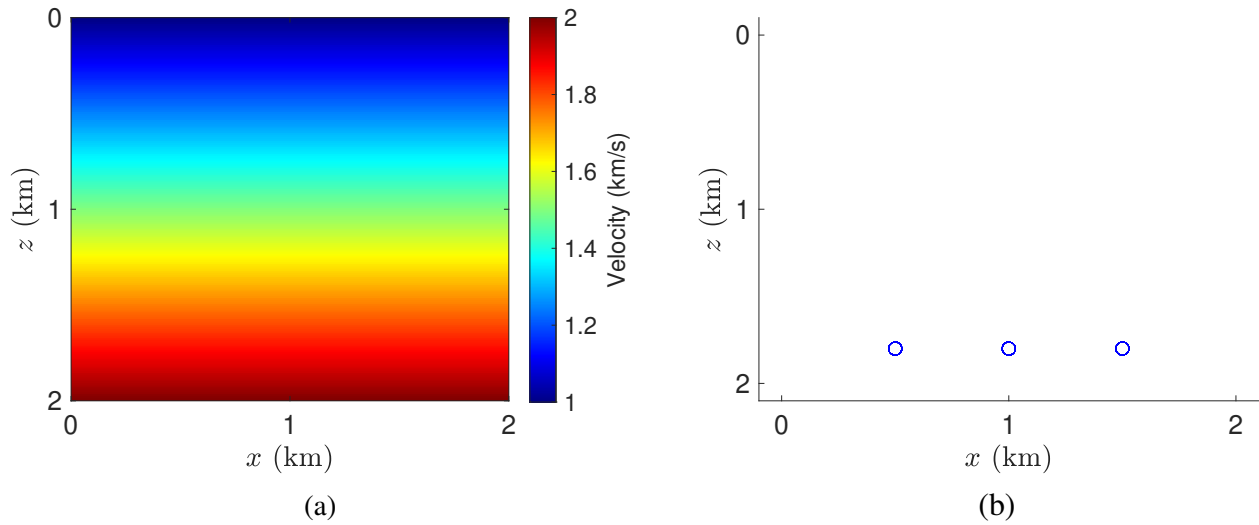
Figure 7.16: Three-point test. (a) True velocity model test described by linear variation in vertical direction. (b) Data positions for three-point test. The three data points of the test are located at 1.8km in vertical direction.

Both stereotomography and CRP tomography methods will be tested under these conditions. First, CRP tomography test will be described.

The Three-point test by CRP tomography

CRP tomography method was applied at the, a priori, difficult task of invert the model based on informations provided by just three points, located at just the same depth level. The parametrizations of the test are:

Input data-observed space: To generate data space, 3 data positions were displayed near the bottom line of the model, as illustrated by Figure 7.16. From each of these positions, 50 pairs of rays were traced to surface line. These rays were propagated with initial double aperture, with respect to vertical direction, varying from $4.5°$ to $45°$ for the center point, and varying from $4.5°$ to $22.5°$ for the data positions near the border of the model. In surface line, the kinematic parameters of emergence positions, slopes and traveltimes were computed. All traveltimes related of rays starting from the same data common-depth-position were summed. Therefore, data space is composed by just 3 data families, each of them with a data total traveltime and 50 samples composed by two data emergence positions and two data slope parameters. Note that this observed space simulates a situation where just three picks were performed in seismic data.

Initial model space: A constant velocity of 1km/s was used as initial velocity model. Interpolation knots were placed at same positions applied to build the true velocity model test. Ray-model space was initialized with the proposed initialization procedure for CRP tomography, returning 3 initial model families, each of them composed by one initial model position in depth and 50 pairs of initial model slopes. CRP tomography initial model depth positions, returned by initialization procedure under a constant initial velocity of 1km/s, are illustrated in Figure 7.17 (c).

Initial regularization weight parameter: Initial regularization parameter λ was set in order to put the relation between regularization term, by original CRP tomography objective function, to a value of 10^{-3} at the first iteration. The parameters to calibrate regularization term were set to the following values: $\epsilon_{xx} = \epsilon_{zz} = 1$, and $\epsilon_{vv} = 10^{-4}$.

CRP tomography results: Under the previous boundary and initial conditions, the results proposed by CRP tomography are illustrated by Figure 7.17. Since the challenge represented by the use of only three points can't be left aside, the objective of this test is not to produce a very similar inverted velocity model, with respect to true velocity model, as it was done during validation tests. Therefore, just the ability of CRP tomography method in reasonably recover the vertical velocity variation is pretty remarkable. Note that, under these unfavorable conditions, the method also inverted good model positions for all three model common-depth-points. Obviously, as it was already shown at validations tests section, by the improvement of initial conditions and number of input data samples, the result of the method can be improved.

The Three-point test by Stereotomography

The results obtained by stereotomography method, using the same parametrization described before for CRP tomography method, will be now exhibited. As stereotomography method perform just two ray tracing from each data point in depth (stereotomography does not use common-reflection-point information), observed space for stereotomography has only three samples of one two-way traveltime information, plus pairs of surface positions and slopes. This situation illustrates the analogues for stereotomography of the case where just three picks are performed. Under these conditions, observed data space for stereotomography method is significantly smaller. This last feature turns the challenge of invert the proposed model, under unfavorable conditions, even harder for stereotomography method.
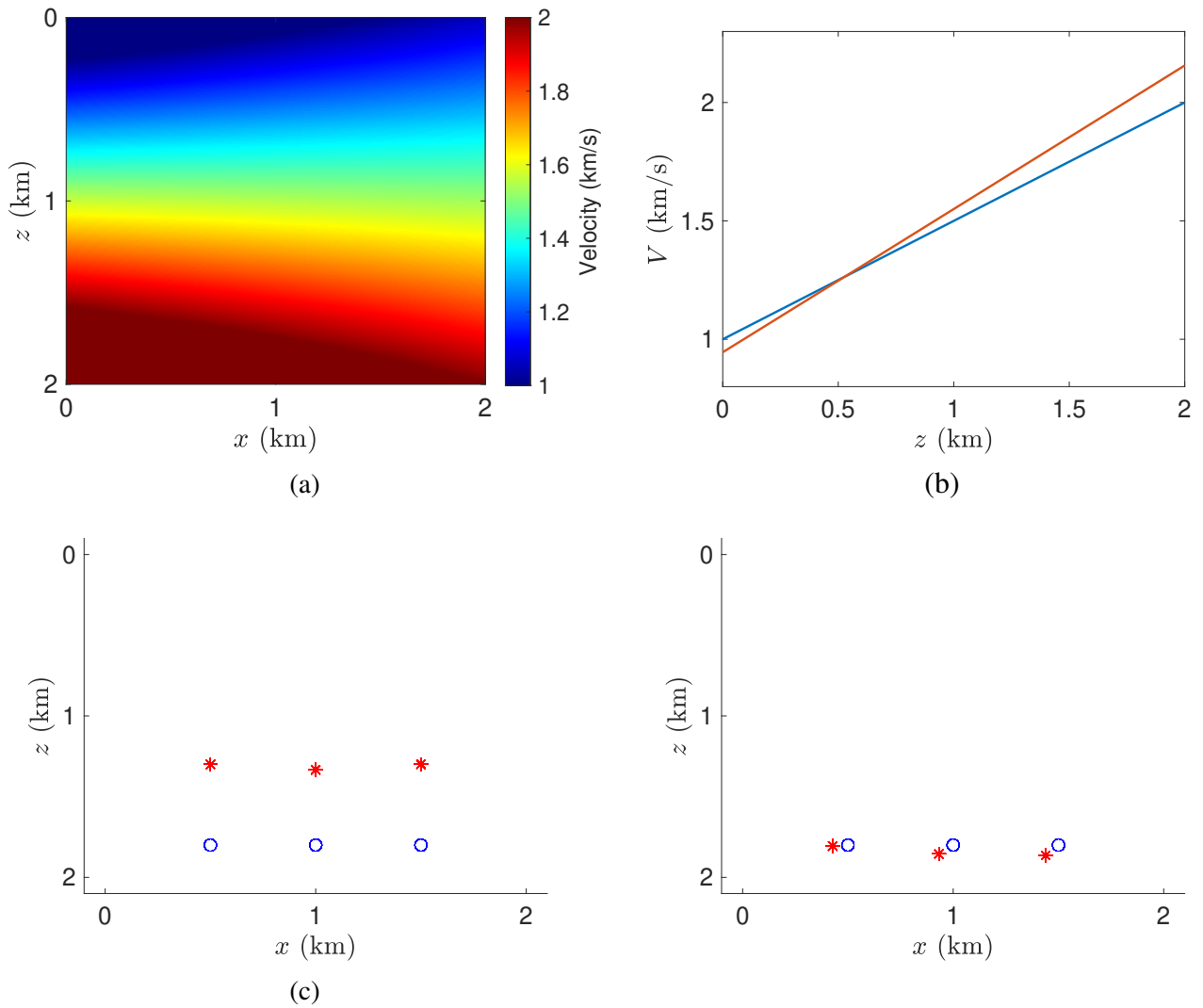
Figure 7.17: CRP tomography result for three-point test. (a) Inverted velocity model. (b) Vertical slices of inverted (red) and true (blue) velocity models. (c) Initial model (red) and true (blue) data positions. (d) Inverted model (red) and true data (blue) positions.

Input data-observed space: To generate stereotomography data space, the same 3 data positions used for CRP tomography test were displayed through the model. From each of these positions, one pair of rays were traced to surface line. The rays were propagated with initial initial double aperture, with respect to vertical direction, of $22.5°$, for positions near the border of the model, and $45°$ for the center point. In surface line, the kinematic parameters of emergence positions, slopes and traveltimes were computed. Therefore, data space is composed by just 3 data samples, each of them composed by two data emergence positions, two data slopes and one data traveltime parameter.

Initial model space: The same initial velocity model from last test was used, that is, a constant initial velocity model of 1km/s. Ray-model space was initialized with the proposed initialization procedure for stereotomography, returning 3 model samples, each of them composed by one initial model position in depth and one pair of initial model slopes.

Initial regularization weight parameter: Due to the small computational effort to run this particular stereotomography test, the method were executed by many different values of initial regularization parameter. Since just a very small input observed data space was used, this approach consisted in try to constrain the model by the use of more external regularization. However, in none of the performed tests, the method converged to a reasonable solution. The figures for stereotomography case in this section illustrate the result obtained with the same level of regularization applied to CRP tomography test.

Stereotomography results: The results obtained by stereotomography, under the previous conditions for the three points test, are illustrated in Figure 7.18. Firstly, it is important to highlight that the method didn't converge at all. In other words, it didn't stop because a very small value of objective function was reached. In fact, the method was stopped at early iterations because it couldn't find improved model spaces that could decrease the value of stereotomography objective function. Therefore, no enough information were available in order to allow stereotomography to search for improvements for model space. Here, just one result is exhibited. The illustrated result does not resemble any aspect of true velocity model. An inversion of the direction of vertical velocity variation was returned by the method. Thus, inverted velocity is bigger near the surface acquisition. Despite this huge difference, the positions were returned not too distant from true data positions. Under the use of greater initial regularization parameter, the velocity became with higher values, near a constant velocity, but still presenting the inversion of the direction of vertical velocity variation. For smaller initial regularization parameters, this aspect of the final velocity model becames more highlighted, that is, the inversion of the direction of vertical velocity variation became even bigger.
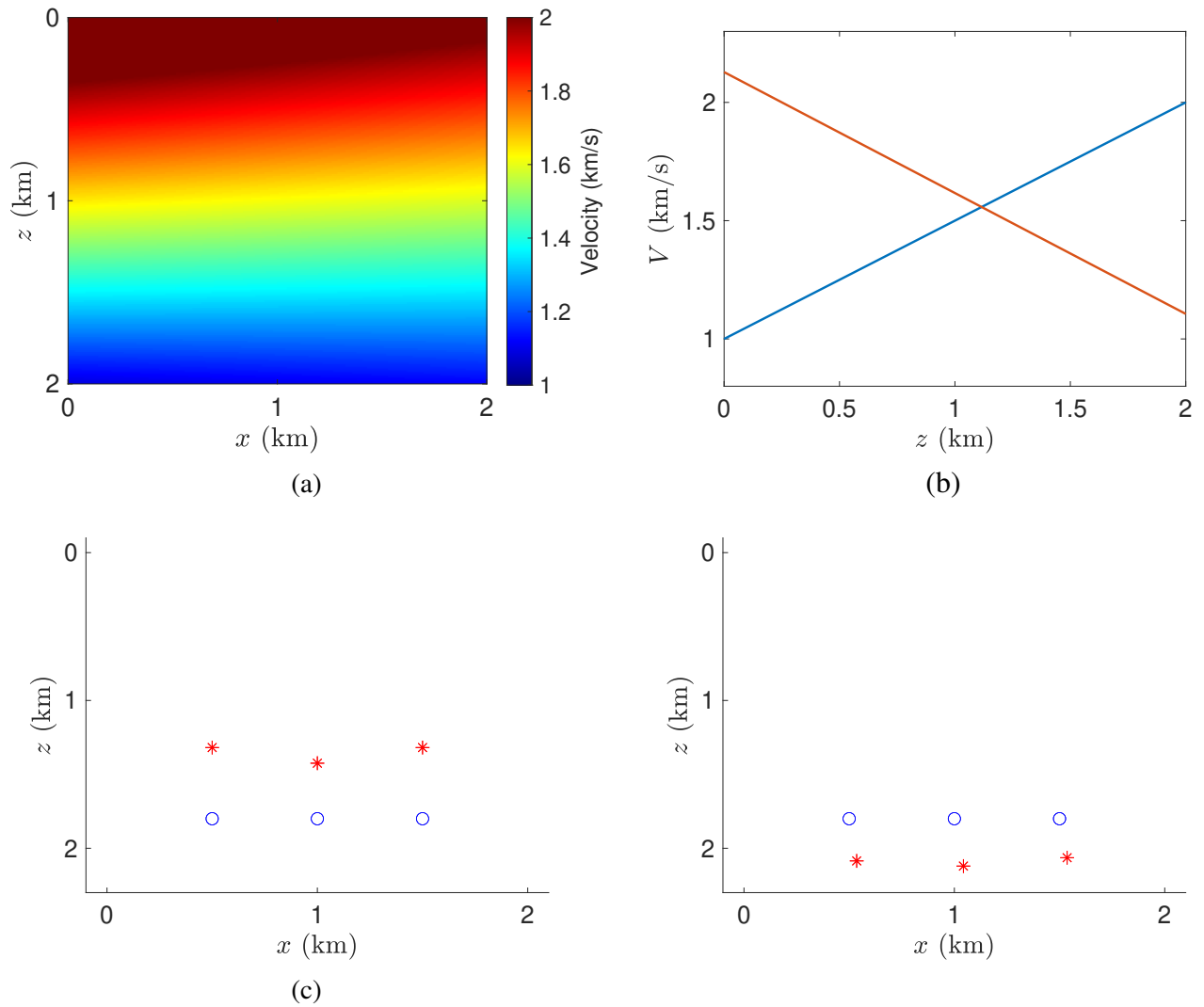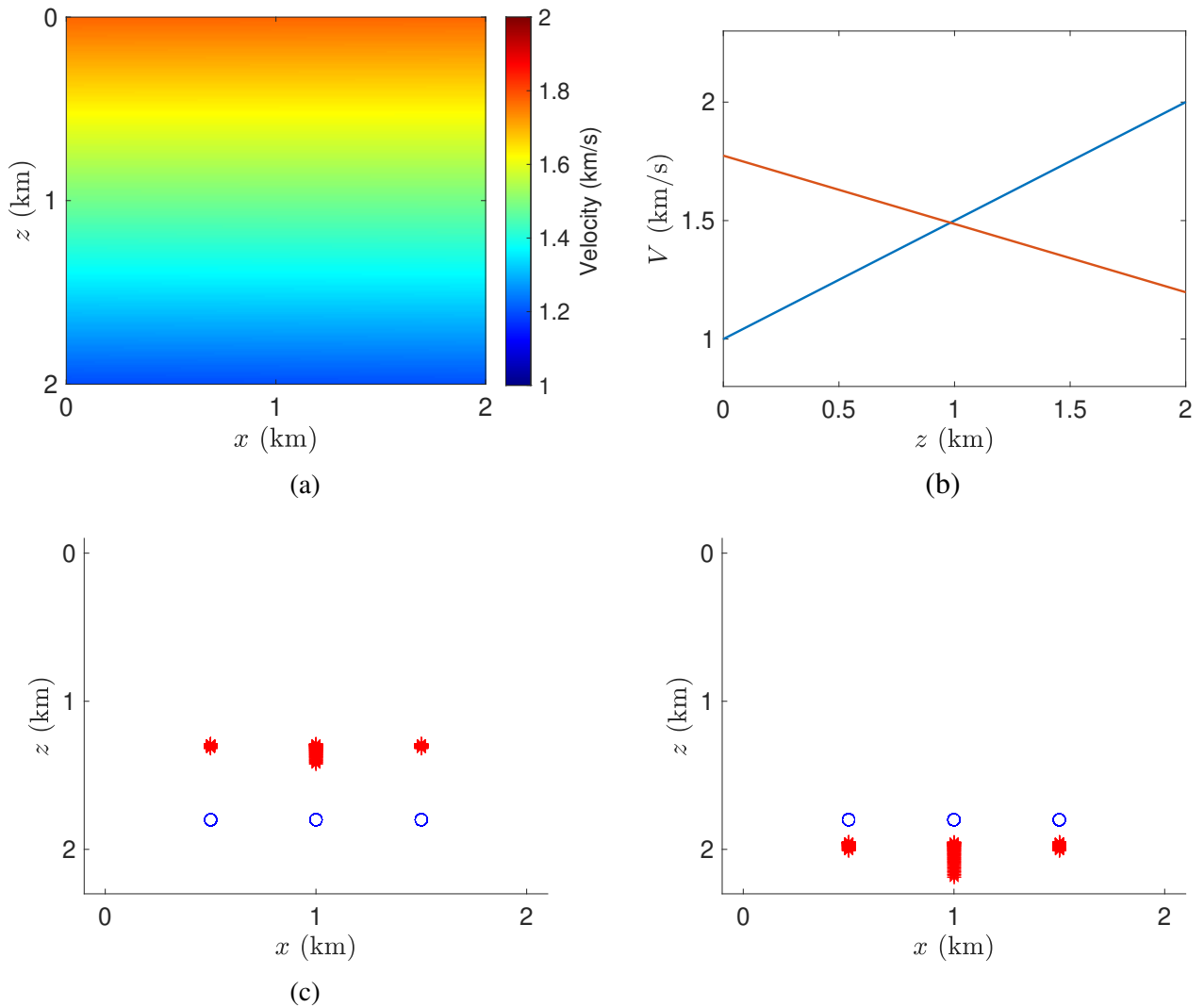
Figure 7.18: One example of stereotomography inversion for the three points test. (a) Inverted velocity model. (b) Vertical slices of inverted (red) and true (blue) velocity models. (c) Initial model (red) and true (blue) data positions. (d) Inverted model (red) and true data (blue) positions.

The Three-point test by Stereotomography with 300 rays - 150 redundant data positions

This new test is designed to answer the question that emerged in last section: the better results provided by CRP tomography was just because of the more number of rays applied during iteration process, or the common-depth-point information is a crucial information to improve the task of constrain the model?

To answer the previous question, in the particular context of the present three-point test, a new approach will be used for stereotomography method. The new approach consists in using the same number of rays applied during three-point test performed by CRP tomography method. Therefore, at each of the data positions of previous test, 50 redundant data positions are placed. From each of the these redundant data positions, a pair of rays will be traced to surface direction in order to build input-observed data space. Thus, 300 rays are considered by this new approach, the same number of rays applied in CRP tomography test. Therefore, input data space will be composed by 150 samples of two-way traveltime and pairs of emergence positions and slopes. These pair of rays starts the propagations with the same angles used to generate input observed data space for CRP tomography test. Note that, under this situation, the rays used to build input data space for both methos are the same. However, one big difference remains between these tests, the stereotomography method does not use common-reflection-point information. Therefore, while in CRP tomography method, information provided by one hundred ray propagations are used simultaneously to provide improvements to the model common-depth-point, in stereotomography, 150 independent different model depth points are considered. Remind the correspondence between data and model samples. Despite the fact that, to generate observed-data space, they are placed at the same three positions in depth (50 data depth points for each localization), trough iterations of the method, each of these 150 related model depth points changes their localization just by the information provided by one specific pair of rays. Therefore, 150 model depth points are distributed in 3 localizations just at the generation of input observed-data space. Through the inverse processes, they are located through 150 different locations. It does not happen in CRP tomography where just three points are considered during the role inverse process. For stereotomography, it is not known that the input data information belongs to just three points in depth. They are treated as independent information.

The parametrization for this new stereotomography test is summarized as follows:

Input data-observed space: To generate observed-data space, 50 redundant data positions were placed at each of the same three data localizations of the previous test. From each of these data positions (there are 150 of them), one pair of rays were traced to surface line. The rays were propagated with initial initial double aperture, with respect to vertical direction, analogues to the ones applied

for CRP tomography test. It was made in order to use exactly the same set of rays used for CRP tomography test to generate input observed-data space. In surface line, the kinematic parameters of emergence positions, slopes and traveltimes were computed. Therefore, data space is composed by 150 data samples, each of them composed by two data emergence positions, two data slopes and one data traveltime parameter.

Initial model space: The same constant initial velocity model of 1km/s was used for this test. Ray-model space was initialized with the proposed initialization procedure for stereotomography, returning 150 model samples, each of them composed by one initial model position in depth, one pair of initial model slopes and one pair of model traveltimes.

Initial regularization weight parameter: This test was executed by many different values of initial regularization parameter. However, in none of the executed tests, the method returned a reasonable solution. The figures for stereotomography case in this section illustrate the result obtained with the same level of regularization applied to CRP tomography test.

Stereotomography results with 300 **rays:** Firstly, remind that, during validation tests, stereotomography presented a good result for this velocity model test by the use of 49 data positions. This new test proposes 150 data depth positions, which is a much higher value. However, at the present test, the information provided by this 150 data positions are redundant. Therefore, the challenge presented by this test is much harder than the challenge presented by previous validation test. The result provided by stereotomography, using this new approach, is illustrated in Figure 7.19. Even after the addition of more samples for input observed-data space, the method did not converge. Once more, the algorithm stopped not because a very small value for optimization function was found. It stopped because it couldn't find improvements for model space. Again, no enough information were available for the method in order to allow the inverse process to recover original model informations. Note that, even under a bigger (redundant) observed-data space, stereotomography returned a final velocity model with the same inversion of the direction of vertical velocity variation presented previously. For stereotomography, the addition of these new input data information did not represented a remarkable contribution as, for this method, only redundant information was added.

Summary and conclusions: By the particular context of the present three-point test, the better results provided by CRP tomography method is not only attributed to the more number of rays. In fact, the common-reflection-point information is a crucial information to better constrain the model when

Figure 7.19: One example of stereotomography inversion for the three-point test using 300 rays. (a) Inverted velocity model. (b) Vertical slices of inverted (red) and true (blue) velocity models. (c) Initial model (red) and true (blue) data positions. Note that, as stereotomography does not use common-reflection-point information, the 150 model positions were initialized at different localizations. (d) Inverted model (red) and true (blue) data positions.

unfavorable conditions are presented. As the same rays were used to generate data space for both methods, what turned possible, for CRP tomography method, to generate reasonable final velocity models, was exactly the common-reflection-point information. For stereotomography, the use of more rays didn't help the inverse problem because, for the method, just redundant informations were added. However, what is redundant for stereotomography, is a fundamental source of new information for CRP tomography. This brought new information to the inverse process, which turned possible the constrain of the model. Furthermore, it can be seen as a decrease of the liberty degree for the inverse process, which is a very good feature to unstable inverse problems.

7.4   Soft Marmousi Test

In this section, the same smooth version of Marmousi model (Figure 7.20), the soft marmousi, that was previously used in last chapter for stereotomography method, will be used to test CRP tomography.
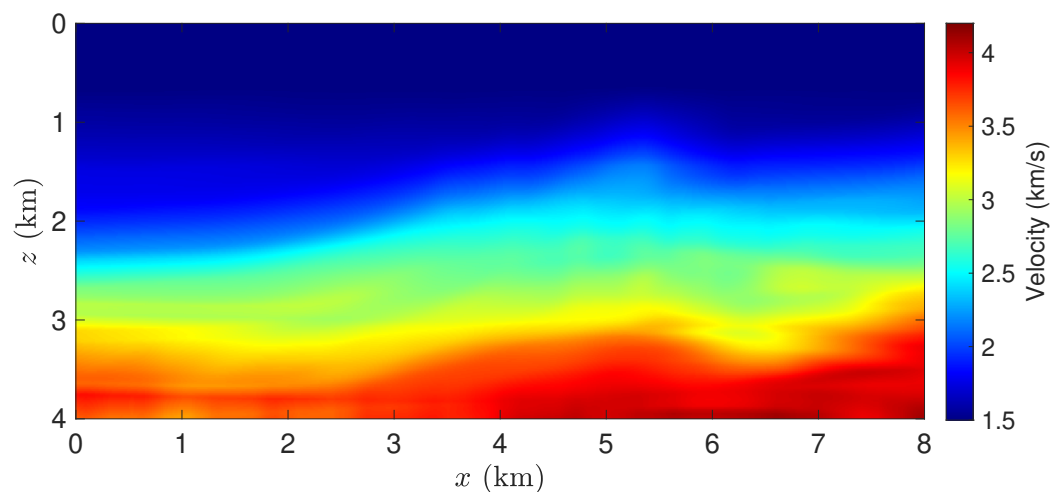
Figure 7.20: Soft Marmousi model.

In last chapter, the stereotomography inversion of soft marmousi model was made by subsequent tries. There, just two tries were sufficient. At first try, an initial velocity model described by a linear velocity variation in vertical direction was used. Also, at first try, just 208 data depth positions were distributed through the velocity model in order to generate input kinematic parameters for data space by means of direct ray tracing. Remind that this was considered a very small number of input data information. Under that specific parametrization, stereotomography returned a velocity model

where some differences appeared at the deeper half of the model. At second try, an improvement was done at the number of data depth positions, which accounts for a bigger data space. In that case, 357 data depth positions were used to generate observed-data space. Under the same initial velocity model, stereotomography provided a good final velocity model, with small differences just in regions near the bottom of model or border regions, where a small number of information was available.

To test the ability of CRP tomography method to constrain soft Marmousi model under not too favorable conditions, the same number and localization of data depth positions, used at first try of stereomography test, will be used for CRP tomography test. In the context of CRP tomography, each depth point is a common-depth-point for a family of rays. At this test, for each common-depth-point, eight pairs of rays will be used to generated input data space. Hence, for the CRP tomography test, in comparison with previous stereotomography test, more number of rays will be traced, at each iteration, in order to generate simulated kinematic parameters. However, as it has been discussed in last experiment, it seems that the important information added by CRP tomography is the common-reflection-point information. However, one more challenge will be proposed to CRP tomography test. Differently of what was done in stereotomography test for soft Marmousi model, a homogeneous velocity model will be used as initial velocity model for CRP tomography test. The proposed initial homogeneous velocity model is illustrated in Figure 7.21.
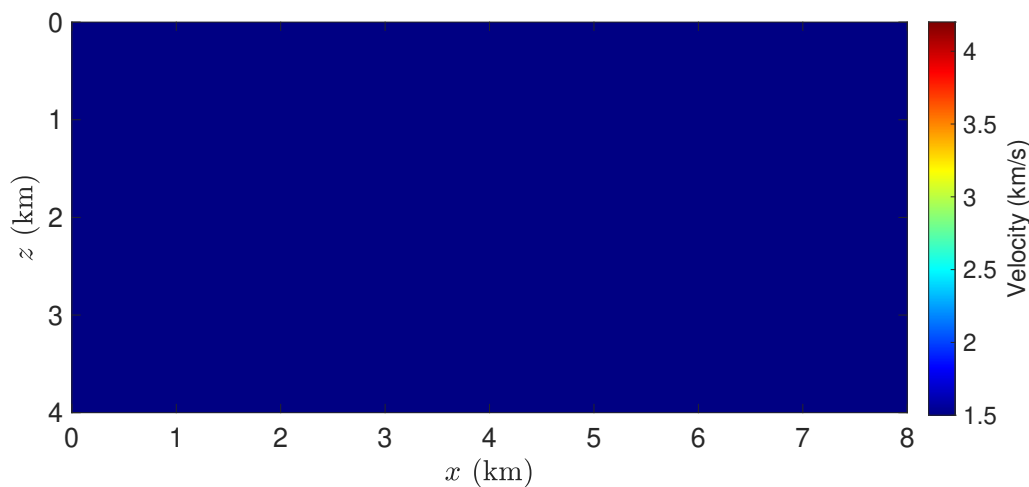
Figure 7.21: Soft Marmousi test - First try. Initial velocity model for CRP tomography test.

In order to allow further comparisons, the same parametrization (except initial velocity model) used in last chapter for stereotomography first try will be kept. They are summarized as follows:

Input observed-data space: To generate observed-data space, 208 data depth positions were displayed through soft Marmousi model (see Figure 7.22). They were placed at the same positions used for first try of stereotomography soft Marmousi test. From each of these positions, eight pairs of rays were traced through the model and the kinematic parameters of emergence positions, traveltime and slopes were computed at surface line. These rays were propagated with initial double aperture, with respect to vertical direction, varying from $4.5°$ to $45°$. All traveltimes related with rays starting from the same data common-depth-position were summed. Therefore, data space is composed 208 data families, each of them with one data total traveltime and 8 samples composed by two data emergence positions and two data slope parameters.

Initial model space: Differently of what was done at first try of stereotomography soft Marmousi test, where an initial velocity model described by a vertical constant gradient was used, for CRP tomography test, a worse initial velocity model will be applied. It accounts for a homogeneous velocity model of 1.5km/s of Figure 7.21. Therefore, CRP tomography will be tested under more unfavorable boundary initial conditions. The interpolation knots were distributed with vertical spacing of 0.4km and horizontal spacing of 0.5km, the same configuration of previous stereotomography test. Remind that, at this particular test, the soft Marmousi velocity model was not generated by means of B-spline interpolation at these set of knots. Therefore, it is not previously known if this kind of interpolation, used to build velocity models through CRP tomography iterations, is capable to perfectly construct the true velocity model test. Finally, ray-model space was initialized with the proposed initialization procedure for CRP tomography, returning 208 model families, each of them composed by one initial model position in depth and 8 pairs of initial model slopes. The initial model depth positions, derived by CRP tomography initialization procedure under the initial homogeneous velocity model of Figure 7.21, are illustrated in Figure 7.22 together with data positions. Note that, because of the use of the proposed homogeneous velocity model, the initial model depth positions are concentrated just at the shallower part of the model, which represents another challenge for CRP tomograpy method.

Initial regularization weight parameter: Initial regularization parameter λ was set in order to keep the same level of regularization used for stereotomography soft Marmousi test. Therefore, at first iteration, the relation between the regularization term with respect to the objective function was set as 5.10^{-5}. Moreover, $\epsilon_{zz} = 10^{-2}$, $\epsilon_{xx} = 1$ and $\epsilon_{vv} = 10^{-4}$ were set to calibrate regularization term.

CRP tomography results: Under the initial conditions and parametrizations previously described, CRP tomography returned the final model illustrated by Figure 7.23. Under the proposed number
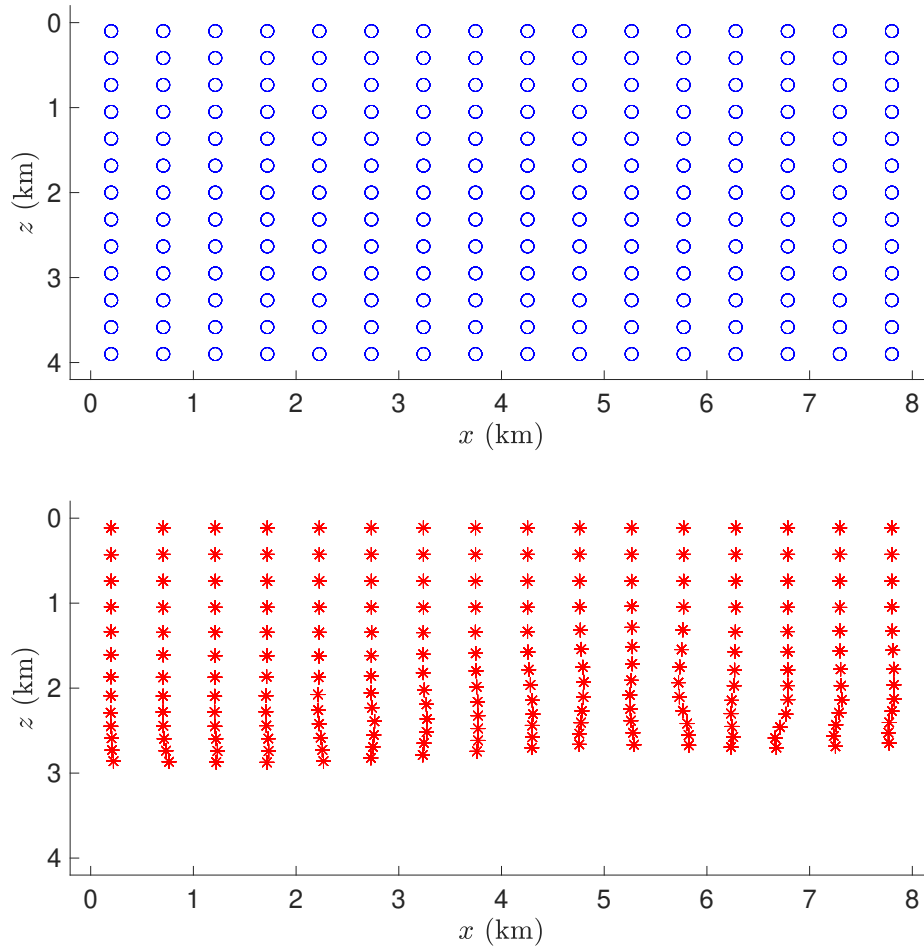
Figure 7.22: Soft Marmousi test - CRP tomography. Top: Data positions. Bottom: Initial model positions returned by initialization step. Note that initial model positions are concentrated at the shallower part, due to use of the proposed initial homogeneous velocity model of Figure 7.21.

of input data positions and a constant initial velocity model, CRP tomography method provided a reasonably good final velocity model. Until 3km in depth, the inverted velocity model is similar with the true velocity model. Among this area, almost all relative errors fall under 2.5%. Note how the velocity contour lines of this part of the model are almost identical to the soft Marmousi model test. Some differences appear just in regions near the bottom line of the velocity model. Furthermore, as illustrated by Figure 7.24, almost all final model common-depth-positions were repositioned very close to the right data positions, even under a poor initial localization of these points at first iteration.

For comparison reasons, CRP tomography method could return a satisfactory result under more unfavorable boundary conditions than the ones proposed for stereomography first try, since, for CRP tomography, a homogeneous initial velocity model was used. Remind that, to improve the quality of stereotomography result, a bigger data space was provided for second try. Here, once again, it seems that the use of common-reflection-point information played an importante role to the inverse process, assisting the constrain of the proposed model.

It is important to highlight the smoothest aspect presented by CRP tomography inverted model. The same initial level of regularization was used by both stereotomography and CRP tomography tests. However, the inverted model presented by CRP tomography is smoother then the one presented by the first try of stereotomography test (the comparison is fairer with this test, since the same number of data depth points was used) and even with relation to the second try, where a bigger data space was given to stereotomography. CRP tomography method uses more internal information then other tomography methods, since it makes use of the common-reflection-point information. The addition of this information to the inverse problem, somehow, decreases some level of freedom of the naturally unstable tomographic problem. Also, based on the results provided so far, it can turn the method less dependent of the particular choice of initial conditions, presenting more ability in constrain different kinds of velocity models under unfavorable conditions. Between these conditions, is the important particular choice of initial regularization parameter. All tomography methods are very dependent of a good choice for initial regularization parameter, mainly when unfavorable conditions are presented, as poor initial velocity models or small number of input data information. Therefore, a right choice for initial regularization parameter is a fundamental key to tomographic inverse process. In this experiment, the same level of (external) regularization was applied to both methods, but CRP tomography result appears to be more "regularized". It happened not just in the present test, but also at the laterally heterogeneous model test (see previous sections). Next section will investigate how the use of common-reflection-point information can turn the inverse process slightly less dependent of the particular choice for initial regularization paramter. The investigation will be based on a very simple numerical test.
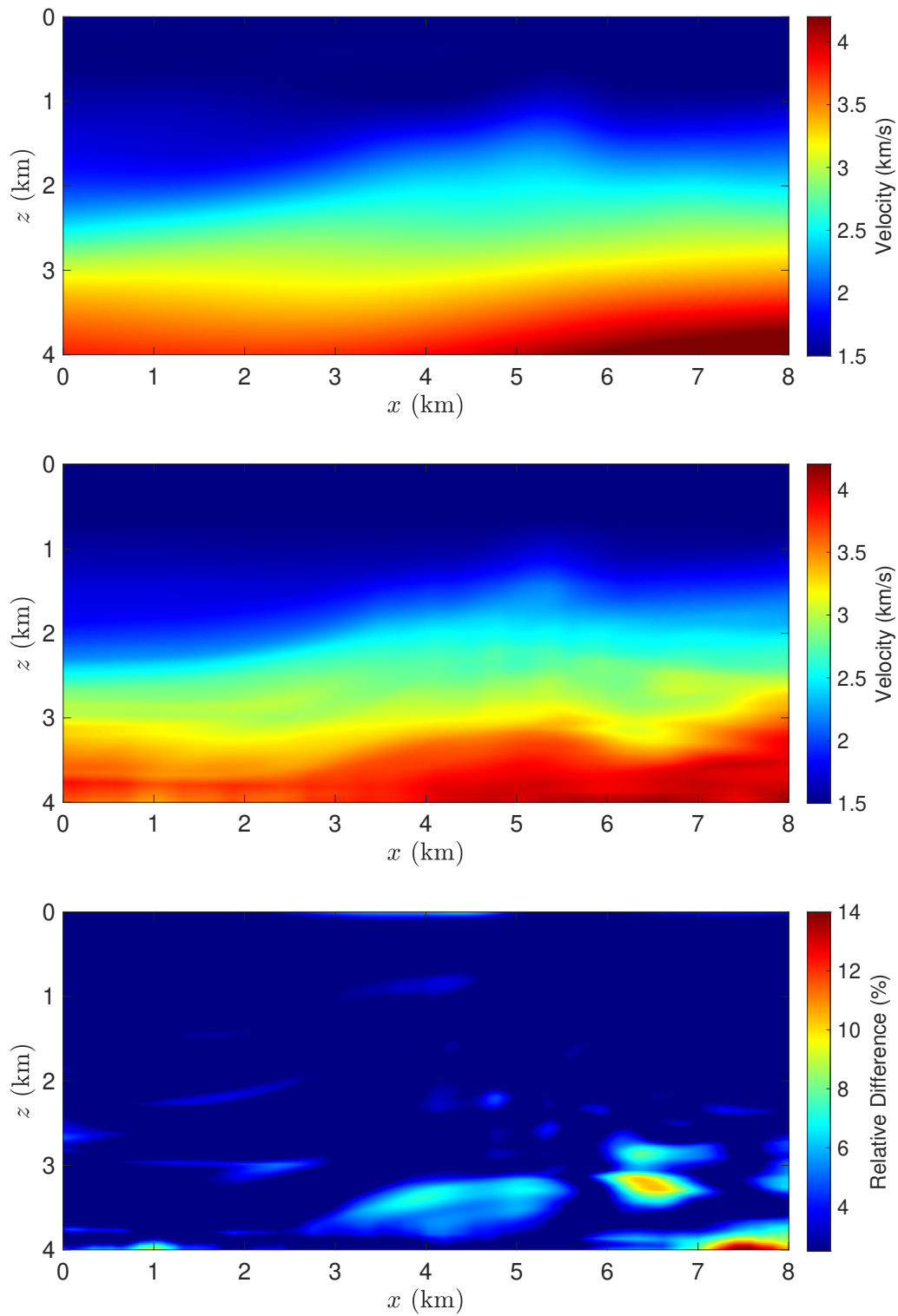
Figure 7.23: Soft Maroumousi test - CRP tomography result. Top: Inverted velocity model. Middle: True velocity model test - Soft Marmousi. Bottom: Percentage difference between inverted and true velocity models.
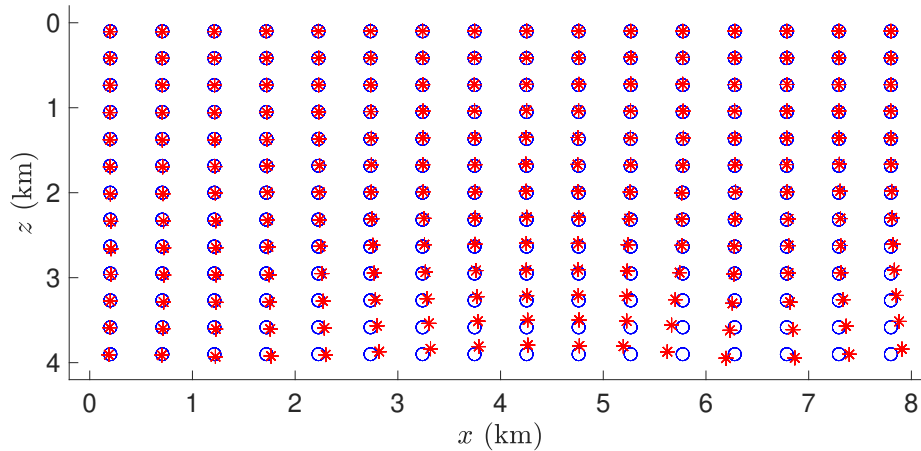
Figure 7.24: Soft Maroumousi test - CRP tomography result. Inverted model positions (red) and true data positions (blue).

7.5 A practical experiment about sensitivity with respect to initial regularization parameter

In this section, another kind of experiment will be illustrated using, again, the simple velocity model test described by a linear variation at vertical direction, very similar to the one used before in second validation test and for three-point test. In laterally heterogeneous model and soft marmousi tests, an arbitrary (although reasonable) choice of a value for the initial regularization parameter was made. Then, this value was kept unchanged through all the tests. For example, for stereotomography tests, these models were inverted by subsequent tries, which consisted in improving initial velocity model conditions or the number of input data provided to the method. Then, the same first parametrization, which included the value for the initial regularization parameter, was used for CRP tomography test. The result of those tests, both by stereotomography and CRP tomography, could be improved by searching and optimum value for initial regularization parameter. Therefore, the inverted models exhibited in this theses are not the best possible ones for all tomography methods. However, as the search of an optimum value for initial regularization parameter consists in another optimization problem, it is not the focus of this thesis. Furthermore, it consists in a computational expensive task, and can be seen as a kind of external help to assist seismic tomography inverse problem.

Here, a simple experiment will show how the tomography methods can be sensitive to the particular choice of initial regularization parameter. For this reason, the same experiment will be executed for many values of different initial regularization parameter, while all other parametrizations and conditions will be kept constant. Therefore, this approach can be seen, somehow, as an "orthog-
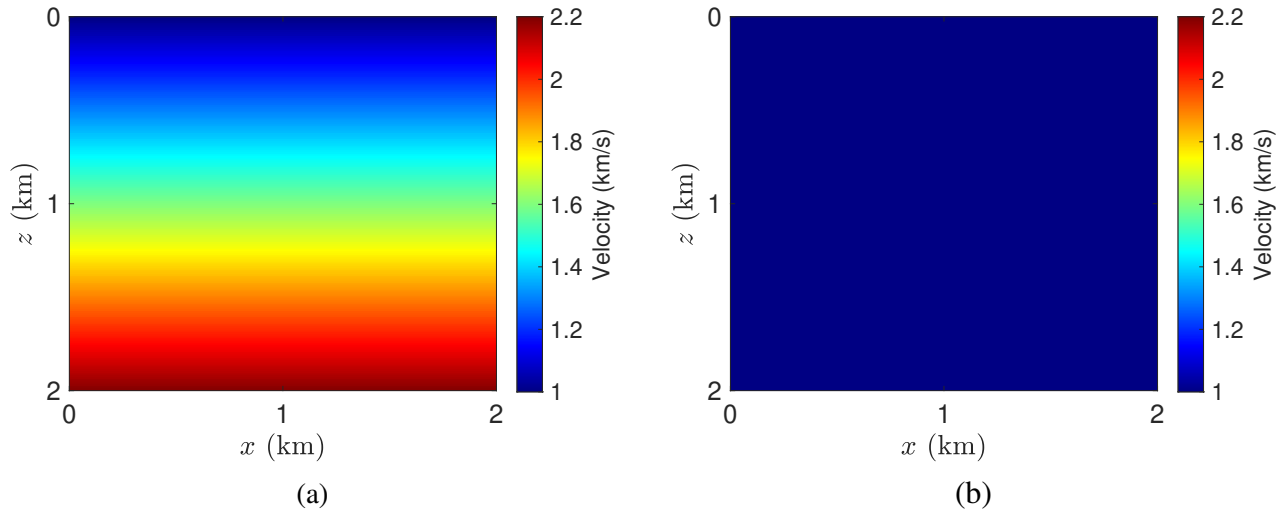
Figure 7.25: (a) True velocity model test. (b) Initial velocity model for the experiment.

onal" experiment with respect to the previous ones. Finally, the quality of inverted velocity models obtained by each of these many values of initial regularization parameter, measured by the residual difference between inverted and true velocity models by a chosen norm, will be exhibited.

At the present section, results obtained by stereotomography and CRP tomography method will be compared. The objective is to investigate how the use of the common-reflection-point information allows a larger range of initial regularization parameter to be chosen, without turn the inverted model a meaningless one. Also, to illustrate the effect of using more number of rays during inverse process, but without the use of commmon-reflection-point information, stereotomography will also be performed with more number of input data samples (more number of data positions).

To perform the proposed experiment, as many tests have to be processed, a very simple test was formulated. As it was already mentioned, it consists, again, in the problem of inverting a velocity model with linear vertical velocity variation. The velocity model grows linearly from 1km/s, at surface line, to 2.2km/s at bottom line. An initial constant velocity model of 1km/s will be used during all tests. Velocity model test and initial velocity models for the present exeperiment are illustrated by Figure7.25. Velocity models of Figure7.25 were construct using B-spline interpolation with knots uniformly distributed through the model, with both vertical and horizontal spacing of 0.4km.

This time, in a grid of dimension 2km$\times$2km, 16 data depth positions were used to generate input data space. These 16 data depth positions were uniformly distributed trough the model. Thus, differently of what was done at three-point test, these points do not form a redundant set of data information source. Thus, reasonable solutions can be obtained by both methods. As it will be showed, it depends on the particular choice for initial regularization parameter. The experiment in-

volving stereotomography with more data depth points will be executed with 36 data depth positions uniformly distributed through the grid. Data positions are illustrated by Figure 7.26.

Observed data space: To generate the samples of data space, in stereotomography, two rays were propagated from each of the 16 data depth points to surface line, with double initial aperture, with respect to vertical direction, of 30°. For CRP tomography method, ten pairs of rays were propagated from each of these points to surface line, with initial double aperture, with respect to vertical direction, varying from 5° to 45°. Finally, for the experiment involving stereotomography with more data depth points, 36 data depth positions uniformly distributed through the grid. Thus, based on the uniformly distribution of data positions, in fact, new input information was provided to stereotomography method. Again, to build observed-data space, two rays were propagated from each of these 36 data depth positions to surface line, with initial double aperture, with respect to vertical direction, of 30°. At surface line, the kinematic parameters demanded for each of the methods were computed.

Initial model space: An initial homogeneous velocity model of 1km/s was used for all tests (see Figure7.25). Ray-model space was initialized by the proposed initialization procedure of each of the techniques. Figure 7.26 illustrates data positions and respective initial model positions returned by the initialization step, under the initial constant velocity model of 1km/s.

Initial regularization weight parameter: It is the parameter to be investigated by this test. Therefore, both techniques will execute a series of tests, each of them with a different value for initial regularization weight parameter.

Discussion about experiment results

        The results obtained by this experiment can be summarized by the graphic in Figure 7.27. The graphic illustrates the quality of the inverted velocity model with respect to the initial amount of regularization term for all the three approaches mentioned before. To measure the quality of the inverted velocity model, the vertical axis exhibits a quantity related to the Frobenius norm (see, e.g, Watkins (2004)) of the difference between the matrices which represents inverted and true velocity models. To turn these results more comparable, the vertical axis was normalized. Then, the minimum value reached by this norm through all experiments of all methods (in this case, it was reached by CRP tomography method), was set equal to one. Then, all other values of the graphic accounts for the reason of the norm of the difference of velocity models with respect to this minimum. In other words,
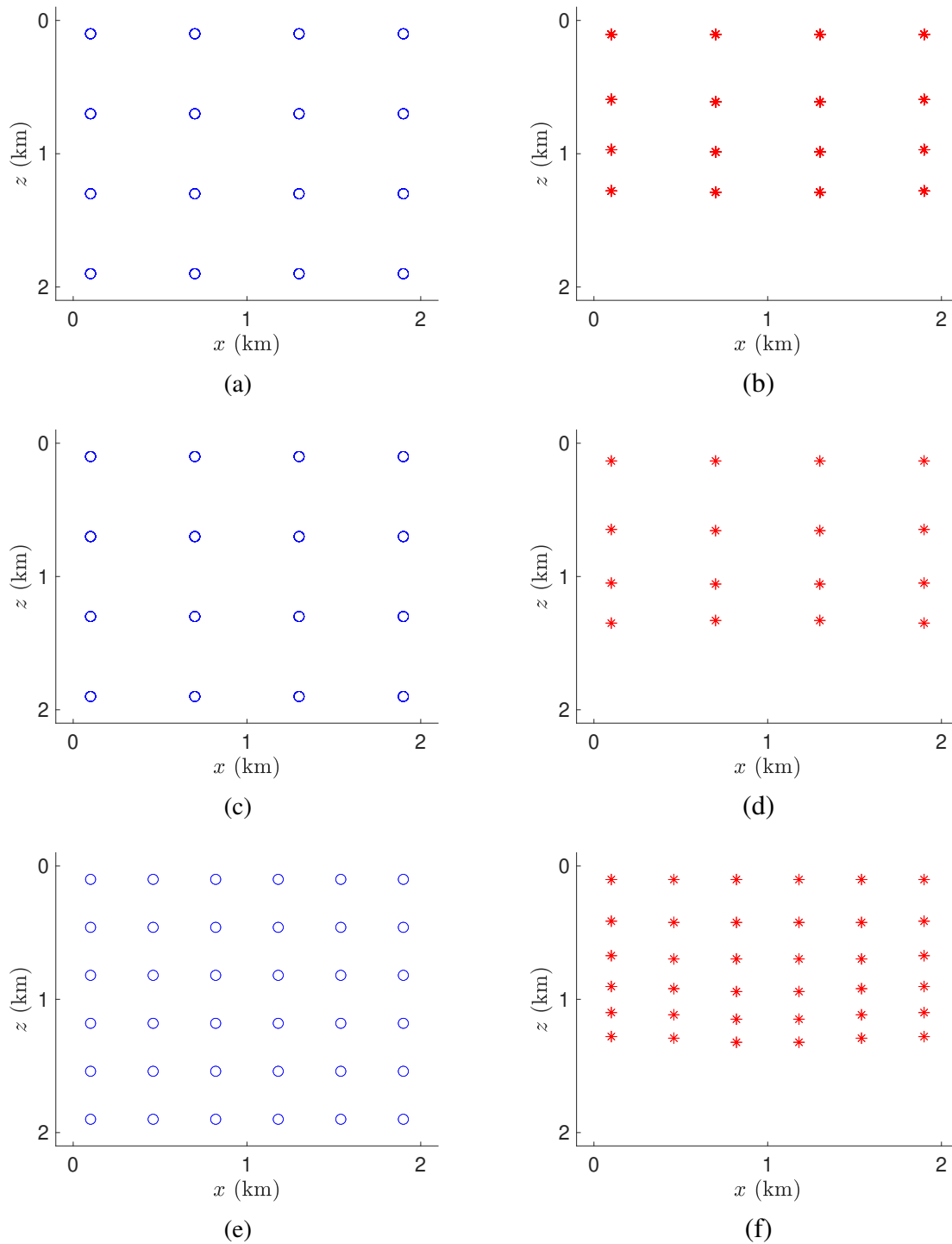
Figure 7.26: (a) Data positions used to build input data space for CRP tomography tests. (b) Model initial positions for CRP tomography tests. (c) Data positions used to build input data space for stereotomography tests with 16 data positions. (d) Model initial positions for stereotomography tests with 16 data positions. (e) Data positions used to build input data space for stereotomography tests with 36 data positions. (f) Model initial positions for stereotomography tests with 36 data positions.

vertical axis exhibits how bigger is the Frobenius norm of the difference between inverted and true velocity models, with respect to the minimum value reached. The idea is to show how the solution becomes better or worse varying the particular choice of initial regularization parameter.
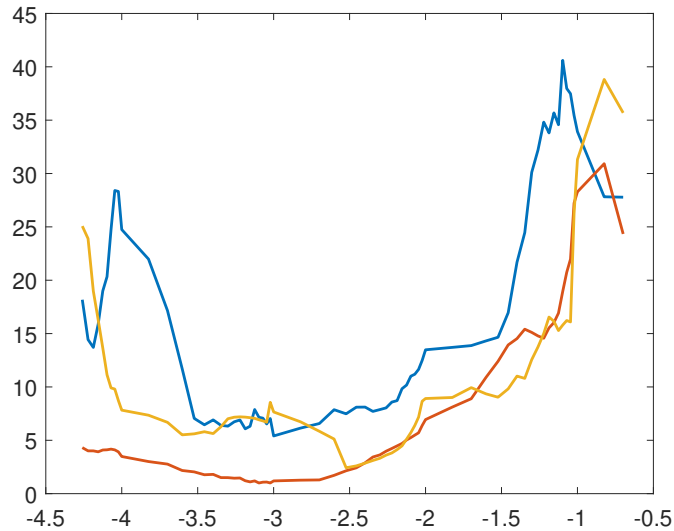
Figure 7.27: Normalized Frobenius norm of the difference between inverted velocity model and true velocity model with respect to the initial level of regularization. Each of the three curves is related to the results provided by one specific method: Red - CRP tomography, blue - stereotomography with 16 data positions, yellow - stereotomography with 36 data positions. The horizontal axis is in log10 scale. This axis shows the relation between the sizes of the regularization term R by the original tomographic objective function $(S - R)$ at the first iteration. Then, the value of -3 indicates that this relation amounts 0.001 or, in other words, indicates that, at first iteration, the regularization term R represents 0.1% of the original objective function $(S - R)$.

The horizontal axis of the graphic is displayed in log10 scale. It indicates the log10 of the relation $\dfrac{R}{(S - R)}$, where R is the value of the regularization operator at first iteration and S is the value of the objective function for the specific tomography method at first iteration. Therefore, $S - R$ corresponds to what could be called original tomographic objective function. In other words, the value of the objective function that would be computed without the presence of the necessary regularization term. This was the way found to turn the regularizations comparable between different methods and approaches. Furthermore, it allows a better evaluation of the graphic, since it is possible to identify how much of relative regularization is necessary for each approach to constrain the proposed model. For example, the value of -3, at horizontal axis, indicates that the regularization term R initiates the inverse process with a value that amounts 0.1% of the original objective function $(S - R)$.

Figure 7.27 indicates, for this particular experiment, that CRP tomography method can be a

slightly more robust technique with respect to the particular choice of initial regularization parameter. Note how the quality of the CRP tomography final velocity model still presents reasonable values while the initial regularization term becomes smaller. Furthermore, for most of initial regularizatinon term values, CRP tomography method inverted models with better quality, here measured as a Frobenius norm of the matrix which represents the difference betwenn inverted and true velocity models. The same experiment was made using norm 2 of the difference between these matrices, and the main features of the graphic did not change. This graphic is not exhibited here.

Note how tomography methods are sensible to the particular choice for initial level of regularization. For higher levels of initial regularization term, the quality of the inverted velocity model is usually not good. Under these levels for initial regularization tem, the optimization function is dominated by the regularization term and, therefore, inverse tomographic process is left aside. On the other hand, small levels of initial regularization term turns the inverse process too unstable and, hence, meaningless solutions are provided. If the graphic of Figure 7.27 would be extended to consider even more smaller values for initial regularization, also CRP tomography would return meaningless velocity models. However, the important feature illustrated by the previous graphic is that CRP tomography allows, for this experiment, a larger range of values for initial regularization parameter, keeping reasonable quality for inverted velocity model. Although is possible to generate good solutions with stereotomography, the choice of initial value for regularization parameter becomes more restrict. Other aspect that has to be highlighted is that, even if stereotomography is processed with more input data samples (36 for this experiment), CRP tomography method still presents better solutions for this particular test and, which is more important for this experiment, more robustness in respect with the choice of initial value for regularization parameter.

Some examples of the performed tests

To illustrate the results of the previous graphic of Figure 7.27 by examples, two results obtained by CRP tomography and stereotomography performed with 16 and 36 data depth points will be exhibited.

If some seismic tomography experiment has to be performed, an initial choice for initial regularization parameter has to be made. However, before the execution of practical experiments and, moreover, if it is a huge experiment, the search for reasonable initial regularization parameter can be too expensive. Moreover, if the true model is unknown, the measure of good quality for the inverted model is harder to be made. Therefore, suppose that is the case of the present experiment and an arbitrary choice for initial regularization parameter has to be made to run the experiment. For this

task, suppose that an initial amount of initial regularization was made in order to put the relation $\frac{R}{(S - R)} = 0.0001$ at first iteration. In the graphic of Figure 7.27, it would correspond to the horizontal coordinate of -4. Then, by a direct analysis of the previous graphic, just CRP tomography method and, maybe, stereotomography test with 36 data depth points, would return reasonable solutions. In fact, this is what happened. The results obtained by these methods, under this choice of initial amount for regularization term, are illustrated in Figures 7.28, 7.29 and 7.30. Note how the result provided by CRP tomography method is quite good, even by the use of a not so good (for this case) initial value for the regularization parameter. The result presented by stereotomography with the same number of depth data positions is notably meaningless, which is a consequence of the small value applied for initial regularization parameter. However, the method repositioned model depth positions in reasonable positions and the objective function was in fact decreased. In situations where the true velocity model is not previously known, it is not a great feature, since it would indicate a possible good velocity model, which is obviously not the case. On the other hand, the result obtained by stereotomography test with 36 data depth positions is better and quite reasonable. However, the inverted velocity model exhibits more oscillations than the one provided by CRP tomography. In this simple test, CRP tomography technique could play the role of input more internal regularization to the problem, with the use of common-reflection-point information. Also, more rays are applied in this method. Here, the use of more number of data depth positions allowed stereotomography to return an acceptable solution. However, if the choice of the initial regularization parameter would be slightly smaller, then even this approach wouldn't provide reasonable solutions, as the Graphic 7.27 indicates.

Now, suppose that an initial choice of regularization parameter was made in order to put the relation $\frac{R}{(S - R)} = 0.003$ at first iteration. In the graphic of Figure 7.27, it would correspond, approximately, to the horizontal coordinate of -2.5. By a direct analysis of the graphic 7.27, in this case all methods are able to return reasonable solutions. With this particular value, it seems that, when 36 depth positions are considered, stereotomography can return as good solutions as CRP tomography. The results obtained by the methods, under these choice for initial regularization parameter, are illustrated by Figures 7.31, 7.32 and 7.33. Note that all proposed solutions are reasonable, which can be noted by the figures illustrating the vertical slices of the models.

Final remarks about the experiment

This experiment was formulated with unfavorable conditions on purpose. Here, the unfavorable conditions are represented by the considerably small number of input samples for data space. If a more conditioned experiment was considered, the differences between the methods could not be so ev-
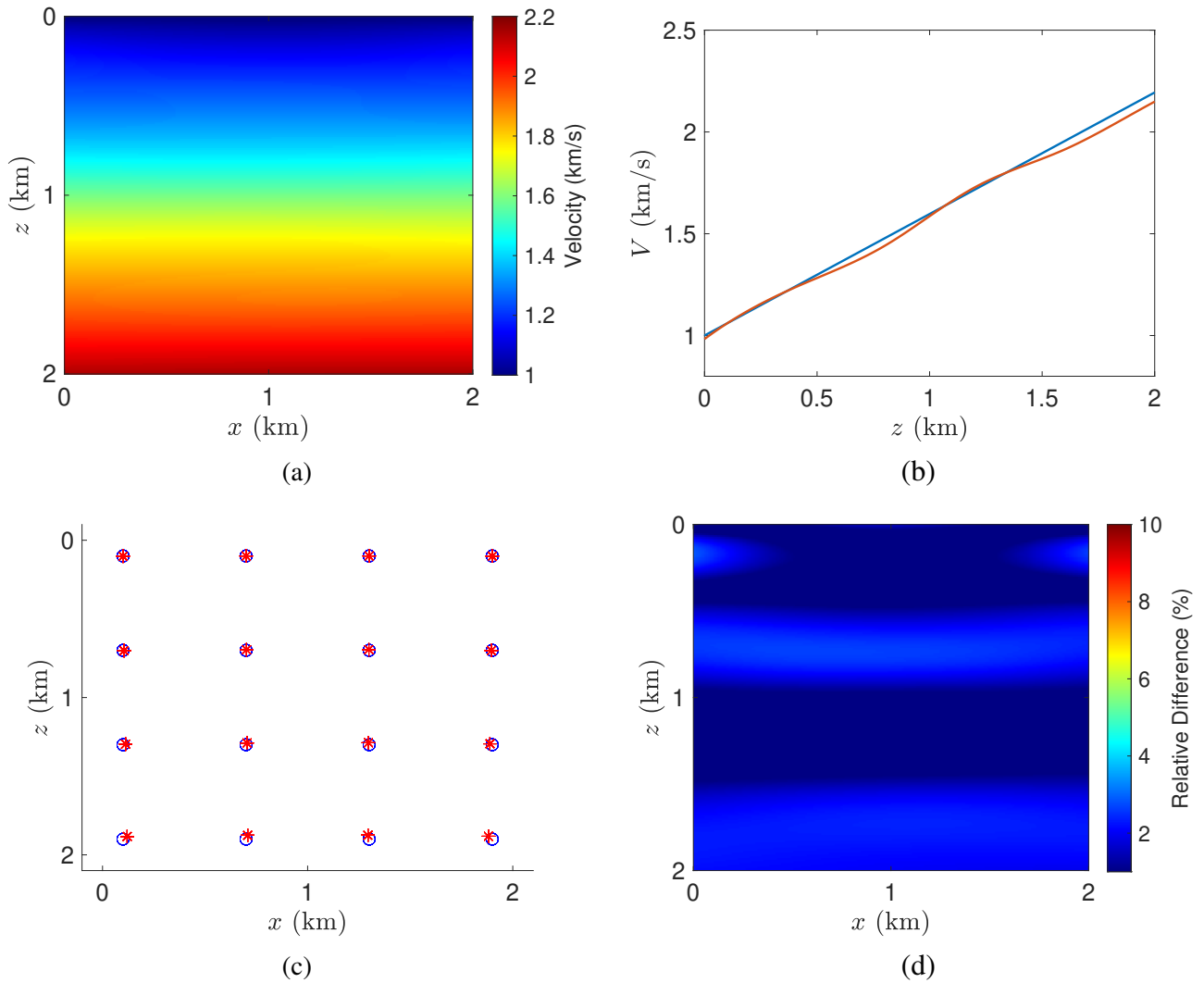
Figure 7.28: (a) Final velocity model proposed by CRP tomography under an initial regularization parameter that accounts for horizontal component of -4 at the Graphic 7.27. (b) Vertical slices of inverted (red) and true (blu) velocity models. The slices were taken at the middle of the models. (c) Inverted model positions (red) and true data positions (blue). (d) Percentage difference between inverted and true velocity models.
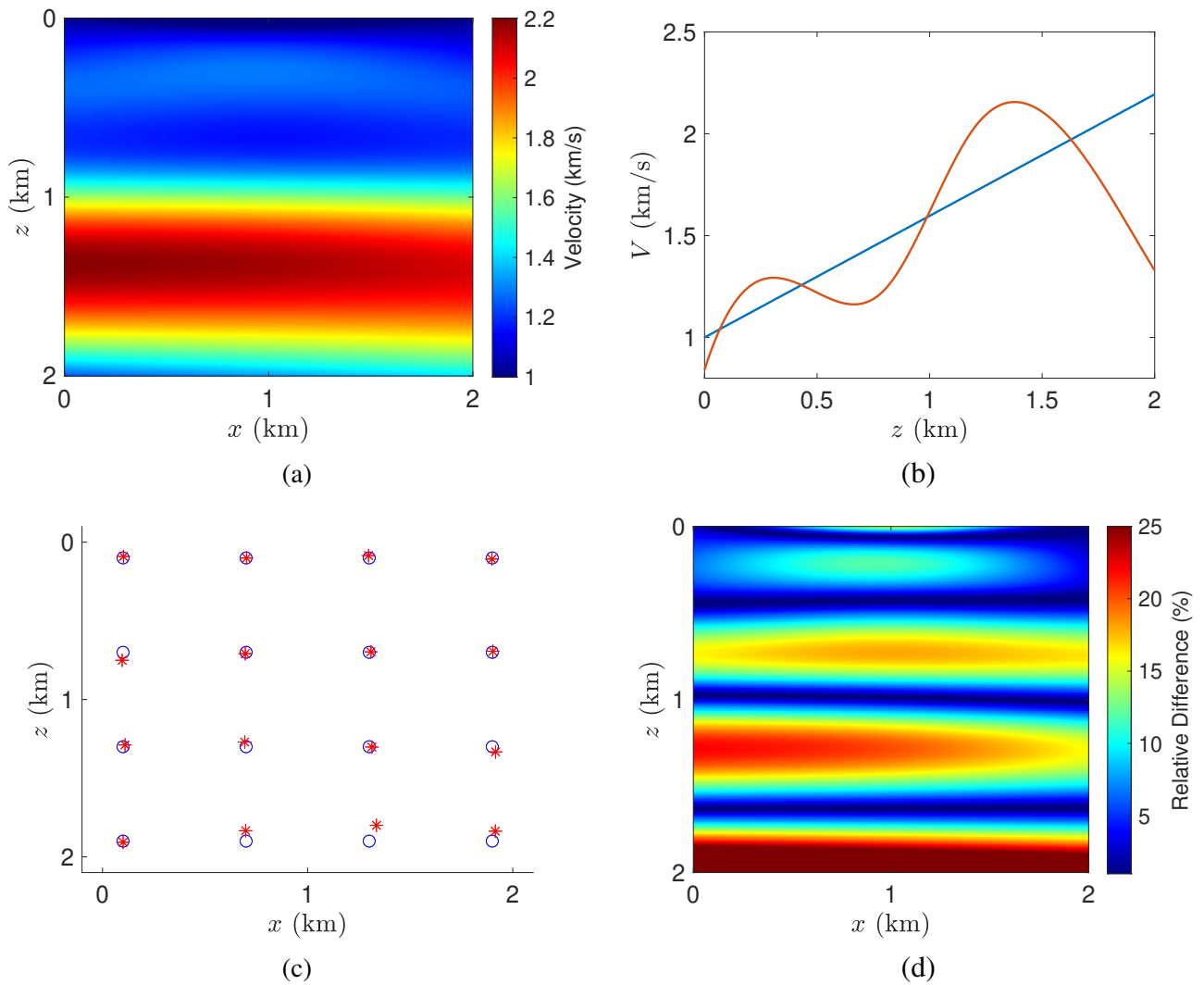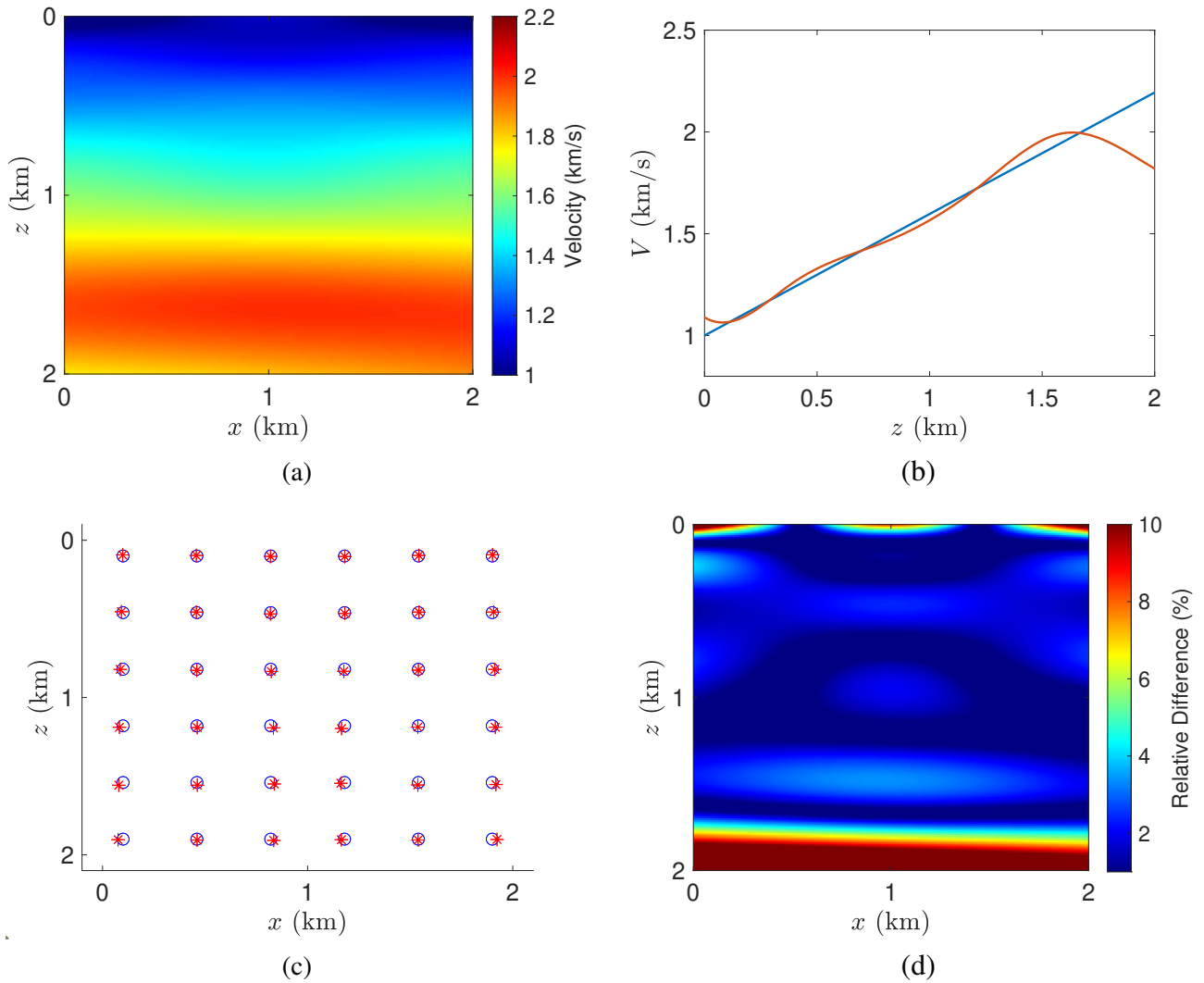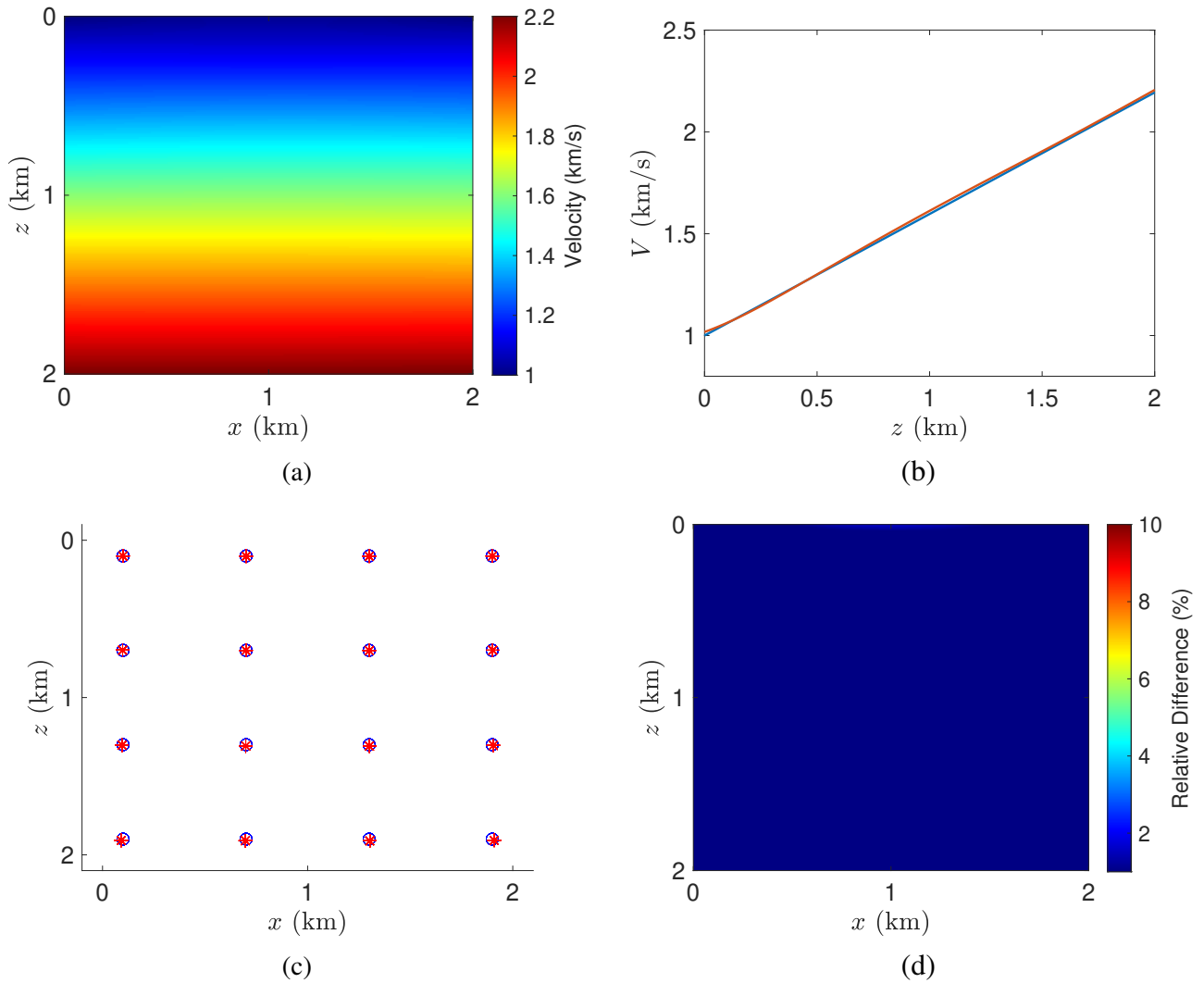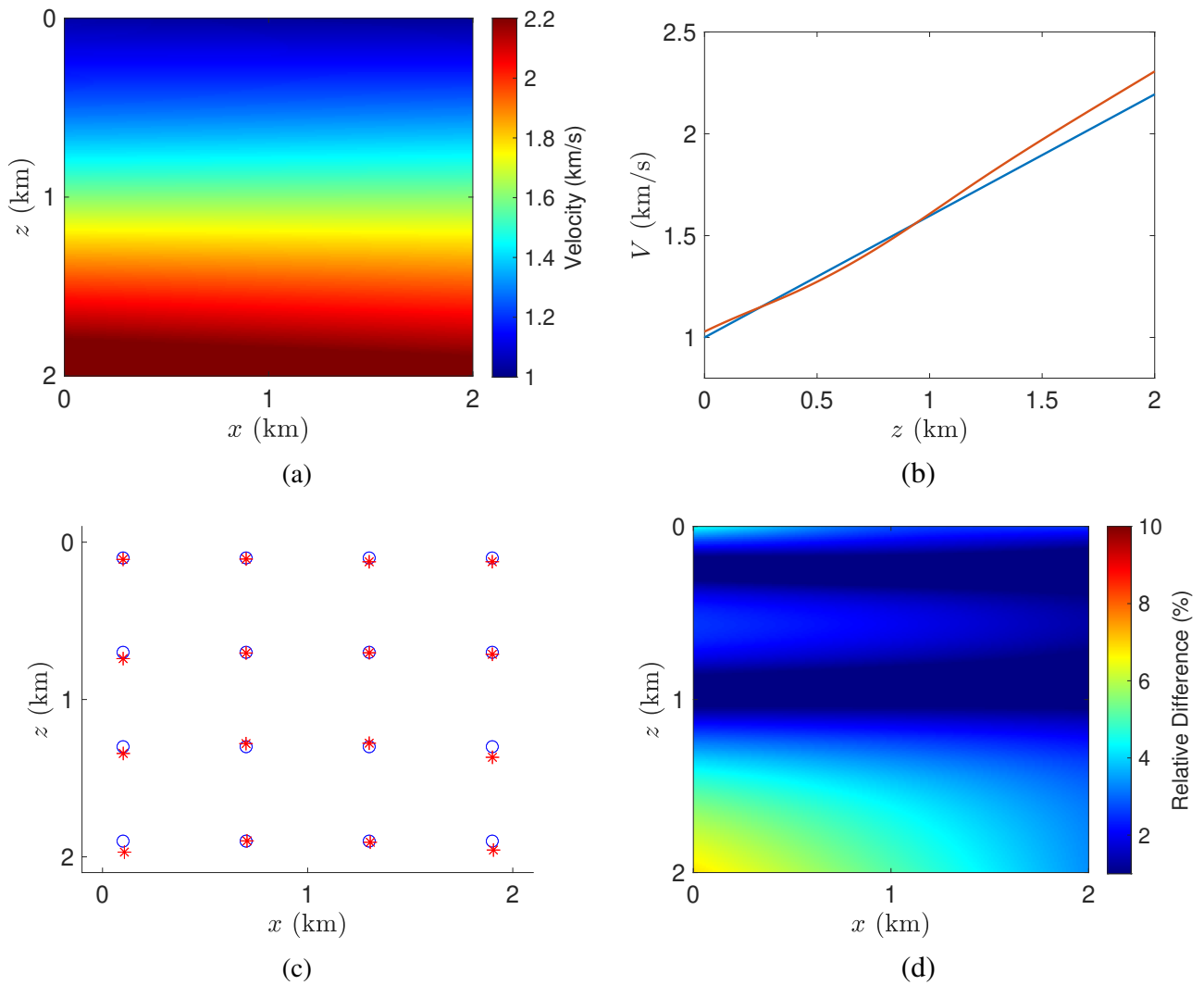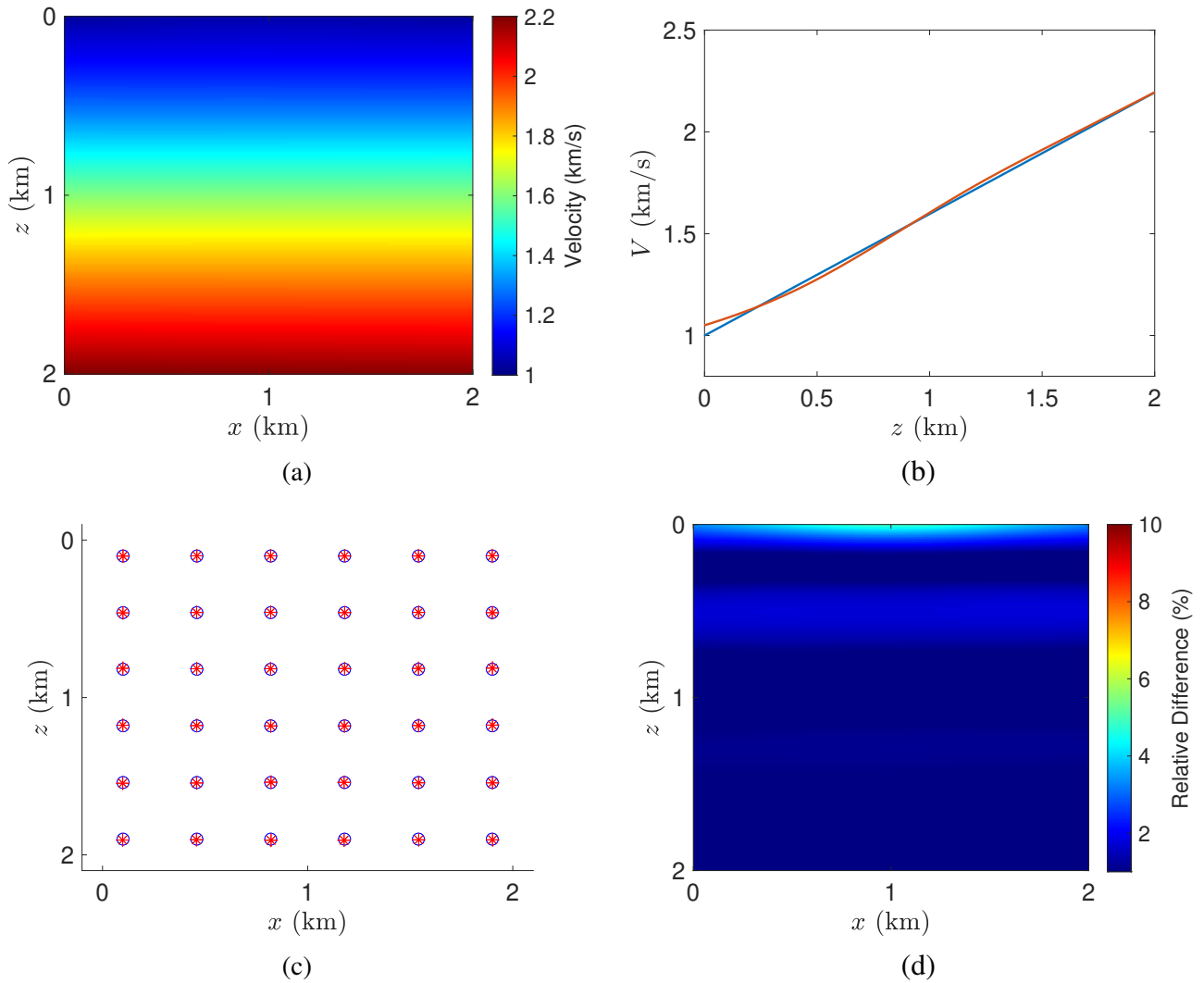
Figure 7.29: (a) Final velocity model proposed by stereotomography, with 16 data depth positions, under an initial regularization parameter that accounts for horizontal component of −4 at the Graphic 7.27. (b) Vertical slices of inverted (red) and true (blue) velocity models. The slices were taken at the middle of the models. (c) Inverted model positions (red) and true data positions (blue). (d) Percentage difference between inverted and true velocity models.

Figure 7.30: (a) Final velocity model proposed by stereotomography, with 36 data depth positions, under an initial regularization parameter that accounts for horizontal component of -4 at the Graphic 7.27. (b) Vertical slices of inverted (red) and true (blue) velocity models. The slices were taken at the middle of the models. (c) Inverted model positions (red) and true data positions (blue). (d) Percentage difference between inverted and true velocity models.

Figure 7.31: (a) Final velocity model proposed by CRP tomography under an initial regularization parameter that accounts for horizontal component of, approximately, -2.5 at the Graphic 7.27. (b) Vertical slices of inverted (red) and true (blue) velocity models. The slices were taken at the middle of the models. (c) Inverted model positions (red) and true data positions (blue). (d) Percentage difference between inverted and true velocity models.

Figure 7.32: (a) Final velocity model proposed by stereotomography, with 16 data depth positions, under an initial regularization parameter that accounts for horizontal component of approximately, -2.5 at the Graphic 7.27. (b) Vertical slices of inverted (red) and true (blue) velocity models. The slices were taken at the middle of the models. (c) Inverted model positions (red) and true (blue) data positions. (d) Percentage difference between inverted and true velocity models.

Figure 7.33: (a) Final velocity model proposed by stereotomography, with 36 data depth positions, under an initial regularization parameter that accounts for horizontal component of approximately, -2.5 at the Graphic 7.27. (b) Vertical slices of inverted (red) and true (blue) velocity models. The slices were taken at the middle of the models. (c) Inverted model positions (red) and true (blue) data positions. (d) Percentage difference between inverted and true velocity models.

ident. The use of a small input data space turned the tomographic problem more dependent of external regularization. It is an important feature, since the analysis of dependence and sensitivity with respect to the regularization term is the main objective of this experiment. Here, CRP tomography was the most robust method in respect with these features. This new seismic tomography technique considers more internal information, the common-reflection-point information, which, somehow, decreases some level of natural instability of the inverse problem. For this same reason, the tests performed by CRP tomography on this thesis could be done with a relative small number of input data samples under small values for initial regularization parameter.

However, this experiment can't be viewed as a standard case that represents all possible experiments. In fact, the unique valley presented by the graphic of Figure 7.27 related to this simple experiment, is not a standard case. Generally, more than one valley, which corresponds to local minimum with respect to the variation of the initial regularization parameter, are presented. Also, the curve that represents CRP tomography will not be, always, the best for all values of the regularization parameters. As this experiment is very simple, the pattern of the graphic kept constant through the decrease of the level of regularization term. However, oscillations may occur in more complex experiments. Moreover, oscillations generally occur. Then, at more complex experiments, for some values for initial level of regularization term, stereotomography can presents better quality on the inverted velocity model solution than the respective CRP inverted velocity model under the same conditions. However, what have been noted so far, during to the different tests performed, is that CRP tomography is less sensitive to the particular choice of initial regularization parameter, which explain the tests already described in this thesis.

Similarities with previous synthetic tests - Laterally Heterogeneous and Soft Marmousi cases: Now, the results obtained during the tests of laterally heterogeneous and soft Marmousi models can be viewed in a more general way. There, an optimization search for the initial value for regularization parameter was not made. An arbitrary amount of the initial value for the relation between regularization term and original tomography optimization function was chosen. Then, all the tests were executed without any change in the value of the initial regularization parameter. There, for that specific values for initial level of regularization, CRP tomography method returned reasonable final model solutions, while stereotomography couldn't do the same. In the previous graphic context, for that chosen level of initial regularization, the curve related to sterotomography would be above the curve related to the CRP tomography method. Then, bigger data space was provided to stereotomography and the respective result was improved. In the context of the previous graphic, the curve related to the addition of more data positions is under the curve related with less data positions. Thus, for that case, as both CRP tomography and stereotomography with more data positions presented very good solutions, the

curves that would represent both approaches would be closer to each other.

7.6 The Three-layer Test

Inspired by the discussion of last section, CRP tomography will be tested by the three-layer test. Three-layer model test is displayed in the Figure 7.34, among with a vertical slice of the velocity model.
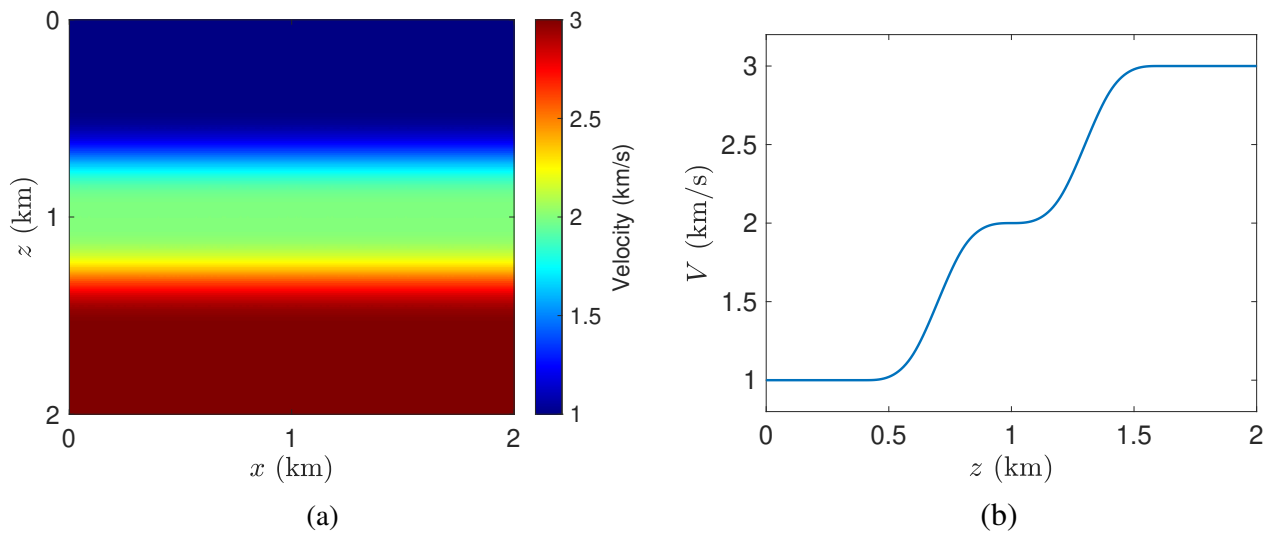

Figure 7.34: (a) Three-layer velocity model test. (b) Vertical slice of the velocity model. The slice was taken at the middle of the model. Note that the second layer is smaller than the others. Note also the abrupt velocity variation in vertical direction.

Three-layer test was very important for the present research, since it was decisive to the choice of not incorporate curvature parameter in CRP tomography method (see the discussion in Appendix B). In respect with the results presented by stereotomography on the three-layer test, first the method inverted this model test by the use of data samples provided by one hundred input data depth positions. Then, the method was challenged to invert the model test with subsequent decrease of the number of data depth positions. Thus, the method inverted the model test successfully with 49 data depth positions but, by the use of just 36 data positions, the method failed in detect the presence of the second layer, the smallest of them. Would CRP tomography be capable to reasonably invert the model from three-layer test by the use of input data samples provided by just the same 36 data depth positions?

Before answer the previous question, CRP tomography method was challenged to, at least, repeat the performance of stereotomography and provide good final velocity model solutions by the use of input data space generated by 49 data depth positions uniformly distributed through the model. In order to allow comparisons between the results of both methods, the same parametrization were applied. They are summarized as follows:

Input observed-data space: To generate observed-data space, 49 data depth positions were uniformly displayed through three-layer model (see Figure 7.35). These positions are exactly the same ones used before in stereotomography test with 49 data positions in Chapter 6. From each of these positions, ten pairs of rays were traced through the model and the kinematic parameters of emergence positions, traveltime and slopes were computed at surface line. These rays were propagated with initial double aperture, with respect to vertical direction, varying from $5°$ to $30°$. All traveltimes related of rays starting from the same common-depth-position were summed. Therefore, data space is composed 49 data families, each of them with a total data traveltime and ten samples composed by two data emergence positions and two data slope parameters.

Initial model space: An homogeneous initial velocity model of 1km/s will be used, which is the same initial velocity model applied to stereotomography test. The B-spline interpolation knots, used to build both three-layer model test and velocity models iteratively constructed by CRP tomography inverse process, were distributed at the same positions of stereotomography test. Ray-model space was initialized with the proposed initialization procedure for CRP tomography, returning 49 model families, each of them composed by one initial model position in depth and ten pairs of initial model slopes. Initial model depth positions are illustrated by Figure 7.35.

Initial regularization weight parameter: Following what was done in stereotomography test, a previous search was made in order to find a good initial value for regularization parameter λ. Due to this previous search, λ was set in order to, at first iteration, the relation between the regularization term with respect to the objective function would be 3.10^{-6}. To calibrate regularization term, the same values used for stereotomography test were applied: $\epsilon_{zz} = 10^{-3}$, $\epsilon_{xx} = 1$ and $\epsilon_{vv} = 10^{-4}$.

CRP tomography results with 49 **data positions:**   The results provided by CRP tomography for three-layer model test are illustrated by Figure 7.36. Firstly, remind that the main challenges offered by this test are the abrupt velocity variation in vertical direction and the existence of a small second layer. Also, as the true velocity model presents strong vertical variations, the regularization applied
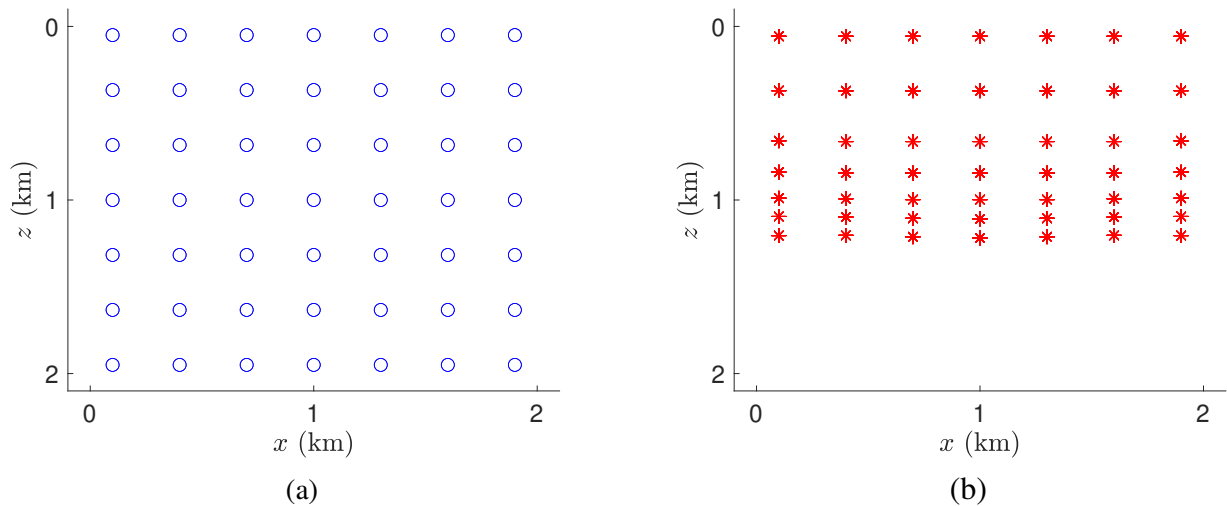
Figure 7.35: (a) Data positions for the test with 49 data points. (b) Respective initial model positions returned by CRP tomography initialization procedure under the initial homogeneous velocity model of 1km/s.

plays against the inversion process. In this case, the challenge is to set a good trade-off between regularization and invert a model velocity near the true velocity. As illustrated by Figure 7.36, CRP tomography succeeded in the task of provide a good final velocity model by the presence of just 49 data positions. Note that CRP tomography could identify the existence of a small layer at the middle of model and also provided good estimates for the velocity values of the different layers. Also, model depth positions were repositioned very close to the true data positions.

CRP tomography results with 36 **data positions:**   Now, the question formulated at the beginning of this section will be answered. Despite the good performance exhibited in inverting three-layer test with just 49 data positions, CRP tomography method failed in the task of provide a good inverted velocity model when just 36 data positions, uniformly distributed through the model, are provided. The results will not be presented here, but they are very similar to the results presented by stereotomography with this same parametrization (see Chapter 6). Therefore, under just 36 data positions, the method no more is capable to identify the second layer, the smallest of them. For both methods, many initial regularization parameters were tested, without any success case. Remind that, as this model represents a trade-off between the smoothness proposed by the regularization term and the strong velocity variations presented by the three-layer velocity model, this test is particularly very sensible to the choice of initial regularization parameter.

(a)

(b)

(c)

(d)
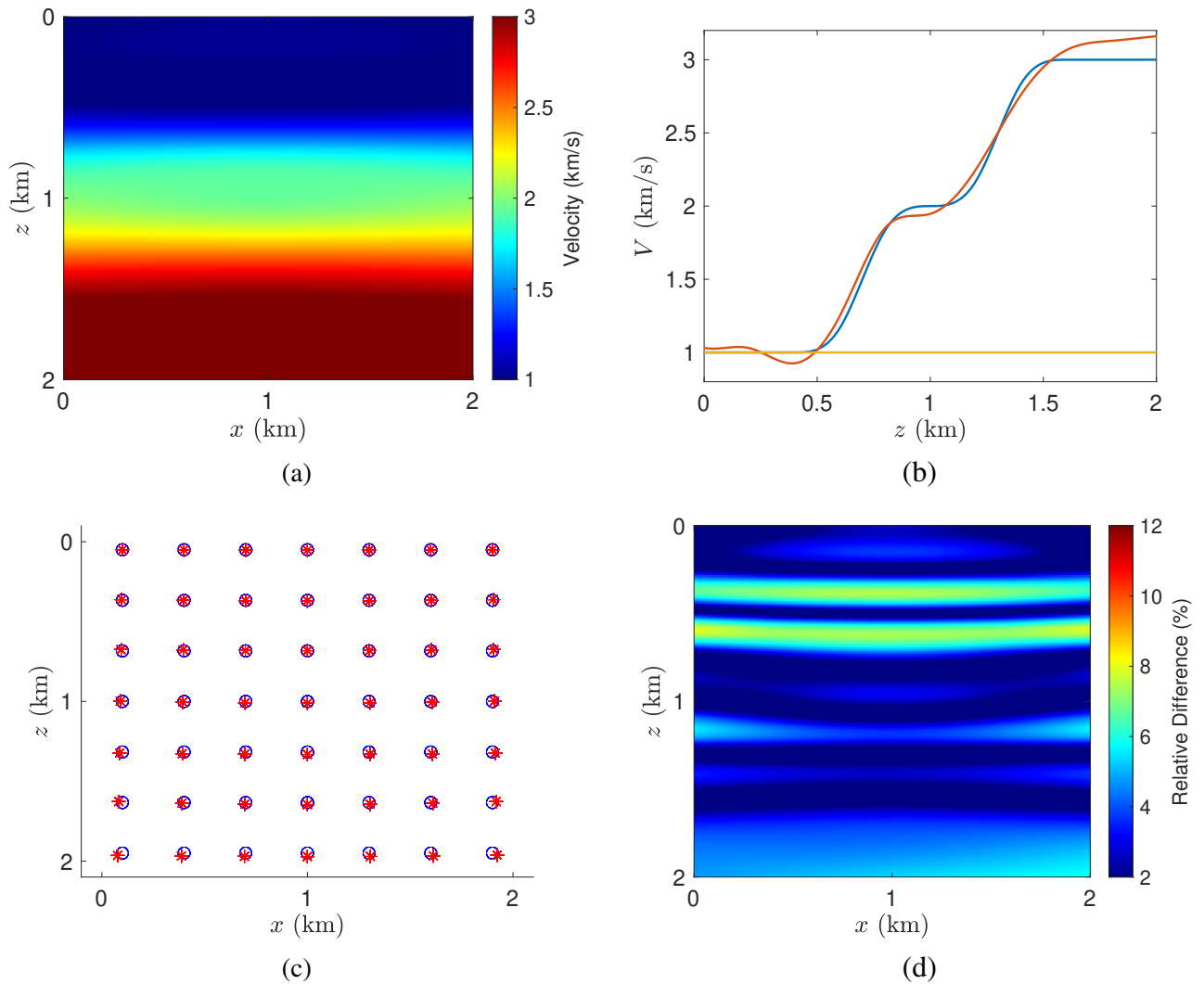
Figure 7.36: Three-layer test - CRP tomography results with 49 data points. (a) Inverted velocity model proposed by CRP tomography. (b) Vertical slices of inverted (red), true (blue) and initial (yellow) velocity models. Slices were taken at the middle of the models. (c) Inverted model positions (red) and true data positions (blue). (d) Percentage difference between inverted and true velocity models.
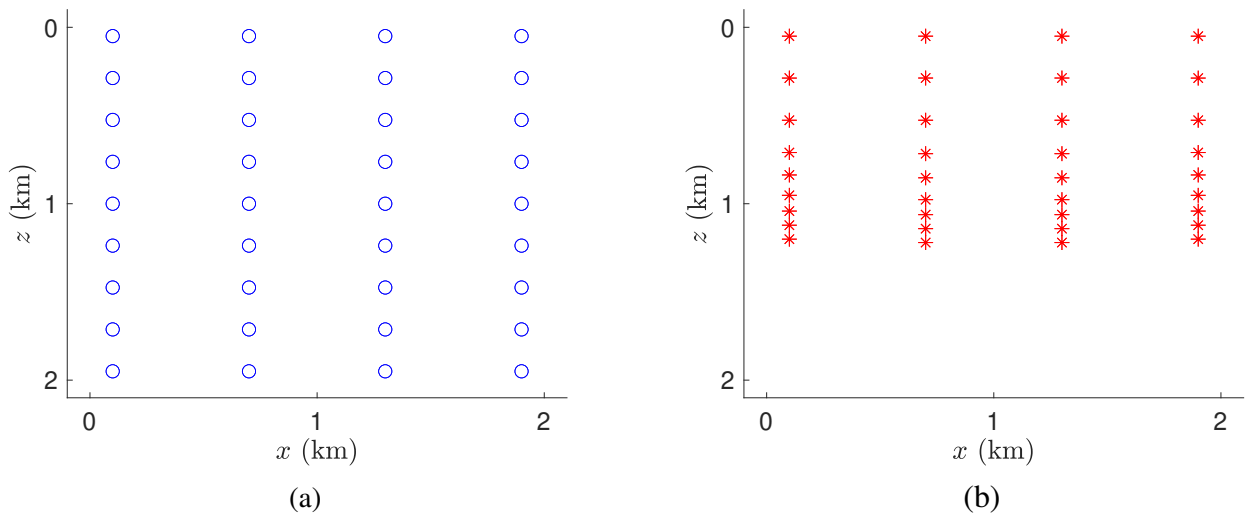
Figure 7.37: Three-layer test with 36 data positions distributed mainly through vertical direction. (a) True data positions. (b) Model initial positions returned by CRP tomography initialization process.

Another distribution of data positions: For this particular model, where the velocity presents strong variations in vertical direction at some specific partis of the model, the use of common-depth-position, and further use of more number of rays, did not help to constrain the model, as it did in three-point test (and other synthetic tests already reported in this thesis). There, the true velocity model was described by a linear variations of the velocity. Then, to recognize the pattern of the linear velocity variation, just 3 data points in depth were necessary. However, to recognize the "jumps" in vertical direction presented by three-layer model test, a refined distribution of data depth positions is necessary. In fact, it is possible to invert three-layer test with just 36 data depth positions. However, the positions can't be uniformly distributed through the model. To recognize all the "jumps", the important information is the existence of sources of information (data depth positions) distributed in the most dense way through vertical direction. Therefore, if the previous parametrization is kept and data positions are distributed mainly in vertical direction, as it is illustrated by Figure 7.37, CRP tomography is capable to provide good final velocity model for three-layer test.

The results provided by CRP tomography under this new distribution of the 36 data positions are illustrated by Figure 7.38. Note that, in some aspects, it is an even better result than the previous one with 49 data points, due to the most dense distribution of data depth positions through vertical direction, which is the important information demanded by this test.

The good result under this new parametrization is not an exclusivity of CRP tomography method. If the same strategy of redistribution of data depth positions is done for stereotomography, the method also provides good final velocity model solution. A considerable drawback of this strategy
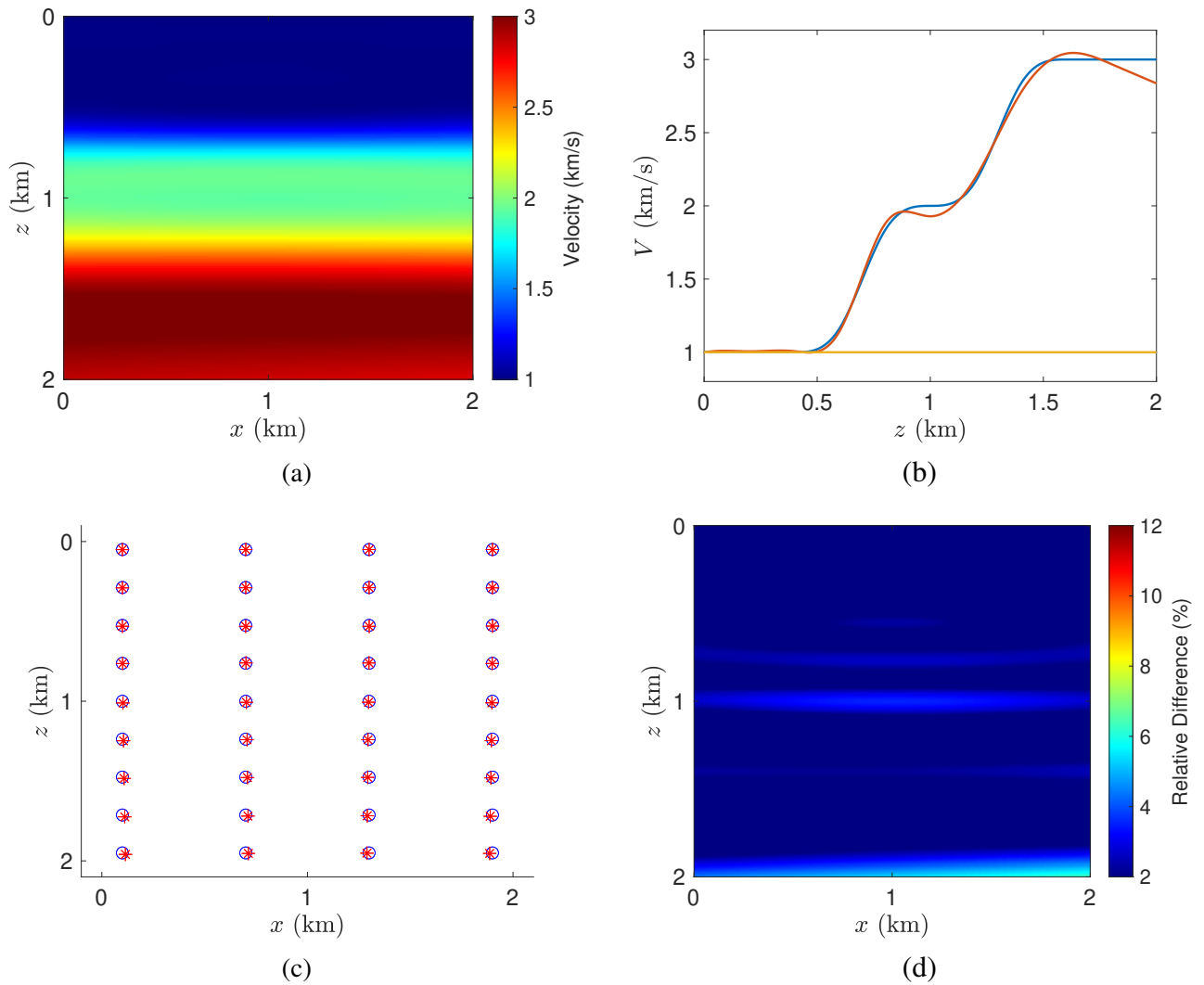
Figure 7.38: Three-layer test with 36 data positions distributed mainly through vertical direction. (a) CRP tomography final velocity model. (b) Vertical slices of inverted (red), true (blue) and initial (yellow) velocity models. Slices were taken at the middle of the models. (c) Inverted model positions (red) and true data positions (blue). (d) Percentage difference between inverted and true velocity models.

is that it couldn't be reproduced in real applications. While in the present synthetic test, it's possible to choose data depth locations, in real applications, it's generally not possible at all.

7.7   Second Laterally Heterogeneous Model Test

Before finishing the chapter, one last test will be exhibited. It is named second laterally heterogeneous test, due to the presence of noted lateral velocity variations through all over the velocity model, while the term *second* is beacause of the previous test (with a different model) performed in section 7.3. This model is illustrated in Figure 7.39. The fact that these variations are presented in a small grid of dimension 2km×2km, turns the velocity heterogeneity more noted. Even near the surface line, velocity lateral heterogeneity is presented. Other challenge proposed by this test is that the direction of velocity variation slightly changes through the model. It can be noted by the velocity contours. At surface, velocity lateral heterogeneity presents different direction than those presented at regions near the bottom line. Another difficulty presented by this model test is that it was not constructed by means of direct B-spline interpolation. Thus, it is not previously known if this model could be perfectly reconstructed by the interpolation rule used by CRP tomography method.
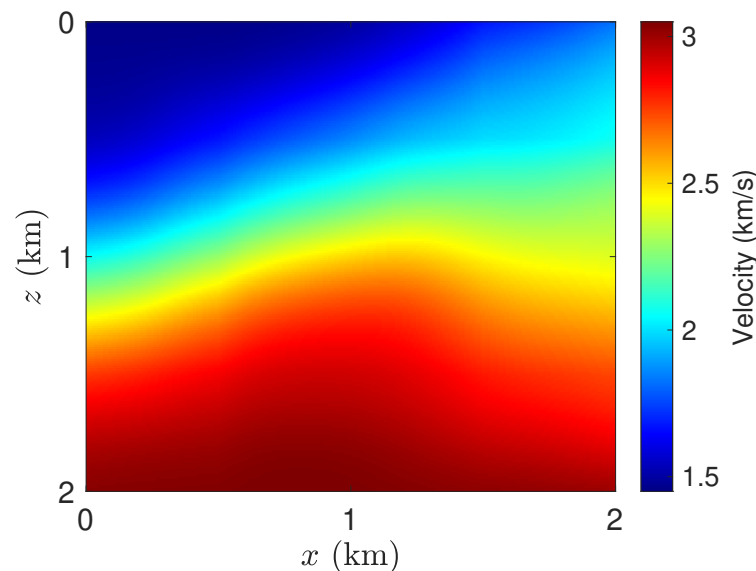
Figure 7.39: Second laterally heterogeneous velocity model test. Note the presence of lateral velocity variations through all over the model.

In order to turn the inverse process even more challenger, an initial constant velocity model of 1.5km/s, Figure 7.40, was considered. As the proposed true velocity model presents strong lat-

eral variation even at surface line, the initial velocity model does not resemble true velocity in any aspect. Despite the bigger challenge, the use of a constant velocity model has the objective of keeping the evaluation of the capability of CRP tomography to constrain different kinds of models under unfavorable conditions.
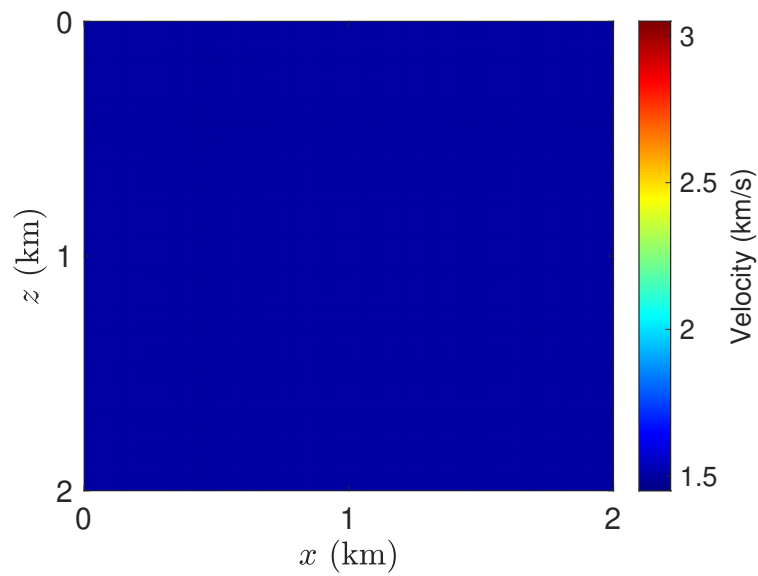
Figure 7.40: Initial homogeneous velocity model for CRP tomography second laterally heterogeneous model test. The proposed initial velocity model does not resemble true velocity in any aspect.

The parametrization used for this last test is summarized as follows:

Input observed-data space: To generate observed-data space, 196 data depth positions were uniformly displayed through the model (see Figure 7.41). From each of these positions, six pairs of rays were traced through the model and the kinematic parameters of emergence positions, traveltime and slopes were computed at surface line. The rays were propagated with initial double aperture, with respect to vertical direction, varying from 8° to 40°. All traveltimes related with rays starting from the same data common-depth-position were summed. Therefore, data space is composed 196 data families, each of them with a total data traveltime and six samples composed by two data emergence positions and two data slope parameters.

Initial model space: The homogeneous velocity model of Figure 7.40 was applied as initial velocity model. During the iterative inverse process, velocity model are constructed using B-spline interpolation with knots uniformly distributed through the model, with both horizontal and vertical spacing of

0.2km. Ray-model space was initialized with the proposed initialization procedure for CRP tomography, returning 196 model families, each of them composed by one initial model position in depth and six pairs of initial model slopes. Initial model positions are displayed in Figure 7.41. Note that, because of the use of a lower constant initial velocity model, the initial model positions are concentrated most at the shallower half of the model, which is not a good initial condition.

Initial regularization weight parameter: Initial regularization parameter λ was set in order to, at first iteration, the relation between the regularization term with respect to the objective function was equal to 8.10^{-4}. To calibrate regularization term, the following values were considered: $\epsilon_{zz} = 4.10^{-3}$, $\epsilon_{xx} = 8.10^{-3}$ and $\epsilon_{vv} = 10^{-4}$. Note the use of a smaller value for ϵ_{xx}, in comparison with previous tests, due to the presence of remarkable lateral heterogeneity.

CRP tomography results: The final model proposed by CRP tomography, under the previously mentioned conditions, is illustrated by Figure 7.42. Taking into account that the proposed second laterally heterogeneous model test is not a simple model test, due to the heterogeneities presented through all over the model and, reinforced by the use of a initial constant velocity model, the results proposed by CRP tomography are reasonably good. Until 1.5km in depth, where more information are covered by input data space, relative errors fall under 3% (see Figure 7.43). At regions near the bottom line, relative errors around 5% appear. Despite the corners of the model, where almost no information is available, the relative errors at bottom region are concentrated in just one region. Note how the velocity contour line of the velocity model, except at bottom area, have been well reconstructed by CRP tomography. Model depth positions were also well repositioned by CRP tomography, as illustrated by Figure 7.44.

A velocity model building procedure: Following previous synthetic tests, CRP tomography was capable, once again, to reasonably invert the proposed model test by the presence of a simple initial velocity model. On a more general picture of the role process to reach a final velocity model, these inverted models can be used as input, for example, for full waveform methods (FWI), in order to recover more details (high-frequence content) about the velocity model. While FWI is very dependent of a good initial velocity model, CRP tomography has been shown to be a robust technique with respect to initial velocity models. Therefore, a very simple velocity model can be firstly used as input to the process. Then, the smooth final velocity model provided by CRP tomography can be used as input for FWI application, providing a more detailed high resolution final velocity model, which gives rise to a velocity model building procedure. This role process will be illustrated in chapter 9. First, in
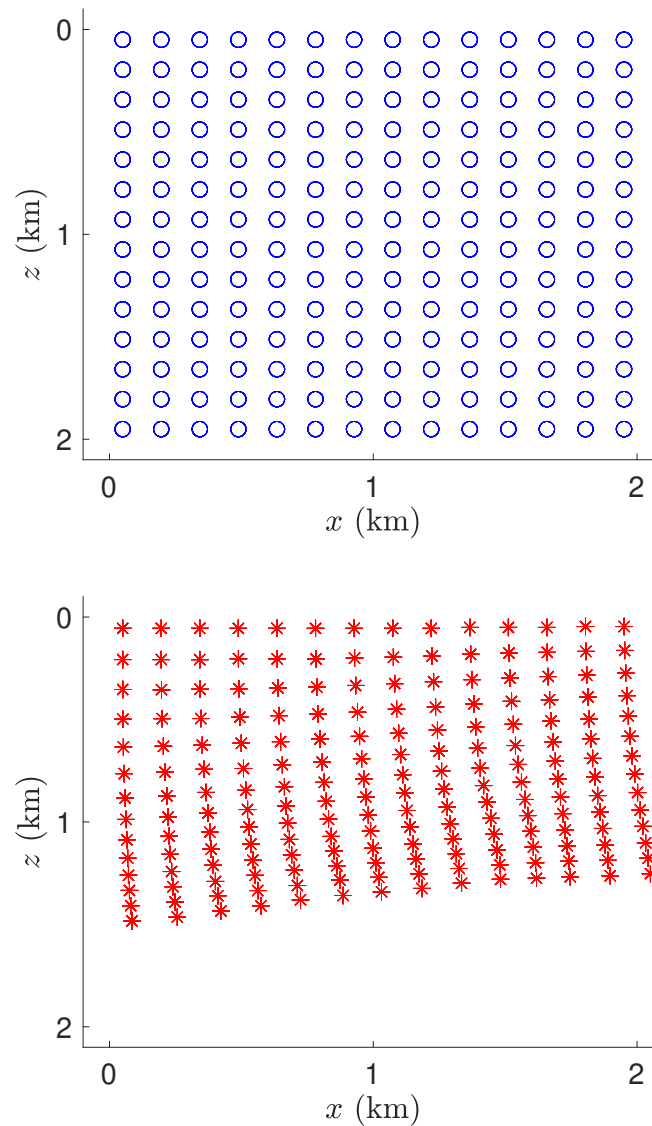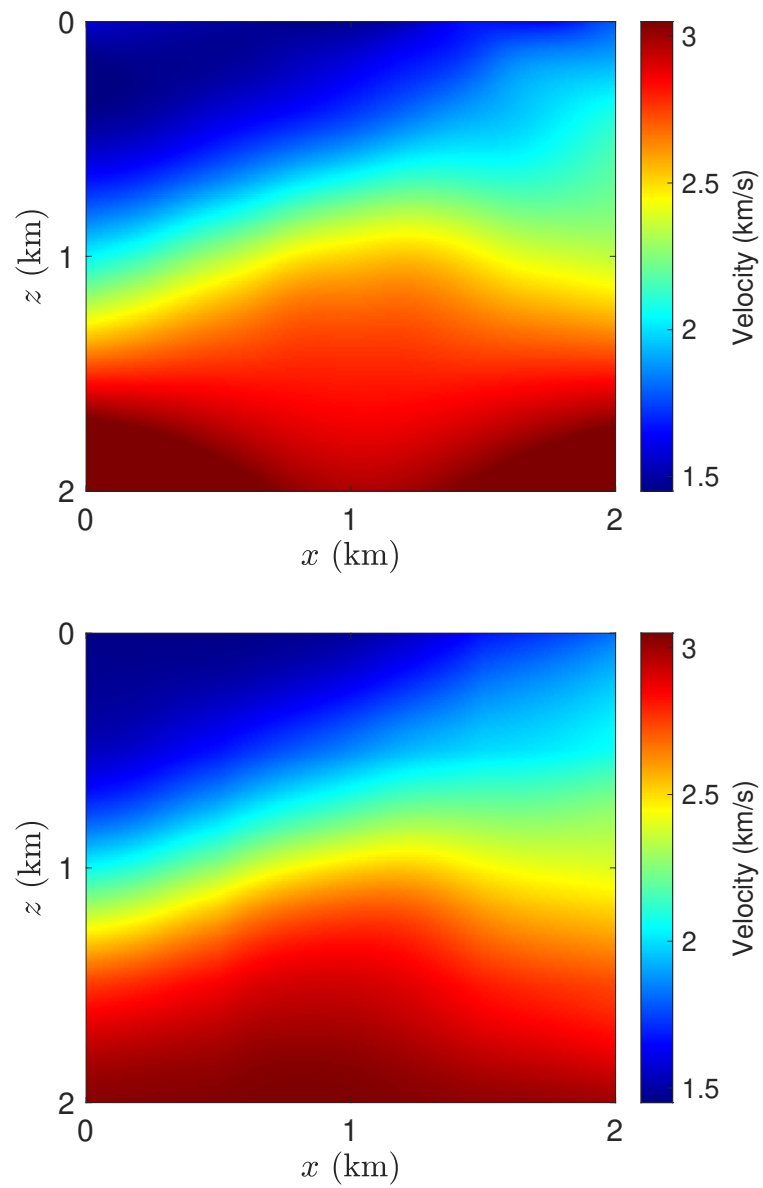
Figure 7.41: Second laterally heterogeneous model test. Top: Data positions in depth used to generate ibserved-data space by means of direct ray-tracing. Bottom: Initial model positions returned by CRP tomography initialization procedure under an initial homogeneous velocity model of 1.5km/s. Note that, because of the use of a lower constant initial velocity model, the initial model positions are concentrated most at the shallower half of the model.

Figure 7.42: Second laterally heterogeneous model test. (a) CRP tomography inverted velocity model. (b) Second laterally heterogeneous velocity model test.
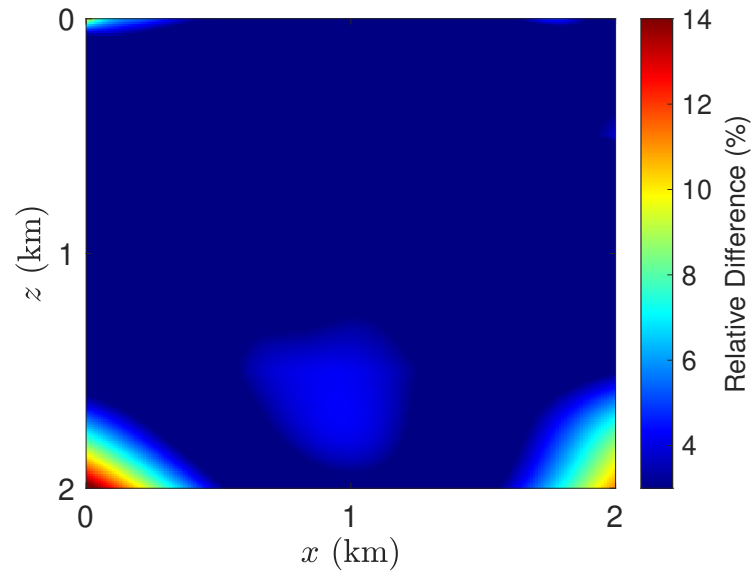
Figure 7.43: Second laterally heterogeneous model test. Percentage difference between inverted and true velocity models.
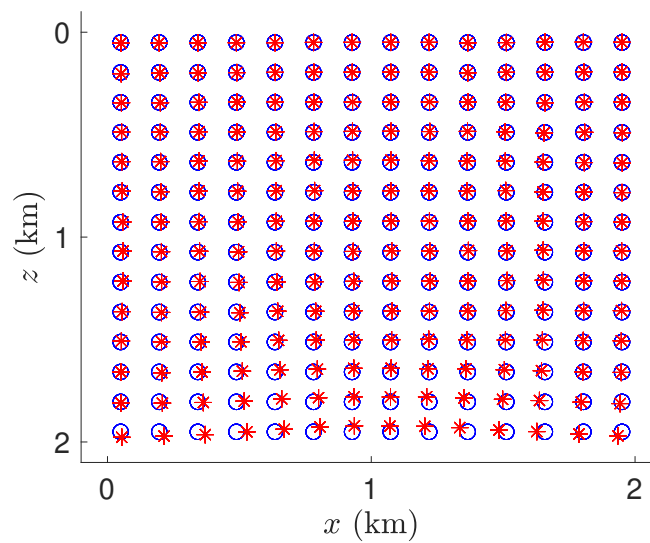
Figure 7.44: Second laterally heterogeneous model test. Percentage difference between inverted and true velocity models. Inverted model positions (red) and true data positions (blue).

chapter 8, CRP tomography will be tested on even more challenging synthetic tests, by the presence of noisy input data and data depth positions not uniformly distributed through the model.

Chapter 8

Further numerical tests - noisy input data and interfaces

The objective of this chapter is to test the proposed CRP tomography method on synthetic experiments that simulate more realistic situations. In previous chapter, CRP tomography method was tested on synthetic tests with error-free input data parameters. Moreover, the data positions, which accounts for the source of data information in depth, were generally distributed uniformly through the true velocity model. This uniform distribution guarantees that almost all parts of the true velocity model were covered by input information on input data space.

None of the previous assumptions hold for real applications. In fact, as data space would be composed by kinematic parameters extract from seismic data by a picking procedure, input data space would not be an error-free set. Moreover, the pickings are usually performed along reflection events on seismic data, which also turns the uniform distribution of data positions a non-realistic assumption.

As this thesis does not aim to research and construct a picking procedure to build data space for CRP tomography, data space will be, once again, generated by direct ray-tracing on true velocity model. However, in this chapter, noisy data will be added to computed data parameters and will be provided as input for CRP tomography. Moreover, in this chapter, data positions will not be uniformly distributed through the model. Data positions will be placed along synthetic interfaces.

The modifications proposed for the tests of this chapter are summarized as follows:

Noisy input data space: In further real situations where CRP tomography can be applied, data space would be derived from a picking procedure on seismic data. Moreover, some kinematic param-

eters would not be directly extracted from prestack seismic gathers. This is the case of input slope parameters, estimated by coherence analysis along traveltime equations on seismic data. Therefore, in further real situations, data space will be composed by not perfect accurate input kinematic parameters.

Uncertainty in data traveltime and position paramaters are dominated by picking errors. On the other hand, uncertainty in data slope parameters are dominated by coherence analysis, limitations of estimation procedure and, moreover, on the noise level in prestack data. Therefore, the relative expected magnitude for errors in data slope parameters is bigger than the expected errors in traveltime and position parameters.

In this chapter, the robustness and stability of proposed CRP tomography method with respect to noisy input data will be studied by means of practical experiments. For this propose, random noise will be added to data space built by direct ray-tracing. To turn the experiment more realistic, a noise of relative bigger magnitude will be added to input slope parameter.

Data positions placed along synthetic interfaces: In future real applications of CRP tomography method, each sample of data space will be related to a specific picking performed on seismic data. Usually, pickings are performed just on reflection events of seismic data. On the other hand, in this thesis, synthetic input data space is generated by direct ray tracing on true velocity model. Thus, data positions are placed in depth on true velocity model from where rays are traced until surface line, where kinematic parameters are computed and used to compose input data space. Note that, in the synthetic experiments that illustrate this thesis, data positions in depth play the role of picking locations on seismic data.

Almost all synthetic tests performed so far in this thesis for CRP tomography method were executed under a uniform distribution of data positions. This fact obviously assist the tomographic inversion process. Although is not a realistic assumption, this assumption is usually applied to test tomography methods on synthetic experiments (see, e.g, Billette and Lambaré (1998), Duveneck (2004b)).

In this chapter, a different approach for data position distribution will be applied. Synthetic interfaces will be proposed together with the model tests. Data positions will be placed just on these interfaces. Therefore, the synthetic interfaces will play the role of locations where reflection events occur in depth. Hence, data locations will not be uniformly distributed, being placed just along the proposed interfaces. Moreover, to build input data space, rays will be traced from these data positions with initial slopes given by a double aperture with respect to the normal vector of these interfaces. In all tests executed so far, these rays were traced with double aperture with respect to the vertical

direction.

In next sections, two velocity models with synthetic interfaces will be used to test CRP tomography method under non-uniform data distribution and input noisy data. Stereotomography will also be performed for comparison reasons.

8.1 First Synthetic Experiment

The first synthetic experiment consists in a velocity model with a region of high velocity localized at the middle of the model. Figure 8.1 exhibits the proposed velocity model.
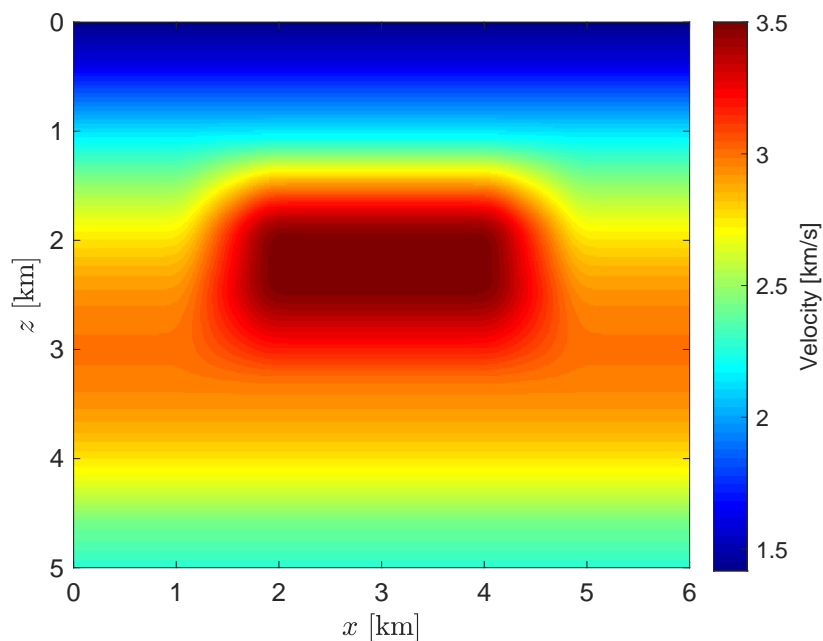

Figure 8.1: Velocity model for first experiment. The model presents a region of high velocity at the middle of the model

The velocity model is placed on a grid of 5km×6km. At the shallow half of the model, until the region of high velocity is reached, velocity presents a crescent velocity variation mainly on vertical direction. At the deeper half, the velocity decreases from the region of high velocity until the bottom line. At the middle of the model, lateral heterogeneity is presented, due to the presence of the high velocity region. The region of high velocity at the middle of the model presents a remarkable challenge for seismic tomography applications (see, e.g, Neckludov et al. (2006)).

Both CRP tomography and stereotomography will be tested on this model. Firstly, numerical tests will be performed with perfect accurate data space. The objective is to first investigate the performance of both methods on a noise-free test. However, the first test will carry one of the previous proposed challenges: data positions will be distributed along synthetic interfaces. Further, a second test will be performed under the presence of noisy input data, where the robustness of CRP tomography in respect with no perfect accurate data will be investigated.

Synthetic interfaces: To perform the first test with data positions distributed along synthetic interfaces, some interfaces were proposed to the model. The synthetic interfaces are illustrated by Figure 8.2. Note that synthetic interfaces follow the velocity variations. Data positions are distributed along these proposed structures. For this experiment, 198 data positions were considered. The distribution of data positions along synthetic interfaces is illustrated in Figure 8.3.
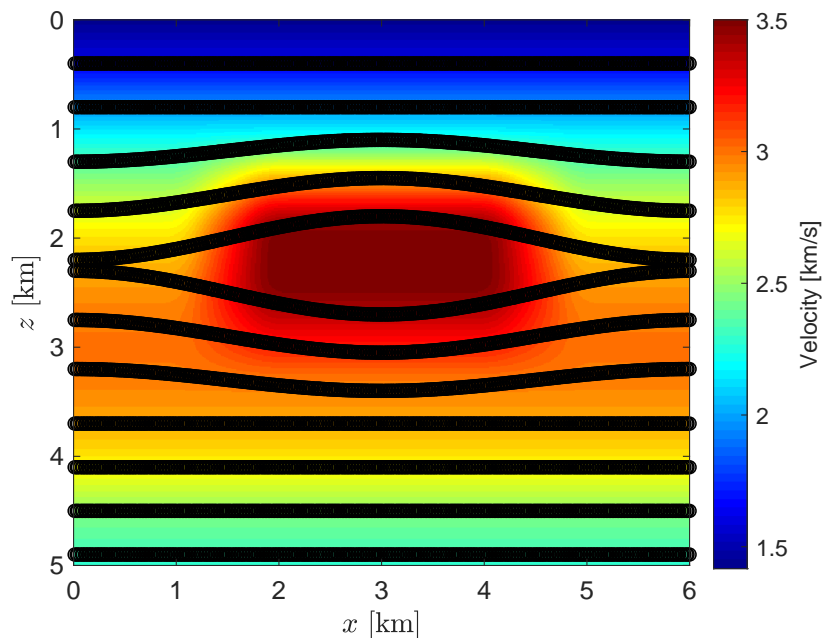
Figure 8.2: Velocity model with synthetic interfaces for first experiment.

Note that, under the premise of placing data positions just along synthetic interfaces, the region of high velocity at the middle of the model is not covered by data points. Moreover, this high velocity region represents the major challenge of this experiment. Therefore, this experiment will test if CRP tomography and stereotomography methods can recover this region under these conditions. First, stereotomography will be tested.
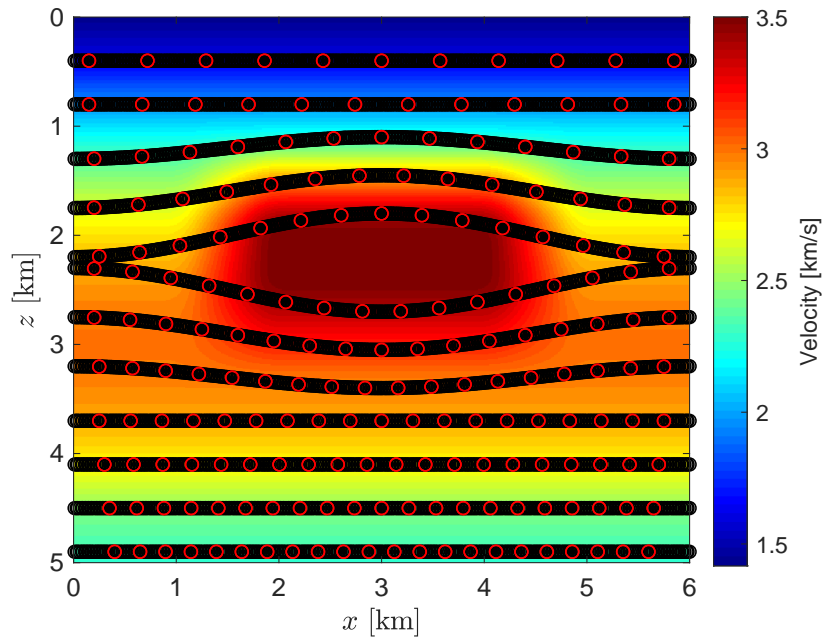
Figure 8.3: Data positions (red circles) for first experiment.

Stereotomography case

The following parametrization was applied for stereotomography test:

Input data space: To generate data space, from each of the 198 data positions of Figure 8.3, one pair of rays was traced until surface line with initial slopes given by a double aperture with respect to the normal vector of the respective interface. The initial double aperture varies through the different data positions and interfaces. Figure 8.4 illustrates the ray paths used to build input data space for stereotomography test. At surface line, kinematic parameters of positions, slopes and traveltimes were computed to compose data space. Therefore, data space is composed by 198 samples of two positions, two slope parameters, and one two-way traveltime parameter. At this first test, no noise was added to data parameters.

Initial model space: The initial velocity model was arbitrarily chosen to be a homogeneous velocity model of 1.45km/s. Therefore, initial velocity model does not resembles at all the true velocity model. Remind that, from the results of previous tests of this thesis, this fact turns the stereotomography test even harder. For interpolation purposes, knots were displayed uniformly through the model, with horizontal and vertical spacing of 0.2km. Ray-model space was initialized by the proposed initialization procedure for stereotomography, returning 198 initial model samples, each of them composed
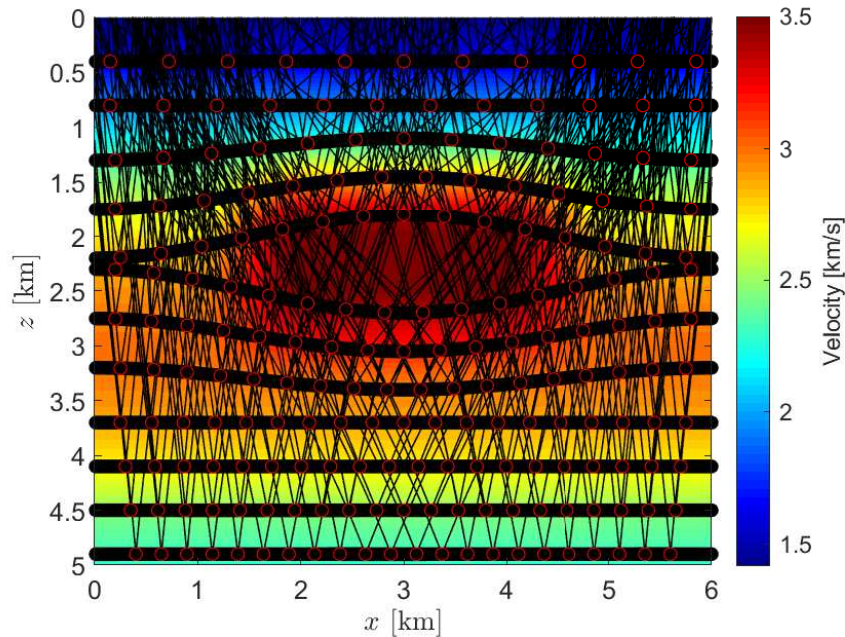
Figure 8.4: Ray paths used to build input data space for stereotomography test. Rays were traced with initial double aperture with respect to the normal vector of the respective interface.

by one initial model position, one pair of initial model slopes and one pair one model traveltimes. Initial model positions returned by the proposed initialization procedure for stereotomography, under the constant velocity model of 1.45km/s, are illustrated by Figure 8.5. Compare with the true data positions in Figure 8.3.

Initial regularization weight parameter: To perform this test, a previous search was made in order to find a reasonable initial regularization parameter. Therefore, this test was performed many times, with different values of initial regularization parameter. For relative high initial values for regularization parameter, the objective function, to be minimized, did not reach a final reasonable (small) value. Therefore, the initial value of regularization parameter was subsequently decreased until the objective function fell below an acceptable value. For even smaller values of initial regularization parameter, the final value of objective function increases again and the method starts to return non-regularized velocity models. For this test, between all values tested for the parameter, the initial regularization parameter for which the final objective function reached the minimum value was chosen. Thus, initial regularization parameter λ was set in order to, at first iteration, the relation between the regularization term with respect to the objective function, would be 10^{-7}. To calibrate regularization term, the following values were considered: $\epsilon_{xx} = \epsilon_{zz} = 1$ and $\epsilon_{vv} = 10^{-4}$.
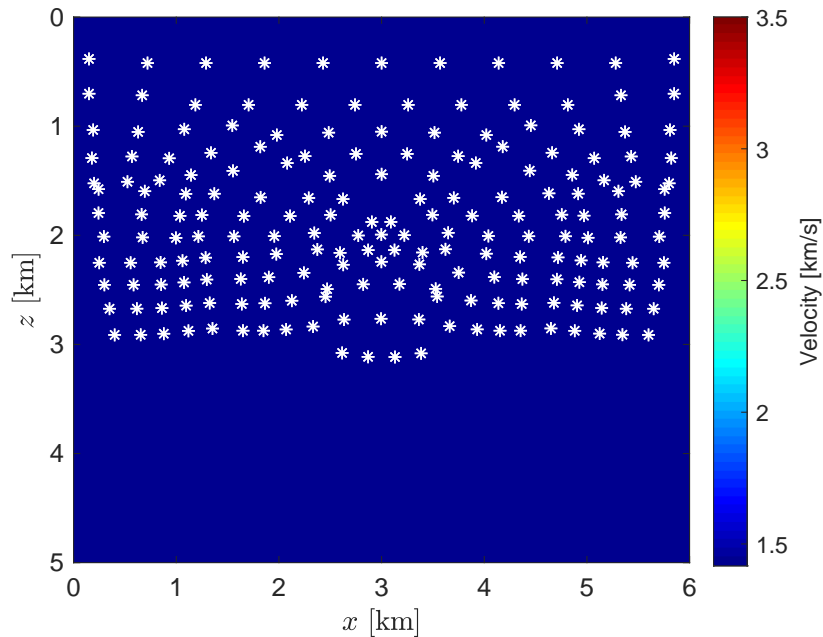
Figure 8.5: Initial model for stereotomography test. A homogeneous velocity model of 1.45km/s was applied. White asterisks denote model initial positions.

Final model proposed by stereotomography: Under the previously mentioned conditions, the final model proposed by stereotomography is illustrated in Figure 8.6. The method couldn't invert correctly the region below the high velocity area of the model. In fact, the high velocity area at the middle of the model represents the division between good and bad results provided by the method. Note that, above the high velocity area, stereotomography was capable to recover both true velocity and model positions. However, bellow this region, both velocity and model positions were affected by the presence of high velocity area. Figure 8.7 illustrates inverted model positions by stereotomography. Figure 8.8 exhibits relative errors of inverted velocity model by stereotomography.

The performed test by stereotomography resembles the results presented in Neckludov et al. (2006). There, stereotomography was also tested with a velocity model with a high velocity area at the middle of the model. Regions above this high velocity area were reasonably inverted, while regions bellow this area were affected by the presence of high velocity area, returning meaningless velocity values. There, a method named *residual stereotomographic inversion*, which was performed using, as input, the final model of stereotomography method, was proposed to increase the quality of the result. For more details, the interest reader can consult the reference Neckludov et al. (2006). In this thesis, we will show how CRP tomography can improve the previous results under the same parametrization.
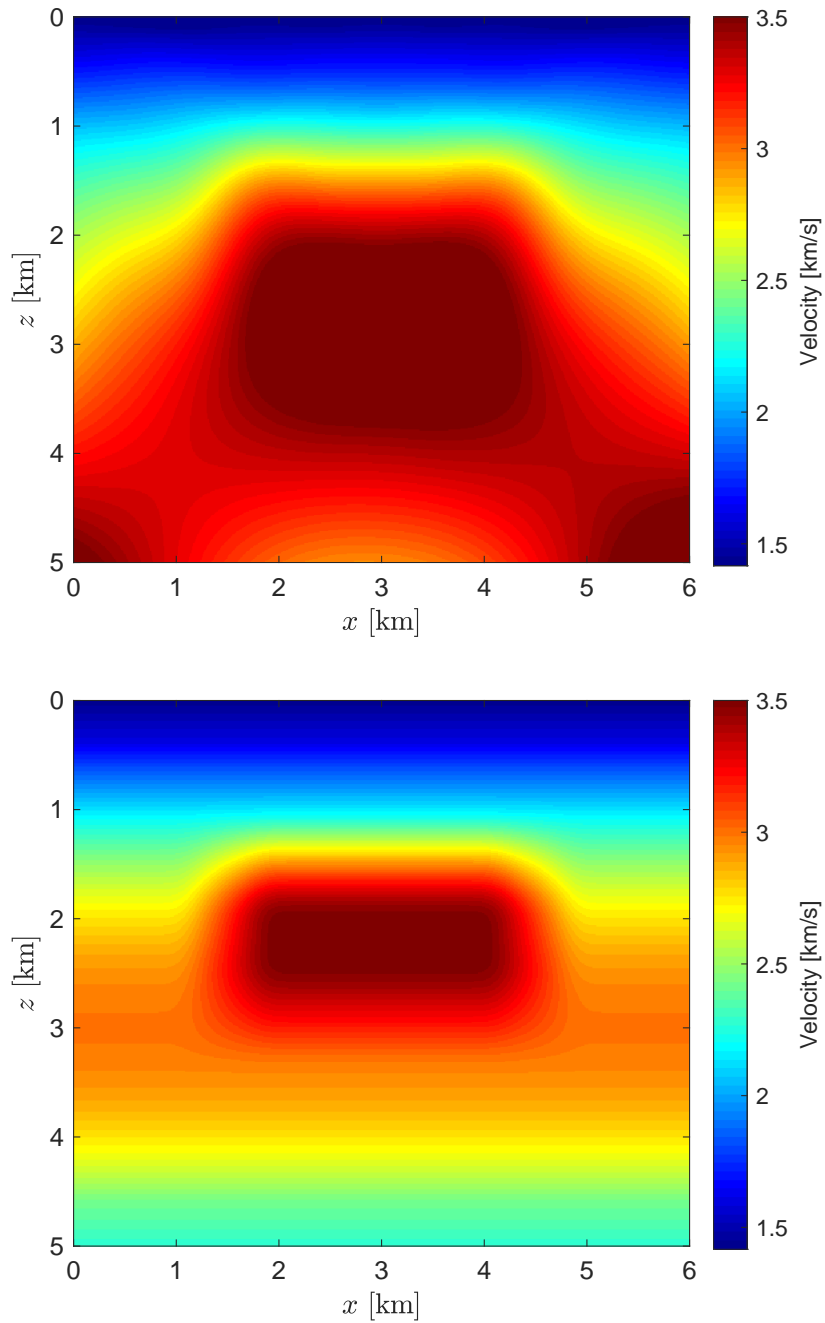
Figure 8.6: Final velocity model of stereotomography test (top image). True velocity model for first experiment (bottom image). Stereotomography couldn't invert correctly the high velocity region presented in true velocity model.
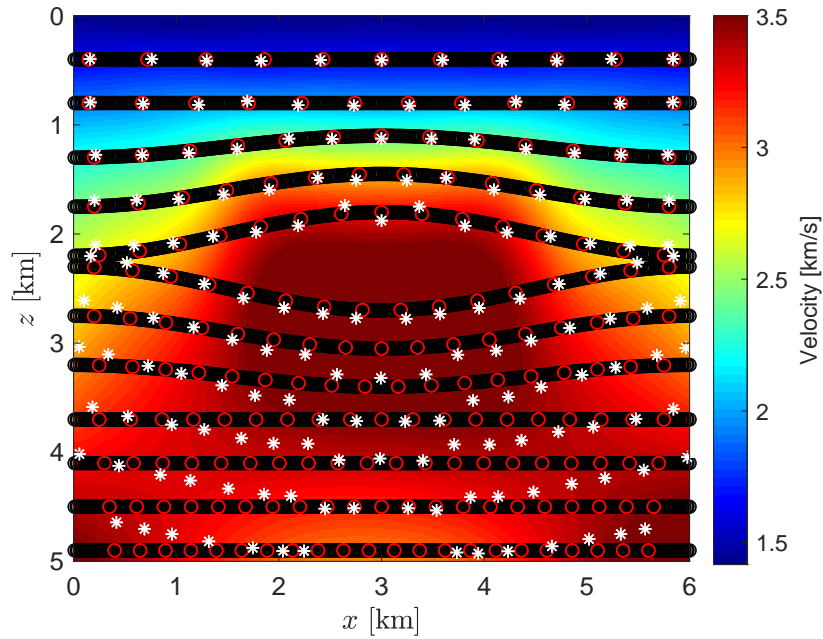
Figure 8.7: Final model depth positions returned by stereotomography. Red circles denote data positions, while white asterisk denote model positions. Model positions were not correctly repositioned below high velocity region.
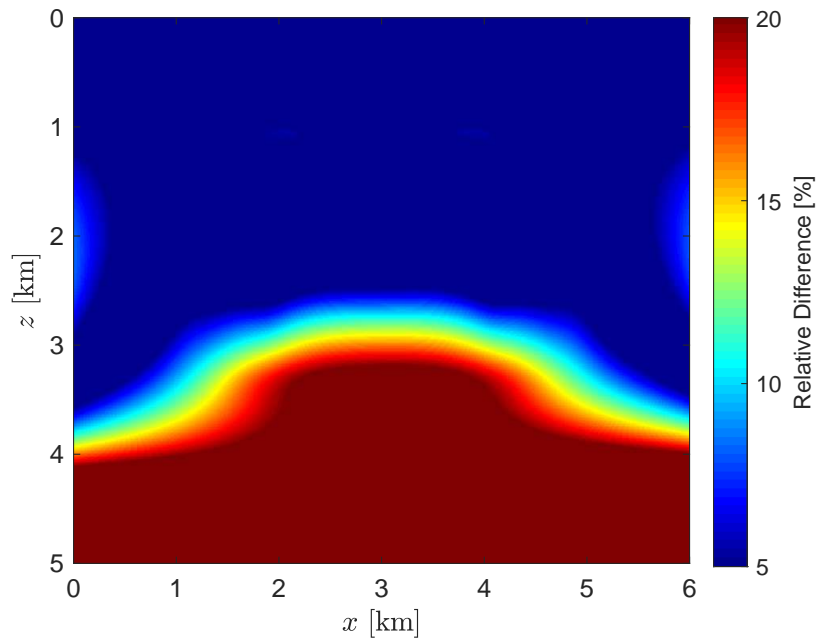

Figure 8.8: Relative errors of stereotomography inverted velocity model. Relative errors of great magnitude are presented at the deepest half of the model.
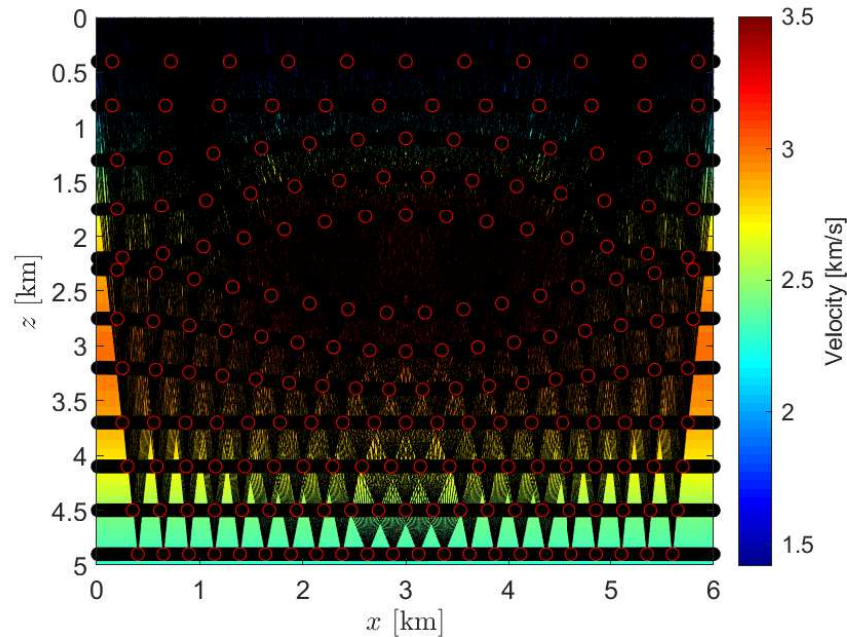
Figure 8.9: Ray paths used to build input data space for CRP tomography test. Note the significantly more number of rays used to build CRP tomography input data space.

CRP tomography - noise-free case

As previously mentioned, CRP tomography will be tested under the same parametrization applied for stereotomography test. In CRP tomography context, the parametrization applied was:

Input data space: To generate data space, from each of the 198 data positions of Figure 8.3, ten pairs of rays were traced until surface line. Each pair was propagated with different initial double apertures with respect to the normal vector of the respective interface. The initial double aperture varies through the different data positions and interfaces. Figure 8.9 illustrates the paths of the rays used to build input data space for CRP tomography test. Note the significantly higher number of rays considered by CRP tomography test (compare with the respective Figure 8.4 of stereotomography test). The more number of rays accounts for a bigger input data space in synthetic context, keeping the same the number of data positions. In a real context, a bigger input data space would be provided by the same number of performed pickings. At surface line, kinematic parameters of positions, slopes and traveltimes were computed to compose data space. Therefore, data space is composed by 198 families, each of them composed by a total family traveltime, plus ten pairs of positions and slope parameters.
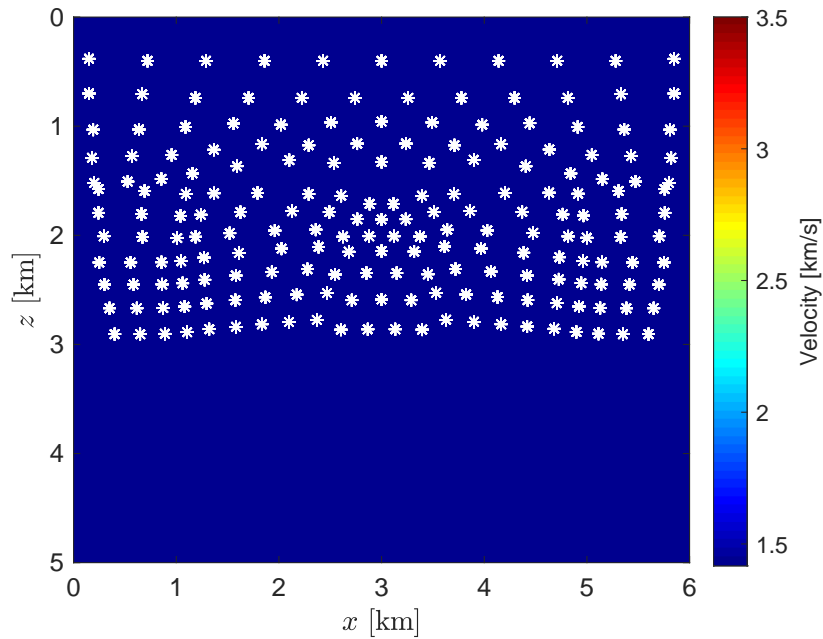
Figure 8.10: Initial velocity model and initial model depth positions for CRP tomography test. A homogeneous velocity model of 1.45km/s was applied. White asterisks denote initial model positions.

Initial model space: The same initial homogeneous velocity model of 1.45km/s was used as input for CRP tomography case. Also, the same mesh of knots for B-spline interpolation applied to stereotomography test was used. Ray-model space was initialized by the proposed initialization procedure for CRP tomography, returning 198 model families, each of them composed by one initial model depth position, plus ten pairs of initial model slopes. Initial model positions for CRP tomography noise-free case are illustrated by Figure 8.10.

Initial regularization weight parameter: To perform CRP tomography test, the same procedure used to find a good initial value for regularization parameter for stereotomography test was applied. As a result of such procedure, initial regularization parameter λ was set in order to, at first iteration, the relation between the regularization term with respect to the objective function, would be 4.10^{-8}. Note that CRP tomography allowed a relative smaller level than stereotomography for initial regularization. The parameters to calibrate regularization term were kept the same: $\epsilon_{xx} = \epsilon_{zz} = 1$ and $\epsilon_{vv} = 10^{-4}$.

Final model proposed by CRP tomography - noise-free case: The result provided by CRP tomography under the previous parametrization is illustrated by Figure 8.11. Note how CRP tomography could recover good informations about almost all parts of the model. Obviously, the presence of a

high velocity area at the middle of the model is still a problem for tomographic approaches. In CRP tomography context, the presence of the high velocity area at the middle of the model resulted in a final model that couldn't perfectly localize this area, which can also be a limitation of the applied interpolation mesh. However, differently of the result provided by stereotomography method, CRP tomography identified the existence of a high velocity area at the middle of the model and placed it approximately near the true position. The shallow half of the model was almost perfectly recovered. Also, the decreasing of velocity model in the deeper half of the model could be identified. Figure 8.13 exhibits the relative errors of CRP inverted velocity model. Errors are concentrated in regions where almost no information are available in input data space. Moreover, as is illustrated by Figure 8.12, model depth positions could be repositioned very close to the true data positions. Except for the deepest interface, final model positions were placed along the synthetic interfaces, which is a remarkable result provided by CRP tomography. Figure 8.14 exhibits the evolution of both velocity and model depth positions proposed by CRP tomography method through iterations.

CRP tomography - noisy input data space

Due to the good results provided by CRP tomography on previous test, another challenge will be proposed for CRP tomography method: random noise will be added to input data parameters. The objective is to investigate the robustness of the method in respect with inaccurate input data. The parametrization of the previous test will be kept the same and just the data space will be changed. The random noise applied to input data space obeys the following rule:

Noisy-input data space: A discussion about the different sources of input data errors for positions, traveltimes and slopes has already been made in this chapter. In this test, a random error provided by uniform distribution will be applied to each of these data parameters. Although the assumption of a uniform random noise is not physically justified, it can be used to study the robustness of the proposed new method in respect with errors in input data space. As already explained, in practical real context, the main source of data errors for CRP tomography is the slope parameter. Therefore, for input slope parameters, a relative higher noise value will be added in comparison with other input kinematic parameters. The level of random noise to be added at each input kinematic parameter will be the following:

- **Time:** a random value of the interval $[-5.10^{-3}\text{s}, 5.10^{-3}\text{s}]$ will be added to each traveltime input parameter.
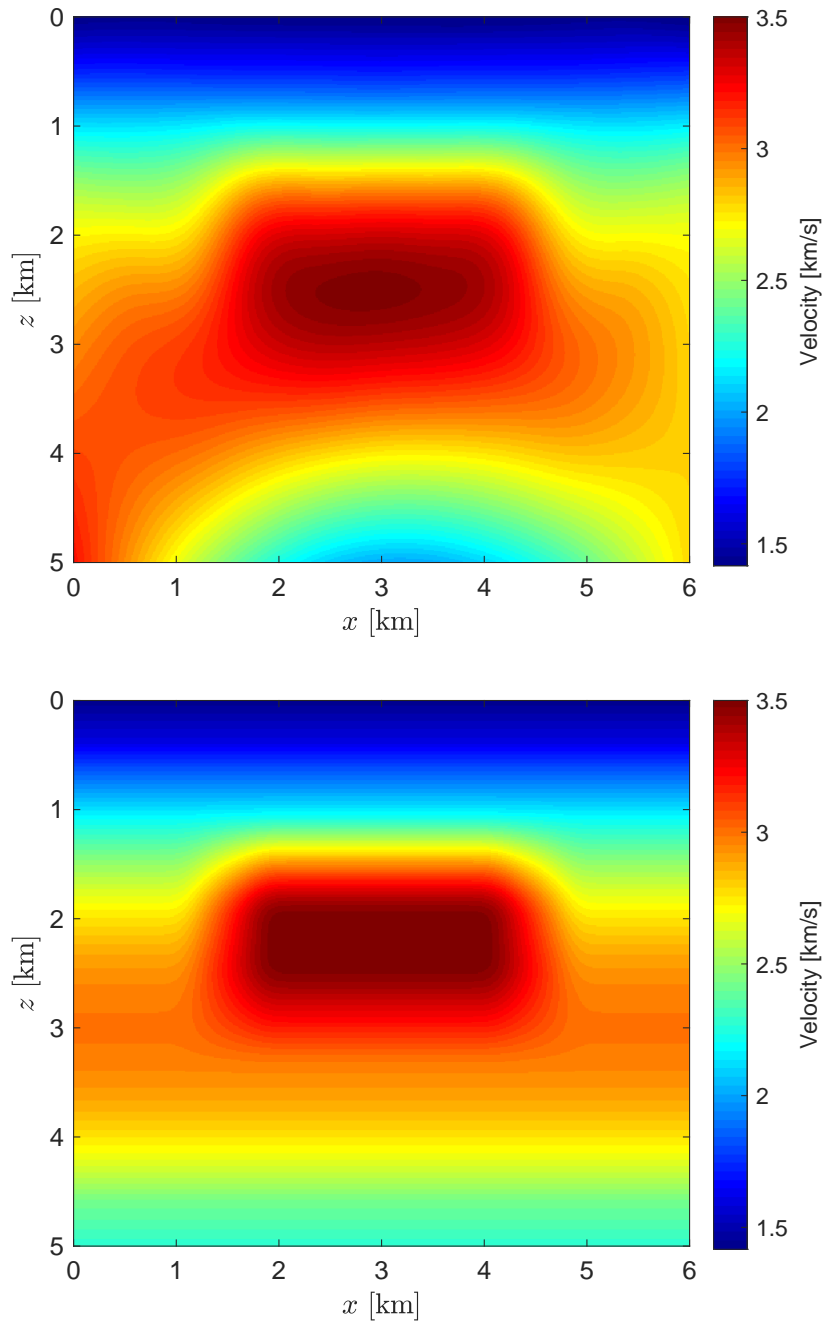
Figure 8.11: Final velocity model of CRP tomography test (top image). True velocity model for first experiment (bottom image). CRP tomography identified the existence of a high velocity area the middle part of the model and recovered good informations about almost all parts of the model.
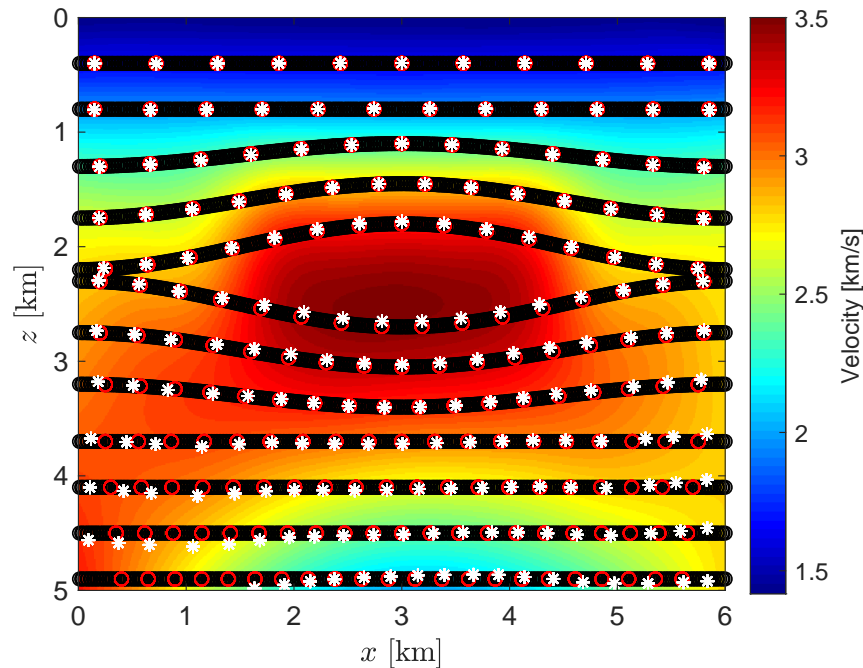
Figure 8.12: Final model depth positions returned by CRP tomography. Red circles denote data positions, while white asterisk denote model positions. Except for the deepest interfaces, model depth positions were repositioned over the synthetic interfaces.

- **Position:** a random value of the interval $[-5m, 5m]$ will be added to each position input parameter.

- **Slope:** a random value of the interval $[-3.10^{-5}s/m, 3.10^{-5}s/m]$ will be added to each slope (slowness vector) input parameter. The boundary values of this interval account for approximately 5% for the inverse of the velocity at surface line.

Final model proposed by CRP tomography - noisy input data case: The CRP tomography final result for this noisy input data experiment is illustrated by Figure 8.15. The presence of noise in input data space has not significantly affected the quality of the tomographic final model. The same good features presented by noise-free result remain at the present test. Except for regions near the bottom line of the model, the inverted velocity model resembles the true velocity model, as it can be noted by Figure 8.16, which illustrates the relative errors of velocity model. Note also the good quality of inverted model positions in Figure 8.17, most of them repositioned over the synthetic interfaces.

By the results illustrated by the Figures 8.15, 8.16 and 8.17, it is possible to say that CRP tomography method demonstrated to be, at this particular synthetic test, a robust technique with respect
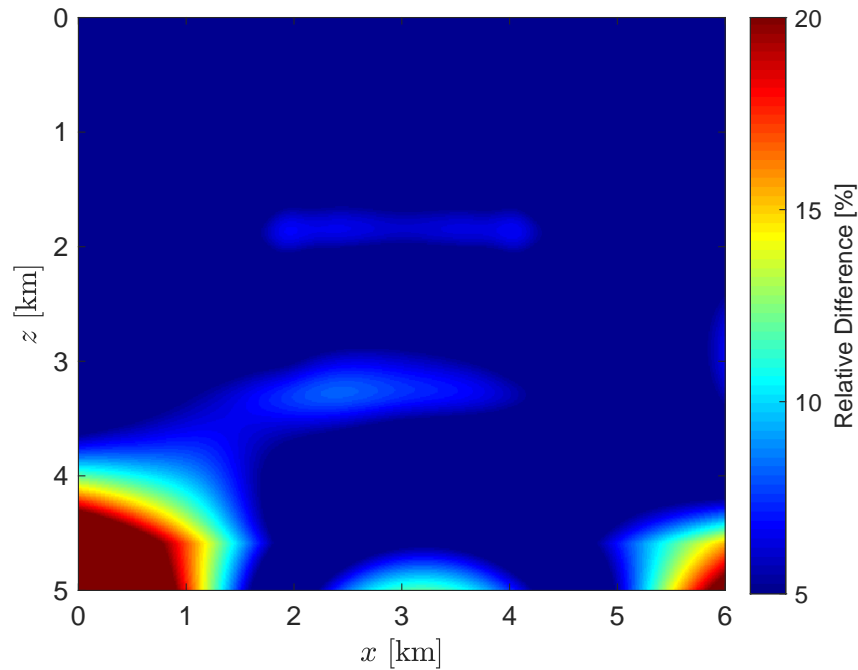
Figure 8.13: Relative errors of CRP tomography inverted velocity model. Errors are concentrated in regions where almost no information are available in input data space. Interpolation limitations contribute to relative errors near the high velocity area.

to the proposed uniformly distributed random noise. To keep the investigation about the robustness of CRP tomography method in respect with noisy input data space, another test will be performed. This time, the level of noisy will be increased by the following level of random noise:

- **Time:** a random value of the interval $[-10^{-2}\text{s}, 10^{-2}\text{s}]$ will be added to each traveltime input parameter.

- **Position:** a random value of the interval $[-10\text{m}, 10\text{m}]$ will be added to each position input parameter.

- **Slope:** a random value of the interval $[-7.10^{-5}\text{s/m}, 7.10^{-5}\text{s/m}]$ will be added to each slope (slowness vector) input parameter. The boundary values of this interval account for approximately 10% for the inverse of the velocity at surface line.

The solution provided by CRP tomography under the increased level of noise in input data space is summarized by Figures 8.18, 8.19 and 8.20. As expected, with increased level of noise in input data space, the quality of inverted CRP tomography velocity model has been a little more affected. However, once again, the main features and qualities presented before remain at the proposed final
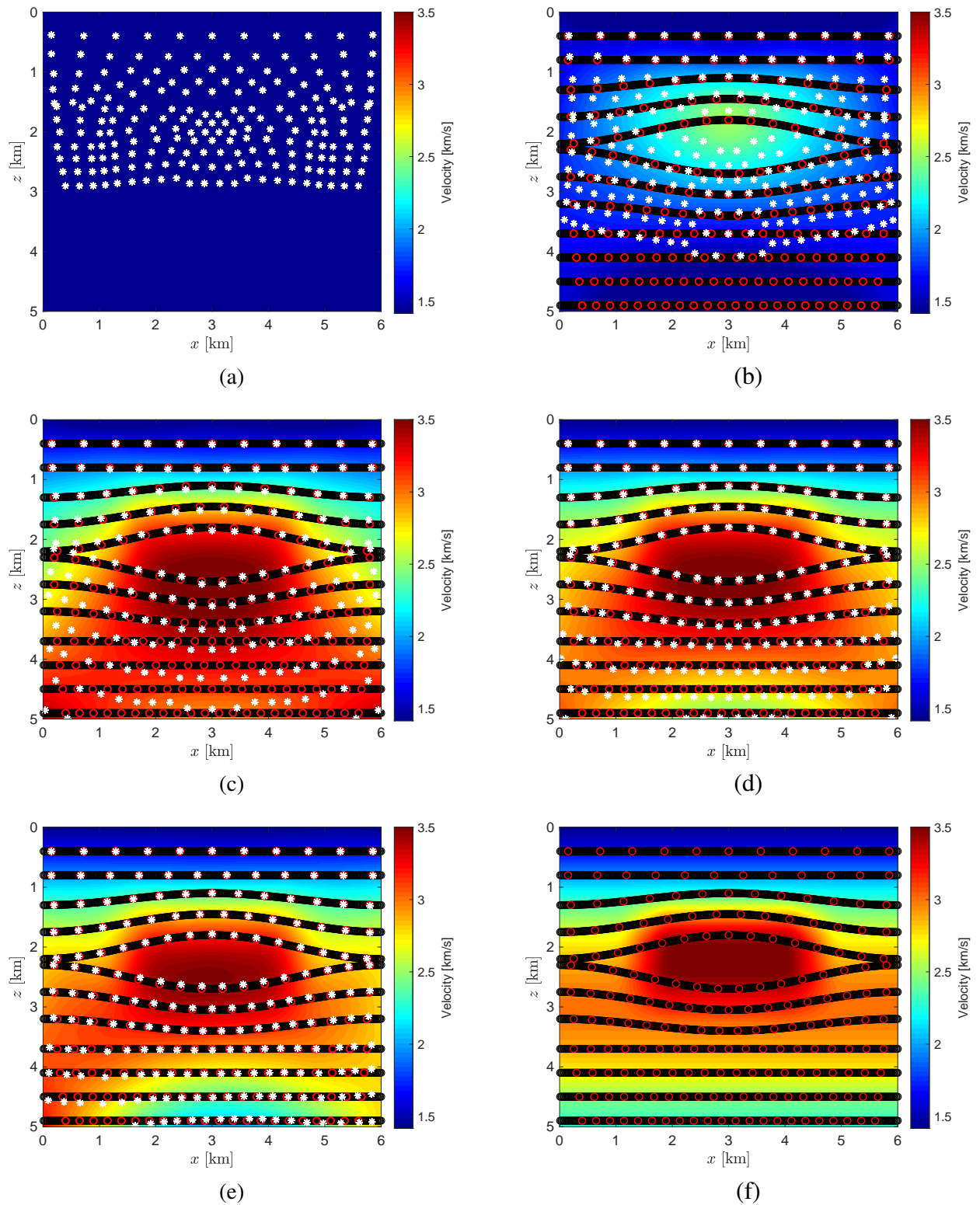
Figure 8.14: Evolution of CRP tomography model through iterations. (a) Initial model. (b) Current model at iteration 3. (c) Current model at iteration 6. (d) Current model at iteration 9. (e) Final CRP tomography model - iteration 14. (f) True velocity model and data positions.
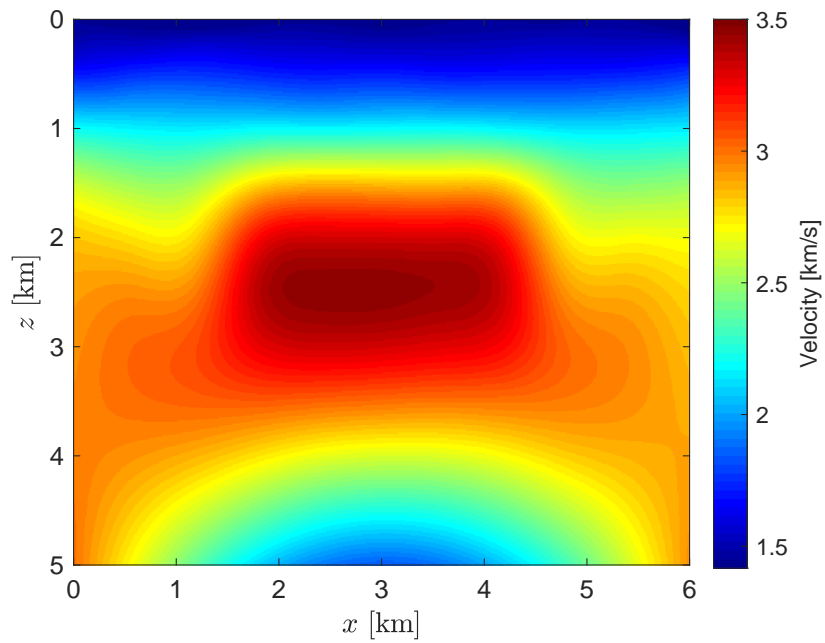
Figure 8.15: Final velocity model of CRP tomography noisy input test. The good features presented by noise-free result remain at the noisy input test.
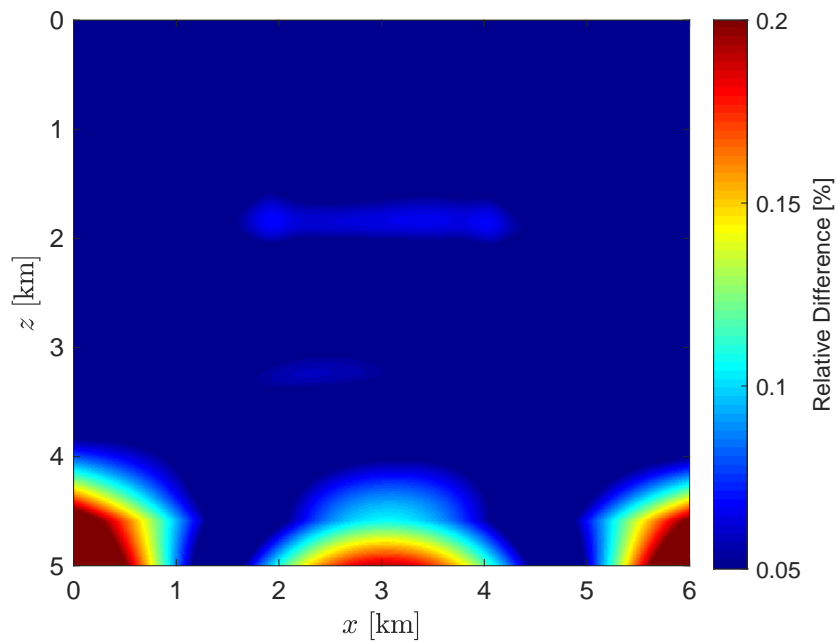

Figure 8.16: Relative errors of CRP tomography inverted model for noisy input test. Once again, errors, are concentrated in regions where almost no information are available in input data space.
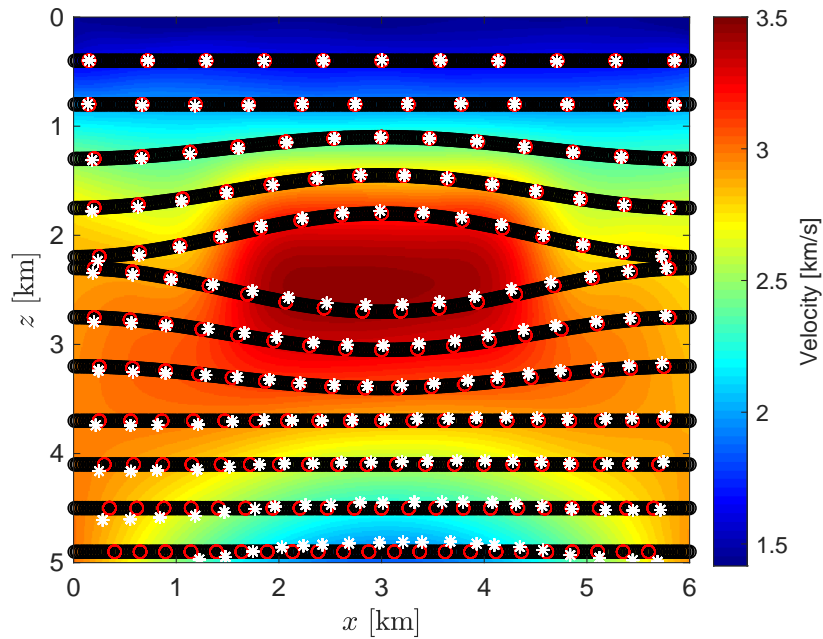
Figure 8.17: Final model depth positions returned by CRP tomography for noisy input test. Red circles denote data positions, while white asterisk denote model positions. Model depth positions were well repositioned over synthetic interfaces, except for deepest ones.

model. Hence, even at the presence of a higher level of noise, CRP tomography could approximately localize, at the middle of proposed model, the high velocity area. Moreover, CRP tomography could still identify the decrease of velocity below the high velocity area. Inverted model depth positions were also repositioned, except for the deepest structures, along the synthetic structures. Finally, note that the corners of model concentrates the major errors of inverted CRP tomography velocity model. However, these regions are not covered by informations in input data space.

8.2 Second Synthetic Experiment

The second experiment of this chapter will be performed following the same steps of previous experiment. Therefore, the velocity model for second experiment will be used to test both stereotomography and CRP tomography. Following the main objectives of this chapter, synthetic interfaces will be proposed for the model, where data positions will be placed. A noisy-input data space will be provided in order to investigate the robustness of CRP tomography in respect with non-accurate input parameters for this test.
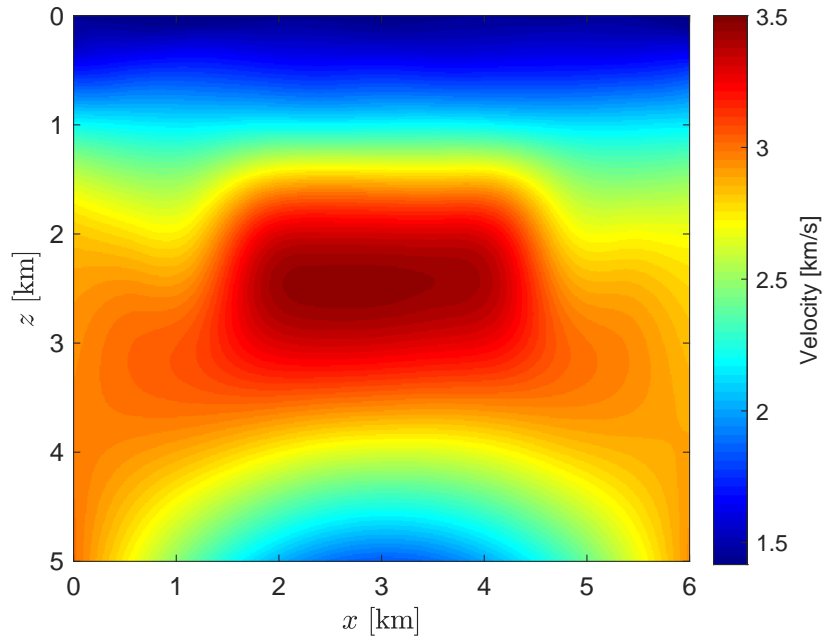
Figure 8.18: Final velocity model of CRP tomography for the test with increased level of noise. Most of the good features presented by noise-free result still remain under the increased level of noise in input data space.
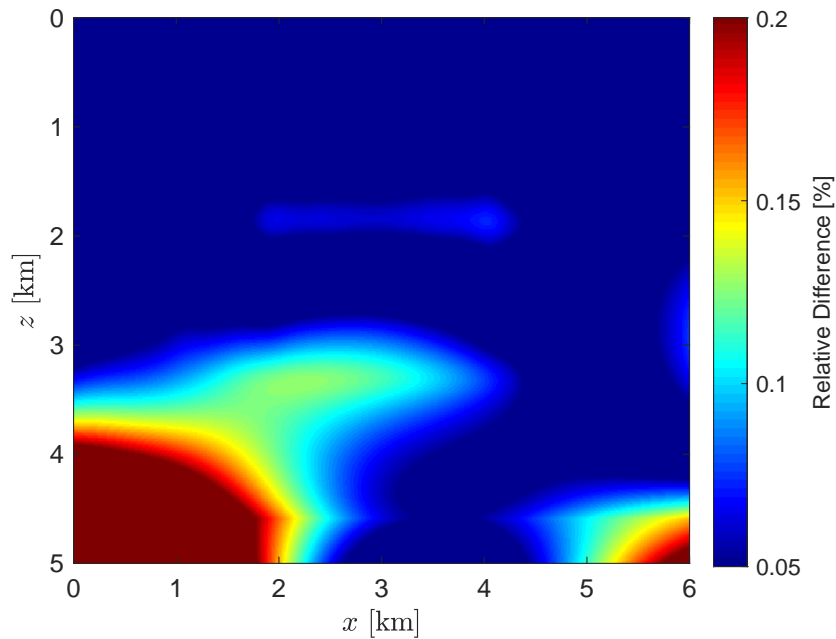

Figure 8.19: Relative errors of CRP tomography inverted model for the test with increased level of noise. Note the presence of higher relative errors near the bottom line of the model.
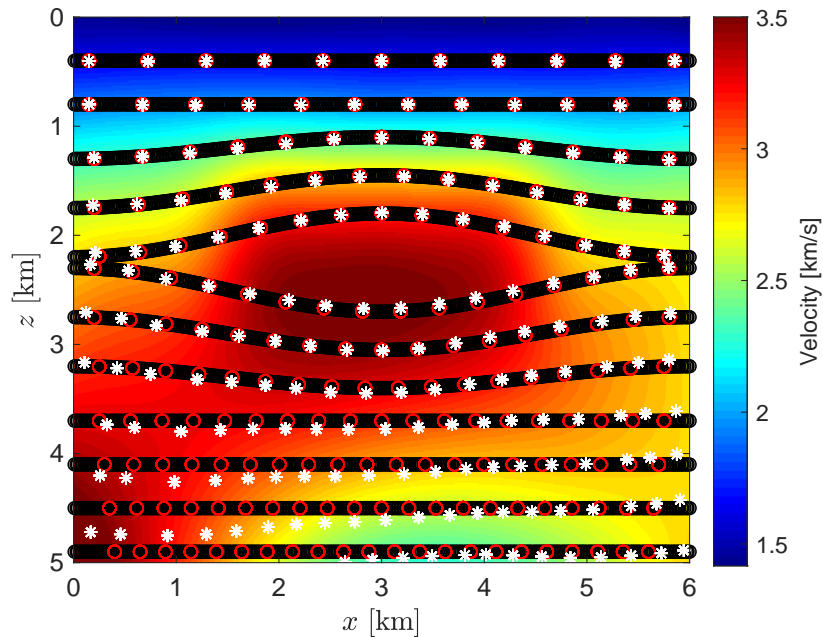
Figure 8.20: Final model depth positions returned by CRP tomography for the test with increased level of noise. Red circles denote data positions, while white asterisk denote model positions. Model depth positions were slightly worse repositioned.

Figure 8.21, exhibits the proposed velocity model for the present experiment. The model has dimension 4km×5km and was not generated by B-spline interpolation, which represents another challenge for tomographic inversion problem. Figure 8.22 exhibits the velocity model with synthetic interfaces proposed for the second experiment.

In previous experiment, the main challenge was represented by the complex velocity model, due to the presence of a high velocity region at the middle of the model. For this second experiment, the velocity model does not represent a remarkable big challenge. Although it is not a simple model, because of the presence of lateral velocity variations, the velocity model does not present complex velocity variations as the high velocity area of previous experiment. However, the synthetic interfaces for this experiment are considerably more complex than the ones proposed for previous experiment. The more complex configuration represents the biggest challenge of this experiment for both tomography methods, mainly in respect with the correct repositioning of model depth positions along the proposed interfaces. Once again, data positions will be placed over these interfaces, from where pair(s) of rays will be traced to surface line in order to compute kinematic parameters to build input data space. Random noise will be added to these computed parameters. For this experiment, 242 data positions will be used. Figure 8.23 illustrates the data positions over the proposed interfaces.
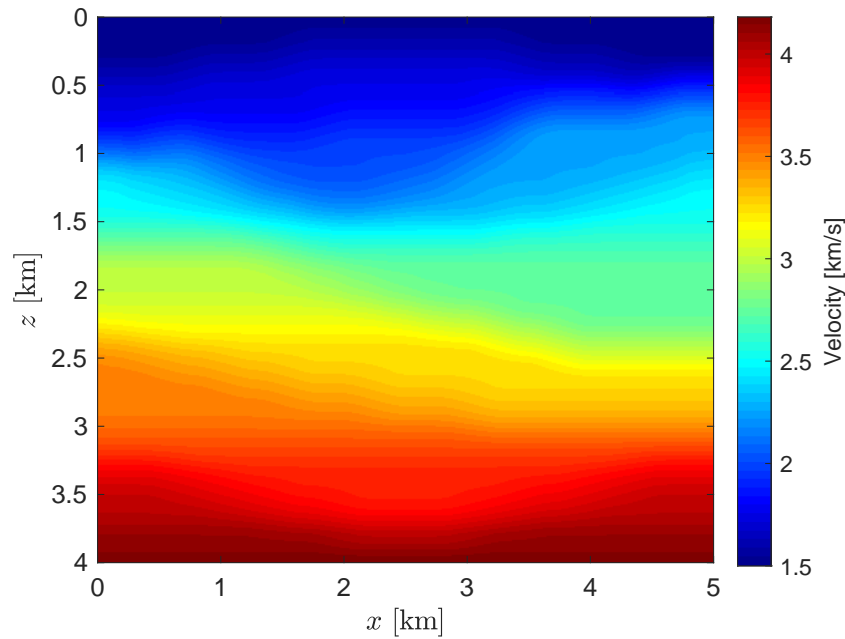
Figure 8.21: Velocity model for second experiment.

Stereotomography case

Stereotomography will be performed with a noise-free input data space. The following parametrizations were applied for this test:

Input data space: To generate data space, from each of the 242 data positions of Figure 8.23, a pair of rays were traced until surface line with initial slopes given by a double aperture with respect to the normal vector of the respective interface. The initial double aperture varies through the different data positions and interfaces. Figure 8.24 illustrates the rays paths used to build input data space for stereotomography test. At surface line, kinematic parameters of positions, slopes and traveltimes were computed to compose data space. Therefore, data space is composed by 242 samples of two positions, two slope parameters and one two-way traveltime parameter. No noise was added to data parameters.

Initial model space: The initial velocity model was arbitrarily chosen to be a homogeneous velocity model of 1.5km/s. For interpolation purposes, knots were displayed with vertical spacing of 0.4km and horizontal spacing of 0.5km. Ray-model space was initialized by the proposed initialization procedure for stereotomography, returning 242 initial model samples, each of them composed by one initial model position, one pair of initial model slopes and one pair of model traveltime parameters. Initial model positions for stereotomography case at the present second experiment are illustrated by
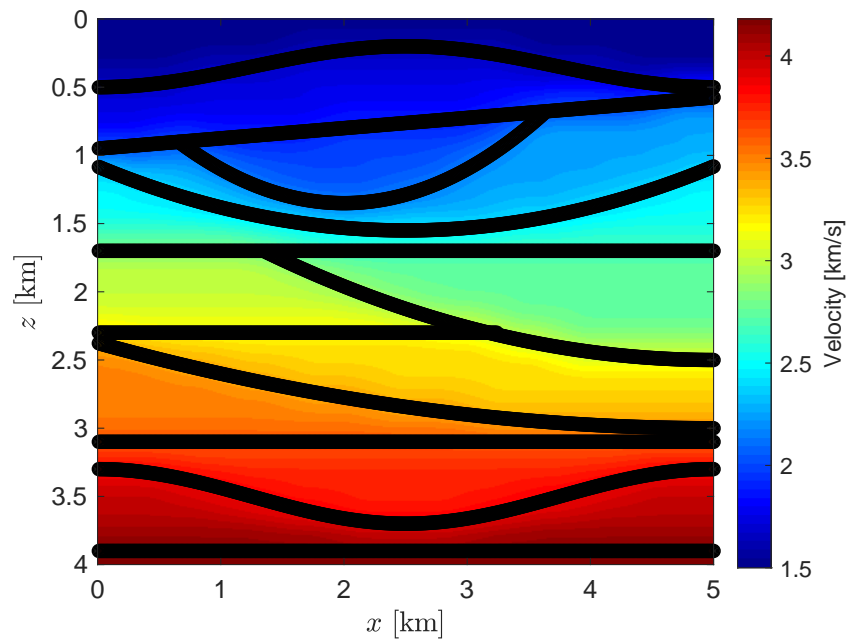
Figure 8.22: Velocity model for second experiment with synthetic interfaces. The proposed interfaces are more complex then the ones of previous experiment.
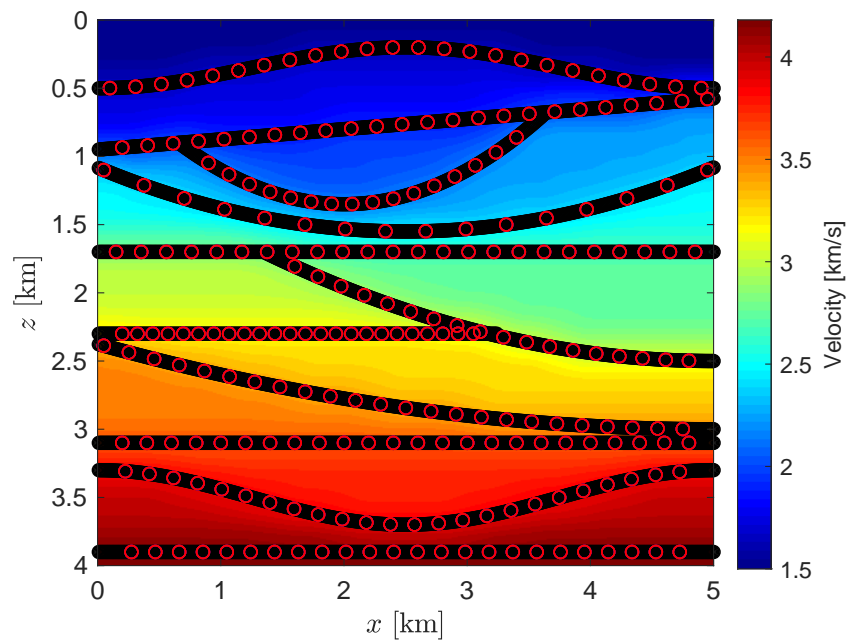

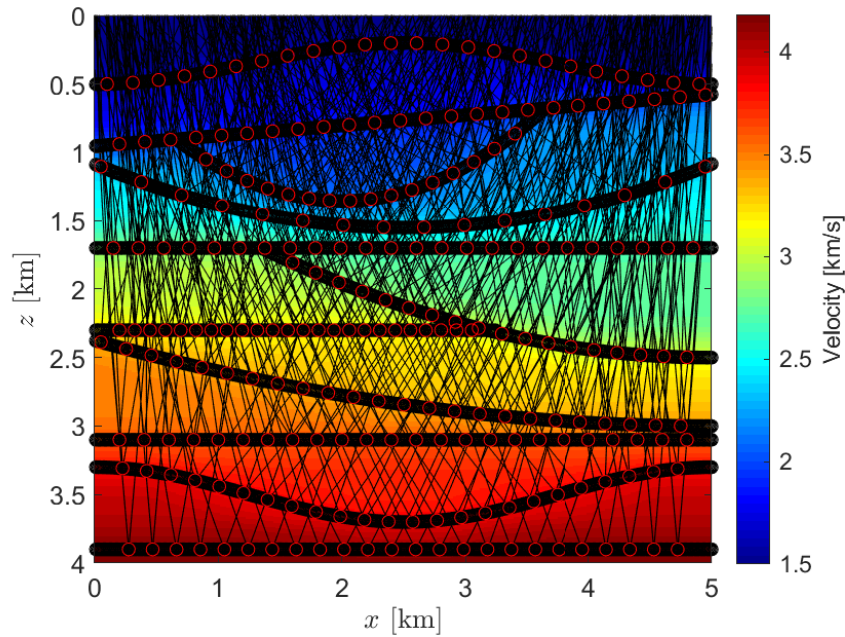Figure 8.23: Data positions (red circles) for second experiment.

Figure 8.24: Ray paths used to build input data space for stereotomography test for second experiment. Rays were traced with initial double aperture with respect to the normal vector of the respective interface.

Figure 8.25. Model initial positions were derived by stereotomography initialization step under the proposed initial homogeneous velocity model. Note how the model initial positions are concentrated in the shallower half of the model due to the proposed homogeneous initial velocity model. Compare with the true data positions of Figure 8.23.

Initial regularization weight parameter: To perform this test, a previous search was made in order to find a reasonable initial regularization parameter following the same procedure used for stereotomography case at first experiment. Thus, initial regularization parameter λ was set in order to, at first iteration, the relation between the regularization term with respect to the objective function, would be 9.10^{-5}. To calibrate regularization term, the following values were considered: $\epsilon_{xx} = 0.5$, $\epsilon_{zz} = 0.02$ and $\epsilon_{vv} = 10^{-4}$.

Stereotomography final model: Under the above parametrizations, the final model proposed by stereotomography is illustrated in Figure 8.26. Also, Figure 8.27 exhibits the relative error of stereoto-mography velocity model with respect to the true velocity model. Note that the main features of the velocity model were recovered by stereotomography. For example, the crescent variation of velocity model on vertical variation is presented on inverted velocity model. However, note that some of the
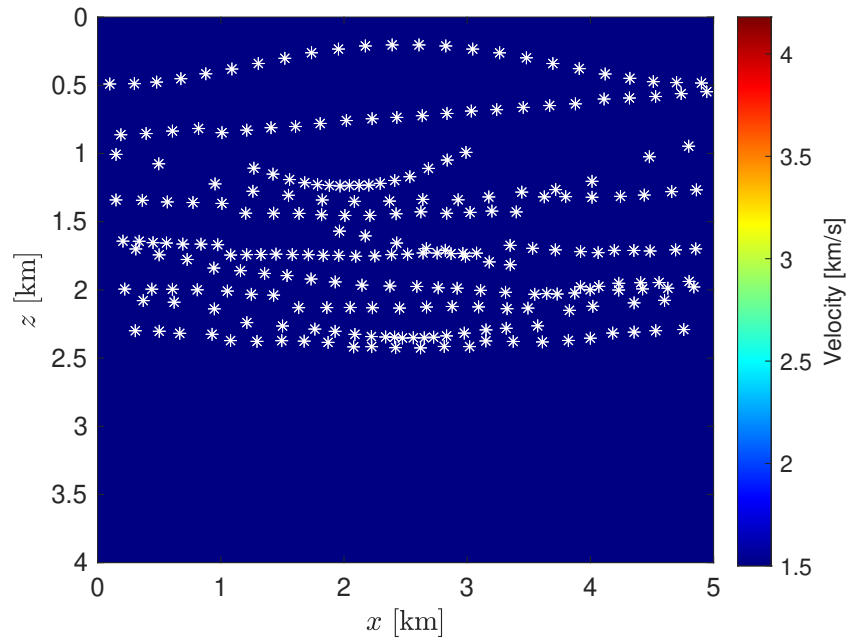
Figure 8.25: Initial model for stereotomography test for second experiment. Model initial positions are concentrated in the shallower half of the model due to the proposed homogeneous initial velocity model.

lateral variation is not presented on final velocity model proposed by stereotomography. For example, compare the inverted velocity value on the synthetic layer situated between 2.4km and 3.1 in depth.

However, the main objective of this experiment, due to the simple velocity model but slightly complex interfaces, is to test the correct repositioning of model depth positions on true data positions. Figure 8.28 exhibits final model depth positions returned by stereotomography. Once again, the main features of inverted positions were satisfactorily recovered. For example, note that most of the model positions were replaced along the proposed structures. However, some of the model depth positions were not perfectly repositioned to the respective true data positions.

CRP tomography - noise-free case

CRP tomography will be first tested at this experiment receiving, as input, a perfect accurate data space. The parametrization used before for stereotomography method will be kept the same. The main objective is to investigate how the use of common-reflection-point information can improve inverted model depth positions.
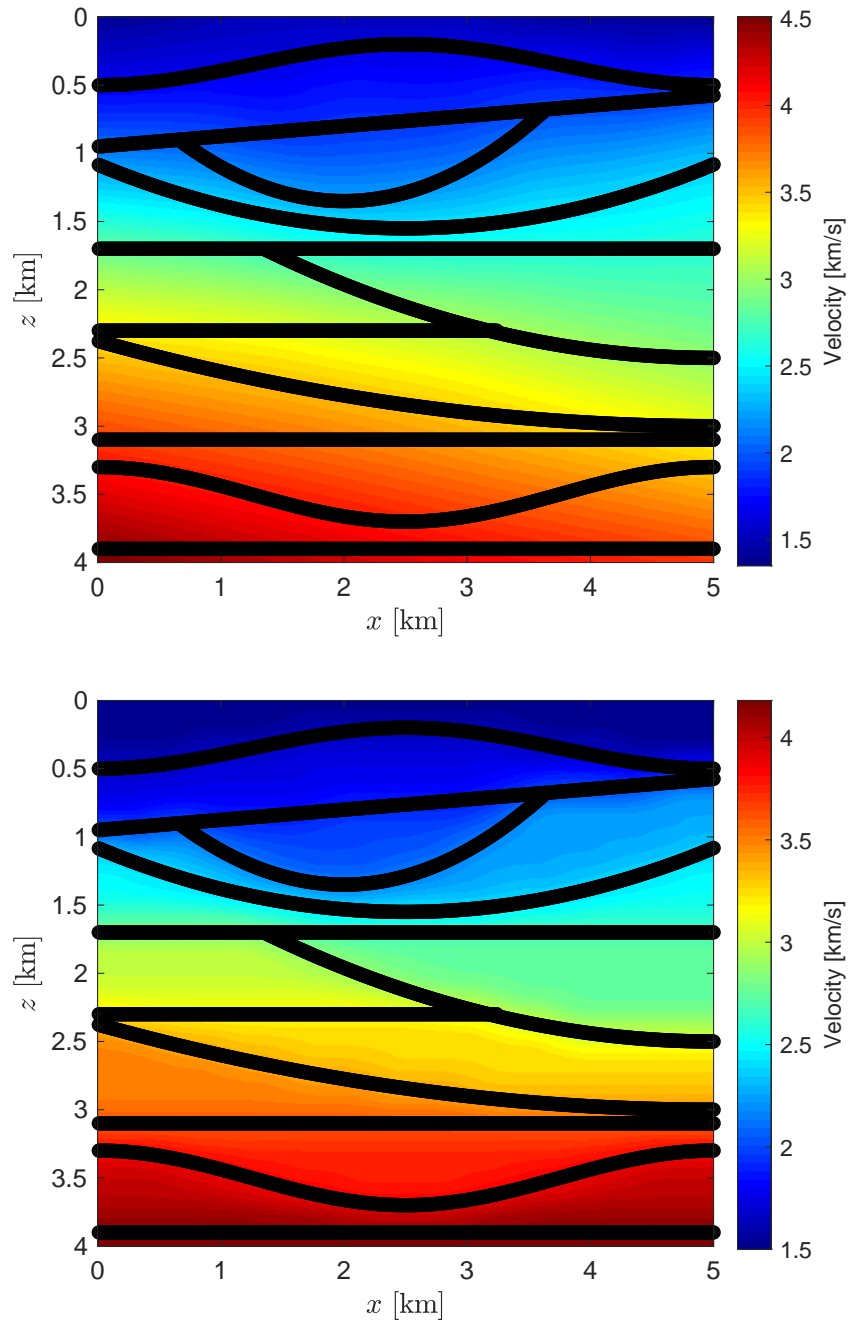
Figure 8.26: Final velocity model of stereotomography test for second experiment (top image). True velocity model for second experiment (bottom image). Interfaces were displayed together with the velocity models.
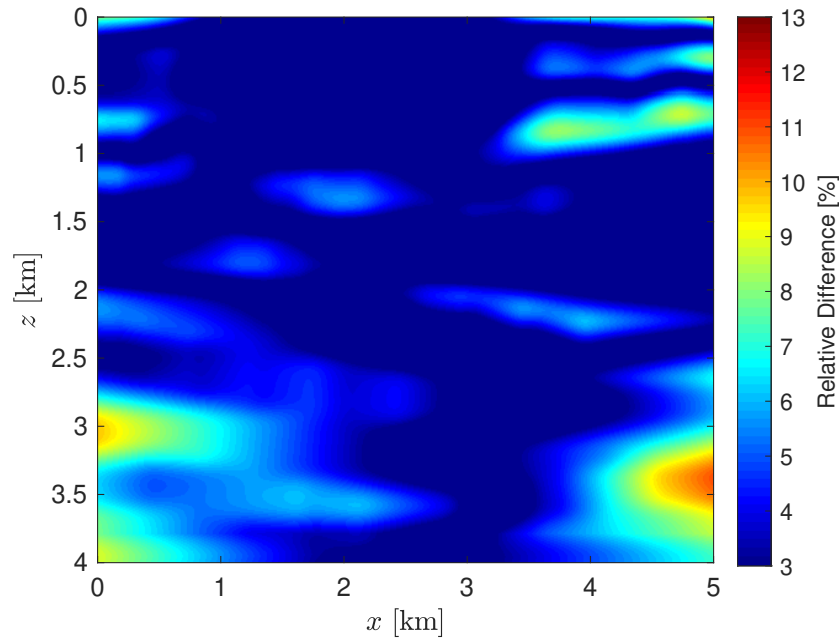
Figure 8.27: Relative errors of stereotomography inverted velocity model of second experiment.

Input data space: To generate data space, from each of the 242 data positions of Figure 8.23, seven pairs of rays were traced until surface line. Each pair was propagated with different initial double aperture with respect to the normal vector of the respective interface. The initial double aperture varies through the different data positions and interfaces. Figure 8.29 illustrate the ray paths used to build input data space for CRP tomography test. Note the significantly more number of rays considered by CRP tomography test when compared to stereotomography case. The more number of rays accounts for more number of input data information in respect with each data position. As it will be showed, this is a crucial feature to improve the quality of the inverted model. At surface line, kinematic parameters of positions, slopes and traveltimes were computed to compose data space. Therefore, data space is composed by 242 data gathers, each of them composed by a total traveltime, plus seven pairs of positions and slope parameters.

Initial model space: The same initial homogeneous velocity model of 1.5km/s will be used as input for CRP tomography case. Also, the same mesh of knots for B-spline interpolation applied to stereotomography test will be used. Ray-model space was initialized by the proposed initialization procedure for CRP tomography, returning 242 model gathers, each of them composed by one initial model depth position, plus seven pairs of initial model slopes. Initial model positions, for CRP tomography noise-free case, returned by initialization step, are illustrated by Figure 8.30. CRP tomography model initial positions are concentrated in the shallower half of the model due to the proposed homogeneous initial
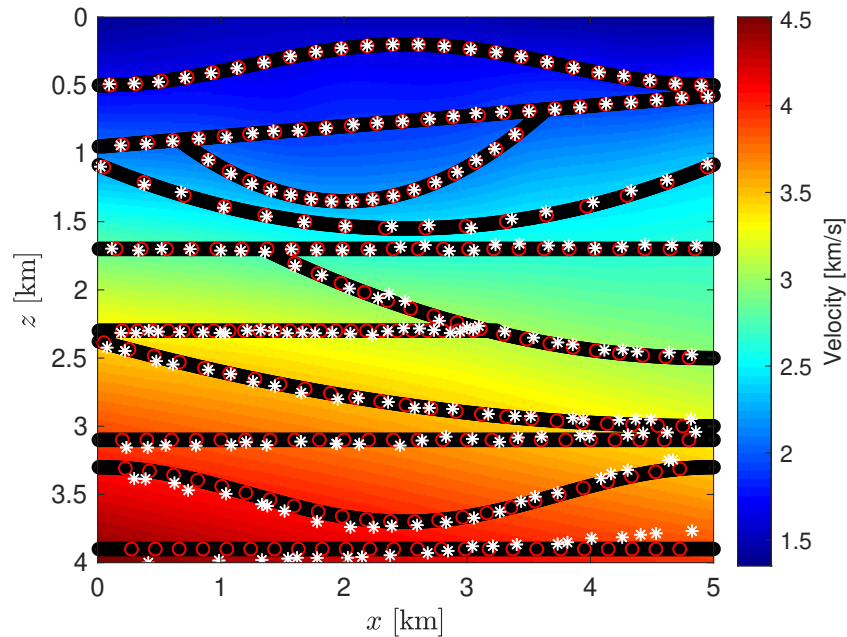
Figure 8.28: Final model depth positions returned by stereotomography for second experiment. Red circles denote data positions, while white asterisks denote model positions.

velocity model.

Initial regularization weight parameter: CRP tomography test will be performed using the same level of initial regularization parameter used for stereotomography. Therefore, initial regularization parameter λ was set in order to, at first iteration, the relation between the regularization term with respect to the objective function, would be 9.10^{-5}. The parameters to calibrate regularization term were: $\epsilon_{xx} = 0.5$ $\epsilon_{zz} = 0.02$ and $\epsilon_{vv} = 10^{-4}$.

CRP tomography final model for noise-free case: The result provided by CRP tomography for second experiment is illustrated by Figure 8.31. In respect with the inverted velocity model, CRP tomography kept the same good features presented by stereotomography case. However, note how CRP tomography was able to better recover the velocity of the layer situated between 2.4km and 3.1km in depth. Moreover, relative errors illustrated by Figure 8.32 are smaller than the ones presented by stereotomography test.

With respect to the main objective of this experiment, CRP tomography notably improved the quality of inverted model depth positions. As it can be seen in Figure 8.33, model depth positions were repositioned almost perfectly over data positions. Compare with the inverted model depth positions
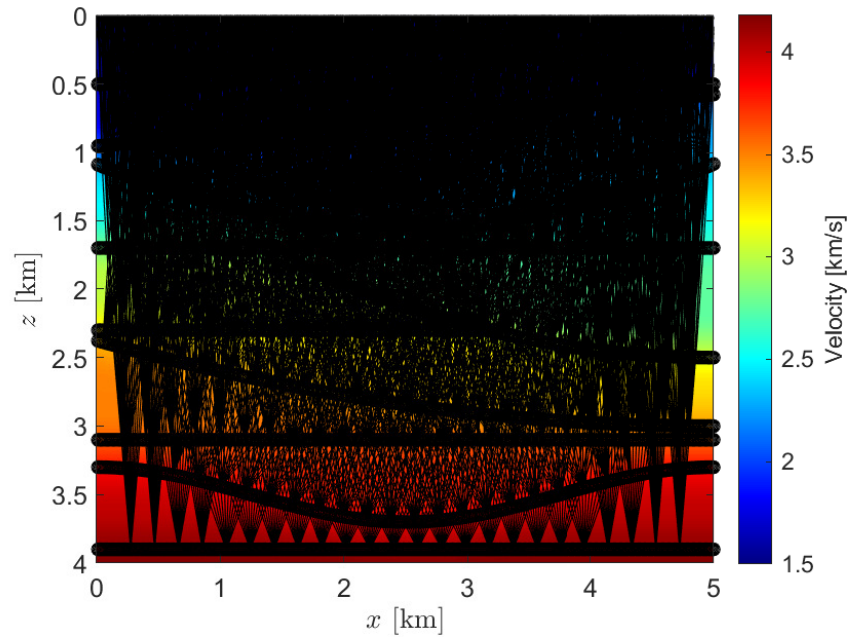
Figure 8.29: Ray paths used to build input data space for CRP tomography test for second experiment. Note the significantly more number of rays considered by CRP tomography test when compared to stereotomography case.
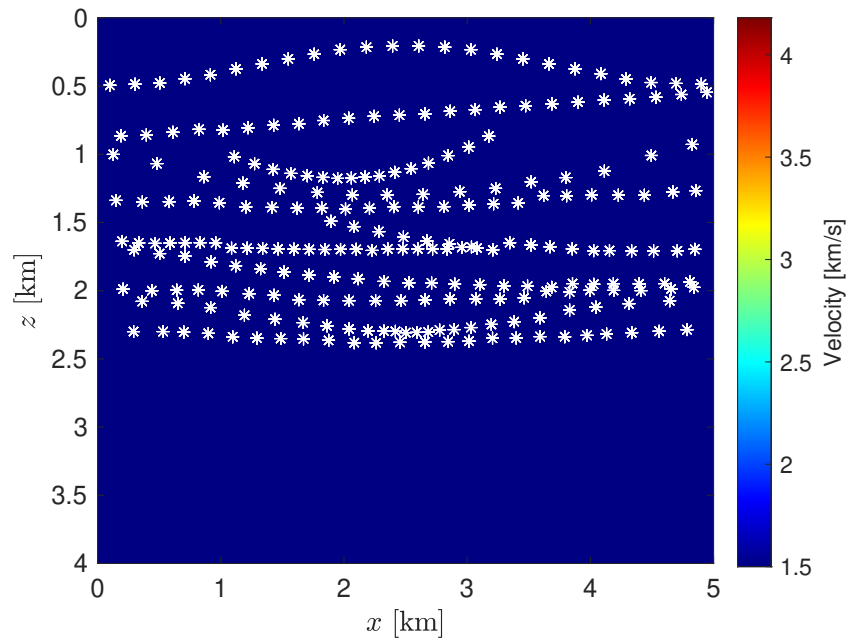
Figure 8.30: Initial model for CRP tomography test for second experiment. Model initial positions are concentrated in the shallower half of the model due to the proposed homogeneous initial velocity model.

Figure 8.31: Final velocity model of CRP tomography test for second experiment (top image). True velocity model for second experiment (bottom image). Interfaces were displayed together with the velocity models.

Figure 8.32: Relative errors of CRP tomography inverted velocity model of second experiment.

provided by stereotomography in Figure 8.28. This experiment exemplifies how the use of common-reflection-point information can be used to improve the quality of tomographic final model positions.

CRP tomography - noisy input data space

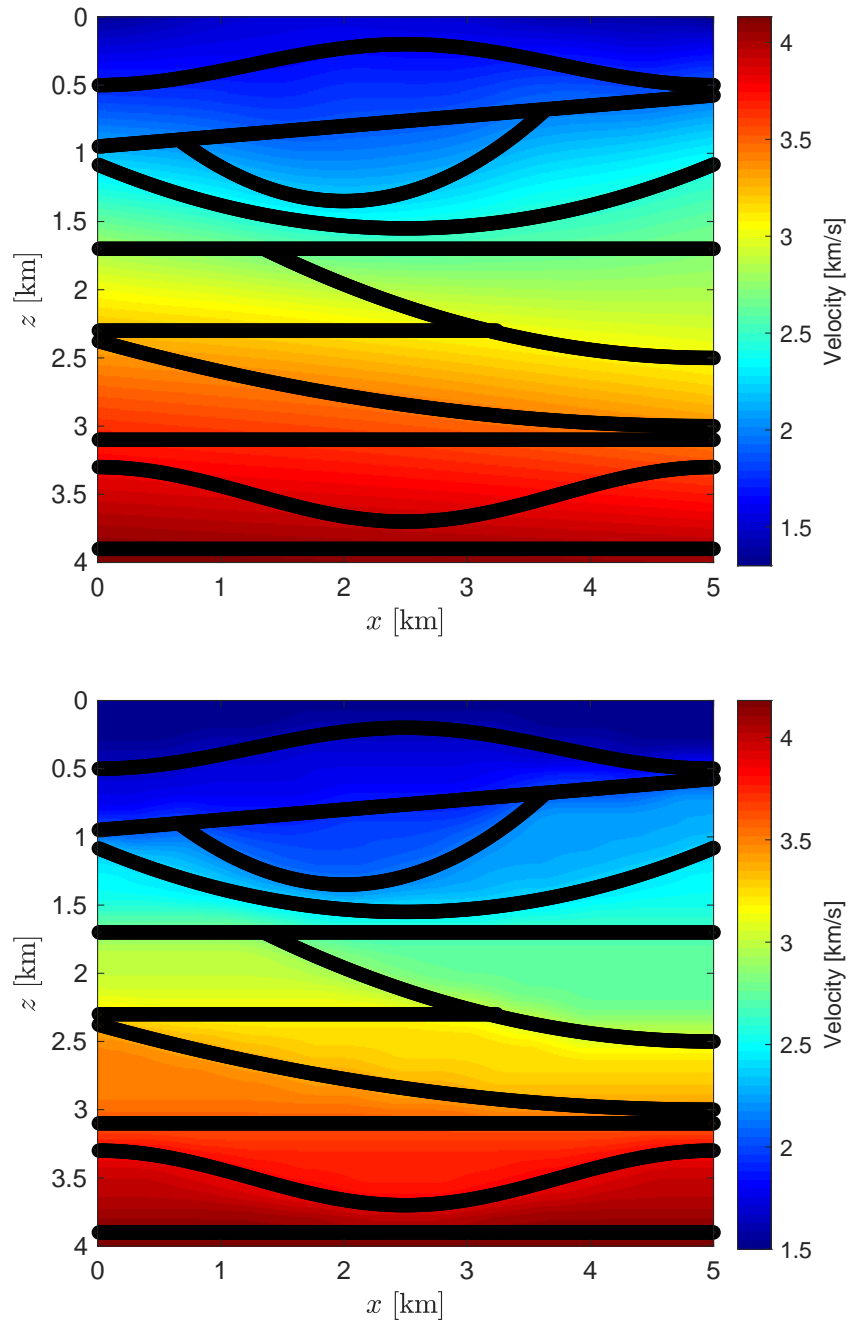CRP tomography will be tested for this experiment, once again, under a noisy-input data space. The objective is to evaluate the robustness of the method, mainly the quality of inverted model depth positions, in respect with inaccurate input data parameters. Parametrization of previous test will be kept the same. Just data space will be changed by random noise (under a uniform distribution) applied to all data kinematic parameters by the following rule:

- **Time:** a random value of the interval $[-10^{-2}\text{s}, 10^{-2}\text{s}]$ will be added to each traveltime input parameter.

- **Position:** a random value of the interval $[-7.5\text{m}, 7.5\text{m}]$ will be added to each position input parameter.

- **Slope:** a random value of the interval $[-5.10^{-5}\text{s/m}, 5.10^{-5}\text{s/m}]$ will be added to each slope (slowness vector) input parameter. The boundary values of this interval account for approximately 7.5% for the inverse of the velocity at surface line.

Figure 8.33: Final model depth positions returned by CRP tomography for second experiment. Red circles denote data positions, while white asterisks denote model positions. Almost all model depth positions were repositioned on correct data positions.

The previous random noise obeys an uniform distribution, and represents an intermediate level of random noise when compared to the level of noise applied for both two tests of first experiment.

CRP tomography final model - noisy input data case: CRP tomography proposed result for noisy-input data experiment is illustrated by Figure 8.34. The presence of noise in input data space has slightly affected the quality of tomographic final model, as illustrated by Figure 8.35. Under the presence of noisy input data space, mainly at the regions near the bottom line, inverted model positions couldn't be repositioned over the exact data depth position. However, they were still repositioned over the synthetic interfaces and, most of them, very close to the true data positions. Figure 8.36 illustrates the final model depth positions.
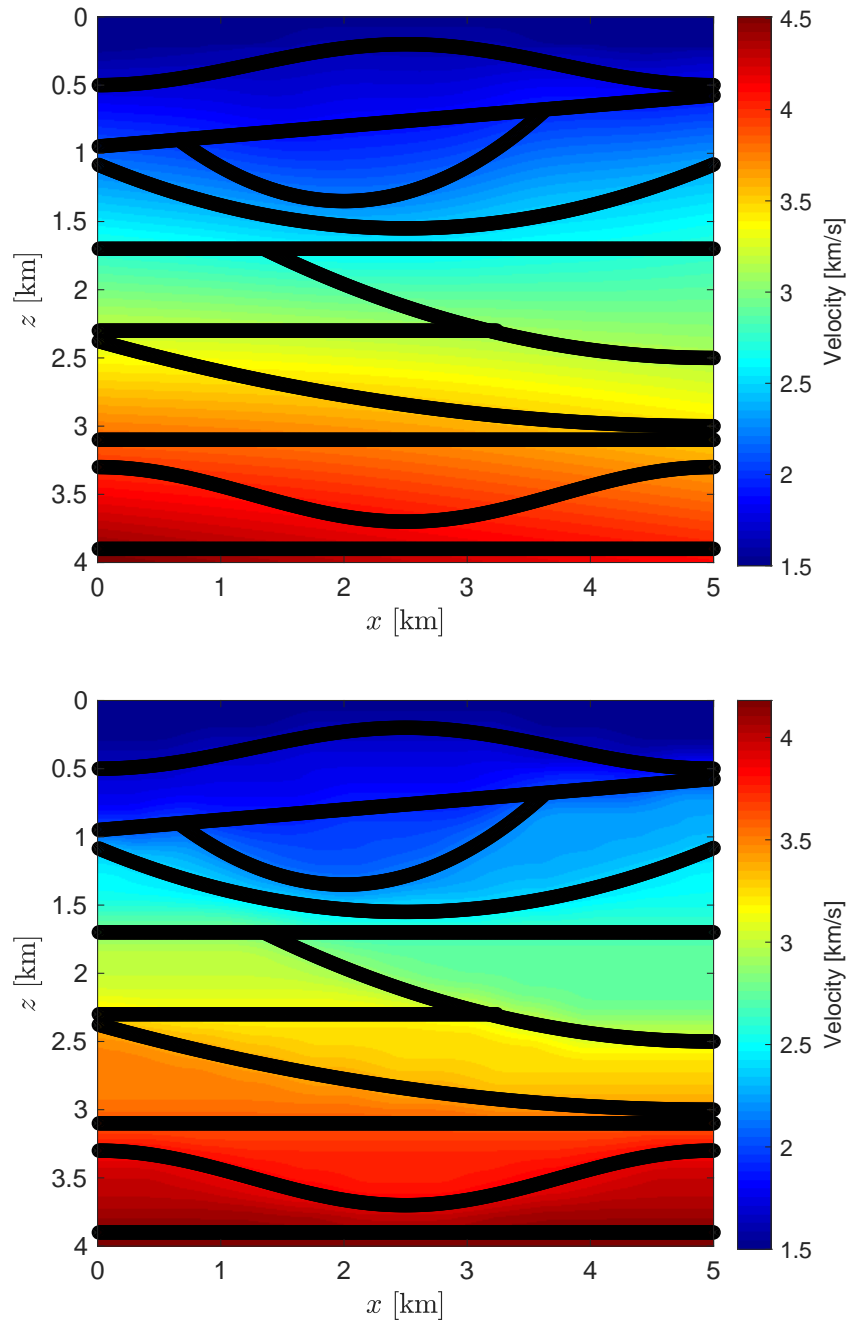
Figure 8.34: Final velocity model of CRP tomography noisy input test for second experiment (top image). True velocity model for second experiment (bottom image). Interfaces were displayed together with the velocity models.
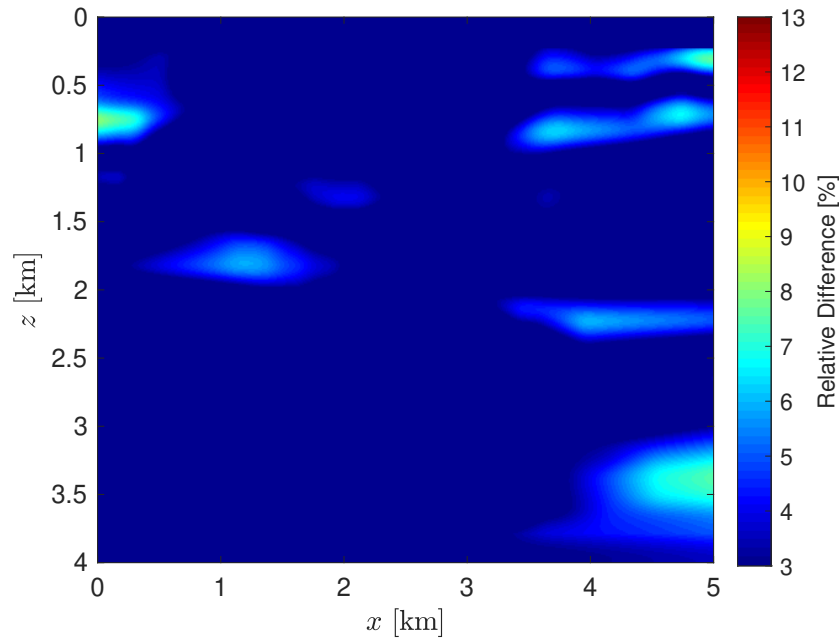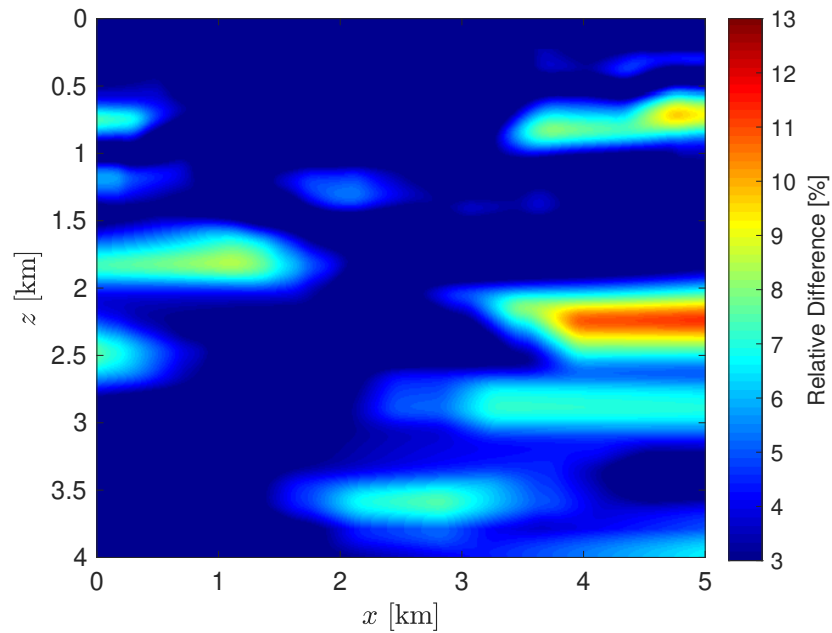
Figure 8.35: Relative errors of CRP tomography inverted velocity model for noisy input test of second experiment. Relative errors are greater than the ones presented by the noise-free test.
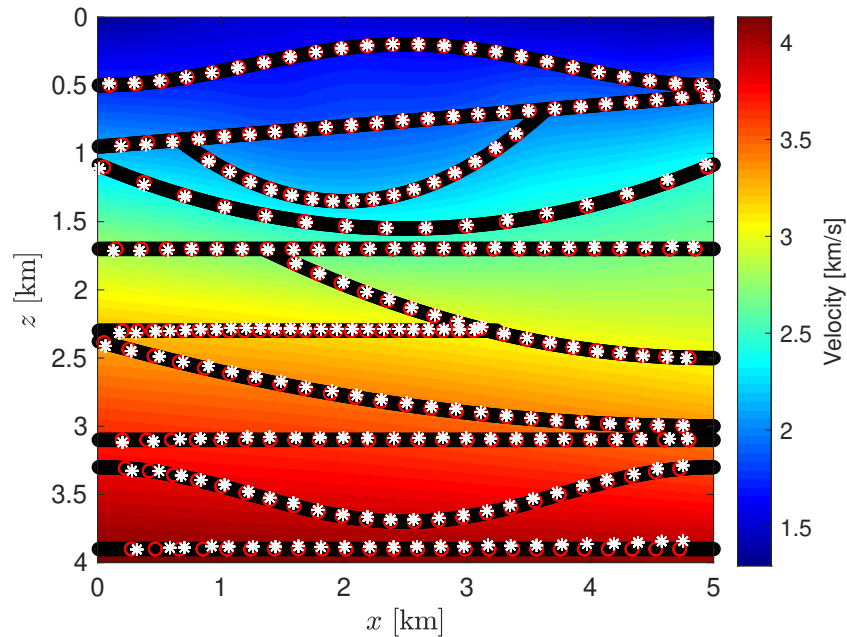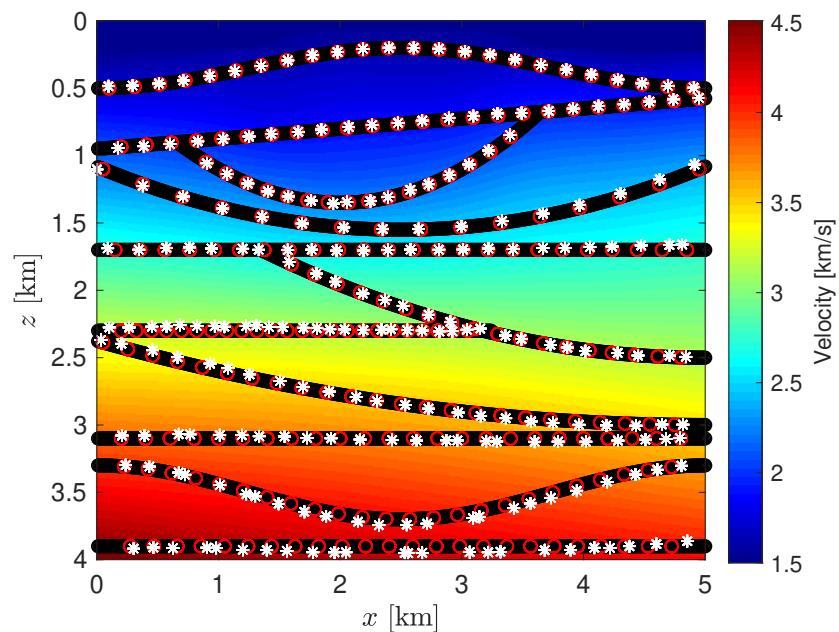

Figure 8.36: Final model depth positions returned by CRP tomography for noisy input test of second experiment. Red circles denote data positions, while white asterisks denote model positions. Despite the region near the bottom line, model depth points were repositioned very close to the respective true data positions.

Chapter 9

CRP tomography velocity model as input for FWI - A velocity model building procedure

This chapter illustrates the velocity model building procedure proposed in this thesis. This procedure consists of the use of CRP tomography velocity model as input for FWI application. The proposed velocity model building procedure will be further tested in a synthetic experiment.

Given a region of interest in depth, the proposed velocity model building procedure can be summarized as follows:

- (a) An arbitrary (simple) velocity model is chosen as initial velocity model for the velocity model building procedure. This velocity model is used as input for CRP tomography method.

- (b) CRP tomograpy data input components are collected/picked in input siesmic data and input parameters are specified. CRP tomography is performed under the chosen user-selected parametrization, picked input data components and the initial velocity model of item (a). In this thesis, the procedure of collect data input components is synthetically done by direct computation of such kinematic parameters by means of ray-tracing.

- (c) Under the input sets and parametrizations given by itens (a) and (b), a final (smooth) CRP tomography velocity model is obtained.

- (d) CRP tomography final velocity model is used as input for FWI application. As input data, FWI uses the role set of traces of input seismic data. In this thesis, these traces are directly computed by means of wave propagation.

- • (e) Under the input sets given by item (d), a final FWI velocity model is obtained, providing a high resolution final velocity model for the region of interest in depth.

The velocity model building procedure described above is summarized by the flowchart of Figure 9.1.
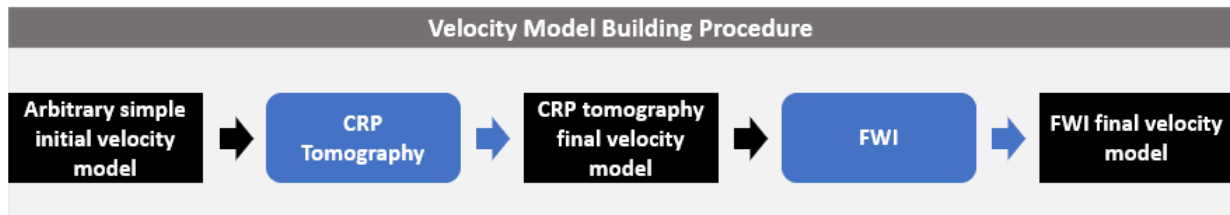
Figure 9.1: Flowchart of the proposed velocity model building procedure of this thesis.

The previous procedure was designed to overcome the crucial dependence on a good model-space initial guess for successful FWI inversion. Moreover, FWI has, most of the time, extreme demands on computational costs, wich turns the use of a good initial velocity model even more important to avoid too many applications of FWI method. On the other hand, CRP tomography iteration updates can be carried out by efficient computational implementation. Furthermore, CRP tomography can satisfactorily recover low-frequence content of the velocity field of the region of interest in depth, which is an important information required for good initial velocity models for FWI (see, e.g, Virieux et al. (2017)). As discussed in chapter 4, once the problem of initial velocity model dependence is overcomed, FWI can provide high resolution velocity models, recovering most of the high-frequence content of the velocity field of the region of interest in depth. Based on the results obtained so far in numerical tests reported in this thesis, CRP tomography is able to provide good final smooth velocity models by the use of very simple initial velocity models. Therefore, our proposed velocity model building procedure can starts with a simple initial velocity model and finishes the procedure providing a reasonable high resolution velocity model.

Here, it will be exemplified how CRP tomography final velocity model can overcome such crucial FWI dependence on initial velocity models, that is, it can be used as a good velocity model-space initial guess for successful FWI inversion. The example test will be carried out in a synthetic experiment using Marmousi velocity model, starting with a very simple, homogeneous velocity model. The use of a simple velocity model is important to reinforce the robustness of the proposed velocity model building procedure, being independent of any previous information about true velocity field in depth.

9.1   Velocity model building procedure application - Marmousi model

This section will illustrate one example of the proposed velocity model building procedure by means of a synthetic experiment. Marmousi model (Figure 9.2) was chosen as the velocity model to be tested by the proposed procedure. Before describe the experiment steps and obtained results, some brief comments about the FWI implementation used by the present experiment will be provided below.

FWI method to be performed uses the main features and details described in chapter 4. However, different of what was done for all seismic tomography methods presented in this thesis, FWI method was not implemented during the present research. Therefore, in order to illustrated the proposed velocity model building procedure, the present experiment uses one example of FWI implementation in the user role. The development and coding of all FWI algorithmic used in this experiment have been carried out in house at the High-Performance Geophysics (HPG) Laboratory at the Center for Petroleum studies (CEPETRO) at the University of Campinas (UNICAMP). The development was mainly inspired by reference Camargo (2019). For more details about the quasi-Newton optimization scheme applied, together with the step length Armijo's rule, the interest reader is reffered to Camargo (2019).

To perform the present experiment, it was considered the idealized situation of an ocean-bottom-node (OBN) seismic acquisition performed on the Marmousi velocity model subsurface illustrated in Figure 9.2. We suppose that the sea bottom is planar at depth $z = 500$m and the water velocity is 1.5km/s. Under such conditions, input observed data space for FWI, that is, synthetic seismic data traces, will be direct computed by means of wave propagation using finite-difference method (FMD). For more details about FMD, the interest reader can consult Camargo (2019).

FWI input observed-data space: To generate data space for FWI, shot records that correspond to 321 surface point sources and 601 receivers at a planar sea bottom surface located at 500m depth were considered. Figure 9.2 exhibits both the proposed planar sea bottom, where receivers were positioned, and surface line, where sources were placed. The shot records were simulated as the solutions of the acoustic wave equation (see chapter 4). A shot separation of 25m and a receiver separation of 10m was considered. Note that, with this acquisition parametrization, 8km of surface line is covered by point sources, with 25m of separation between them. Figure 9.2 exhibits the first and last sources of the line. On the other hand, receivers cover an extension of 6km of the proposed planar sea bottom, placed at
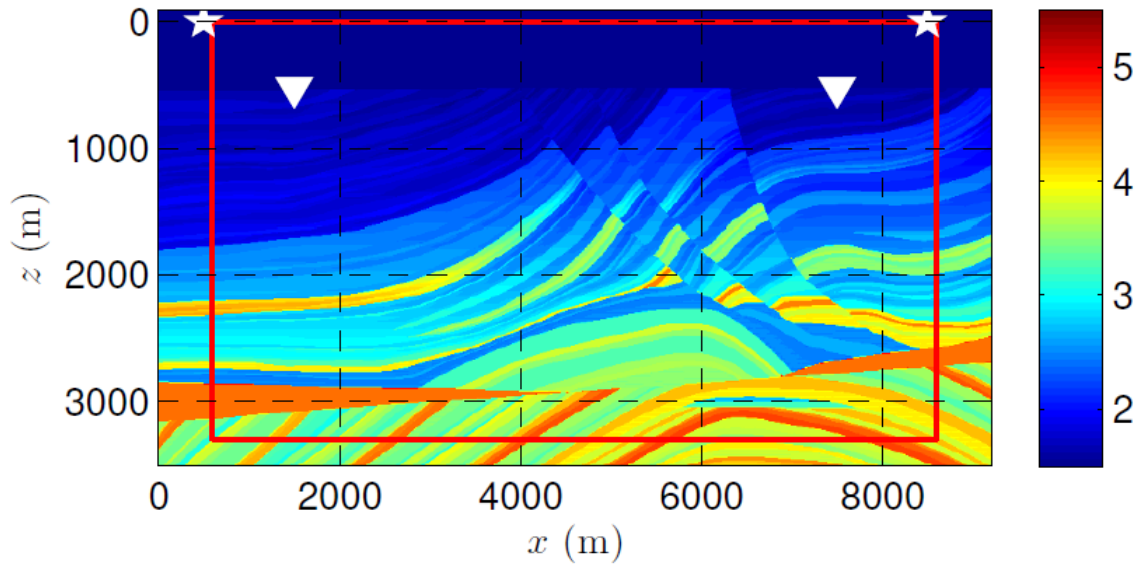
Figure 9.2: Marmousi velocity model. Colormap corresponds to velocity measured in km/s. Both the proposed planar sea bottom, where receivers were positioned, and surface line, where sources were placed, are illustrated. Just the first and last source/receiver are displayed. The red rectangle marks the region of interest for the present experiment. It takes into account border aspects for seismic inverse problems implementations and focuses the results on the region with more amount of data information.

the middle of the proposed sea bottom surface, with 10m of separation between them. Figure 9.2 also illustrates this distribution, showing the first and last receiver positions. Finally, the point sources were given by a Ricker wavelet with peak frequence of 20Hz. The FDM parameters considered were $\Delta x = \Delta z = 10$m, $\Delta t = 1$ms and a maximum record $T = 3$s. Under this configuration, FWI observed-data space is composed by 192921 observed seismic data traces.

The red rectangle of Figure 9.2 marks the region of interest for the present experiment. It takes into account border aspects for seismic inverse problems implementations. The region outside the red rectangle is the region with the least amount of input information. Therefore, the focus will be on the region inside the red rectangle. Note that it is delimited, in x-direction, by the source positions in surface line.

FWI initial model space: Following the proposed velocity model building procedure, CRP tomography velocity model will be proposed as initial velocity model for FWI experiment. Thus, before FWI method, CRP tomography will be performed in the present Marmousi test. Due to the complex velocity variation of Marmousi model in both directions, the velocity model of Figure 9.2 is unfeasible for ray-tracing purposes. Therefore, input data-observed kinematic parameters for CRP tomography

will be computed on a smooth version of Marmousi velocity model of Figure 9.2. The smooth version of Marmousi model (soft Marmousi) is displayed in Figure 9.3, where the red rectangle, sea bottom and surface lines were kept for comparison reasons. This smooth velocity model is very similar to the soft Marmousi velocity model presented in chapters 6 and 7. It was obtained by applying smoothing filter, i.e., a central moving average applied in eighty one points for each side to the original Marmousi velocity model of Figure 9.2.
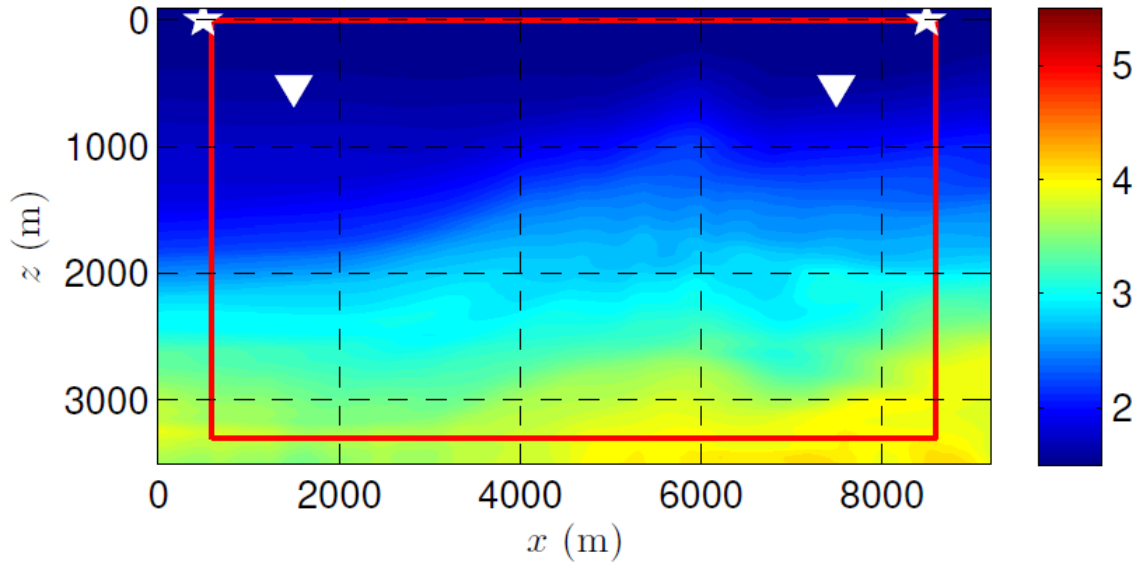
Figure 9.3: Smooth version of Marmousi velocity model of Figure 9.2. It was obtained by applying a central moving average applied in eighty one points for each side to the original Marmousi velocity model. This smooth version of Marmousi velocity model is used to construct input observede-data space for CRP tomography method, due to the fact that Marmousi model is unfeasible for ray-tracing purposes.

From now on, in order to perform CRP tomography step of the proposed velocity model building procedure, CRP tomography will be performed using a similar approach already used before in this thesis during soft marmousi test in chapter 7. Therefore, CRP tomography will be performed using, as input data space, kinematic wave parameters computed by ray-tracing performed in soft marmousi velocity model of Figure 9.3. A very simple initial homogeneous velocity model of 1.5km/s will be given as input velocity-model space for CRP tomography application. The parametrization used for CRP tomography test is summarized as follows:

CRP tomography input observed-data space: To generate observed-data space, 540 data depth positions were uniformly displayed through the red rectangle of soft Marmousi model of Figure 9.3. From each of these positions, ten pairs of rays were traced through the model and the kinematic

parameters of position, traveltime and slopes were computed at surface line. The rays were propagated with initial double aperture, with respect to vertical direction, varying from 5° to 40°. All traveltimes related with rays starting from the same data common-depth-position were summed. Therefore, data space is composed 540 families, each of them with a data total traveltime and ten samples composed by two data positions and two data slope parameters.

CRP tomography initial model space: A homogeneous velocity model of 1.5km/s was used as initial velocity-model space for CRP tomography. Therefore, CRP tomography was performed with no a priori knowledges about true velocity model. The interpolation knots were distributed through interpolaiton grid, with vertical and horizontal spacing of 0.5km. Finally, inital CRP ray-model space was initialized with the proposed initialization procedure of chapter 5, returning 540 gathers of model samples, each of them composed by one initial model position in depth and ten pairs of initial model slopes.

Initial regularization weight parameter: Initial regularization parameter λ was set in order to keep the same level of regularization used for soft marmousi test in chapter 7. Therefore, at first iteration, the relation between the regularization term in respect to the objective function was set as 5.10^{-5}. Also, $\epsilon_{zz} = 10^{-2}$, $\epsilon_{xx} = 1$ and $\epsilon_{vv} = 10^{-4}$ were set to calibrate regularization term.

CRP tomography velocity model: Under the initial conditions and parametrizations previously described, CRP tomography final velocity model is illustrated by Figure 9.4. As can be noted, CRP tomography method could provide a good smooth velocity model for Marmousi model. Note how the inverted velocity model is much similar to the soft marmousi velocity model in almost all regions of the model. Compare with Figure 9.3. As expected, CRP tomography final velocity model is a smooth model, without high-frequence content. To recover high-frequence content, CRP tomography final velocity model illustrated by Figure 9.4 will be used as input for FWI method.

FWI application: Now, in order to finish the illustration of the proposed velocity model building procedure, CRP tomography final velocity model of Figure 9.4 will be used as initial velocity model for FWI. As it is known, FWI is dependent of a good initial velocity model that contains low-frequence information about the velicty field of the region of interest in depth (see, e.g, Virieux et al. (2017)). Here, it will be shown how CRP tomography velocity model can be used to overcome this dependence. Through FWI inverse process, the same numerical scheme of finite-difference considered to construct input FWI observed-data space is used to iteratively generate synthetic traces under
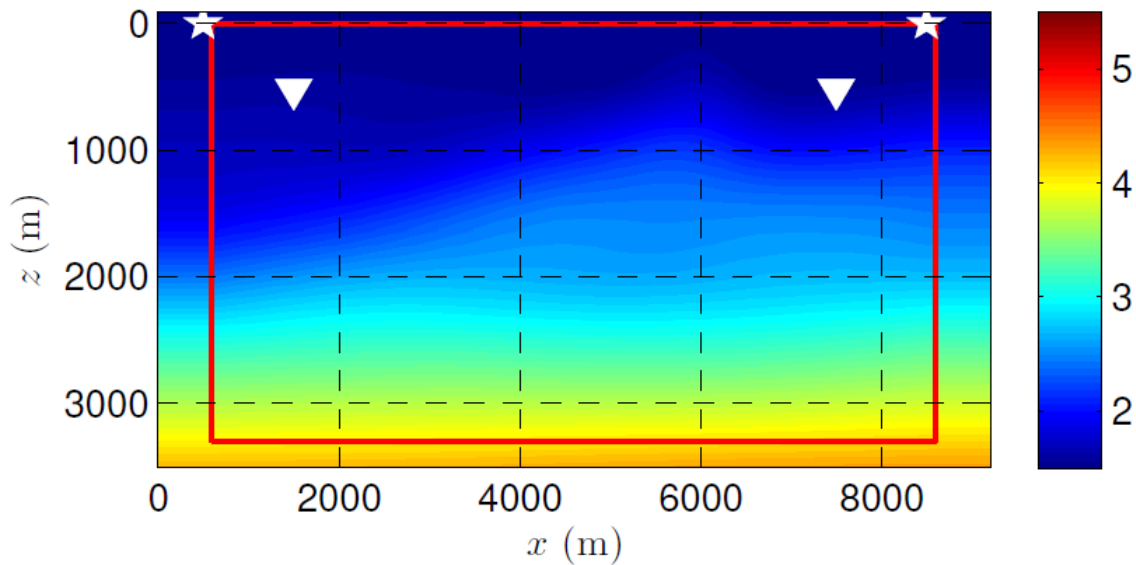
Figure 9.4: CRP tomography final velocity model for the present experiment. An initial homogeneous velocity model of 1.5km/s was used as input for the method. Note how the inverted velocity model is much similar to the soft marmousi velocity model in almost all regions of the model. Compare with Figure 9.3. This model is used as initial velocity model for FWI application.

current model conditions. A maximum of 200 iterations was adopted as a stop criteria.

FWI final result: Figure 9.5 illustrates FWI final velocity model for the present experiment. Note that the final solution presents the proposed desired features, that is, given a initial velocity model with good content of low-frequence about the velocity model of the region of interest in depth, FWI method could recover high-frequence content and generate a high resolution final velocity model. The present result validades our proposed velocity model building procedure in Marmousi experiment context and, consequently, the use of CRP tomography velocity model as input for FWI.

Under CRP tomography velocity provided as initial velocity model for FWI method, FWI could iteratively recovered most of the high frequence content of marmousi velocity model. Note how it was possible, by the present velocity model building procedure, to derive a quite good final velocity model for Marmousi test by using, as initial velocity model guess for the role procedure, a very simple (homogeneous) velocity model. Moreover, no initial previous velocity model knowledge was used in all steps of our present synthetic test. Once CRP tomography has been shown, so far, to be a robust technique with respect to the choice of initial velocity models, this procedure can also be robust to this particular choice, allowing the use of arbitrary simple initial velocity models for the proposed velocity model building procedure.

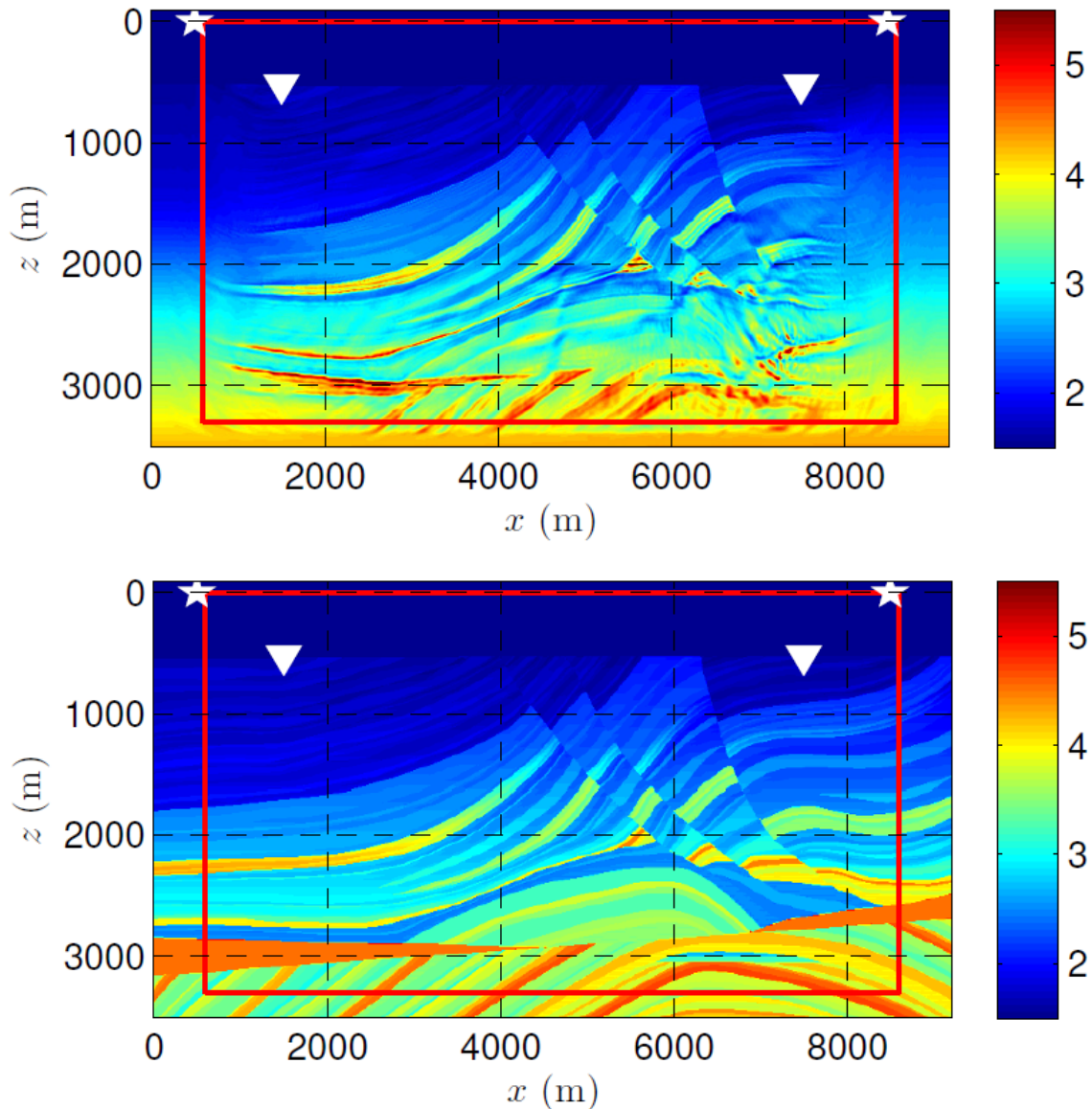Figure 9.5: Top: Final velocity model proposed by FWI under the use of CRP tomography velocity as input for FWI inverse process. Two hundred iterarions were performed. Bottom: true Marmousi velocity model for comparison reasons. Under CRP tomography velocity provided as initial velocity model for FWI method, FWI could iteratively recover most of the high frequence content of Marmousi velocity model.

9.2   Velocity model building procedure without CRP tomography step

To illustrate the strong dependence of FWI on a good initial velocity model and reinforce the important role played by CRP tomography in the proposed velocity model building procedure, the present Marmousi experiment was performed, once again, without the CRP tomography step. In other words, the initial homogenous velocity model used as initial velocity model for CRP tomography step will be provided as initial velocity model for FWI. Therefore the intermediate step of CRP tomography will not be considered, and the initial homogeneous velocity model of the role velocity model building procedure will be direct used as an initial guess for FWI.

The velocity model building procedure without the intermediate CRP tomography step is illustrated by the flowchart of Figure 9.6.
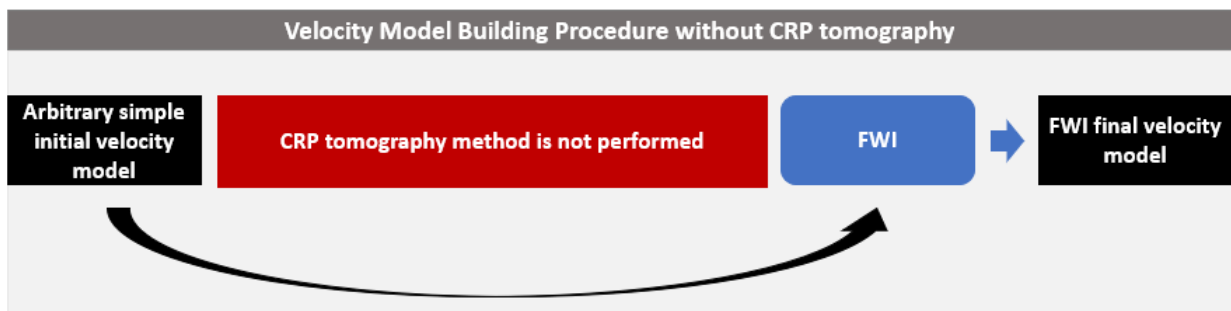
Figure 9.6: Flowchart of the velocity model building procedure without CRP tomography step.

Figure 9.7 illustrates FWI final velocity model of this experiment. Note that FWI could not recover a reasonable velocity model under the use of an initial homogenous velocity model. As the initial velocity model does not contain the necessary low-frequence content about the velocity model of interest, FWI couldn't recover the high-frequence information and further generate a good high resolution velocity model. This experiment exemplifies the strong dependence of FWI on a good initial velocity model and justifies the importance of CRP tomography (or any other type of seismic tomography method) as an intermediate step of the proposed velocity model procedure.
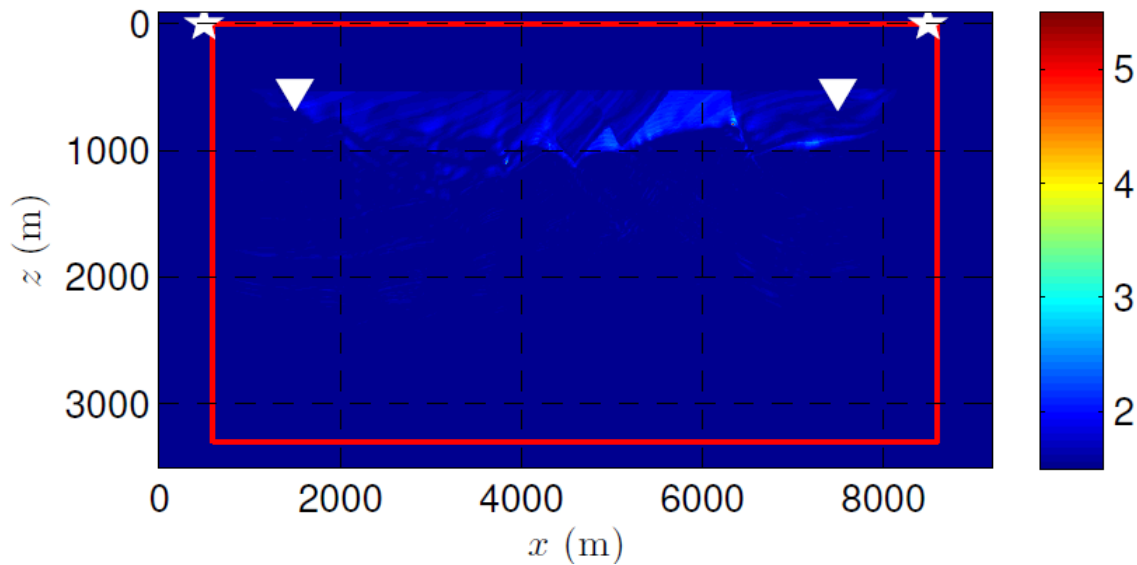
Figure 9.7: Final velocity model proposed by FWI under the use of a homogeneous velocity model of 1.5km/s as input for FWI inverse process. Under this simple initial velocity model, FWI could not invert a reasonable final velocity model. This experiment exemplifies the strong dependence of FWI on a good initial velocity model that contains low-frequence content about the velocity model of the region of interest.

9.3   Other strategies to generate initial velocity model for FWI

Other strategies and procedures have been researched so far to overcome the strong depencence of FWI on a good initial velocity model. Next paragraph will mention some of this strategies, mainly the *two-phase FWI approach* proposed by Camargo (2019).

Two-phase FWI approach and other strategies: The use of a good initial velocity model is, in fact, very important for FWI applications. Camargo (2019) discusses similar FWI tests using very simple initial velocity models, where no reasonable velocity final is obtained. Here, CRP tomography velocity model could overcome this depencence on a good initial velocity model for succesful FWI inversion. In Camargo (2019), the difficulty of deriving reasonable initial velocity model for FWI is mitigated with FWI applied after the application of preliminary simplified versions of full FWI. This is called *two-phase FWI approach*. In the first phase, FWI is formulated as a constrained nonlinear problem by means of the augmented Lagrangian method. A first version of the initial velocity model is parametrized as a linear combination of specific basis functions, e.g., constant vertical gradient, horizontal interfaces, radial basis functions, among others. To assist the inversion process, information extracted from well-log data are, if available, applied. In second phase, the obtained first-phase,

velocity-model is used as input for another, this time box-constrained, FWI problem. That problem is solved by the spectral gradient project (SPG), proposed in Birgin et al. (2000). In summary, the strategy uses a first-phase scheme to guide the initial model into a region near an attractive basin, while a second-phase scheme is applied to improve the model resolution. Introduction of a priori information, such as, e.g., well-data and uncertainty estimations, can be also quite useful (see, e.g, Virieux et al. (2017)). Other examples of procedures derived to provide good initial velocity models for FWI can also be addressed in references Biondi and Almomin (2013) and Symes (2008).

Chapter 10

Summary and conclusions

In this thesis, a new seismic tomography method was proposed. Named common-relfection-point (CRP) tomography, this new method relies on recent results on CRP (also referred to as offset-continuation) seismic processing and imaging. CRP tomography has stereotomography as its mains source of inspiration and can be considere an advanced version of stereotomography. Both methods are designed for unstacked domain and can be classified as slope tomography methods. However, independent data points of stereotomography were replaced with CRP data gathers in new CRP tomography method. In fact, it represents the main difference between stereotomography and CRP tomography. Therefore, instead of individual, independent picked/extracted data points used in stereotomagraphy, CRP tomography uses a collection of CRP data gathers. More specifically, each CRP gather consists of all source-receiver pairs within the input data for which the primary-reflection rays for a certain interface have the same (common) reflection point. Those gathers provide, at feasible computation costs, not only a more comprehensive coverage of the subsurface region under investigation, but also redundancy that is useful to the inversion process. Moreover, when compared to individual data points of stereotomography, the inclusion of CRP gathers does not increase the number of necessary picks to be collected in seismic data.

The present research assumed a proof-of-concept framework: for illustrative synthetic-data examples for which CRP gathers are known in advance, the task is to evaluate the actual potential and benefits of CRP tomography, as compared to state-of-the-art approaches such as stereotomography. An in-depth discussion on how CRP gathers are actually extracted from the input data, was not of prime concern, although an explanation about how this process can be carried out was provided in Appendix F. Following its proof-of-concept framework, all synthetic-data examples in this thesis were carried by means of ray tracing performed on given velocity models.

In Chapters 6 and 7, several tests carried out on a variety of synthetic tests confirmed the good expectations of the proposed CRP tomography. In comparison with stereotomography results, CRP tomography was capable to better invert synthetic velocity models by the use of a smaller number of data points and/or worse initial velocity models. The need of a smaller number of data points (gathers) has shown to be a good feature of CRP tomography method, since it depends to a smaller number of picks to be performed. At least in the set of synthetic tests illustrating this thesis, CRP tomography was seen to be quite robust with respect to initial velocity models, which is a quite attractive feature. In the same way, robustness with respect to variations of initial regularization parameter was also shown by CRP tomography.

In Chapter 8, further synthetic tests with included interfaces and noisy data have also shown a good performance of the CRP tomography. Those tests illustrated how the introduction of CRP gathers could improve the inversion quality, not only of the velocity models, but also the positioning of model depth points. In particular, almost all depth points on synthetic interfaces were brough to correct positions, even in the presence of noisy input data. In fact, CRP tomography was the only method to be capable to satisfactorily invert the more complex model test with a high velocity region in the middle of the model.

In Chapter 9, a final velocity model of CRP tomography applied to the Marmousi, was tested as input for an FWI experiment. There, the CRP-tomographic velocity model was able to overcome the recognized FWI initial-velocity dependence to achieve a successful inversion.

As a final remark, we observe that the CRP tomography method has been greatly benefited from an in-depth analysis of NIP wave tomography and related literature. Valuable insights and understanding were gained from actual 2D implementations, in particular the adoption of the originally-proposed NIP-tomography regularization term.

Last but not least, all tomographic methods reported in this thesis, e.g, stereotomography, NIP wave tomography and CRP tomography were fully implemented during the present research. All features of the inversion method were derived from actual implementations. That included all schemes employed for ray tracing, B-spline interpolations, mathematical methods to solve ill-conditioned linear systems, initialization procedure and regularization. Building all those schemes from scratch was of paramount importance to fully understand the relevant aspects of the tomographic inverse process, as well as to spot possible points where advances could be made.

10.1 Future research

The present thesis represents a first report on the CRP tomography method. Here, the method was presented for the very first time and tested over a set of synthetic model tests. As a first presentation, the method was conceived for two dimensional isotropic space and synthetic tests were carried out under a proof-of-concept framework. Several researches have to be made in order to continue the development of the new proposed seismic tomography method, both in theoretical and practical aspects. Some of the possible future researches in CRP tomography are listed below:

On the theoretical side:

- Extend CRP tomography method to three dimensional space.

- Extend and validate CRP tomography to elastic isotropic and anisotropic media.

- Develop efficient procedures for picking, as well as corresponding CRP-gather estimations.

On the practical side:

- Efficient computational implementation of CRP tomography method and its proposed extensions.

- Subject CRP-tomography to real-data application.

References

Billette, F., Bégat, S. L., Podvin, P., and Lambaré, G. (2003). Practical aspects and applications of 2d stereotomography. *Geophysics*, 68(3):1008–1021.

Billette, F. and Lambaré, G. (1998). Velocity macro-model estimation from seismic reflection data by stereotomography. *Geophysical Journal International*, 135(2):671–690.

Biondi, B. (1992). Velocity estimation by beam stack. *Geophysics*, 57(8):1034–1047.

Biondi, B. and Almomin, A. (2013). Tomographic full-waveform inversion (tfwi) by combining fwi and wave-equation migration velocity analysis. *The Leading Edge*, 32(9):1074–1080.

Birgin, E. G., Martínez, J. M., and Raydan, M. (2000). Nonmonotone spectral projected gradient methods on convex sets. *SIAM Journal on Optimization*, 10(4):1196–1211.

Bishop, T., Bube, K., Cutler, R., Langan, R., Love, P., Resnick, J., Shuey, R., Spindler, D., and Wyld, H. (1985). Tomographic determination of velocity and depth in laterally varying media. *Geophysics*, 50(6):903–923.

Bleistein, N. (1986). Two-and-one-half dimensional in-plane wave propagation. *Geophysical Prospecting*, 34(5):686–703.

Bleistein, N., Cohen, J. K., John Jr, W., et al. (2013). *Mathematics of multidimensional seismic imaging, migration, and inversion*, volume 13. Springer Science & Business Media.

Camargo, A. W. (2019). *Full wave inversion by the augmented Lagrangean method (in Portuguese*. PhD thesis, University of Campinas.

Cerveny, V. (2005). *Seismic ray theory*. Cambridge university press.

Chalard, É., Podvin, P., Le Begat, S., Berthet, P., and David, B. (2002). 3d stereotomographic inversion on real data set. In *SEG Technical Program Expanded Abstracts 2002*, pages 946–948. Society of Exploration Geophysicists.

Chang, X., Liu, Y., Wang, H., Li, F., and Chen, J. (2002). 3-D tomographic static correction. *Geophysics*, 67(4):1275–1285.

Chauris, H., Noble, M. S., Lambare, G., and Podvin, P. (2002). Migration velocity analysis from locally coherent events in 2-d laterally heterogeneous media, part i: Theoretical aspects. *Geophysics*, 67(4):1202–1212.

Chernyak, V. and Gritsenko, S. (1979). Interpretation of the effective common-depth-point parameters for a three-dimensional system of homogeneous layers with curvilinear boundaries. *Geologiya i Geofizika*, 20(12):112–120.

Claerbout, J. F. (1971). Toward a unified theory of reflector mapping. *Geophysics*, 36:467–481.

Claerbout, J. F. (1985). *Imaging the earth's interior*, volume 1. Blackwell scientific publications Oxford.

Coimbra, T. A., Faccipieri, J. H., Rueda, D. S., and Tygel, M. (2016a). Common-reflection-point time migration. *Studia Geophysica et Geodaetica*, 60(3):500–530.

Coimbra, T. A., Novais, A., and Schleicher, J. (2012). Offset continuation (oco) ray tracing using oco trajectories. *Studia Geophysica et Geodaetica*, 56(1):65—-82.

Coimbra, T. A., Novais, A., and Schleicher, J. (2016b). Offset-continuation stacking: Theory and proof of concept. *Geophysics*, 81(5):V387–V401.

de Boor, C., De Boor, C., Mathématicien, E.-U., De Boor, C., and De Boor, C. (1978). *A practical guide to splines*, volume 27. Springer-Verlag New York.

Dell, S., Gajewski, D., and Tygel, M. (2014). Image-ray tomography. *Geophysical Prospecting*, 62(3):413–426.

Dormand, J. R. and Prince, P. J. (1980). A family of embedded runge-kutta formulae. *Journal of computational and applied mathematics*, 6(1):19–26.

Dümmong, S., Meier, K., Gajewski, D., and Hübscher, C. (2008). Comparison of prestack stereotomography and nip wave tomography for velocity model building: Instances from the messinian evaporites. *Geophysics*, 73(5):VE291–VE302.

Duveneck, E. (2004a). 3d tomographic velocity model estimation with kinematic wavefield attributes. *Geophysical Prospecting*, 52(6):535–545.

Duveneck, E. (2004b). *Tomographic determination of seismic velocity models with kinematic wavefield attributes*. PhD thesis, Karlsruhe, Univ., Diss., 2004.

Duveneck, E. (2004c). Velocity model estimation with data-derived wavefront attributes. *Geophysics*, 69(1):265–274.

Duveneck, E. and Hubral, P. (2002). Tomographic velocity model inversion using kinematic wavefield attributes. In *SEG Technical Program Expanded Abstracts 2002*, pages 862–865. Society of Exploration Geophysicists.

Faccipieri, J. (2016). *Método CRS interativo com controle semiautomático de aberturas*. PhD thesis, Universidade de Campinas.

Farra, V. and Madariaga, R. (1987). Seismic waveform modeling in heterogeneous media by ray perturbation theory. *Journal of Geophysical Research: Solid Earth*, 92(B3):2697–2712.

Farra, V. and Madariaga, R. (1988). Non-linear reflection tomography. *Geophysical Journal International*, 95(1):135–147.

Fichtner, A., Bunge, H.-P., and Igel, H. (2006). The adjoint method in seismology: I. theory. *Physics of the Earth and Planetary Interiors*, 157(1-2):86–104.

Gauthier, O., Virieux, J., and Tarantola, A. (1986). Two-dimensional nonlinear inversion of seismic waveforms: Numerical results. *Geophysics*, 51(7):1387–1403.

Gray, S. H., Etgen, J., Dellinger‡, J., and Whitmore, D. (2001). Y2K Review Article: Seismic migration problems and solutions. *Geophysics*, 66(5):1622–1640.

Hadamard, J. (1902). Sur les problèmes aux dérivées partielles et leur signification physique. *Princeton University Bulletin*, 13:49–52.

Holberg, O. (1987). Computational aspects of the choice of operator and sampling interval for numerical differentiation in large-scale simulation of wave phenomena. *Geophysical prospecting*, 35(6):629–655.

Hubral, P. (1983). Computing true amplitude reflections in a laterally inhomogeneous earth. *Geophysics*, 48(8):1051–1062.

Iversen, E., Tygel, M., Ursin, B., and de Hoop, M. V. (2012). Kinematic time migration and demigration of reflections in pre-stack seismic data. *Geophysical Journal International*, 189(3):1635–1666.

Jones, I. F. (2010). *An introduction to: Velocity model building*. Eage Publications.

Kelly, K., Ward, R., Treitel, S., and Alford, R. (1976). Synthetic seismograms: A finite-difference approach. *Geophysics*, 41(1):2–27.

Kosloff, D., Sherwood, J., Koren, Z., Machet, E., and Falkovitz, Y. (1996). Velocity and interface depth determination by tomography of depth migrated gathers. *Geophysics*, 61(5):1511–1523.

Lambaré, G. (2004). Stereotomography–past, present and future. In *66th EAGE Conference and Exhibition-Workshops*.

Lambaré, G. (2008). Stereotomography. *Geophysics*, 73(5):VE25–VE34.

Lambaré, G., Alerini, M., Baina, R., and Podvin, P. (2004). Stereotomography: a semi-automatic approach for velocity macromodel estimation. *Geophysical Prospecting*, 52(6):671–681.

Lavaud, B., Baina, R., and Landa, E. (2004). Post-stack stereotomography: a robust strategy. In *Expanded Abstracts*, page C22. EAGE.

Le Bégat, S., Podvin, P., and Lambaré, G. (2000). Application of 2d stereotomography to marine seismic reflection data. In *SEG Technical Program Expanded Abstracts 2000*, pages 2142–2145. Society of Exploration Geophysicists.

Maharramov, M. (2016). *Time-lapse inverse theory*. PhD thesis, Stanford Univesrity.

Mann, J. (2002). *Extensions and applications of the common reflection surface stack method*. Logos-Verlag.

Müller, T. (1999). *The common reflection surface stack method: Seismic imaging without knowledge of the velocity model*. Der Andere Verlag.

Neckludov, D., Baina, R., and Landa, E. (2006). Residual stereotomographic inversion. *Geophysics*, 71(4):E35–E39.

Nemeth, T., Normark, E., and Qin, F. (1997). Dynamic smoothing in crosswell traveltime tomography. *Geophysics*, 62(1):168–176.

Nguyen, S., Baina, R., Alerini, M., Lambaré, G., Devaux, V., and Noble, M. (2008). Stereotomography assisted by migration of attributes. *Geophysical Prospecting*, 56(5):613–625.

Nocedal, J. and Wright, S. (2006). *Numerical optimization*. Springer Science & Business Media.

Paige, C. C. and Saunders, M. A. (1982). Lsqr: An algorithm for sparse linear equations and sparse least squares. *ACM Transactions on Mathematical Software (TOMS)*, 8(1):43–71.

Plessix, R. E. (2006). A review of the adjoint-state method for computing the gradient of a functional with geophysical applications. *Geophysical Journal International*, 47(2):495–503.

Popov, M. M. (2002). *Ray theory and Gaussian beam method for geophysicists*. Edufba.

Pratt, R. and Chapman, C. (1992). Traveltime tomography in anisotropic media—ii. application. *Geophysical Journal International*, 109(1):20–37.

Pratt, R. G., Shin, C., and Hick, G. (1998). Gauss–newton and full newton methods in frequency–space seismic waveform inversion. *Geophysical Journal International*, 133(2):341–362.

Press, W. H., Teukolsky, S. A., Vetterling, W. T., and Flannery, B. P. (1988). Numerical recipes in c.

Riabinkin, L. (1957). Fundamentals of resolving power of controlled directional reception (cdr) of seismic waves. *Slant-stack processing: SEG*, pages P36–P60.

Rieber, F. (1936). A new reflection system with controlled direction sensitivity. *Geophysics*, 1(1):97—-106.

Santos, L., Schleicher, J., and Tygel, M. (1997). 2.5-d true-amplitude offset continuation. *Journal of Seismic Exploration*, 6(2-3):103–116.

Schleicher, J., Tygel, M., and Hubral, P. (1993). Parabolic and hyperbolic paraxial two-point travel-times in 3d media1. *Geophysical Prospecting*, 41(4):495–513.

Stork, C. (1992). Reflection tomography in the postmigrated domain. *Geophysics*, 57(5):680–692.

Sword, C. H. (1987). *Tomographic determination of interval velocities from reflection seismic data: The method of controlled directional reception*. PhD thesis, Stanford University.

Sword Jr, C. H. (1986). Tomographic determination of interval velocities from picked reflection seismic data. In *SEG Technical Program Expanded Abstracts 1986*, pages 657–660. Society of Exploration Geophysicists.

Symes, W. W. (2008). Migration velocity analysis and waveform inversion. *Geophysical prospecting*, 56(6):765–790.

Tarantola, A. (1984). Linearized inversion of seismic reflection data. *Geophysical Prospecting*, 32(6):998–1015,.

Tarantola, A. (1987). Inverse problem theory: Methods for data fitting and model parameters estimation. *Elsevier*.

Tygel, M., Schleicher, Joerg, H. P., and Santos, L. T. (1998). 2.5-d true-amplitude kirchhoff migration to zero offset in laterally inhomogeneous media. *Geophysics*, 63(2):557–573.

Tygel, M., Ursin, B., Iversen, E., and Maarten, V. (2012). Estimation of geological dip and curvature from time-migrated zero-offset reflections in heterogeneous anisotropic media. *Geophysical prospecting*, 60(2):201–216.

Tykhonov, A. N. and Arsenin, V. J. (1977). Solutions of ill-posed problems. *Wiley*.

Ursin, B. (1982). Quadratic wavefront and traveltime approximations in inhomogeneous layered media with curved interfaces. *Geophysics*, 47(7):1012–1021.

Van Loan, C. F. and Golub, G. H. (1983). *Matrix computations*. Johns Hopkins University Press Baltimore.

Virieux, J., Asnaashari, A., Brossier, R., Métivier, L., Ribodetti, A., and Zhou, W. (2017). An introduction to full waveform inversion. In *Encyclopedia of exploration geophysics*, pages R1–1. Society of Exploration Geophysicists.

Virieux, J. and Operto, S. (2009). An overview of full-waveform inversion in exploration geophysics. *Geophysics*, 74(6):WCC1–WCC26.

Washbourne, J. K., Rector, J. W., and Bube, K. P. (2002). Crosswell traveltime tomography in three dimensions. *Geophysics*, 67(3):853—-871.

Watkins, D. S. (2004). *Fundamentals of matrix computations*, volume 64. John Wiley and Sons.

Whiting, P. M. (1991). Practical reflection tomography and maximum entropy imaging. In *SEG Technical Program Expanded Abstracts 1991*, pages 986–989. Society of Exploration Geophysicists.

Williamson, P. (1990). Tomographic inversion in reflection seismology. *Geophysical Journal International*, 100(2):255–274.

Yedlin, M. J. and van Vorst, D. G. (2010). Tutorial on the continuous and discrete adjoint state method and basic implementation. *CREWES Research Report*, 22:91.1–91.11.

Zhang, H., Sarkar, S., Toksoz, M. N., Kuleli, H. S., and Al-Kindy, F. (2009). Passive seismic tomography using induced seismicity at a petroleum field in oman. *Geophysics*, 74(6):WCB57–WCB69.

Zhu, X., Szxta, D. P., and Angstman, B. P. (2009). Tomostatics: Turning-ray tomography + static corrections. *The Leading Edge*, 11(12):15–23.

Appendix A

NIP wave tomography

This appendix will provide a brief summary about NIP wave tomography method. It is not the objective of this appendix a full detailed description of the method, as it was done in Chapter 3 for stereotomography and Chapter 5 for CRP tomography method. Therefore, justa data, model and synthetic spaces, as well as initialization procedure for NIP wave tomography will be described. Since iterative process is very similar to the ones presented before for stereotomography and CRP tomography in this thesis, just some comments will be provided. For a more detailed explanation, the interested reader can consult the main reference Duveneck (2004b).

A.1   Introduction

Normal incidence point wave tomography, or simply NIP wave tomography, is a curvature tomography method in the zero-offset domain. The name NIP comes from the name of the point in subsurface where a point source is positioned to generate the hypothetical *NIP wavefront* (see, e.g, Hubral (1983)). NIP wave tomography aims to invert smooth velocities models, as well as positions and slopes in depth, that might be used, for example, as an initial velocity model for depth migration or FWI. For this purpose, the method uses information of kinematic wavefield parameters estimated by means of common reflection surface (CRS) stacking procedure (see, e.g, Faccipieri (2016), Mann (2002), Müller (1999)) as input for the tomographic inversion processes. The kinematic wavefield parameters are: normal ray traveltime, horizontal slowness vector, second spatial traveltime derivatives (related to the curvature of hyphotetical NIP wavefront) and the zero-offset position. All the information are related to the normal ray of NIP wavefront at the surface acquisition and estimated

by CRS parameters. Given an arbitrary set of model positions and slopes in subsurface, plus an arbitrary velocity model, these input kinematic wavefield parameters can be synthetically computed by dynamic-ray tracing (see Appendix C). The misfit between synthetic computed and observed kinematic parameters are used as the objective function to invert the desired velocity model, as well as model depth positions and slopes.

Two of the remarkable innovations of NIP wave tomography method, when firstly presented in early 2000s, were: the use of kinematic parameters related to curvature of hyphotetical NIP wavefront and the extraction of input parameters in CRS stack panels. Thus, NIP wave tomography depends on wavefield attributes resulting from the application of CRS stacking operator and, therefore, it is based on a hyperbolic second-order traveltime approximation. If traveltimes of reflection events in seismic data are reasonably well described by hyperbolic second-order approximations, the information contained in the kinematic wavefield attributes can be used for the determination of a laterally heterogeneous velocity model for depth imaging. The approximation details are outside the scopus of this work and, therefore, will not be discussed here. The interested reader can consult Duveneck (2004c) and Müller (1999) for more details on this subject. Also, one of the great contributions of the method, the picking process in CRS panels, which has better signal-to-noise resolution, will not be discussed in this thesis, since all the synthetic tests were performed without the necessity of picking process, once input parameters were direct computed by dynamic-ray-tracing. All tests were performed in 2D media by the use of regularization term given by the minimization of second derivatives of the velocity model, which was inspired by reference Duveneck (2004b).

In this appendix, only NIP wave tomography for 2D media will be described. For formulations of NIP wave tomography in 3D media, the reader can consult Duveneck (2004a). We assume that the kinematic wavefield attributes, associated with hypothetical NIP waves, can be reliably extracted from CRS stacking operator. These parameters will be used to formulate a tomographic inversion method for the determination of smooth velocity models in depth. For more details about CRS stacking process, extraction and estimation of the kinematic wavefield parameters in coherence panels, smart search strategies, as well as the physical interpretation of those parameters, the reader may consult the references Duveneck (2004b), Faccipieri (2016)], Mann (2002), Müller (1999), Schleicher et al. (1993) and Ursin (1982). Here, just the CRS stacking operator and further brief comments will be presented.

A.2 Observed-data and model spaces

NIP wave tomography is a curvature tomography method described as a LSQR seismic inverse problem. Here, the general formulation of the LSQR method will be revised for NIP wave tomography context. As a first step, observed-data and model spaces will be introduced.

Observed-data space: The domain of NIP wave tomography input kinematic parameters differs from stereotomography and CRP tomography methods. NIP wave tomography uses information extracted from poststack seismic gathers by means of CRS stack panels. CRS stacking process generates simulated zero-offset sections by means of a multiparametric traveltime (see, e.g, Mann (2002), Müller (1999)). It takes into account arbitrary configurations of source-receiver pairs at the vicinity of a specific given central zero-offset point (t_0, ξ_0). Thus, CRS stacknig considers traces refered to an area around a central point in depth. The multiparametric traveltime is a second order approximation around a central point of the seismic data. In 2D media, CRS stacking operator represents a hyperbolic surface composed by three parameters. CRS operator can be described as follows (see, e.g, Schleicher et al. (1993)):

$$t^2(x, h) = (t_0 + 2p_x\Delta\xi)^2 + 2t_0(M_N\Delta\xi^2 + M_{NIP}h^2), \tag{A.1}$$

where ξ and h are, respectively, the midpoint and offset coordinates. Distance of the central midpoint is given by $\Delta\xi = \xi - \xi_0$. The three parameters that rules the operator are p_x, M_{NIP} and M_N. The parameters p_x and M_N can be interpreted as the first and second horizontal spatial traveltime derivatives related to an hypothetical wavefront at ξ_0, due to an exploding reflector element placed at the normal-incidence point (NIP) of the zero-offset ray on the reflector. Rays that compose this wave are called *normal rays* and the hypothetical wave is called *normal wave*. The parameter M_{NIP} can be interpreted as the second horizontal traveltime derivative related to a hypothetical wavefront at ξ_0, due to a point source placed at the NIP point on the reflector. The associated hypothetical wave is the so called *NIP wave*.

If v_0 is the velocity near the surface acquisition in position ξ_0, and the structures at subsurface are invariant in the perpendicular direction of acquisition line (2.5D case, see, e.g, Bleistein (1986)), the kinematic parameters p_x and M_{NIP} can be related with the emergence angle α and curvature k_{NIP} of the hypothetical NIP wavefront. The relationship between these parameters are the following (see, e.g, Duveneck (2004b)):

$$\begin{cases} p_x & = & \dfrac{\sin(\alpha)}{v_o}, \\[4mm] M_{NIP} & = & \dfrac{\cos^2(\alpha)}{v_o} k_{NIP}. \end{cases} \tag{A.2}$$

By the previous equation, parameter M_{NIP} is, in fact, direct related to the curvature of NIP wavefront. For this reason, in this text, this parameter will be treated as a parameter related to the curvature of NIP wavefront at position ξ_0 in surface acquisition. Relate M_{NIP} to the curvature of the hypothetical NIP wavefront requires the validity of NIP wave theorem (see, e.g, Chernyak and Gritsenko (1979), Hubral (1983)). From this theorem, to second order in offset direction, common midpoint (CMP) reflection traveltimes and traveltimes along rays passing through the NIP of the zero-offset ray are identical.

For a data driven description of CRS stacking operator A.1, the reader can consult the reference Faccipieri (2016). Here, CRS stacking operator described by physical parameters was exhibited in order to briefly illustrate the extraction of kinematic parameters by CRS stacking process.

The observed-data space of NIP wave tomography, $\mathbf{d}^{obs}$, is composed by N kinematic parameter vectors d_i^{obs} extracted from locally-coherent events of the poststack seismic data. Such points are selected by the user by a picking process. In symbols:

$$\mathbf{d}^{obs} = [\mathbf{d}_i^{obs}]_{i=1}^N = [(\xi, p_x, t, M_{NIP})_i^T]_{i=1}^N. \tag{A.3}$$

All parameters refer to NIP rays kinematic parameters. Each subscript i is reffered to one specific NIP ray. Therefore, each ray starts propagation at a diffraction location in subsurface and reaches surface line at emergence position ξ with slope (horizontal slowness) p_x, curvature k_{NIP}, which is related to M_{NIP} (see equation A.2), and t is the propagation traveltime. See Figure A.1.

Model space: NIP wave tomography model space $\mathbf{m}$ is the union of two model-space subsets:

$$\mathbf{m} = \mathbf{m}^{vel} \cup \mathbf{m}^{ray}, \tag{A.4}$$

where $\mathbf{m}^{vel}$ is the velocity-model space and $\mathbf{m}^{ray}$ is the ray-model space.

The description of NIP wave tomography model space by the union of two model subsets follows the same approach used for stereotomography and CRP tomography. In fact, velocity-model
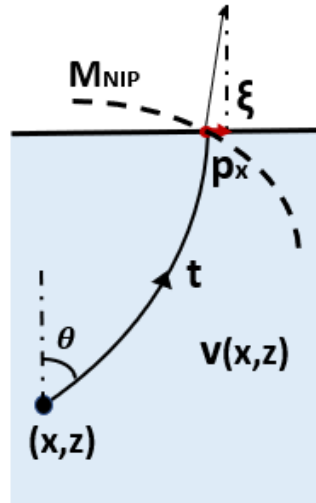
Figure A.1: Data parameter (ξ, p_x, t, M_{NIP}) corresponds, in the exact (unkown) velocity model, to primary diffraction ray that connects the midpoint in zero-offset domain to a primary diffraction point (x, z) in depth.

space $\mathbf{m}^{vel}$ is exactly the same velocity-model subset explained before in this thesis for stereoto-mography, chapter 3, and CRP tomography, chapter 5. Therefore, in this appendix, only NIP wave tomography ray-model space $\mathbf{m}^{ray}$ will be described. For velocity-model space description, the reader can go back to chapters 3 or 5.

Ray-model space: NIP wave tomography ray-model space, $\mathbf{m}^{ray}$, is composed by N kinematic parameter vectors $\mathbf{m}_i^{ray}$. In symbols:

$$\mathbf{m}^{ray} = [\mathbf{m}_i^{ray}]_{i=1}^N = [(x, z, \theta)_i^T]_{i=1}^N, \tag{A.5}$$

Each three-component parameter vector $\mathbf{m}_i^{ray}$ corresponds to its counterpart four-component parameter vector $\mathbf{d}_i^{obs}$ in observed data-space. In symbols, we have a one-to-one correspondence:

$$\mathbf{m}_i^{ray} = (x, z, \theta)_i^T \leftrightarrow (\xi, p_x, t, M_{NIP})_i^T = \mathbf{d}_i^{obs}. \tag{A.6}$$

Assuming that perfect velocity modeling conditions hold, a natural interpretation of this correspondence can be provided (see Figure A.2). The components of $\mathbf{m}_i^{ray}$ specify a model depth position (x, z) (diffraction point), as well as one up-going ray starting from the diffraction point with initial model slope θ. Under perfect modeling conditions, this ray hits the measurement seismic line at

point ξ, whith horizontal slowness p_x and related curvature that matches the second order parameter M_{NIP}. Also, total traveltime of this ray path amounts t.
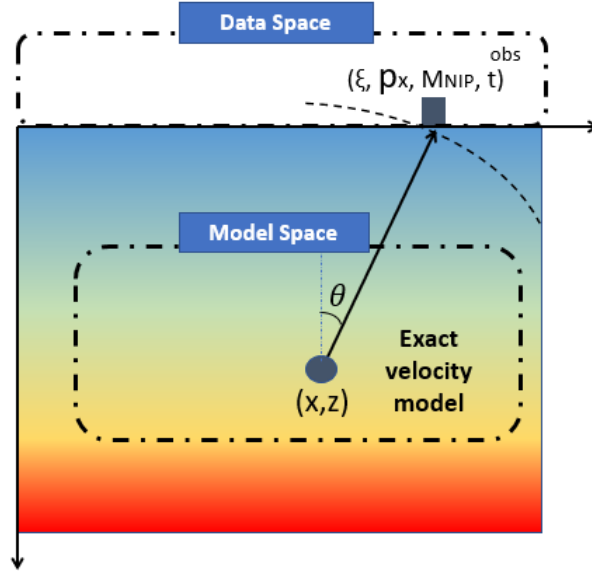

Figure A.2: Under perfect modeling conditions, the parameters (x, z) locates a diffraction point from which one up-going ray is specified by model slope θ. Such ray hits the measurement seismic line in such a way that the location, horizontal slowness, curvature and traveltime (ξ, p_x, M_{NIP}, t) matches the parameters given by the observed space. Color map represents the exact velocity model.

A.3   Forward-model engine

Forward-modeling engine of NIP wave tomography is dynamic-ray tracing. A brief description of dynamic ray-tracing needed for NIP wave tomography forward-modeling is provided in Appendix C. For more details about dynamic-ray tracing and paraxial ray-theroy, the interested reader is reffered, once again, to classical literature, e.g, (Cerveny, 2005) and (Popov, 2002).

The forward-modeling engine transforms a given model space $\mathbf{m}$ onto a corresponding synthetic data space $\mathbf{d}^{syn}$, which has the same form as the given (invariant) observed data space $\mathbf{d}^{obs}$. Therefore, synthetic space is composed by N four-component kinematic parameter vectors $\mathbf{d}_i^{syn}$. In symbols:

$$\mathbf{d}^{syn} = [\mathbf{d}_i^{syn}]_{i=1}^N = [(\xi, p_x, t, M_{NIP})_i^{syn}]_{i=1}^N. \qquad (A.7)$$

The construction of a synthetic data space $\mathbf{d}^{syn}(\mathbf{m})$ for arbitrary model space $\mathbf{m} = \mathbf{m}^{vel} \cup \mathbf{m}^{ray}$ is illustrated in Figure A.3 and can be explained along the same lines previously used in the case of perfect modeling conditions (Figure A.2). Assuming an arbitrary velocity-model space $\mathbf{m}^{vel}$, let $(x, z, \theta)_i$ parameterize the single vector $\mathbf{m}_i^{ray}$ of $\mathbf{m}^{ray}$. Then the previous procedure produces the model diffraction point (x, z), as well one up-going ray defined by the model-angle θ. By means of dynamic-ray propagation, the related synthetic data vector $\mathbf{d}_i^{syn}(\mathbf{m})$ is fully parameterized by the vector $(\xi^{syn}, p_x^{syn}, M_{NIP}^{syn}, t^{syn})_i$, where (ξ^{syn}, p_x^{syn}) represents the location and horizontal slowness at the endpoints of the ray, M_{NIP}^{syn} is related to the associated curvature (see Equation A.2) and t^{syn} is the traveltime of the ray path.
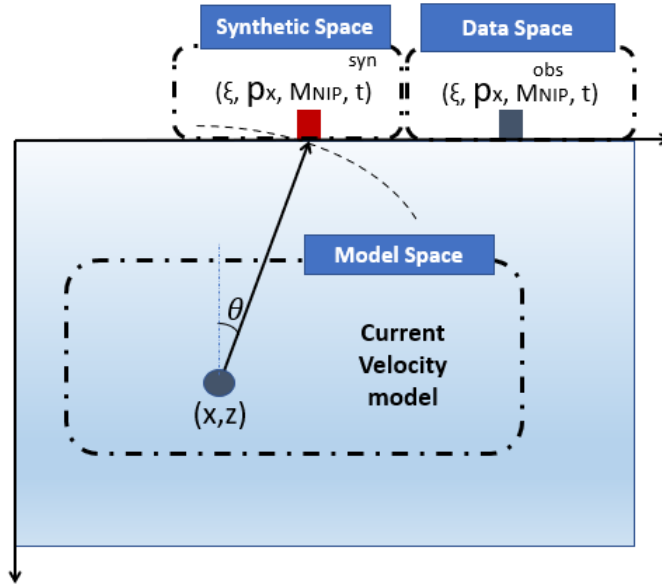

Figure A.3: Synthetic data space $\mathbf{d}^{syn}(\mathbf{m})$ for arbitrary model space $\mathbf{m} = \mathbf{m}^{vel} \cup \mathbf{m}^{ray}$. Color map represents the beta-spline velocity function provided by $\mathbf{m}^{vel}$. Also, (x, z, θ) represents a single model parameter $\mathbf{m}_i^{ray}$ vector of $\mathbf{m}^{ray}$. Under the same procedure of Figure A.2, model diffraction point (x, z) together with the model slope θ, define one up-going ray. The endpoint location at measument surface plus slowness vector, curvature and traveltime measured at the same endpoint, parameterize the related synthetic data vector $\mathbf{d}_i^{syn}$ from $\mathbf{d}^{syn}$. Note that, without perfect modeling conditions, $\mathbf{d}^{syn} \neq \mathbf{d}^{obs}$.

Note that each synthetic parameter vector $\mathbf{d}_i^{syn}(\mathbf{m})$ corresponds to is counterpart ray-model parameter vector $\mathbf{m}_i^{ray}$, which coresponds to its counterpart observed-data parameter vector $\mathbf{d}^{obs}$. In symbols:

$$\mathbf{d}_i^{obs} \leftrightarrow \mathbf{m}_i^{ray} \leftrightarrow \mathbf{d}_i^{syn}. \tag{A.8}$$

A.4   Misfit function and iteration process

Following the same approach of stereotomography and CRP tomogrpahy, classical least-square-root (LSQR) inversion is applied to solve the NIP wave tomography inverse problem. Moreover, the proposed numerical method to solve LSQR inversion is, once again, a Gauss-Newton iterative procedure applied to a regularized misfit function that measures, for any given trial model space $\mathbf{m}$, the discrepancy $\mathbf{\Delta d(m)} = \mathbf{d}^{syn}(\mathbf{m}) - \mathbf{d}^{obs}$ between the synthetic and observed data spaces.

As this approach was repeatedly explained and addressed throughout this thesis (see chapters 2, 3 and 5), here, just the NIP wave tomography misfit function will be exhibited. Further iterative steps to numerically solve the optimization problem by Gauss-Newton approach will be omitted. However, this steps are analogues to the ones presented in previous chapters. For more details of this steps in the context of NIP wave tomography, the reader is reffered to standard referece Duveneck (2004b).

Misfit function: Given a current model space $\mathbf{m}$, NIP wave tomography misfit function is given by:

$$S(\mathbf{m}) = \frac{1}{2}[\mathbf{\Delta d}^T(\mathbf{m})\mathbf{W}_D^{-1}\mathbf{\Delta d(m)} + \lambda \mathbf{m}^{vel^T}\mathbf{R}^{(v)}\mathbf{m}^{vel}], \qquad (A.9)$$

where $\mathbf{W}_D^{-1}$ is the diagonal matrix that accounts for a priori data information and brings the different data types to a comparable size and the expression $\lambda \mathbf{m}^{vel^T}\mathbf{R}^{(v)}\mathbf{m}^{vel}$ denotes the regularization term applied to current velocity-model space $\mathbf{m}^{vel}$. In this thesis, the same regularization term applied to stereotomography and CRP tomography will be used to NIP wave tomography. Therefore, the minimization term of misfit function A.9 accounts, mainly, for the minimization of second order derivatives of current velocity model. This term was already explained in previous chapters for stereotomography and CRP tomography context. The interested reader can go back to chapters 3 and 5 for more details about this regularization operator. Also, the construction of regularization matrix $\mathbf{R}$ is detailed in Appendix E.

Iteration process: By the Gauus-Newton approach to solve the problem given by the minimization of misfit function A.9, an user-selected initial model space $\mathbf{m}_0$ is required. Then, an iterative scheme $\{\mathbf{m}_k\}$, $(k = 1, 2, \ldots)$ is carried out to progress to the desired solution. Given a current model space $\mathbf{m}_k$, its subsequent iteration $\mathbf{m}_{k+1}$ is given by:

$$\mathbf{m}_{k+1} = \mathbf{m}_k - \alpha_k \mathbf{\Delta m}_k, \qquad\qquad (A.10)$$

where α_k is scalar that calibrates the size of the updating step and $\mathbf{\Delta m}_k$ is the Gauss-Newton solution of the optimization problem for iteration k. For more details about how to iteratively generate $\mathbf{\Delta m}_k$ for seismic tomography problems, the reader can go back to previous chapters.

NIP wave tomography regularization aspects: The regularization term used in this thesis for all seismic tomography applications was, in fact, inspired by its use for NIP wave tomography in Duveneck (2004b). There, this term was proposed to search, between all possible solutions of the ill-posed inverse tomographic problem, the one with smoothness properties. However, to handle with the natural numerical instability of NIP wave tomography, there, the method was implemented using more than one regularization term. To assit numerical stability of the problem, in Duveneck (2004b), NIP wave tomogrpahy was applied with one additional regularization term that takes into account previously knowledge about some regions of the correct velocity model. The misfit between these previous information and the velocity model generated by NIP wave tomography is added to the objective function and is computed at each iteration. This strategy tries to guide the solution to a velocity model similar to the correct one, at least in regions where previous information are provided. Other type of regularization employed at some tests of NIP wave tomography in the same reference is the *reflector structure regularization*. This another term forces the velocity model to locally follow the reflector structure by minimizing the norm of the velocity gradient in the plane perpendicular to the normal ray at each considered data point in the subsurface. This came from the assumption that velocity variations should mainly occur in direction perpendicular to reflectors. However, the orientations of the reflectors are usually unknown. To suppress this fact, the slopes current model space are used at each iteration as a local approximation of the reflector structure. Also, NIP wave tomography has already been tested with a spatially variable model smoothness regularization. This strategy allows the velocity model to be less regularized in some specific parts of the model, while keeping the other parts with strong regularization. This spatially variable smoothness has been shown to be useful specially at the borders of the velocity field, where commonly no sufficient information is available to locally constrain the model. However, all these other types of regularization are used together with the minimization of velocity derivatives, which is the unique proposed regularization term of this thesis. As one of the objectives of this thesis is to study the ability of different kinds of tomography mothods to constrain different types of synthetic velocity models mainly by internal information (regularization term can be viewd as a type of external information) provided by the method, this task would be deteriorated with a lot of different kinds of regularization terms. For

this reason, only the regularization term related to the minimization of second derivatives of the velocity model was applied to all tomographic tests. Therefore, in this thesis, NIP wave tomography, as well as all seismic tomography methods of this thesis, is proposed and tested by the use of just one regularization term.

A.5   Initial model space for NIP wave tomography

The model initialization procedure to be described here is based on the initialization procedure proposed by Duveneck (2004b) for NIP wave tomography. Following the initialization procedure proposed in this thesis for stereotomography and CRP tomography, the model initialization step for NIP wave tomography is very simple.

The procedure assumes that an arbitrary initial velocity-model space $\mathbf{m}^{vel}$ has already been provided by the user. Each pair $(\xi, p_x)_i$ of observed data space defines a ray that starts at the midpoint position ξ_0 and proceed downward with direction provided by the horizontal slowness p_x. Under these considerations, the ray is traced downward through arbitrary initial velocity-model until the data traveltime t is consumed. Let $(x, z)_i$ be the endpoint of the ray propagation. Moreover, at this endpoint, let θ_i be the angle with respect to the vertical direction. Therefore, all values that define the initial ray-model parameter vector $\mathbf{m}_i^{ray}$ that corresponds to the given observed-data vector parameter $\mathbf{d}_i^{obs}$ are obtained. The process is repeated to all $i = 1, \ldots, N$, where N is the number of observed-data vector parameters in observed-data space. Note that data parameter M_{NIP} is not used for this initialization procedure.

Following initialization procedures of stereotomography and CRP tomography, the initial velocity model is arbitrarily chosen. Moreover, it was used at the previous initialization step to compute the initial ray-model components. Despite it is not a crucial feature for seismic tomography applications, usually, the more similar is the initial velocity with the true velocity model, the better is the answer of the inversion process. However, it usually requires some previous knowledge about true velocity model. Usually, very simple inital velocity models are chosen to initialize NIP wave tomography method (see, e.g, Duveneck and Hubral (2002), Duveneck (2004c)). In this thesis, the same approach will be followed for all NIP wave tomography synthetic tests in Appendix B.
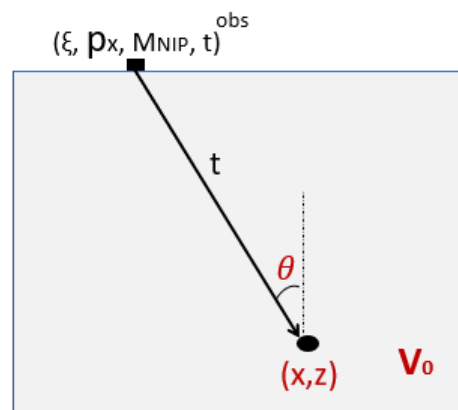
Figure A.4: Initialization procedure for ray-model parameter vector: a velocity model, constructed by an arbitrary given initial velocity-model vector parameter is assumed. Given an observed data sample (ξ, p_x, M_{NIP}, t), the corresponding initial model vector parameter (x, z, θ) is to be constructed. Under the use of the given initial velocity model, one ray is downward propagated from midpoint location ξ, with direction determined by p_x. This ray is propagated until the endpoint (x, z) is attained for the data traveltime t. Also, θ is defined as the angle of the ray path with respect to vertical direction at endpoint (x, z).

Appendix B

Synthetic tests for NIP wave tomography

NIP wave tomography was chosen to illustrate an example of curvature tomography method for this thesis. Following what was done for stereotomography and CRP tomography methods, NIP wave tomography was fully implemented during the phd research period. Some synthetic tests, analogous to the tests illustrated in this thesis for stereotomography and CRP tomography methods, were performed in order to compare the obtained results between curvature and slope tomography methods. The results of these comparative tests were important for the development of CRP tomography method as a slope tomography technique. Some of these synthetic tests for NIP wave tomography will be illustrated at this appendix, where a discussion regarding the use of curvature parameter will be made.

B.1   Validation Tests

In order to validate NIP wave tomography implementation, the method was tested by the same set of validation tests used to validate both stereotomography and CRP tomography implementations. Being the same set of validation tests, the following velocity models were used to validate NIP wave tomography implementation:

1. Model with trigonometric variation in vertical direction.

2. Model with linear variation in vertical direction.

3. Model with quadratic variation in vertical direction.

4. Model with linear variation in horizontal direction.

5. Model with linear variation in horizontal direction and quadratic variation in vertical direction.

The previous set of velocity model tests, all of them constructed by simple mathematical expressions, encompass different kinds of continuous velocity variations. These velocity model tests will be illustrated in following figures, together with NIP wave tomography respective result.

In order to be fair and compare results provided by all tomographic methods, the same parametrization used before for stereotomography and CRP tomography validation tests will be kept. Therefore, a square grid of 2km×2km was used to build velocity models, which are constructed by B-spline interpolation with knots uniformly distributed through the grid. Interpolation knots are spaced by a constant distance of 0.4km, both in vertical and horizontal directions.

For NIP wave tomography validation tests, input data and model spaces and initial parameters were set as follows:

Input observed-data space: To generate data information set, 49 data positions were uniformly distributed in depth through the model. Data depth positions will be illustrated by following figures. These data positions are exactly the same ones used for stereotomography and CRP tomography validation tests. Data positions play the role of hypothetical localization of diffraction events (localization of the point source for hyphotical NIP wave) for these synthetic experiments. Therefore, for comparison reasons, these tests simulate the results that would be obtained by both seismic tomography methods under the same number of pickings. From each of these positions, one ray is propagated parallel to vertical axis to surface direction. In surface line, the kinematic parameters of emergence positions, slopes, curvature and traveltimes were computed. Therefore, data space is composed by 49 data observed samples, each of them composed by one traveltime, one emergence position, one slowness vector (horizontal component) and one parameter related to the curvature (see Appendix A) of NIP wavefront. As the components of data space were computed directly by ray-tracing performed at the true velocity model, despite numerical errors and theoretical approximations, observed-data space is composed by perfect accurate data components. Moreover, the uniform distribution of positions in depth guarantees that all regions of the velocity model are covered by informations in observed-data space.

Initial model space: In order to allow comparisons between the previous results obtained by stereotomography and CRP tomography, the same parametrizations were used for NIP wave tomography validations tests. Thus, all initial velocity model spaces for validation tests were set as a homogeneous

velocity model of 1km/s. The exception is the fourth validation test, the one with linear variation in horizontal direction, where an initial homogeneous velocity model of 1.5km/s was applied. B-spline interpolation knots were uniformly distributed through the model, with vertical and horizontal spacing of 0.4km. Its is exactly the same distribution used to build true velocity models for the tests. Ray-model space was initialized with the proposed initialization procedure proposed NIP wave tomography in this thesis. Therefore, the initialization procedure returned 49 ray-model samples, each of them composed by one initial model position in depth and one initial model slope. Initial model positions will be illustrated by following figures.

Initial regularization weight parameter: Following what was done for stereotomography and CRP tomography tests, initial regularization weight parameter varies through the tests. This was necessary due the different types of velocity variations. For those where the velocity varies in a non-linear way, a smaller parameter was used. Some previous search was made in order to find reasonable initial values for regularization parameter. The parameter decreases through iterations by the previously proposed heuristic (see chapter 5).

Comments about NIP wave tomography validation tests: The results obtained by NIP wave tomography are illustrated by Figures B.1, B.2, B.3, B.4, B.5, B.6, B.7, B.8, B.9 and B.10. The good results provided by the NIP wave tomography method are clear. Except by the last test, relative difference errors between inverted and true velocity models fall below 1% almost for all regions of the velocity grid. Moreover, the (small) errors are concentrated near the bottom line of the grid, which is the region with least amount of available information. The last test, the one with quadratic variation in vertical direction and linear variation in horizontal direction, is a little more challenging, once concentrates variations of different degrees in both directions. Also, this is the only test where initial velocity model equals true velocity model at just one position of the grid, the origin position $(x, z) = (0, 0)$. Even though, the velocity model inverted by NIP wave tomography is very good. Errors follow under 2% almost for all regions of the velocity grid. Near the bottom of the model, the discrepancy is more evident, but it still represents a small error. The result would be even better by the use of a better initial velocity model or more number of input data samples. Hence, NIP wave tomography implementation was able to handle with continuous velocity variations of different types and was successfully applied when faced with lateral heterogeneous velocity models. Therefore, by this set of validation tests, NIP wave tomography implementation was succeded. However, when compared to the results proposed by stereotomography and CRP tomography at the same set of validation tests, the results presented by NIP wave tomography are slightly worse.
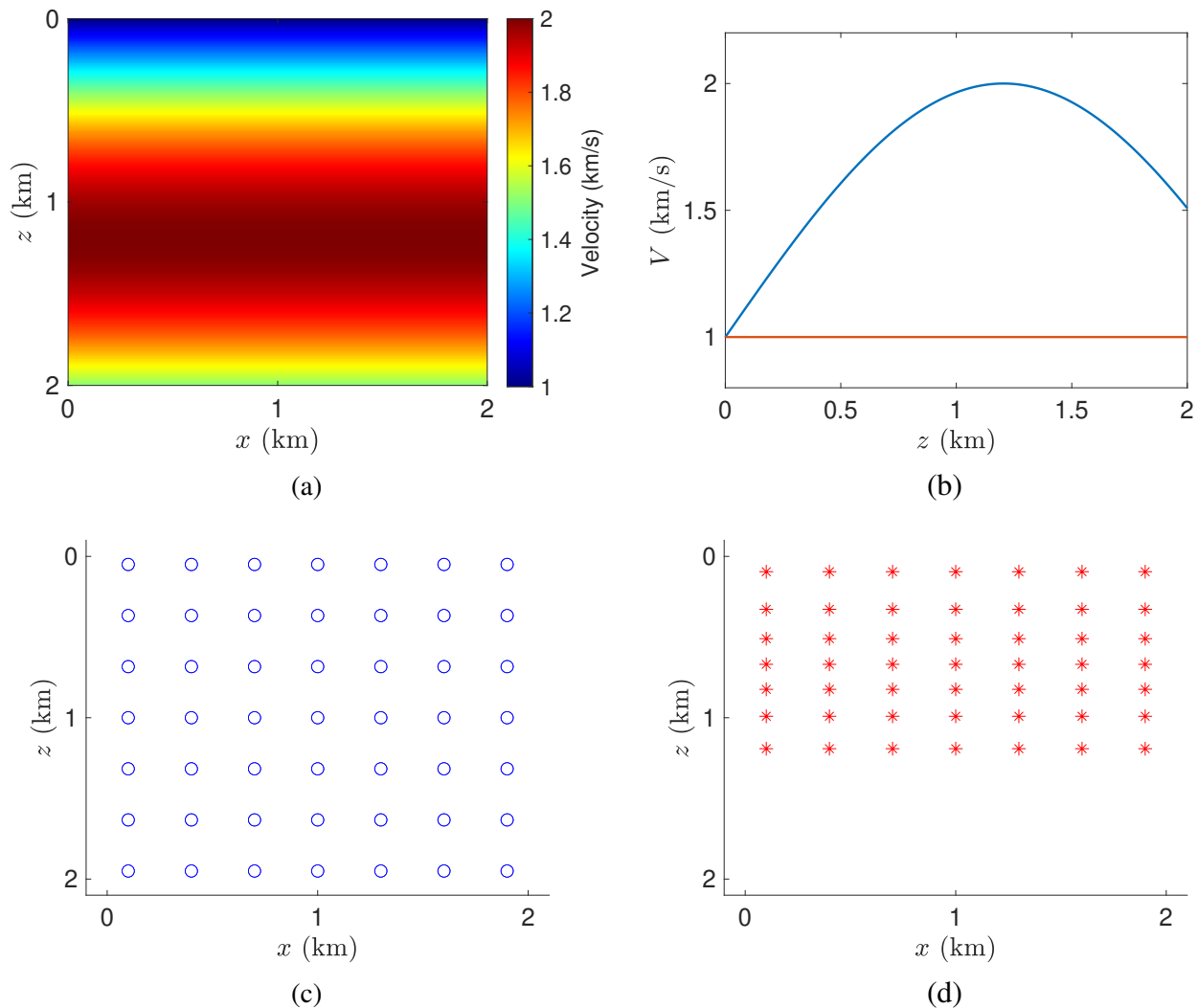
(a)

(b)

(c)

(d)

Figure B.1: First validation test: model with trigonometric variation in vertical direction. (a) True velocity model for first validation test. (b) Vertical slices of initial (red) and true (blue) velocity models. Slices were taken at the middle of the models. (c) Data positions. Observed-data space is composed by kinematic parameters computed by a series of dynamic-ray tracing starting at these positions. (d) Initial model positions returned by initialization process.
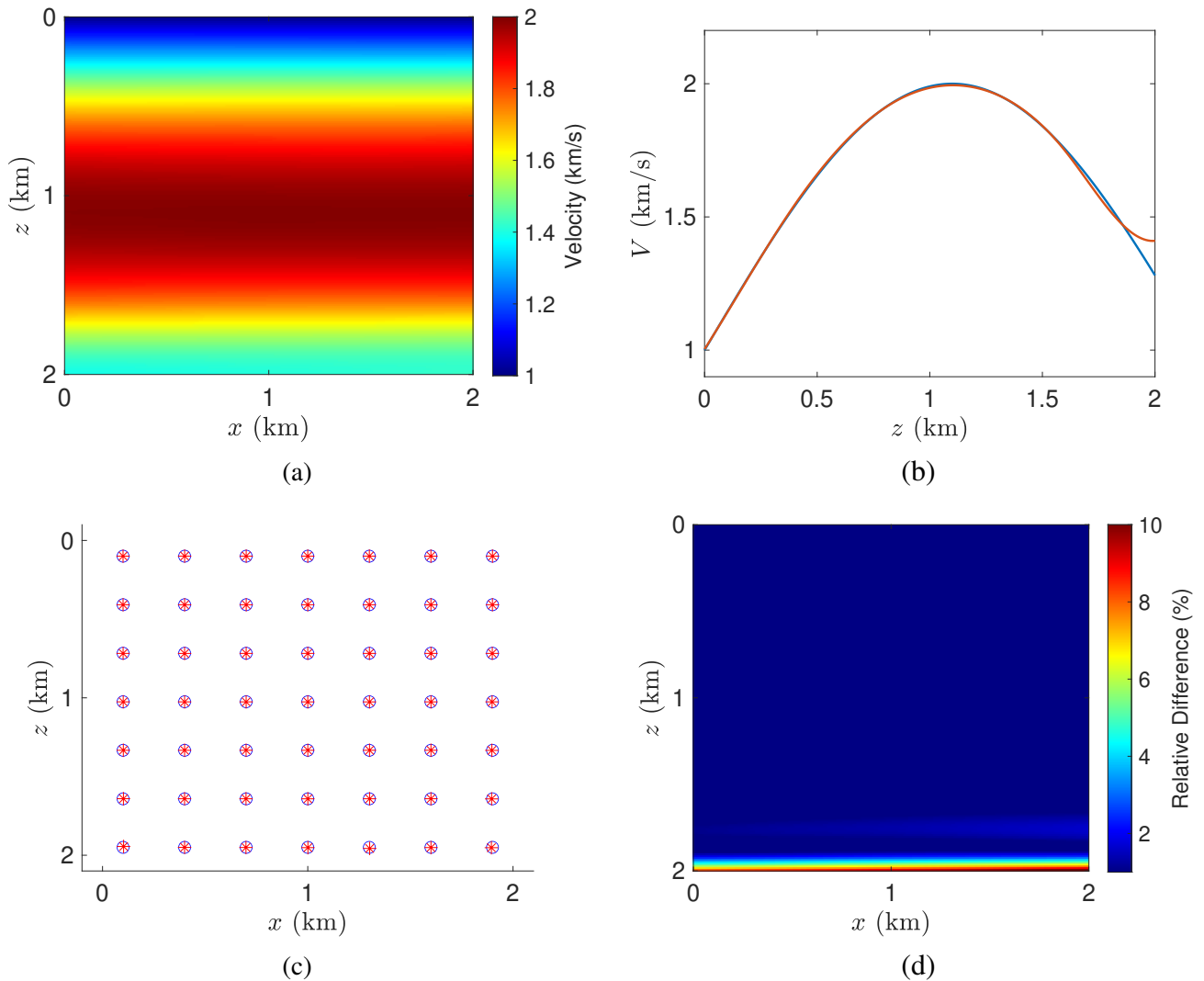
Figure B.2: NIP wave tomography final result for first validation test. (a) Inverted velocity model. (b) Vertical slices of inverted (red) and true (blues) velocity models. Slices were taken at the middle of the models. (c) Inverted model (red) positions and true data (blue) positions. (d) Percentage difference between inverted and true velocity models.
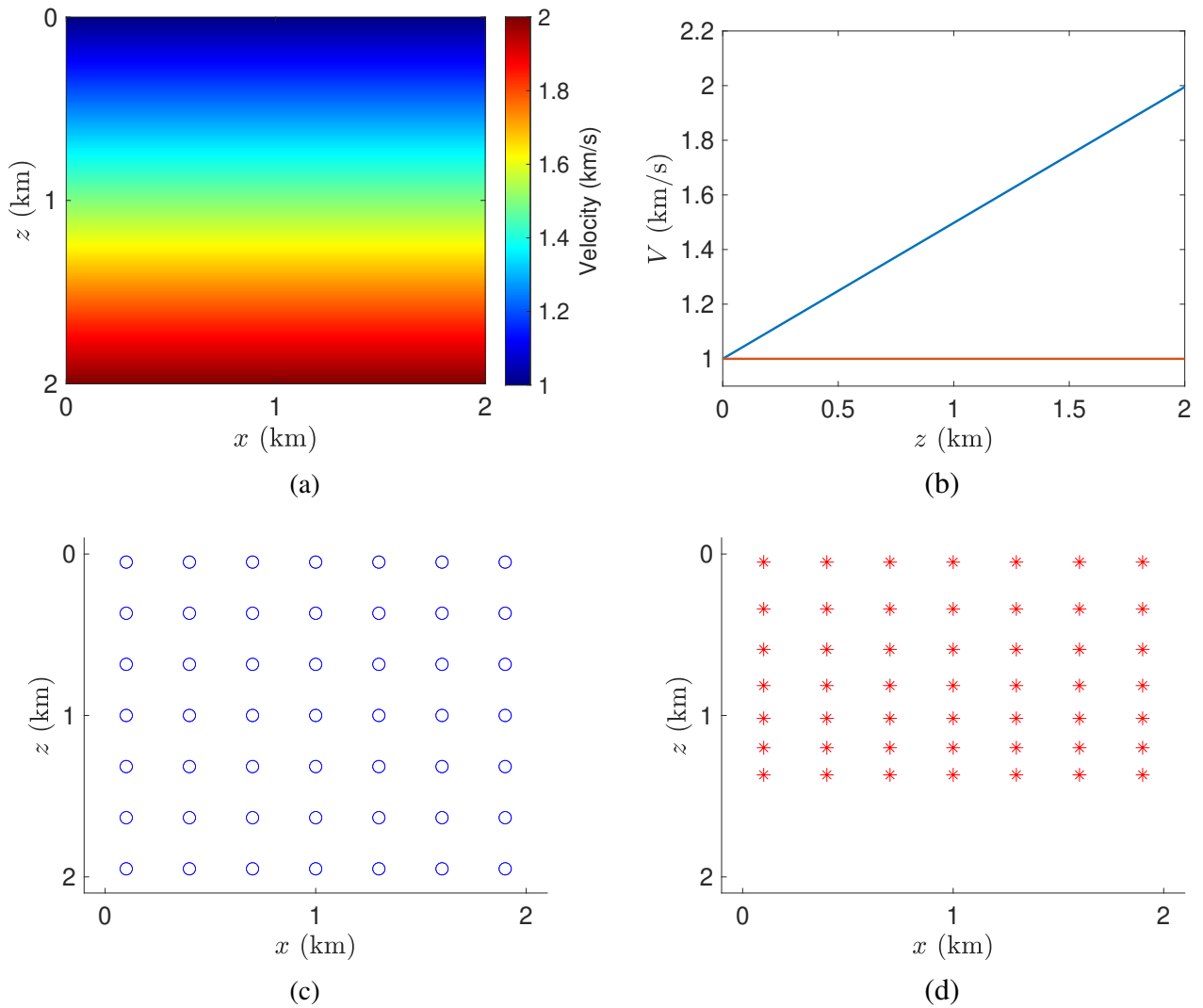
Figure B.3: Second validation test: model with linear variation in vertical direction. (a) True velocity model test. (b) Vertical slices of initial (red) and true (blue) velocity models. Vertical slices were taken at the middle of the models. (c) Data positions. Observed-data space is composed by kinematic parameters computed by a series of dynamic-ray tracing starting at these positions. (d) Initial model positions returned by initialization process.
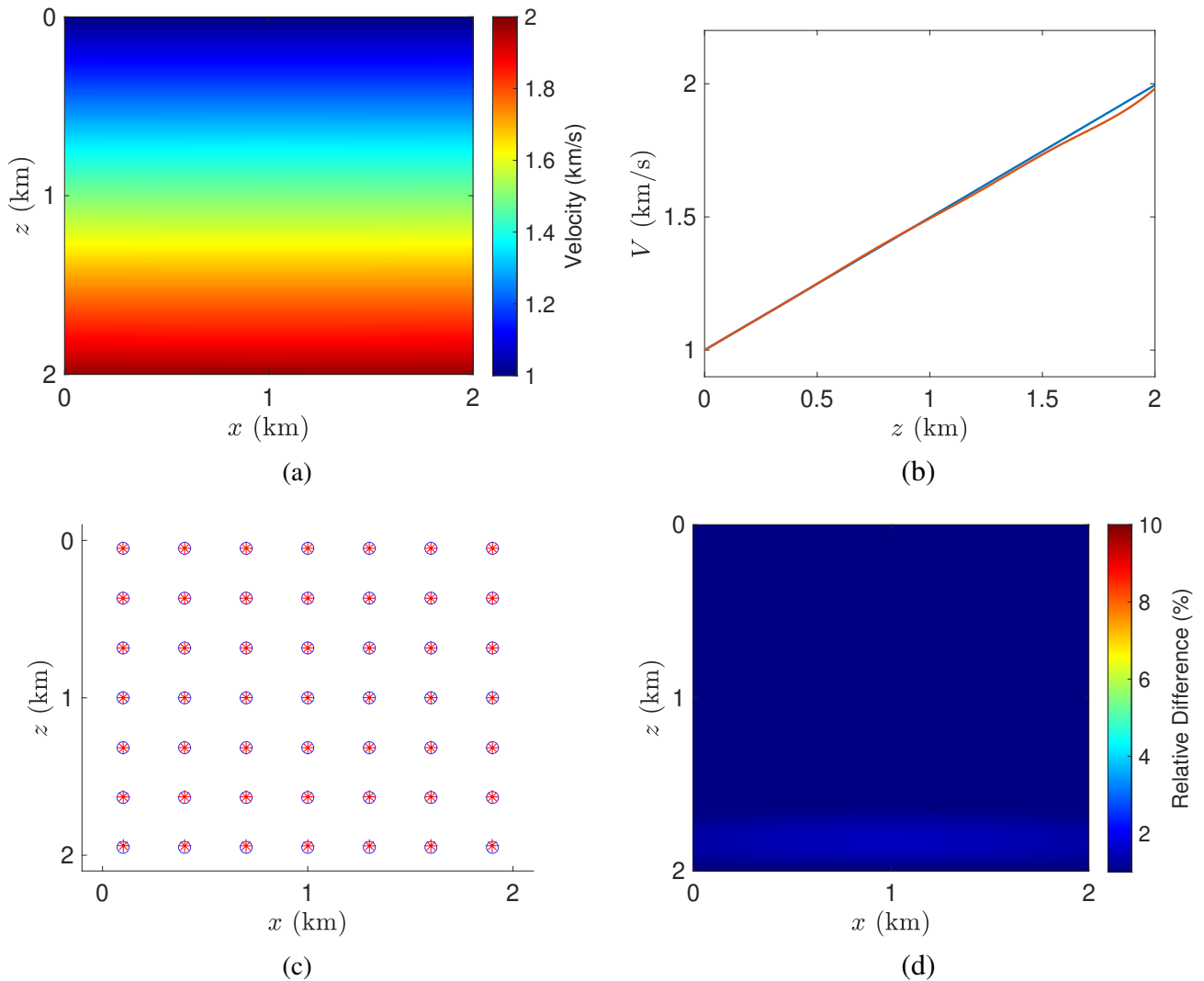
(a)

(b)

(c)

(d)

Figure B.4: NIP wave tomography results for second validation test. (a) Inverted velocity model. (b) Vertical slices of inverted (red) and true (blue) velocity models. Vertical slices were taken at the middle of the models. (c) Final model (red) positions and true (blue) data positions. (d) Percentage difference between inverted and true velocity models.

Figure B.5: Third validation test: model with quadratic variation in vertical direction. (a) True velocity model test. (b) Vertical slices of initial (red) and true (blue) velocity models. Vertical slices were taken at the middle of the models. (c) Data positions. Observed-data space is composed by kinematic parameters computed by a series of dynamic-ray tracing starting at these positions. (d) Initial model positions returned by initialization process.

Figure B.6: NIP wave tomography final result for third validation test. (a) Inverted velocity model. (b) Vertical slices of inverted (red) and true (blue) velocity models. Vertical slices were taken at the middle of the models. (c) Final model (red) positions and true (blue) data positions. (d) Percentage difference between inverted and true velocity models.
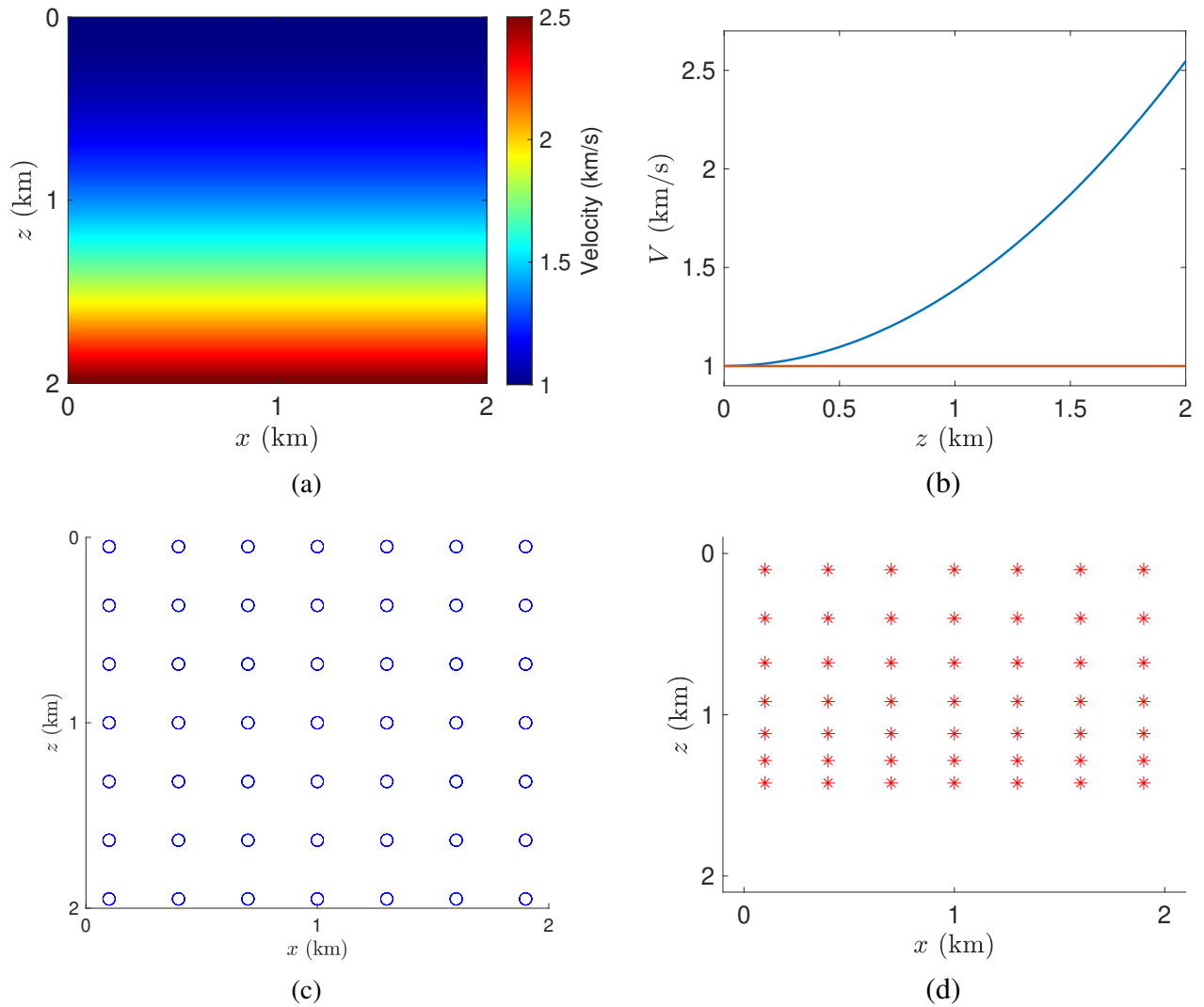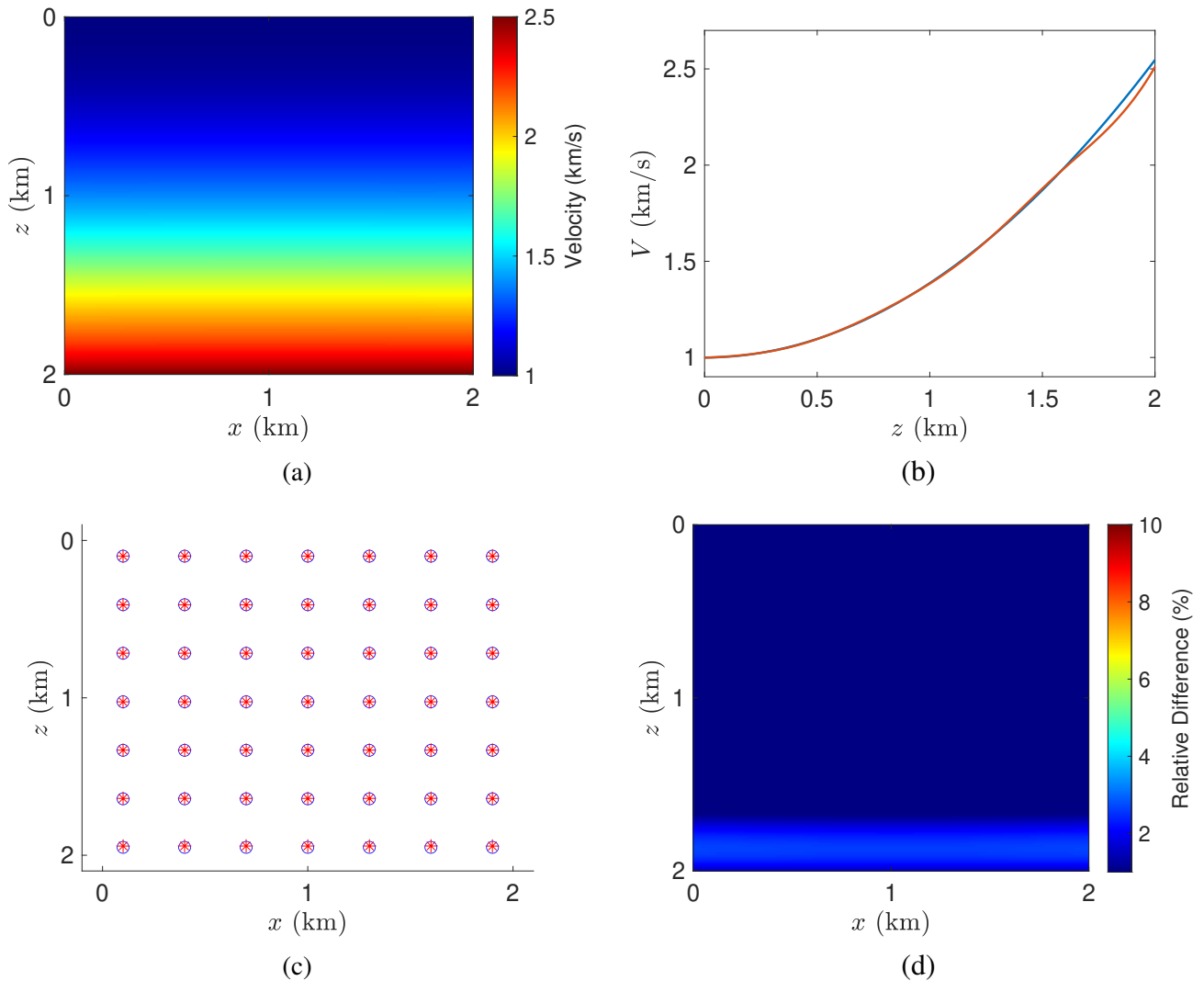
(a)

(b)

(c)

(d)
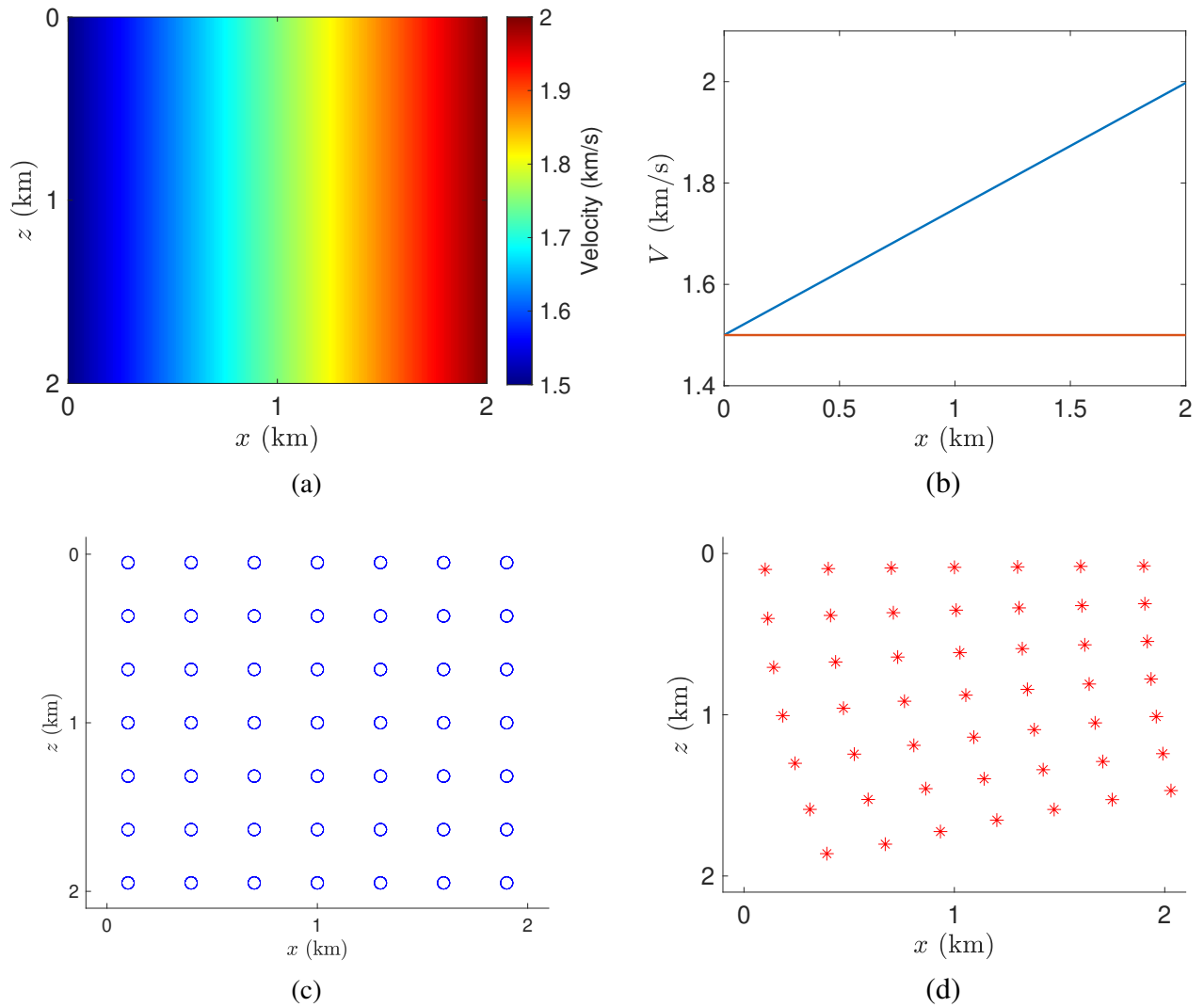
Figure B.7: Fourth validation test: model with linear variation in horizontal direction. (a) True velocity model test. (b) Hotizontal slices of initial (red) and true (blue) velocity models. Slices were taken at the middle of the models. (c) Data positions. Observed-data space is composed by kinematic parameters computed by a series of dynamic-ray tracing starting at these positions. (d) Initial positions of returned by initialization process.

(a)

(b)

(c)

(d)
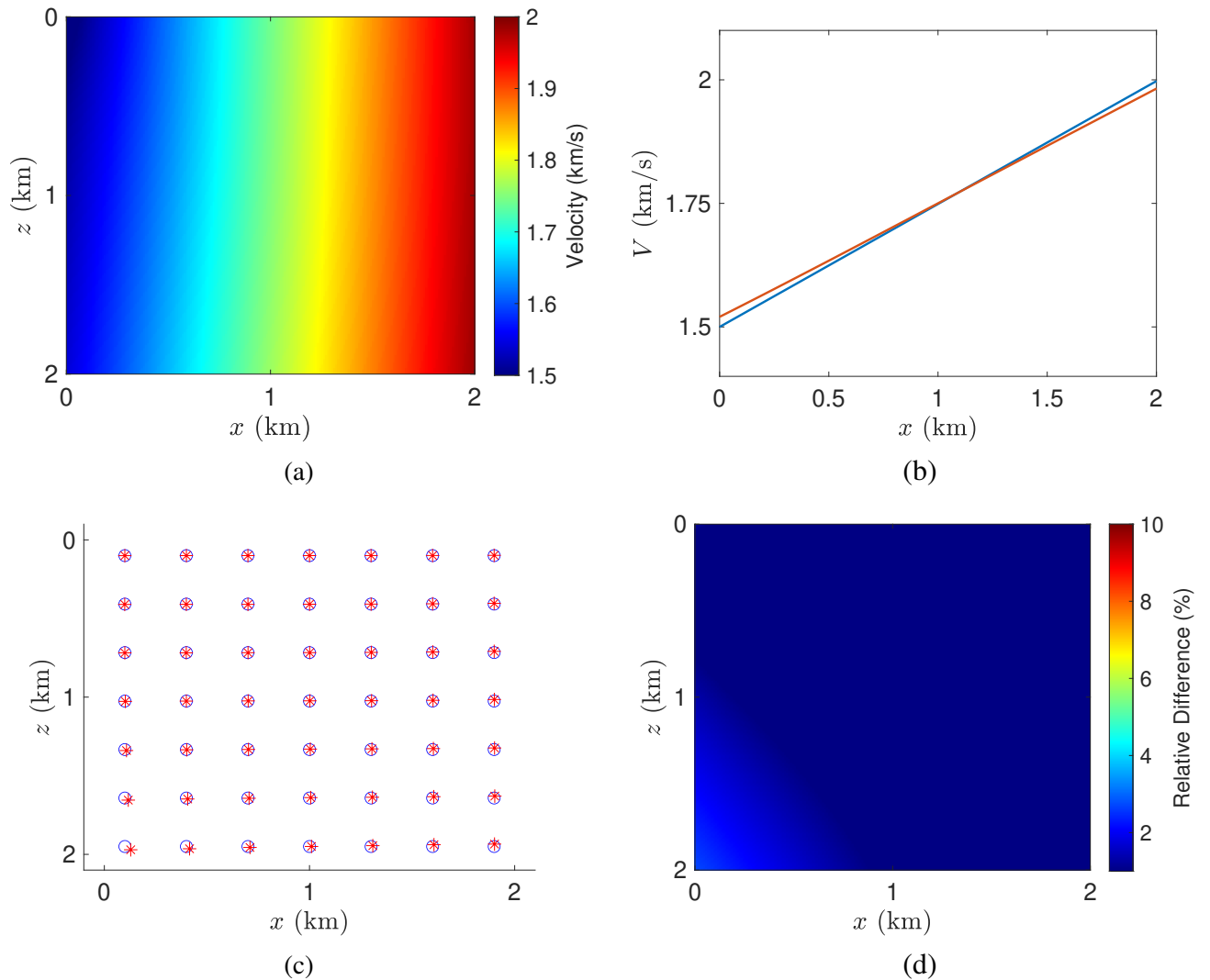
Figure B.8: NIP wave tomography final result for fourth validation test. (a) Inverted velocity model. (b) Horizontal slices of inverted (red) and true (blue) velocity models. Slices were taken at the middle of the models. (c) Final model (red) positions and true (blue) data positions. (d) Percentage difference between inverted and true velocity models.

(a)

(b)

(c)

(d)
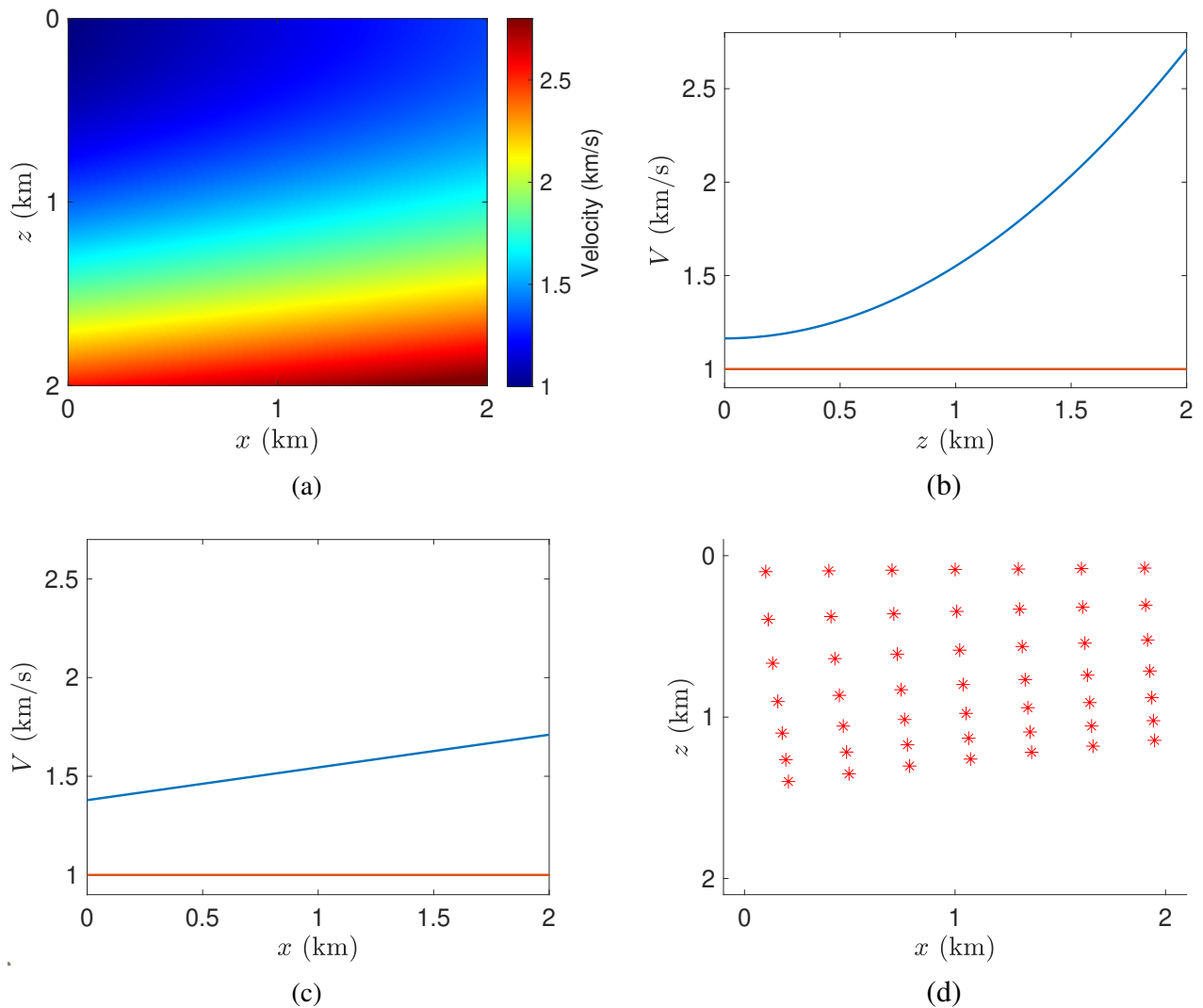
Figure B.9: Fifth validation test: model with linear variation in horizontal direction and quadritic variation in vertical direction. Data positions are the same from previous validation tests. (a) True velocity model test. (b) Vertical slices of initial (red) and true (blue) velocity models. Slices were taken at the middle of the models. (c) Hotizontal slices of initial (red) and true (blue) velocity models. Slices were taken at the middle of the models. (d) Initial model positions returned by initialization process.
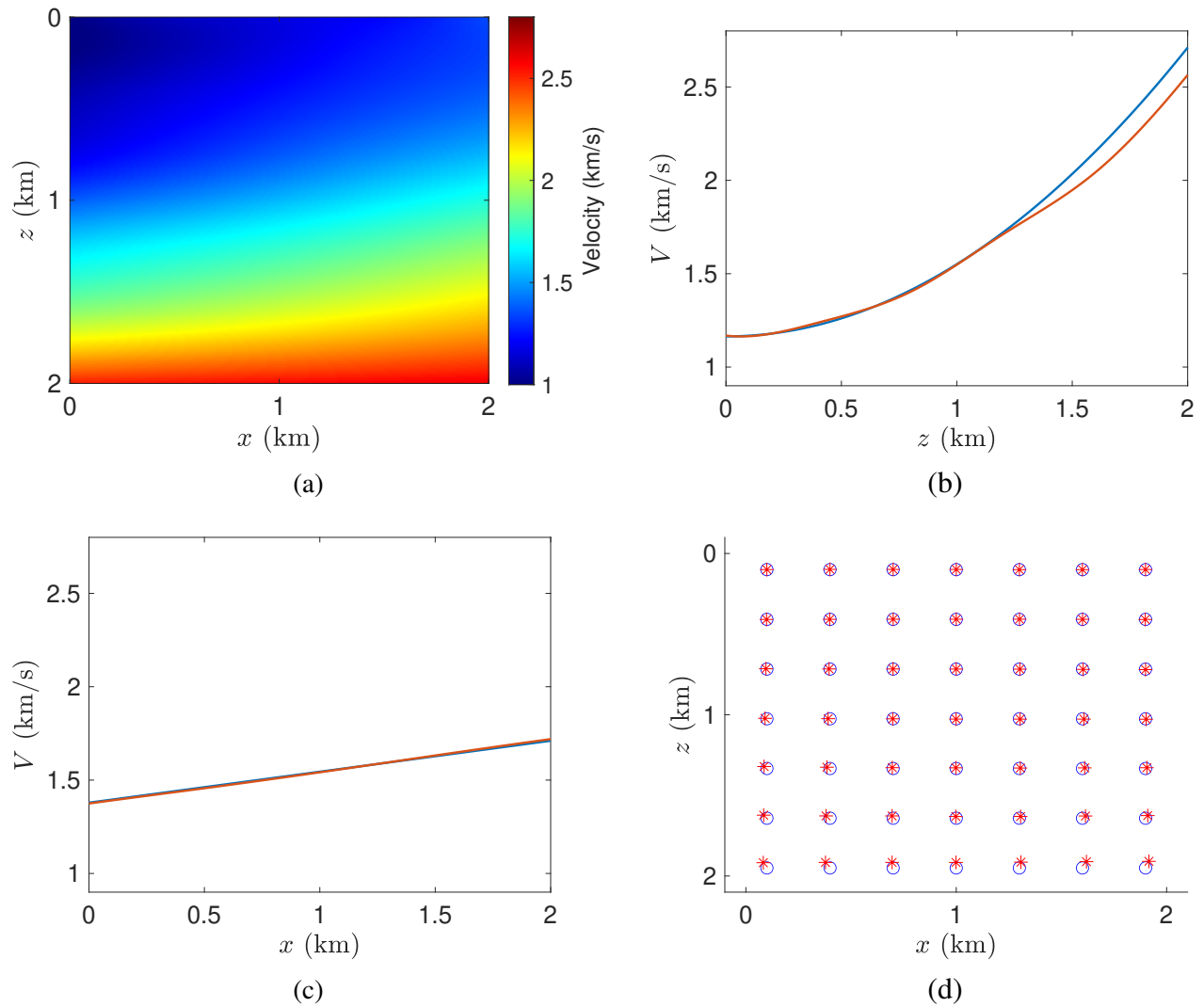
Figure B.10: NIP wave tomography final result for fifth validation test. Data positions are the same from previous validation tests. (a) Inverted velocity model. (b) Vertical slices of inverted (red) and true (blue) velocity models. Slices were taken at the middle of the models. (c) Horizontal slices of inverted (red) and true (blue) velocity models. Slices were taken at the middle of the models. (d) Final model (red) positions and true (blue) data positions.

B.2 The Three-layer Test

This section is dedicated to test the performance of NIP wave tomography on three-layer model test. This test was also executed for both stereotomography and CRP tomography methods. There, both methods provided good final velocity models by the use of a reduced amount of data positions (see chapters 6 and 7). This is a very important test for the present research, since it was decisive to the choice of not incorporate curvature parameters in CRP tomography. The results provided by NIP wave tomography in this test will support this choice.

Three-layer velocity model test is displayed in Figure B.11, together with a vertical slice of the velocity model.

<center>(a)</center> <center>(b)</center>
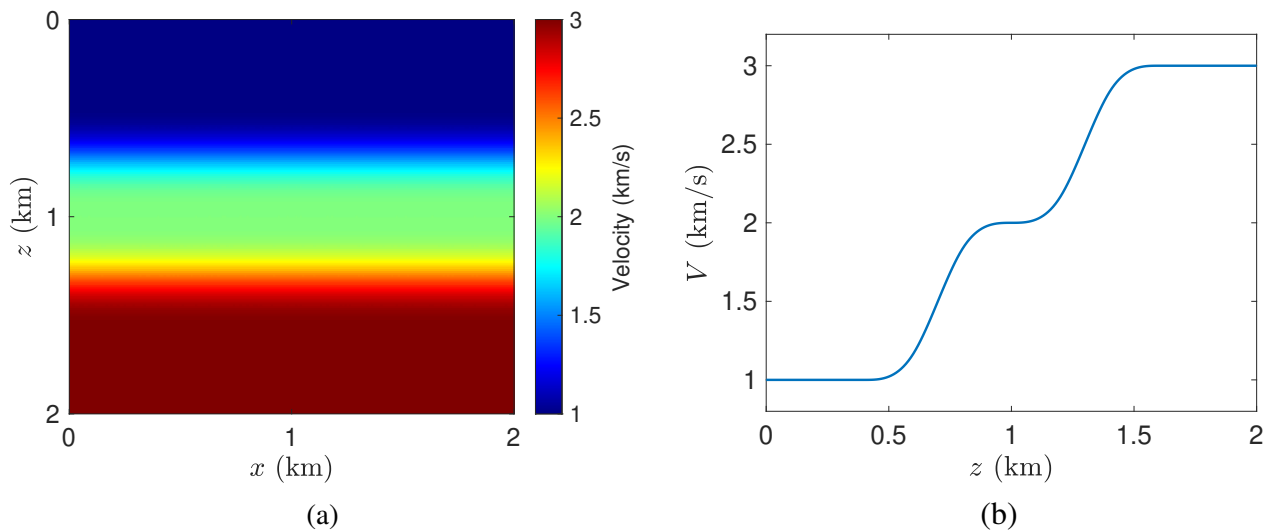
Figure B.11: (a) Three-layer velocity model test. (b) Vertical slice of the velocity model. The slice was taken at the middle of the model. Note that the second layer is smaller than the others. Note also the abrupt velocity variation in vertical direction.

In crescent order of depth, the layers present velocities of 1km/s, 2km/s and 3km/s. Because rays will be traced through the model to generate observed-data space, smoothness properties are required. Thus, it is, in fact, a three-layer model without discontinuity at interfaces. The velocity model was built by means of B-spline interpolation, in a grid of dimension 2km×2km. Interpolation knots were uniformly distributed with vertical and horizontal spacing of 0.2km. B-spline interpolation procedure assures the existence of derivatives demanded both by dynamic-ray tracing, as well as computations of the derivatives for Jacobian matrix.

Remind that the main challenges offered by this test is the abrupt velocity variations in vertical direction, plus the existence of a small second layer at the middle of the model. Also, as the true

velocity model presents strong vertical variations, the regularization term plays against the inversion process. In this case, the challenge is to set a good trade-off between regularization and inversion of a final velocity model that resembles true velocity model. However, for curvature tomographies, another challenge is presented. In order to compute Jacobian matrix, to allow a reasonable estimation of derivatives with respect to curvature parameters, the velocity model must have third continuos derivatives (see, e.g, Duveneck (2004b)). Therefore, the previous mentioned trade-off between regularization and inversion of a final velocity model that resembles true velocity model, is even harder for curvature tomographies, as it will be illustrated by the following NIP wave tomography results on this test.

First, NIP wave tomography will be tested on three-layer test using one hundred data positions. This set of data positions is the same one used for stereotomography in chapter 6. The parametrizations for the test are summarized as follows:

Input observed-data space: To generate input data space, 100 data positions were uniformly distributed in depth through the model (see Figure B.12). These positions are exactly the same ones used for stereotomography in Chapter 6. These positions play the role of hypothetical localization of diffraction events (localization of the point source for hyphotical NIP wave) for this synthetic experiment. From each of these positions, one ray is propagated parallel to vertical axis to surface direction. In surface line, kinematic parameters of emergence positions, slopes, curvature and traveltimes were computed. Therefore, data space is composed by 100 data samples, each of them composed by one traveltime, one emergence position, one slowness vector (horizontal component) and one parameter related to the curvature (see Appendix A) of NIP wavefront. As the components of data space were computed directly by ray-tracing performed at the true velocity model, despite numerical errors and theoretical approximations, observed-data space is composed by perfect accurate data components. Moreover, the uniform distribution of positions in depth guarantees that all regions of the velocity model are covered by informations in observed-data space.

Initial model space: Initial velocity model space was set as a homogeneous velocity model of 1km/s, the same one used for respective stereotomography and CRP tomography tests. B-spline interpolation knots were distributed at the same positions of stereotomography and CRP tomography tests, which is also the same distribution applied to build true velocity model test, the three-layer velocity model of Figure B.11. Ray-model space was initialized with the proposed initialization procedure for NIP wave tomography (Appendix A). Therefore, the initialization procedure returned 100 ray-model samples, each of them composed by one initial model position in depth and one initial model slope. Initial model depth positions are illustrated by Figure B.12.
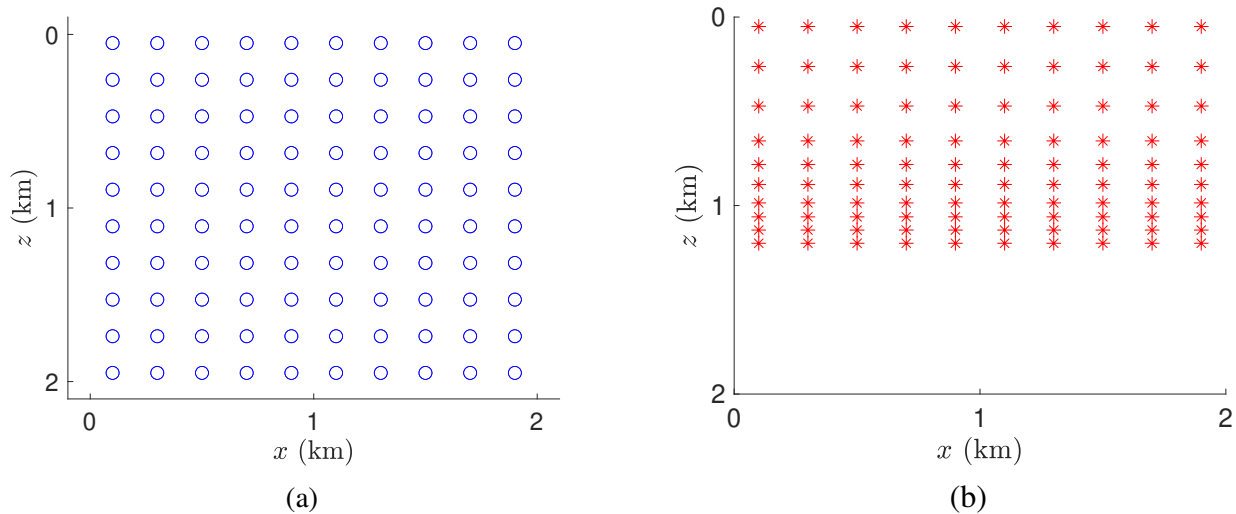
Figure B.12: Three-layer test. (a) Data positions. (b) Initial model positions returned by initialization process under the initial constant velocity model of 1km/s.

Initial regularization weight parameter: Following what was done in stereotomography and CRP tomography tests, a previous search was made in order to find a good initial value for regularization parameter λ. Due to this previous search, λ was set in order to, at first iteration, the relation between the regularization term with respect to the objective function was to equal to 10^{-7}. To calibrate regularization term, the same values used for stereotomography and CRP tomography tests were kept the same: $\epsilon_{xx} = 1$, $\epsilon_{zz} = 10^{-3}$ and $\epsilon_{vv} = 10^{-4}$.

NIP wave tomography results: Under the previous parametrization, NIP wave tomography final results are illustrated by Figure B.13. Although it did not perfectly recover the value of velocity model arround the region of main interest, the second layer, NIP wave tomography could detect the existence of a small layer at the region around 1km in vertical direction. However, a consequence of not recover the exact velocity value for this region was the propagation of the error through the last layer. Furthermore, as a small regularization had to be used, some small velocity oscillations appeared in regions near the seismic line. Nevertheless, the mainframe features of the model were inverted by NIP wave tomography: there are three layers of crescent velocities, the second is the smallest one and, except at regions near the bottom line, final model depth positions were considerably well repositioned. However, some details were not recovered, or recovered with some mistakes. Note that the region near the second layer concentrates the major part of relative error in Figure B.13. These errors are not presented in stereotomography and CRP tomography tests, even when a smaller number of data positions was used.

A question that might be addressed is: what happens if the regularization parameter is increased? The answer is given by Figure B.14, where an initial regularization term, in order to set the relation between regularization term with respect to NIP wave tomography misfit function to a value of 10^5 at the first iteration, was applied.

Figure B.14 shows that increasing initial regularization parameter results in a decrease of the velocity oscillations presented by the final velocity model, which is an expected issue. However, a strong regularization, which corresponds to a strong demand for smoothness features, did not allow the velocity model to recover the two "jumps" presented in true velocity model. This regularized inverted model is obviously worse than the previously presented one. Here, the regularization was "too strong".

On the other hand, decreasing the initial regularization parameter also deteriorates the quality of NIP wave tomography final velocity model, since the oscillations in velocity model become even bigger. Therefore, changing the value of initial regularization parameter, does not seems to be a good way to provide better solutions for NIP wave tomography three-layer test.

Another question that can be addressed is: what happens if the number of data samples given to the problem is increased? In order to investigate this feature, 225 data positions were uniformly distributed through true velocity model test to generate a bigger data space for NIP wave tomography test. The 225 data positions and respective initial model depth positions returned by NIP wave tomography initialization procedure are illustrated by Figure B.15. This test keeps the same parametrization and features of the first test performed.

NIP wave tomography results with 225 **data samples:**   The final model proposed by NIP wave tomography under these conditions is illustrated in Figure B.16. A slightly better inverted velocity model was achieved. This was expected, once more information were initially given as input to the tomographic inversion problem. Note that the solution also presents some kind of improvement of the regularization. For example, the velocity oscillations near the seismic line are not presented at the present final velocity model. In this case, a higher number of input data samples, which corresponds to more internal information, helps to constrain the model. Thus, some kind of internal regularization was provided by the bigger data space. A better initial velocity model would do the same.

Despite the improvements in the final velocity model and inverted model depth positions, a perfect recover of second layer velocity still is a challenge to be solved for NIP wave tomography. The last test succeeded in grow the velocity value until the exact value of second layer velocity. However, a perfect recovering of velocity value was not possible during all the extension of second layer. The consequence, again, is the propagation of the error to the third layer. Nevertheless, the

solution provided by NIP wave tomography, after the introduction of more data samples, is noted better, both for model depth positions and velocity model.

To improve even more the solution, further tests could be done: provide even more input data samples, a better initial velocity model or considering other kind of regularization terms to help the constrain of the model. For example, in Duveneck (2004b), NIP wave tomography is applied with a regularization that assists the velocity model to follow reflector structures. However, the study of more types of regularization terms is not in the scopus of this thesis.

Final remarks for three-layer test: Three-layer test was also performed by slope tomography methods as stereotomography and CRP tomography in this thesis. It has been shown that, with the same parametrization applied here, slope tomogrpahy methods were able to provide a better final velocity model to this problem. Slope tomography techniques do not take into account curvature parameters in data and sythetic spaces. The use of curvature parameters requires extra smoothness of velocity model because continuous third derivatives of velocity models are required to compute related components for Jacobian matrix. Although this requirement was complied by the three-layer test, the use of curvature is more dependent of smoothness of the model than other kinematic parameters. In fact, this feature turns the abrupt velocity variations in vertical direction of three-layer model test, plus the existence of a small layer a the middle of the model, a bigger challenge when curvature parameters are taken into account. This was a very important test for the research addressed by this thesis, since it was decisive to the choice of not incorporate curvature informations in CRP tomography method.

(a)

(b)

(c)

(d)

Figure B.13: Three-layer test - NIP wave tomography results with 100 data points. (a) Inverted velocity model. (b) Vertical slices of inverted (red), true (blue) and initial (yellow) velocity models. Slices were taken at the middle of the models. (c) Inverted model positions (red) and true data positions (blue). (d) Percentage difference between inverted and true velocity models. Note that the region around the second layer concentrates the major part of relative errors.
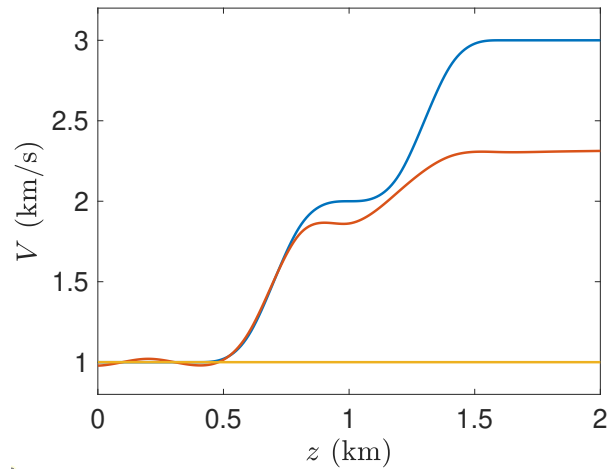
Figure B.14: NIP wave tomography result for three-layer test with 100 data points and an increased level of regularization. Vertical slices of inverted (red), true (blue) and initial (yellow) velocity models are illustrated. Slices were taken at the middle of the model.

(a)

(b)
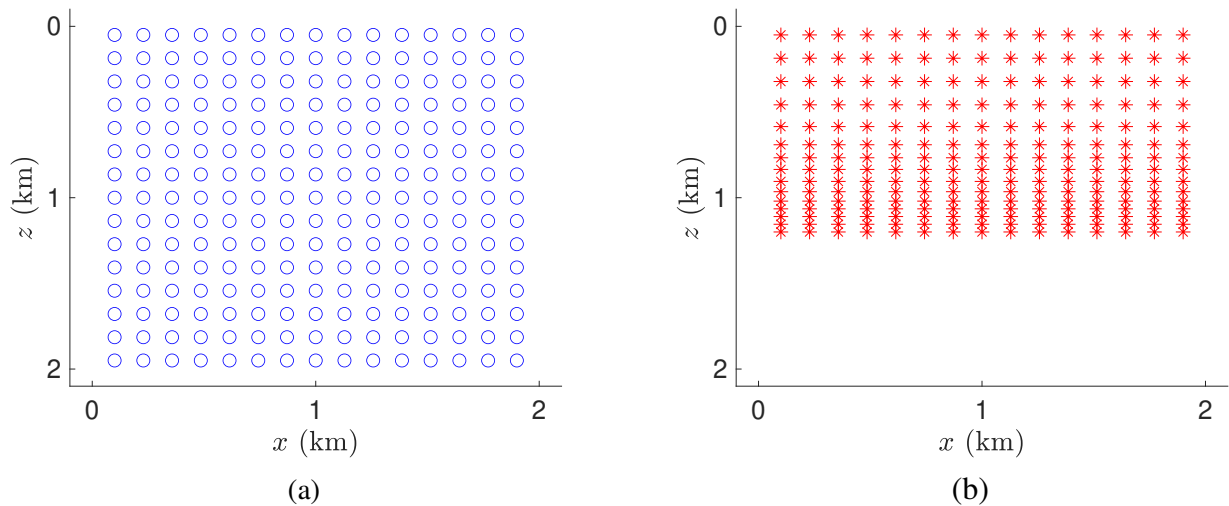
Figure B.15: Three-layer test with 225 data samples. (a) Data positions. (b) Initial model positions returned by NIP wave tomography initialization procedure.
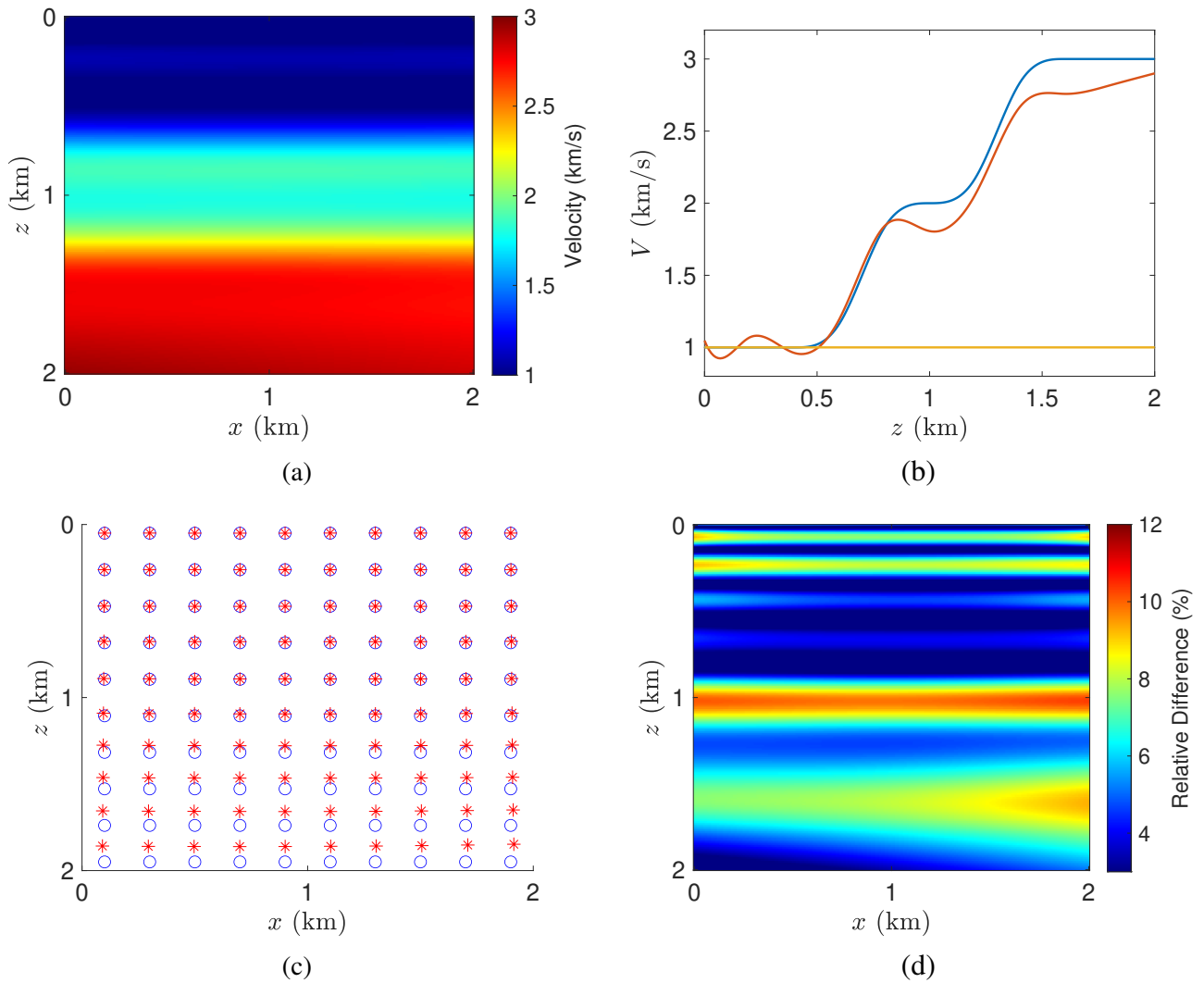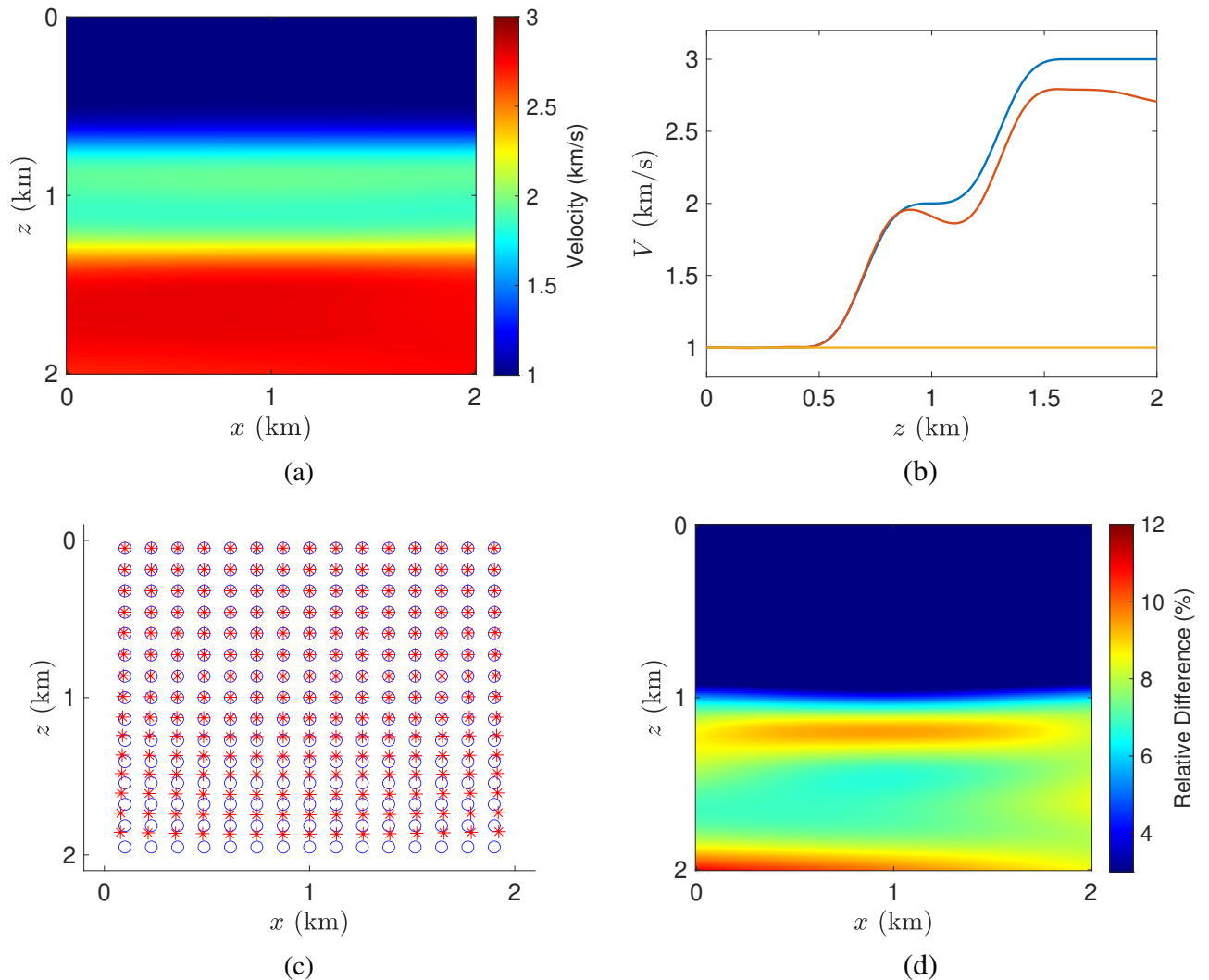
Figure B.16: Three-layer test - NIP wave tomography results with with 225 data samples. (a) Inverted velocity model. (b) Vertical slices of inverted (red), true (blue) and initial (yellow) velocity models. Slices were taken at the middle of the models. (c) Inverted model positions (red) and true data positions (blue). (d) Percentage difference between inverted and true velocity models.

Appendix C

Ray-tracing equations for seismic tomography forward modeling engine

To compute kinematic parameters for seismic tomography synthetic space, forward modeling engine is applied to each iteration of inverse process. For all seismic tomography methods described in this thesis, forward modeling engine accounts for a ray-tracing system. For slope tomography methods, as it is the case of CRP tomography and stereotomography, kinematic ray-tracing is performed in order to generate kinematic parameters as traveltime, positions and slopes. On the other hand, for curvature tomography methods, as it is the case of NIP wave tomography, dynamic-ray tracing has to be applied in order to provide, also, curvature parameters. Current model space provides the necessary boundary initial conditions to perform ray-tracing.

In this appendix, the focus will be at two-dimensional kinematic ray-tracing theory. Therefore, all the equations derived can be used both for CRP tomography and stereotomography methods. Before presenting the system of differential equations used to perform forward modeling engine for slope tomography methods, this appendix will develop some basic concepts of kinematic ray-tracing theory. As NIP wave tomography is addressed and reffered by this thesis, the related system of dynamic-ray tracing will also be presetend, although concepts of paraxial ray-theory will be omitted. As it is not the objective of this appendix to provide a detailed development of ray-theory, the interested reader can consult the classical references Cerveny (2005) and Popov (2002) for a complete development of ray-theory.

Kinematic ray-tracing system: The system of differential equations for CRP tomography and stereotomography forward modeling engine is derived from the *eikonal equation*, which is an asymp-

totic approximation of wave equation solution (see, e.g, Bleistein et al. (2013)). The eikonal equation is given by:

$$||\nabla \mathbf{t}||^2 = \frac{1}{v^2(x, z)}, \tag{C.1}$$

where, in two dimensions, $\nabla \mathbf{t} = \left(\dfrac{\partial t}{\partial x}, \dfrac{\partial t}{\partial z} \right)$ and $v(x, z)$ is the velicty field.

To solve the *eikonal equation*, consider that the ray propagates along a smooth curve parametrized by real parameter s as:

$$\begin{cases} x & = & x(s), \\[2mm] z & = & z(s). \end{cases} \tag{C.2}$$

Denote $x' = \dfrac{dx}{ds}$, and $z' = \dfrac{dz}{ds}$. For the *Lagrangian* $L = L(x', z', x, z)$, the slowness components p_x and p_z of the slowness vector $\mathbf{p}$ are defined by:

$$\begin{cases} p_x & = & \dfrac{\partial L}{\partial x'}, \\[3mm] p_z & = & \dfrac{\partial L}{\partial z'}. \end{cases} \tag{C.3}$$

Thus, the *Hamiltonian* function $H = H(x, z, p_z, p_z)$ is set as:

$$H(x, z, p_z, p_z) = p_x x' + p_z z' - L(x', z', x, z). \tag{C.4}$$

By *Fermat's principal*, given a start point $(x(s_1), z(s_1))$, and a final point $(x(s_2), z(s_2))$ in space, the ray propagates, between these two points, along the curve $(x(s), z(s))$ where the following integral T reaches a minimum:

$$T = \int_{s_1}^{s_2} L(x', z', x, z) ds. \tag{C.5}$$

Applying first variations techniques (see, e.g, Popov (2002)) to the previous integral, *Euler's equations* in *Hamiltonian* form are:

$$
\begin{cases}
x' = \dfrac{\partial H}{\partial p_x}, \\[3mm]
z' = \dfrac{\partial H}{\partial p_z},
\end{cases}
\qquad
\begin{cases}
p'_x = -\dfrac{\partial H}{\partial x}, \\[3mm]
p'_z = -\dfrac{\partial H}{\partial z},
\end{cases}
\tag{C.6}
$$

where $p'_x = \dfrac{p_x}{s}$ and $p'_z = \dfrac{p_z}{s}$.

The solutions of *Euler's equations* describe curves known as *characteristics curves* which, in this particular case, are rays.

Finally, for the point source case, the *Hamiltonian* can be written as (see, e.g, Duveneck (2004b), Popov (2002)):

$$
H(x, z, p_x, p_z) = \frac{v(x,z)}{2}\left(||\nabla \mathbf{t}(x,z)||^2 - \frac{1}{v^2(x,z)} \right) = 0,
\tag{C.7}
$$

with $(p_x, p_z) = \nabla \mathbf{t}$.

Thus, the rays trajectories can be described by the following system of differential equations, given by the characteristics equations:

$$
\begin{cases}
\dfrac{\partial x}{\partial s} = vp_x, \\[3mm]
\dfrac{\partial z}{\partial s} = vp_z,
\end{cases}
\qquad
\begin{cases}
\dfrac{\partial p_x}{\partial s} = -\dfrac{1}{v^2}\dfrac{\partial v}{\partial x}, \\[3mm]
\dfrac{\partial p_z}{\partial s} = -\dfrac{1}{v^2}\dfrac{\partial v}{\partial z}.
\end{cases}
\tag{C.8}
$$

Follows direct by *eikonal equation*:

$$
\begin{cases}
\dfrac{\partial t}{\partial s} = \dfrac{1}{v},
\end{cases}
\tag{C.9}
$$

In three dimension case, surfaces defined by a constant t in *eikonal equation* are called *wavefronts*.

Computation of synthetic kinematic parameters: Equations C.8 and C.9 form the system os differential equations necessary to perform forward modeling engine for CRP tomography method and also stereotomography. For this purpose, initial boundary conditions are given by current model space. Thus, current velocity model (velocity-model space) and initial model depth positions and slopes (ray-model space) are available at each iteration, which is sufficient to numerically solve the

system of equations by some appropriate method. Traditionally, standard Runge-Kutta methods (see, e.g, Dormand and Prince (1980), Press et al. (1988)) are applied to provide numerical solutions for the system of differential equations.

Dynamic ray-tracing system for curvature tomography - basic concepts: For curvature tomography methods, as it is the case of NIP wave tomography, to complete the full computation of synthetic components, it is necessary to derive a way to compute values of curvature of the associated wavefront. This task can be done by paraxial ray theory and the use of ray coordinates system (see, e.g, Cerveny (2005), Popov (2002)). The development of the desired system of differential equations demands application of a considerably more number of accounts, and even approximations, than it is necessary for kinematic ray-tracing system. Thus, as curvature information is not used by the main tomography methods of this thesis, here the system of differential equations will simply be described. Again, the interest reader can consult reference Popov (2002) for a complete development of the demanded equations from paraxial ray-theory.

In a three dimension media, the family of rays corresponding to a certain specified wave may be parameterized by two scalar parameters γ_1 and γ_2 (see, e.g, Popov (2002)). For instance, in the case of a point source, these parameters can be the angles of the spherical polar coordinate system. In two dimension media, only one parameter is necessary. These coordinates, plus eikonal term, form what is called *ray coordinates*.

On the other hand, *ray centered coordinates* is a system of coordinates composed by two orthogonal unit vectors which, at any point of the trajectory described by the specific ray, belong to the plane orthogonal to this ray. Thus, with respect to cartesian coordinates, at any point of the ray trajectory, the unit vectors of the system change their directions. In two dimension media, this system is composed, at a specific point of the ray trajectory, by a unit vector $\mathbf{p}$ parallel to the trajectory, and other unit vector $\mathbf{q}$ orthogonal to the trajectory. This system is of fundamental importance to the devselopment of *paraxial ray theory* and, more generally, *ray perturbation theory* (see, e.g, Farra and Madariaga (1987)).

One of the purposes of dynamic ray tracing is to determine partial derivatives of the central *ray coordinates* with respect to *ray centered coordinates*. In two dimensions, taking γ_1 as the ray coordinate parameter and p and q the scalar coordinates of directions $\mathbf{p}$ and $\mathbf{q}$ respectively, the interested variables, in the context of compute curvatures, are $Q = \dfrac{\partial q}{\partial \gamma_1}$ and $P = \dfrac{\partial p}{\partial \gamma_1}$. After some developments and approximations (see, e.g, Cerveny (2005), Popov (2002)), paraxial ray theory proposes the following system of differential equations to compute these variables:

$$
\begin{cases}
\dfrac{\partial Q}{\partial s} & = & v_s(0,0)P \\[2ex]
\dfrac{\partial P}{\partial s} & = & -\dfrac{1}{v_s(0,0)}\dfrac{\partial^2 v}{\partial q^2}\big|_{q=0}Q,
\end{cases}
\tag{C.10}
$$

where s is a real variable parameter that determines the point of the central ray $(q = p = 0)$ trajectory and $v_s(0,0)$ denotes the velocity at the specific point s where the derivatives are taken. As the interest case for NIP wave tomography is the normal ray of the hypothetical NIP wavefront, the boundary conditions of point source has to be used (see, e.g, Popov (2002)):

$$
P_0 \;\; = \;\; \frac{1}{v_0} \;\;, \;\; Q_0 \;\; = \;\; 0.
\tag{C.11}
$$

Considering wave fronts in a vicinity of central ray, it's possible to show, with some approximations, that (see, e.g, Popov (2002)):

$$
k_s = \frac{1}{R_s} = v_s(0,0)\frac{P}{Q},
\tag{C.12}
$$

where k_s and R_s denotes the curvature and radius of curvature, respectively, of the wave front on the central ray at the specific point s of the central ray trajectory.

Computation of synthetic dynamic parameters: Equations C.10 and C.12, together with initial condition C.11, are sufficient to compute curvature parameters for curvature tomography forward modeling engine. Once again, standard Runge-Kutte methods can be applied to provide numerical solutions for the system of differential equations. The other kinematic paramters also used by curvature tomography methods, as positions, slopes and traveltimes, are computed by the same equations derived before for slope tomography methods.

Before finish the appendix, it is important to mention that the system of differential equations C.10 is a consequence of a set of premisses and approximations that might not be correct in most of the cases. Also, curvature information is the one that is extracted with less reliability from seismic data by CRS stack panels (see, e.g, Faccipieri (2016)). Additionally, the validity of NIP wave theorem (see, e.g, Chernyak and Gritsenko (1979), Hubral (1983)) is required. Then, there is a price to be paid when curvature parameter is used by any tomography method.

Appendix D

B-spline interpolation

Tomographic velocity models have already been described in chapter 3, for stereotomography, and chapter 5, for CRP tomography method. There, brief explanations about velocity models constructed by means of B-spline interpolation were given. In this appendix, B-spline basis functions will be defined and main properties of B-spline interpolation will be summarized. Also, some algorithms to compute B-spline basis functions and respective velocity model derivatives will be given. The interested reader can consult the reference de Boor et al. (1978) for more details about B-spline interpolation.

Firstly introduced in slope tomographies by CDR tomography (see, e.g, Sword Jr (1986), Sword (1987)), all slope tomograpies illustrated by the present thesis uses a velocity model described by a B-spline interpolation scheme. This interpolation processes allows a local control of the velocity model by a reduced number of real coefficients, which stands for a remarkable great property for tomographic iterative process. Moreover, B-spline basis functions, which are invariant over the iterative process, can be constructed by a simple recurisve algorithm. Alos, as it will be showed in this appendix, being generated by B-spline interpolation, tomographic velocity models carry smoothness properties, providing the necessary continuos derivatives to perform ray-traing system in forward modeling step. Furthermore, the demanded derivatives of velocity model for forward modeling step can be easily computed due to B-spline interpolation description. All these properties will be summarized below. First, a definition of B-spline basis function will be provided.

B-spline basis function: Given an arbitrary integer degree $m \geq 0$ and an also arbitrary one-dimensional crescent knot sequence $(x_1, \ldots, x_{k+2})$, with $k \geq m$, a set of $(k + 1 - m)$ B-spline basis functions $\{\beta_{[x_1, \ldots, x_{m+2}]}^{(m)}, \ldots, \beta_{[x_{k-m+1}, \ldots, x_{k+2}]}^{(m)}\}$ are defined on this knot sequence. Each of these

B-spline basis functions is a spline function of degree m defined on a $(x_i, \ldots, x_{i+m+1})$ knot sequence by the recursive algorithm of equations D.1 and D.2, with $i = 1, \ldots, k + 1 - m$. They are spline functions of degree m of minimum lenght, being non-zero only within the respective knot sequence. B-spline basis functions form a basis for the space of spline functions of degree m defined by its values on the given sequence of knots.

A recursive algorithm in m can be used to construct each of the B-spline basis defined by the $(x_i, \ldots, x_{i+m+1})$ knot sequence (see, e.g, de Boor et al. (1978)):

$$\beta^{(m)}_{[x_i,\ldots,x_{i+m+1}]}(x) = \frac{x - x_i}{x_{i+m} - x_i} \beta^{(m-1)}_{[x_i,\ldots,x_{i+m}]}(x) + \frac{x_{i+m+1} - x}{x_{i+m+1} - x_{i+1}} \beta^{(m-1)}_{[x_{i+1},\ldots,x_{i+m+1}]}(x), \qquad (\text{D.1})$$

where, for $m = 0$:

$$\beta^{(0)}_{[x_i,x_{i+1}]}(x) = \begin{cases} 1 & \text{for} \quad x \in [x_i, x_{i+1}), \\ 0 & \text{otherwise} \end{cases} \qquad (\text{D.2})$$

Properties of B-spline basis functions: The main properties of B-pline basis functions are listed bellow. For more properties and proofs of the following statements, the reader can constult reference de Boor et al. (1978):

1. B-spline basis functions of degree m are spline functions of degree m.

2. B-spline basis functions of degree m have continuos derivatives of degree $m - 1$, $m > 0$.

3. $\beta^{(m)}_{[x_i,\ldots,x_{i+m+1}]}(x) = 0$ for $x \notin (x_i, x_{i+m+1})$.

4. $\beta^{(m)}_{[x_i,\ldots,x_{i+m+1}]}(x) \in (0, 1]$ for $x \in (x_i, x_{i+m+1})$.

5. $\sum_{i=-\infty}^{\infty} \beta^{(m)}_{[x_i,\ldots,x_{i+m+1}]}(x) = \sum_{i=j-m}^{j} \beta^{(m)}_{[x_i,\ldots,x_{i+m+1}]}(x) = 1$ for $x \in [x_i, x_{i+m+1}]$.

6. $\frac{d}{dx} \beta^{(m)}_{[x_i,\ldots,x_{i+m+1}]}(x) = m \left(\frac{1}{x_{i+m} - x_i} \beta^{(m)}_{[x_i,\ldots,x_{i+m+1}]}(x) - \frac{1}{x_{1+m+1} - x_{i+1}} \beta^{(m)}_{[x_i,\ldots,x_{i+m+1}]}(x) \right), m > 0$.

Previous properties state some facts already mentioned as that B-spline basis functions are spline functions of degree m (property one) of minimum length (property 3). However, the last properties is of fundamental importance for an implementation point of view, since it states a simple recursive algorithm to evaluate derivatives of B-spline basis functions. These derivatives are demanded

both for ray-tracing system (forward modeling step) (see Appendix C) and computation of regularization matrix (see Appendix E).

Construction of two-dimension velocity models by B-spline interpolation: For our present thesis, tomography methods are restricted to two dimension space. Therefore, two-dimension velocity models are required. Hence, two sequence of knots have to be settled, one in horizontal direction and other in vertical direction. The cartesian product of these sequences defines the mesh where the velocity model will be constructed. Hence, consider a set of crescent spatial knots $(x_1, \ldots, x_{M_{vx}})$ in the horizontal direction and a set of crescent spatical knots $(z_1, \ldots, z_{M_{vz}})$ in the vertical direction (here, it is assumed that z axis points downward). For tomography applications, cubic B-splines basis functions (degree 3) were considered, which assures continuous derivatives required for tomographic inverse problem. Therefore, each B-spline basis function for horizontal direction $\beta_i(x)$ (remind that B-spline basis functions are one-dimensional real functions) is defined at a sequence of 5 crescent knots $(x_i, \ldots, x_{i+4})$, while each B-spline basis function for vertical direction $\beta_j(z)$ is defined at a sequence of 5 crescent knots $(z_j, \ldots, z_{j+4})$. To allow the relation of one interpolation coefficient fo each knot of the interpolation grid (mesh), two border knots will be added to each sequence of knots. Therefore, consider $(x_{i-1}, x_0, x_1, \ldots, x_{M_{vx}}, x_{M_{vx}+1}, x_{M_{vx}+2})$ as the expanded set of crescent spatial knots for horizontal direction with border knots and $(z_{i-1}, z_0, z_1, \ldots, z_{M_{vz}}, z_{M_{vz}+1}, x_{M_{vz}+1})$ as the expanded set of crescent spatial knots for vertical direction.

Under the above sets of spatial knots, given a set of real coefficients $\{v_{ij}\}$, for $i = 1, \ldots, M_{vx}$ and $j = 1, \ldots, M_{vz}$, the velocity model is described by following linear combination of B-spline basis functions defined by the proposed grid of interpolation:

$$v(x, z) = \sum_{j=1}^{M_{vz}} \sum_{i=1}^{M_{vx}} v_{ij} \beta_i(x) \beta_j(z). \tag{D.3}$$

Following the previous paragraphs, at the interval defined by the given knot sequences, B-spline basis functions form a basis for the space of spline functions of degree m. Therefore, on that specific knot sequence, every spline function of degree m can be written as a linear combination of the respective B-spline basis functions. On the other hand, every linear combination of these B-spline basis functions generates a spline function of degree m defined at the respective interval. Therefore, velocity models constructed by means of linear combination of B-spline basis functions are, in fact, spline velocity models of degree m, which assures the important smoothness properties related to any spline functions (see, e.g, de Boor et al. (1978)).

Computation of velocity model derivatives: Tomographic inversion problems as stereotomogra-
phy, CRP tomography and NIP wave tomography, require frequent evaluations of derivatives of the
velocity model as, for example, during dynamic-ray propagation or construction of regularization ma-
trix. The use of B-spline interpolation scheme to build the velocity model also allows a faster way to
evaluate these derivatives. Since B-spline basis functions of degree m are basis for spline functions
of degree m at the same knot sequence, the n-th derivative of the model velocity $v(x, z)$ in respect to
x coordinate is given by:

$$\frac{\partial^n v(x, z)}{\partial x^n} = \sum_{j=1}^{M_{vz}} \sum_{i=1}^{M_{vx}} v_{ij} \frac{d^n \beta_i(x)}{dx^n} \beta_j(z). \tag{D.4}$$

The derivatives with respect to z coordinate and mixed derivatives follow directly. Remind
that B-spline basis functions are invariant through the inverse process. Therefore, together with the
construction of B-spline basis functions, their (invariant) derivatives can be computed at the beginning
of the iterative process. Equation D.4 and respective equations with respect to z direction or higher
order derivatives are used to update velocity model derivative at subsequent iterations. An algorithm
for the computation of B-spline basis functions derivatives was already described by property 6 above.

Number of interpolation knots: The number of interpolation knots is an arbitrary choice made by
the user at the beginning of the tomograpic method. The choice of the number of knots, as well as
their localization, is important to the inversion problem. It depends on many aspects like the degree of
smoothness desired for the velocity model or the number of parameters desired to be invert. The more
is the number of coefficients, more is the capability of the model velocity to recover small details of
true velocity model. On the other hand, the more is the number of coefficients, more computational
effort will be demanded.

Appendix E

Regularization matrix for CRP tomography and stereotomography

The regularization term used in this thesis for seismic tomography applications measures a weighted sum of three integrals, two related to squared second order derivatives of the velocity model with respect to the two cartesian directions, and the other related to squared velocity. In terms:

$$R_v(\mathbf{m}^{vel}) = \int_z \int_x \left(\epsilon_{xx} \left(\frac{\partial^2 v(x,z)}{\partial x^2} \right)^2 + \epsilon_{zz} \left(\frac{\partial^2 v(x,z)}{\partial z^2} \right)^2 + \epsilon_{vv} v^2(x,z) \right) dx dz. \qquad (E.1)$$

In chapters three and five, we stated that this regularization term could be written as a matrix expression, by the use of a regularization matrix $\mathbf{R}^{(v)}$. In terms:

$$\mathbf{R}^{(v)}(\mathbf{m}^{vel}) = \mathbf{m}^{vel^T} \mathbf{R}^{(v)} \mathbf{m}^{vel}, \qquad (E.2)$$

where $\mathbf{m}^{vel}$ is the model vector of current B-spline interpolation coefficients. The B-spline coefficients v_{ij} at the (i, j)-knot of interpolation is given by the w-th component v_w of the velocity model vector $\mathbf{m}^{vel}$, in which:

$$w = (i - 1)M_{vz} + j \quad \text{for} \quad i = 1, \ldots, M_{vx} \quad \text{and} \quad j = 1, \ldots, M_{vz}. \qquad (E.3)$$

In this appendix, we will show how to construct the regularization matrix $\mathbf{R}^{(v)}$.

Using B-spline interpolation properties, the integral over the squared second order derivative of velocity model with respect to x-coordinate can be computed as follows:

$$\int_z \int_x \left(\frac{\partial^2 v(x,z)}{\partial x^2} \right)^2 dxdz = \int_z \int_x \left(\sum_{i=1}^{M_{vx}} \sum_{j=1}^{M_{vz}} v_{ij} \frac{\partial^2 \beta_i(x)}{\partial x^2} \beta_j(z) \sum_{k=1}^{M_{vx}} \sum_{l=1}^{M_{vz}} v_{kl} \frac{\partial^2 \beta_k(x)}{\partial x^2} \beta_l(z) \right) dxdz \tag{E.4}$$

$$= \sum_{i=1}^{M_{vx}} \sum_{j=1}^{M_{vz}} \sum_{k=1}^{M_{vx}} \sum_{l=1}^{M_{vz}} v_{ij} v_{kl} \int_x \frac{\partial^2 \beta_i(x)}{\partial x^2} \frac{\partial^2 \beta_k(x)}{\partial x^2} dx \int_z \beta_j(z) \beta_l(z) dz \tag{E.5}$$

$$= \sum_{i=1}^{M_{vx}} \sum_{j=1}^{M_{vz}} \sum_{k=1}^{M_{vx}} \sum_{l=1}^{M_{vz}} v_{ij} v_{kl} R_{ik}^x R_{jl}^{vz}, \tag{E.6}$$

where R_{ik}^x and R_{jl}^{vz} are real components of matrices $\mathbf{R}^x$ and $\mathbf{R}^{vz}$, both with dimension $M_{vx} M_{vz} \times M_{vx} M_{vz}$, as follows:

$$[\mathbf{R}^x]_{ik} = R_{ik}^x = \int_x \frac{\partial^2 \beta_i(x)}{\partial x^2} \frac{\partial^2 \beta_k(x)}{\partial x^2} dx, \tag{E.7}$$

$$[\mathbf{R}^{vz}]_{jl} = R_{jl}^{vz} = \int_z \beta_j(z) \beta_l(z) dz. \tag{E.8}$$

Now, consider the matrix $\mathbf{R}^{xx}$ of dimension $M_{vx} M_{vz} \times M_{vx} M_{vz}$, where which element $R_{[(i-1)M_{vz}+j,(k-1)M_{vz}+l]}^{xx}$ is given by:

$$R_{[(i-1)M_{vz}+j,(k-1)M_{vz}+l]}^{xx} = R_{ik}^x R_{jl}^{vz}. \tag{E.9}$$

Hence, equation E.6 can be rewritten as:

$$\int_z \int_x \left(\frac{\partial^2 v(x,z)}{\partial x^2} \right)^2 dxdz = \sum_{i=1}^{M_{vx}} \sum_{j=1}^{M_{vz}} \sum_{k=1}^{M_{vx}} \sum_{l=1}^{M_{vz}} v_{ij} v_{kl} R_{ik}^x R_{jl}^{vz} \tag{E.10}$$

$$= \sum_{r=1}^{M_{vx} M_{vz}} \sum_{s=1}^{M_{vx} M_{vz}} v_r^{vel} v_s^{vel} R_{rs}^{xx} = \mathbf{m}^{vel^T} \mathbf{R}^{xx} \mathbf{m}^{vel}. \tag{E.11}$$

Following the same steps, the integral over the squared second order derivative of velocity model with respect to the z-coordinate can be computed as follows:

$$\int_z \int_x \left(\frac{\partial^2 v(x,z)}{\partial z^2} \right)^2 dxdz = \int_z \int_x \left(\sum_{i=1}^{M_{vx}} \sum_{j=1}^{M_{vz}} v_{ij} \frac{\partial^2 \beta_j(x)}{\partial z^2} \beta_i(x) \sum_{k=1}^{M_{vx}} \sum_{l=1}^{M_{vz}} v_{kl} \frac{\partial^2 \beta_l(x)}{\partial z^2} \beta_k(x) \right) dxdz \tag{E.12}$$

$$= \sum_{i=1}^{M_{vx}} \sum_{j=1}^{M_{vz}} \sum_{k=1}^{M_{vx}} \sum_{l=1}^{M_{vz}} v_{ij} v_{kl} \int_z \frac{\partial^2 \beta_j(z)}{\partial z^2} \frac{\partial^2 \beta_l(z)}{\partial z^2} dz \int_x \beta_i(x) \beta_k(x) dx \tag{E.13}$$

$$= \sum_{i=1}^{M_{vx}} \sum_{j=1}^{M_{vz}} \sum_{k=1}^{M_{vx}} \sum_{l=1}^{M_{vz}} v_{ij} v_{kl} R_{jl}^z R_{ik}^{vx}, \tag{E.14}$$

where R_{jl}^z and R_{ik}^{vx} are real components of matrices $\mathbf{R}^z$ and $\mathbf{R}^{vx}$, both with dimension $M_{vx} M_{vz} \times M_{vx} M_{vz}$, as follows:

$$[\mathbf{R}^z]_{jl} = R_{jl}^z = \int_z \frac{\partial^2 \beta_j(z)}{\partial z^2} \frac{\partial^2 \beta_l(z)}{\partial z^2} dz, \tag{E.15}$$

$$[\mathbf{R}^{vx}]_{ik} = R_{ik}^{vx} = \int_x \beta_i(x) \beta_k(x) dx. \tag{E.16}$$

Therefore, consider the matrix $\mathbf{R}^{zz}$ of dimension $M_{vx} M_{vz} \times M_{vx} M_{vz}$, where which element $R_{[(i-1)M_{vz}+j,(k-1)M_{vz}+l]}^{zz}$ is given by:

$$R_{[(i-1)M_{vz}+j,(k-1)M_{vz}+l]}^{zz} = R_{jl}^z R_{ik}^{vx}. \tag{E.17}$$

Equation E.14 can be rewritten as:

$$\int_z \int_x \left(\frac{\partial^2 v(x,z)}{\partial z^2} \right)^2 dxdz = \sum_{i=1}^{M_{vx}} \sum_{j=1}^{M_{vz}} \sum_{k=1}^{M_{vx}} \sum_{l=1}^{M_{vz}} v_{ij} v_{kl} R_{jl}^z R_{ik}^{vx} \tag{E.18}$$

$$= \sum_{r=1}^{M_{vx} M_{vz}} \sum_{s=1}^{M_{vx} M_{vz}} v_r^{vel} v_s^{vel} R_{rs}^{zz} \tag{E.19}$$

$$= \mathbf{m}^{vel^T} \mathbf{R}^{zz} \mathbf{m}^{vel}. \tag{E.20}$$

Furthermore, note that the integral of the squared velocity model can be computed by:

$$\int_z \int_x v^2(x,z)dxdz = \int_z \int_x \left(\sum_{i=1}^{M_{vz}} \sum_{j=1}^{M_{vx}} v_{ij}\beta_i(x)\beta_j(z) \sum_{k=1}^{M_{vz}} \sum_{l=1}^{M_{vx}} v_{kl}\beta_k(x)\beta_l(z) \right) dxdz \qquad \text{(E.21)}$$

$$= \sum_{i=1}^{M_{vz}} \sum_{j=1}^{M_{vx}} \sum_{k=1}^{M_{vz}} \sum_{l=1}^{M_{vx}} v_{ij}v_{kl} \int_x \beta_i(x)\beta_k(x)dx \int_z \beta_j(z)\beta_l(z)dz \qquad \text{(E.22)}$$

$$= \sum_{i=1}^{M_{vz}} \sum_{j=1}^{M_{vx}} \sum_{k=1}^{M_{vz}} \sum_{l=1}^{M_{vx}} v_{ij}v_{kl}R_{ik}^{vx}R_{jl}^{vz}. \qquad \text{(E.23)}$$

Considere the matrix $\mathbf{R^{vv}}$ of dimension $M_{vx}M_{vz} \times M_{vx}M_{vz}$ where which element $R_{[(i-1)M_{vz}+j,(k-1)M_{vz}+l]}^{vv}$ is given by:

$$R_{[(i-1)M_{vz}+j,(k-1)M_{vz}+l]}^{vv} = R_{ik}^{vx}R_{jl}^{vz}. \qquad \text{(E.24)}$$

Therefore:

$$\int_z \int_x v^2(x,z)dxdz = \sum_{i=1}^{M_{vz}} \sum_{j=1}^{M_{vx}} \sum_{k=1}^{M_{vz}} \sum_{l=1}^{M_{vx}} v_{ij}v_{kl}R_{ik}^{vx}R_{jl}^{vz}. \qquad \text{(E.25)}$$

$$= \sum_{r=1}^{M_{vx}M_{vz}} \sum_{s=1}^{M_{vx}M_{vz}} v_r^{vel}v_s^{vel}R_{rs}^{vv} \qquad \text{(E.26)}$$

$$= \mathbf{m}^{vel^T}\mathbf{R}^{vv}\mathbf{m}^{vel}. \qquad \text{(E.27)}$$

Whith the help of matrices $\mathbf{R}^{xx}$, $\mathbf{R}^{zz}$ and $\mathbf{R}^{vv}$, regularization term E.1 can be rewritten as:

$$R_v(\mathbf{m}^{vel}) = \int_z \int_x \left(\epsilon_{xx} \left(\frac{\partial^2 v(x,z)}{\partial x^2} \right)^2 + \epsilon_{zz} \left(\frac{\partial^2 v(x,z)}{\partial z^2} \right)^2 + \epsilon_{vv} v^2(x,z) \right) dxdz \qquad \text{(E.28)}$$

$$= \mathbf{m}^{vel^T} \left(\epsilon_{xx}\mathbf{R}^{xx} + \epsilon_{zz}\mathbf{R}^{zz} + \epsilon_{vv}\mathbf{R}^{vv} \right) \mathbf{m}^{vel}, \qquad \text{(E.29)}$$

$$= \mathbf{m}^{vel^T}\mathbf{R}^{(v)}\mathbf{m}^{vel}, \qquad \text{(E.30)}$$

where the regularization matrix $\mathbf{R}^{(v)}$ of equation E.2 is given by a weighted sum of the matrices $\mathbf{R}^{xx}$, $\mathbf{R}^{zz}$ and $\mathbf{R}^{vv}$:

$$\mathbf{R}^{(v)} = \epsilon_{xx}\mathbf{R}^{xx} + \epsilon_{zz}\mathbf{R}^{zz} + \epsilon_{vv}\mathbf{R}^{vv}. \tag{E.31}$$

In order to keep the propose of smoothness regularization operator, the weight parameters are chosen such that $\epsilon_{xx} >> \epsilon_{vv}$ and $\epsilon_{zz} >> \epsilon_{vv}$. However, to turn $\mathbf{R}^{(v)}$ a positive definite matrix, the parameter ϵ_{vv} has to be positive.

Appendix F

Equations of CRP tomography

In the following, the equations needed for CRP tomography are described and briefly discussed. Those equations are, in principle, valid for a homogeneous (constant-velocity) 2D acoustic medium. In a locally-event framework, these equations are viewed as parametric expressions, in which those parameters are independently inverted for individually picked input-data points. As such, those parameters vary from point to point.

Here, local events of interest are primary reflections or diffractions. Each local event is specified by a data point, called the reference or central point, together with a set of neighboring points that belong to that event. Typically the central point of a local event is user selected (e.g., picked). A set of associated parameters of the central point are also supposed to be picked or extracted from the input data.

Apertures of a local event: In the following, all expressions under consideration refer to a target local event, being defined by the parameters its central point. Such expressions are designed to approximate the traveltime and associate parameters that pertain to that local event in the neighborhood of the central point. As such, those expressions are expected to be valid only in adequately small coordinate apertures relative to those of the central point. It is to observed that such apertures are, in general, empirically specified by the user.

Primary-reflection traveltimes from a same reflector: For a fixed (unknown) reflector, we consider the relationship of primary-reflection traveltimes for different source-receiver pairs. Referring to Figure F.1, we consider, under midpoint and half-offset coordinates, the correspondence

$$(\xi_0, h_0, t_0) \Longleftrightarrow (\xi, h, t), \tag{F.1}$$

in which the reference data vector (ξ_0, h_0, t_0) consists of the midpoint and half-offset coordinates (ξ_0, h_0) of the (reference) source-receiver pair and t_0 the (reference) two-way traveltime of the primary reflection ray of an unknown depth reflector. The data vector (ξ, h, t) of a neighboring reflection ray defines a reflection ray of the same reflector.
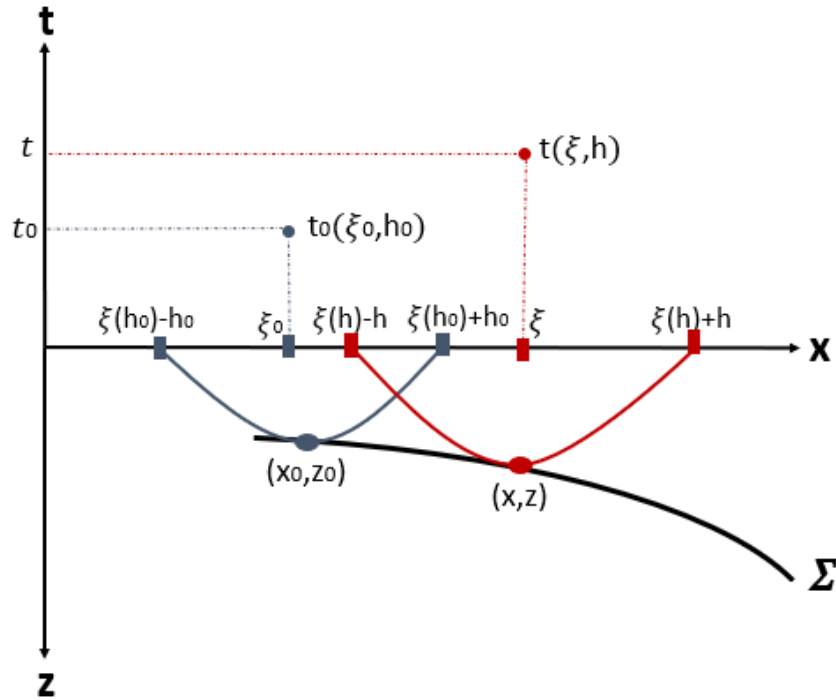

Figure F.1: Illustration of data vectors of reference ray and neighboring reflection ray of the same reflector.

Note that the (unknown) reflection points on the reflector of the two rays are, in general, different. Following Santos et al. (1997), we have the relation

$$t^2(\xi, h; \xi_0, h_0, t_0) = \frac{4h^2}{V_0^2} + \frac{4h^2 t_{n_0}^2}{u^2(\xi, h; \xi_0, h_0)},$$
$$t_{n_0} = \sqrt{t_0^2 - \frac{4h_0^2}{V_0^2}}, \tag{F.2}$$

and

$$u(\xi, h; \xi_0, h_0) = \sqrt{(h + h_0)^2 - (\xi - \xi_0)^2} + s\sqrt{(h - h_0)^2 - (\xi - \xi_0)^2},$$

(F.3)

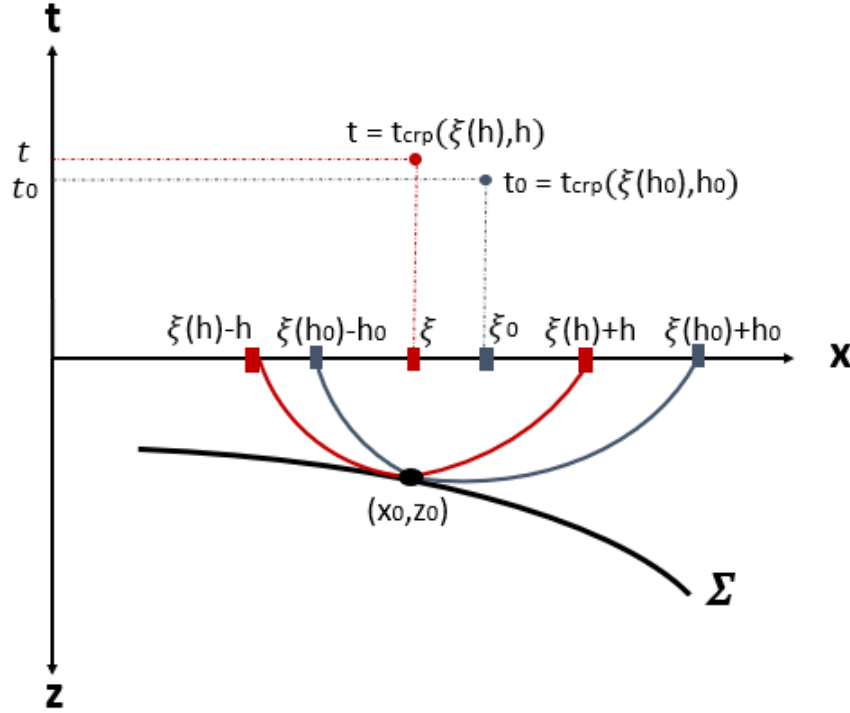$$s = \mathrm{sgn}(h^2 - h_0^2) = \begin{cases} -1 & (h^2 < h_0^2), \\ +1 & (h^2 > h_0^2). \end{cases}$$

Figure F.2: Point $\mathbf{P} = (s, r.a_s, a_r, t)$ within the CRP gather $\mathcal{G}(\mathbf{P}_0)$ attached to a central point $\mathbf{P}_0 = (s_0, r_0.a_{s_0}, a_{r_0}, t_0)$. Ray parameters (a_s, a_r) and (a_{s_0}, a_{r_0}) are not shown.

It is also instructive to observe that the traveltime slopes in midpoint and half-offset direc-tions $a_\xi = (\partial t/\partial \xi)(\xi, h)$ and $a_h = (\partial t/\partial h)(\xi, h)$ are not independent. In fact, this is a consequence of Snell's law. Please note that a_ξ refer to the slope of the common-offset (CO) traveltime defined for offset h and evaluated at midpoint ξ. On the other hand, a_h represents the slope of common-midpoint (CMP) defined for offset ξ and evaluated at half-offset h. As shown in (Coimbra et al., 2016b, equa-tion B-5 with different notation), we have that

$$a_h = \frac{2ht(4 - a_\xi^2 V_0^2)}{V_0^2 t^2 + 4h^2 + \sqrt{16h^4 + 4h^2 t^2 V_0^2(a_\xi^2 V_0^2 - 2) + t^4 V_0^4}},$$

(F.4)

CRP gather: In the case the primary-reflection rays defined by (ξ_0, h_0, t_0) and (ξ, h, t) share the same (unknown) reflection point, it turns out (Coimbra et al., 2016b, equation A-10 with different notation) that the following midpoint relation $\xi = \xi(h)$ holds:

$$\xi(h) - \xi_0 = \frac{2\Upsilon_0(h^2 - h_0^2)}{\sqrt{\Upsilon_0^2\Gamma^2 + 2t_{n_0}^4 + 2\sqrt{t_{n_0}^8 + \Upsilon_0^2 t_{n_0}^4 \Gamma^2 + 16\Upsilon_0^4 h_0^2 h^2}}}, \tag{F.5}$$

$$\Gamma = 2\sqrt{h^2 + h_0^2} \quad \text{and} \quad \Upsilon_0 = t_0 a_{\xi_0}.$$

CRP traveltime: Having obtained the coordinates $(\xi(h), h)$ of all source-receiver pairs that pertain to the CRP gather defined by the central data-point (ξ_0, h_0, t_0), the CRP traveltime $t_{CRP}(h) = t_{CRP}(h; \xi_0, h_0, t_0)$ is simply given by equation F.2 under the substitution of $\xi(h)$ as provided by equation F.5. We find

$$t_{CRP}^2(h) = t(\xi(h), h) = \frac{4h^2}{V_0^2} + \frac{4h^2 t_{n_0}^2}{u^2(\xi(h), h; \xi_0, h_0)} \tag{F.6}$$

CRP slopes: As shown in (Coimbra et al., 2016b, equation 22 with a different notation), within a CRP gather, slopes a_ξ at a point (ξ, h, t) relates to the slope a_ξ in the vicinity of the reference point (ξ_0, h_0, t_0) by the expression

$$a_\xi = a_{\xi_0}\left(\frac{t_n^2 t_0}{t_{n_0}^2 t}\right). \tag{F.7}$$

CRP parameter relations: As a consequence of equations F.2 to F.7, for a point $(\xi(h), h, t)$ within a CRP defined by its reference point (ξ_0, h_0, t_0) and with half-offset h close to h_0, we have the full-parameter correspondence

$$\mathbf{P}_0 = (\xi_0, h_0, a_{\xi_0}, a_{h_0}, t_0) \Longleftrightarrow \mathbf{P} = (\xi(h), h, a_\xi, a_h, t), \tag{F.8}$$

For the present purposes, an important consequence of this result is that, stereotomographic independent picked/extracted from the input data are replaced, in CRP tomography, by corresponding CRP gathers. As such, CRP tomography can benefit from a far greater coverage and redundancy.

Source-receiver coordinates: The above equations, all of them expressed in midpoint and half-offset coordinates (ξ, h), can be recast in source-receiver coordinates (s, r). For that we use the coordinate transformation

$$\xi = (r + s)/2, \quad h = (r - s)/2, \tag{F.9}$$

from which

$$a_\xi = \frac{dt}{d\xi} = \frac{dt}{dr}\frac{dr}{d\xi} + \frac{dt}{ds}\frac{ds}{d\xi} = a_r + a_s,$$

$$\tag{F.10}$$

$$a_h = \frac{dt}{dh} = \frac{dt}{dr}\frac{dr}{dh} + \frac{dt}{ds}\frac{ds}{dh} = a_r - a_s,$$

with analogous transformations for (ξ_0, h_0) and (a_{ξ_0}, a_{h_0}). Substitution into all the above equations provide equivalent ones in source-receiver coordinates.

Appendix G

Example of CRP tomography implementation

In the following link, the reader can find some examples of CRP tomography implementation used to perform some of the numerical tests that illustrate this thesis:

`https://github.com/hpg-cepetro/ignacio_g_phd_crp_tomography`